POROUS HYBRID MATERIALS FOR HETEROGENEOUS CATALYSIS AND GAS
STORAGE

David Joseph Mihalcik

A dissertation submitted to the faculty of the University of North Carolina at Chapel Hill in partial fulfillment of the requirements for the degree of Doctor of Philosophy in the Department of Chemistry.

Chapel Hill
2009

Approved by:

Professor Wenbin Lin

Professor Cynthia K. Schauer

Professor Jeff Johsnon

Professor Joseph Templeton

Professor Marcey Waters

ABSTRACT

DAVID JOSEPH MIHALCIK: Porous Hybrid Materials for Heterogeneous Catalysis and
Gas Storage
(Under the direction of Wenbin Lin)

A series of new Ru(diphosphine)(diamine)Cl$_2$ complexes with siloxy pendant groups
was synthesized and immobilized on mesoporous silica nanoparticles (MSNs) with the hope
of generating highly active heterogeneous catalysts by taking advantage of the very large
channel diameters (~2-5 nm) and short diffusion lengths for the substrates as a result of
nanoparticle sizes of ~300-1000 nm. Upon activation with base co-catalysts, these new Ru
complexes were highly active for homogeneous asymmetric hydrogenation of ketones and
racemic α-branched arylaldehydes with enantiomeric excess (ee) up to 94 and 99%,
respectively. These Ru complexes were readily immobilized onto several types of MSNs via
the siloxy functionalities and the immobilized Ru precatalysts were highly active for the
asymmetric hydrogenation of ketones with up to 82% ee and α-branched arylaldehydes with
ee's of up to 97%.

Highly porous and robust metal organic frameworks (MOFs) were also synthesized
for hydrogen storage and for potential use as asymmetric catalysts. 4,8-connected MOFs of
the **scu** topology based on copper paddlewheels and aromatic-rich octa-carboxylic acid
bridging ligands were synthesized in order to overcome the tendency of MOFs to undergo
framework distortion upon solvent removal. The rigidified MOFs are capable of storing up
to 2.5 wt% of H$_2$ at 1 bar (77 K), and 5.5 wt% of H$_2$ at 30 bar (77 K). A series of homochiral
porous MOFs were synthesized using bridging ligands containing the chiral BINAP oxide

functionalities. The easily accessible catalytic sites make these MOFs interesting candidates

for applications in heterogeneous asymmetric catalysis.

ACKNOWLEDGEMENTS

First and foremost I would like to thank my advisor Dr. Wenbin Lin. From day one he has set the bar high and pushed me to achieve my potential and beyond. His passion for research is infectious and his relentless pursuit of cutting edge science is present day in and day out. I hope to take away from this experience many of the scientific ideals and principles Wenbin stressed from the beginning. I am very grateful to have been given the chance to perform research at this level, under a research scientist that holds such high expectations for himself and those around him.

I would also like to thank some of the colleagues I have had the privilege of working with in the Lin lab. Dr. Aiguo Hu taught me a great deal about organic synthesis and catalysis when I first started. It has been a pleasure working with Dr. Liqing (Sam) Ma whose love of chemistry and devotion to learning and mentoring has helped to make the lab what it is today. Furthermore, I am grateful for the friends I have made in the lab during my time here. Their friendship has made the lab a very enjoyable and rewarding place to work everyday.

Lastly, I would like to thank my wonderful and loving family. Without their encouragement and support, the pursuit of a degree away from home would have been much more difficult. My parents have helped make the place that I call home a place of happiness, love, and safety. Without the past memories I have of my home and family, and those I wish to make in the future, none of this would have been possible.

TABLE OF CONTENTS

Page

Chapter

LIST OF TABLES

LIST OF FIGURES

xiv

LIST OF SCHEMES

LIST OF ABBREVIATIONS

Å	Angstrom
Al^{3+}	aluminum (III) ion
ALB	Al-Li-bis(binaphthoxide)
Ar	aromatic ring
atm	atmosphere
BBr_3	boron tribromide
BET	Brunauer, Emmett, Teller
BDC	1,4-benzenedicarboxylic acid (IRMOF-1)
BINAP	2,2'-bis(diphenylphosphino)-1,1'-binaphthyl
BINAPO	2,2'-bis(diphenylphosphoryl)-1,1'-binaphthyl
BINOL	1,1'-binaphthyl-2,2'-diol
BJH	Barrett, Joyner, Holenda
BnBr	benzyl bromide
BPDC	2,2'-bipyridine-4,4'-dicarboxylate
n-BuLi	*n*-butyl lithium
n-BuOH	*n*—butyl hydroxide
Br_2	bromine
BTB	benzene-1,2,3-tricarboxylate (MOF-177)
BTC	benzene-1,3,5-tricarboxylate (HKUST-1)

bs	broad singlet
°C	degrees Celsius
CBBDC	1,2-dihydrocyclobutabenzene-3,6-dicarboxylic acid (IRMOF-6)
cc	cubic centimeters
Cd^{2+}	cadmium (II) ion
$CDCl_3$	deuterated chloroform
CD_3OD	deuterated methanol
CH_2Cl_2	dichloromethane
Cl^-	chloride anion
ClC_2H_4Cl	dichloroethane
ClO_4^-	perchlorate anion
Co^{2+}	cobalt (II) ion
Cod	cyclooctadiene
CO_2	carbon dioxide
Cr^{3+}	chromium (III) ion
CsF	cesium fluoride
Cu^{2+}	copper (II) ion
CuI	copper iodide
d	days
DABCO	1,4-diazabicyclo[2.2.2]octane
DACH	1,2-diaminocyclohexane
DCP	direct current plasma spectroscopy
DEF	*N,N*-diethylformamide

DHBDC	2,5-Dihydroxyterephtalic acid (MOF-74)
DME	ethylene glycol dimethyl ether
DMF	*N,N*-dimethylformamide
DMSO	deuterated dimethyl sulfoxide
DOE	Department of Energy
DPEN	1,2-diphenylethylenediamine
EA	ethyl acetate
e.e.	enantioselectivity
ED	1,2-ethylenediamine
ESI-MS	electrospray ionization mass spectrometry
EtOH	ethanol
Fe^{3+}	iron (III) ion
FT-IR	Fourier transform infrared spectroscopy
f.u.	formula unit
g	gram
GC	gas chromatography
GCMC	Grand Conical Monte Carlo
h	hour
H_2	hydrogen molecule
HCl	hydrochloric acid
HK	Horvath-Kawazoe
^{1}H NMR	proton nuclear magnetic resonance spectroscopy
H_2O	water

H_2O_2	hydrogen peroxide
HPDC	3,5-pyrazoledicarboxylic (IRMOF-11)
HPLC	high performance liquid chromatography
H_2SO_4	sulfuric acid
Hz	hertz
ICP-MS	inductively coupled plasma mass spectrometry
IR	infrared spectroscopy
K	Kelvin
KO^tBu	potassium *tert*-butoxide
La^{3+}	lanthanum (III) ion
$La(O^iPr)_3$	lanthanum (III) isopropoxide
$LiAlH_4$	lithium aluminum hydride
m	minutes
M	molarity
m^2	square meters
MCM	Mobil composition of matter
MeOH	methanol
Mes	mesitylene
Mg^{2+}	magnesium (II) ion
mg	milligram
$MgSO_4$	magnesium sulfate
mL	milliliter
mm	millimeter

Mn^{2+}	manganese (II) ion
MOF	metal-organic frameowork
MSNs	mesoporous silica nanospheres
m/z	mass to charge ratio
N	nitrogen
N_2	nitrogen molecule
NaOCl	sodium hypochlorite
NaOH	sodium hydroxide
$NaHCO_3$	sodium bicarbonate
NEt_3	triethylamine
Ni^{2+}	nickel (II) ion
$NiCl_2(dppe)$	$NiCl_2[(C_6H_5)_2PCH_2CH_2P(C_6H_5)_2]$
nm	nanometer
NMR	nuclear magnetic resonance
NOC	naphthalene-2,6-dicarboxylate (IRMOF-8)
NO_3^-	nitrate anion
O	oxygen
OH^-	hydroxide anion
P/P_o	partial pressure
Pd	palladium
pcu	primative cubic network
$^{31}P\{^1H\}$	proton decoupled phosphorous NMR
Ph_2PH	diphenylphosphine

ppm	parts per million
^{i}PrOH	isopropanol
psi	pounds per square inch
PXRD	powder x-ray diffraction
py	pyridine
Pd(PPh$_3$)$_4$	tetrakis(triphenylphosphine)palladium(0)
Pd(PPh$_3$)$_2$Cl$_2$	dichloro-bis(triphenylphosphine)palladium(II)
PhMgCl	phenyl magnesium chloride
Rh	rhodium
RT	room temperature
Ru	ruthenium
SA	surface area
SBA	Santa Barbara Amorphous
SBU	secondary building unit
SEM	scanning electron microscopy
Si(OEt)$_3$H	triethoxysilane
SOCl$_2$	thionyl chloride
SEGPHOS	(4,4'-bi-1,3-benzodioxole)-5,5'-diyl-bis(diarylphosphine)
^{tBu}SEGPHOS	(7,7'-tert-butyl-4,4'-bi-1,3-benzodioxole)-5,5'-diyl-bis(diaryl-phosphine)
TEM	transmission electron microscopy
Tf$_2$O	trifluoroacetic anhydride
TGA	thermogravimetric analysis
THF	tetrahydrofuran

Ti^{iv}	titanium (IV) ion
Ti(O^{i}Pr)$_4$	titanium (IV) isopropoxide
TMS	trimethylsilyl
TMS-BINAP	2,2'-bis(diphenylphosphino)-4,4'-bis(trimethylsilyl)-1,1'binaphthyl
TMBDC	tetramethylterephthalate (IRMOF-18)
TOF	turn-over frequency
TON	turn-over number
TTDC	2,2':5',2"-terthiophene-5,5"-dicarboxylate (IRMOF-20)
UMC	unsaturated metal center
UV-vis	ultraviolet-visible spectroscopy
μmol	micromole
wt %	weight %
Xylyl-BINAP	2,2'-bis(di-3,5-xylylphosphino)-1,1'-binaphthyl
Zn^{2+}	zinc (II) ion
ZnEt$_2$	diethylzinc
Zr	zirconium

CHAPTER 1

SUPPORTED ASYMMETRIC CATALYSTS:
FUNDAMENTALS, STRATEGIES, AND HISTORICAL OVERVIEW

1.1 Introduction

Asymmetric catalysis provides a powerful method for the synthesis of chiral molecules that are important ingredients for the pharmaceutical, agrochemical, and fragrance industries.[1] Numerous highly selective chiral catalysts have been developed in the recent decades, and as such, three pioneers in the field of homogeneous asymmetric catalysis were awarded the Nobel Prize in Chemistry in 2001.[2] The practical applications of many homogeneous asymmetric catalysts in industrial processes are however hindered by their high costs as well as difficulties in removing trace amounts of toxic metals from the organic products.[3] Heterogenization of homogeneous asymmetric catalysts represents a logical approach to overcoming these problems.[4] The heterogenized catalysts can potentially provide easily recyclable and reusable solid catalysts that have uniform and precisely engineered active sites similar to those of their homogeneous counterparts, and therefore combine the advantages of both homogeneous and heterogeneous systems. Many heterogenization approaches have been explored, including attaching the chiral catalysts to organic polymers, dendrimers, membrane supports, and porous inorganic oxides and immobilization via biphasic systems.[5] This chapter provides an overview of recent developments in the design of heterogenized asymmetric catalysts based on two distinct

strategies, namely, self-supported asymmetric catalysts that have the potential to provide the highest possible catalyst loading and also the most uniform catalytic sites and more traditional heterogeneous catalysts supported on highly porous silica materials.[6]

1.2 Self-supported asymmetric catalysts

Self-supported asymmetric catalysts can in principle be prepared by incorporating catalytic sites as pendants on a linear organic polymer[7] or in the backbone of an organic polymer.[8] Many of these polymers have low molecular weights and tend to behave as homogeneous catalysts due to their high solubility. As a result, their recovery during catalytic reactions typically requires large amounts of solvents of different polarity. Such polymer-immobilized asymmetric catalysts also tend to have diluted catalytic sites and are not very efficient. On the other hand, heterogeneous catalyst systems have recently been prepared by three distinct strategies that do not rely on any support material (Scheme 1.1). In the first approach, catalytically active subunits are linked by secondary metal centers to form solid catalysts. In the second approach, multitopic ligands containing orthogonal secondary functional groups can be linked by metal centers to form porous solids which are then treated with secondary metal centers to form solid catalysts. In the third approach, multitopic chiral ligands are linked with metal centers to form catalytically active polymeric solids. This section surveys recent advances in the synthesis and catalytic applications of self-supported asymmetric catalysts using these approaches. The advantages and disadvantages of each strategy are also discussed in this section.
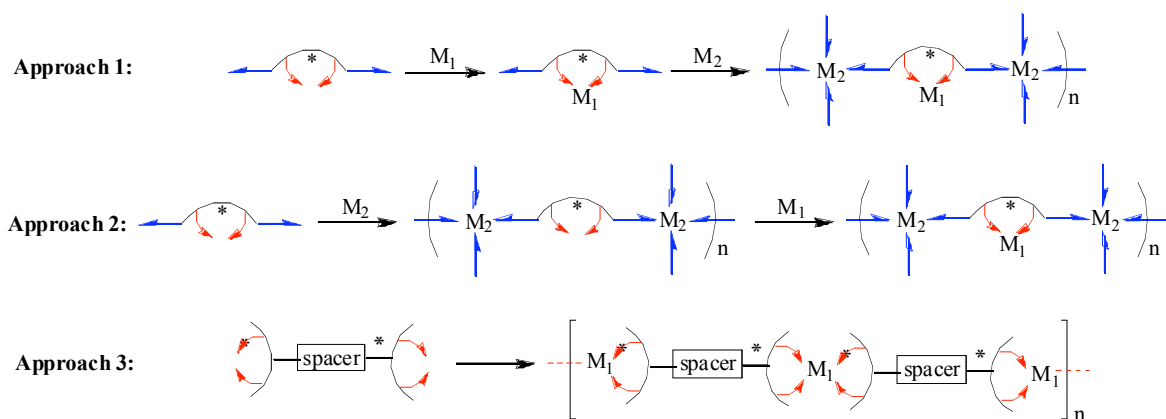
Scheme 1.1 Three distinct strategies for the synthesis of self-supported asymmetric catalysts.

1.2.1 Self-supported asymmetric catalysts formed by linking catalytically active subunits via metal-ligand coordination

Lin et al. prepared a series of chiral, porous, hybrid solids based on zirconium phosphonates for highly enantioselective hydrogenation of β-keto esters. These hybrid materials were prepared based on Approach 1 and designed to combine the robust framework structure of metal phosphonates[9] and enantioselectivity of metal complexes of the chiral bisphosphines.[10] Enantiopure 2,2'-bis-(diphenylphosphino)-1,1'-binaphthyl-6,6'-bis(phosphonic acid), L_1-H_4, was synthesized in three steps starting from the known 2,2'-dihydroxy-1,1'-binaphthyl-6,6'-bis(diethylphosphonate) in 47% overall yield.[11] Treatment [Ru(benzene)Cl$_2$]$_2$ with 1 equiv of L_1-H_4 in DMF at 100 °C led to the complex [Ru(L_1-H_4)(DMF)$_2$Cl$_2$] which was reacted with Zr(O^{t}Bu)$_4$ in reluxing methanol to afford the zirconium phosphonate Zr-Ru-L_1. The analogous solid Zr-Ru-L_2 with the 2,2'-bis-(diphenylphosphino)-1,1'-binapthyl-4,4'-bis(phosphonic acid) ligand, L_2-H_4 was similarly prepared. The chiral porous phosphonates were characterized by thermogravimetric analysis (TGA), nitrogen adsorption isotherms, X-ray diffraction, SEM, IR spectroscopy, and microanalysis.

The compositions of Zr-Ru-**L₁** and Zr-Ru-**L₂** were determined by TGA and microanalysis while the IR spectra suggested the formation of zirconium phosphonate bonds. Zr-Ru-**L₁** exhibits a total BET surface area of 475 m^2/g and a pore volume of 1.02 cm^3/g, whereas Zr-Ru-**L₂** has a total BET surface area of 387 m^2/g and a pore volume of 0.53 cm^3/g. SEM images showed the presence of sub-micrometer particles in the solids while powder X-ray diffraction (PXRD) studies indicated the amorphous nature of the solids.
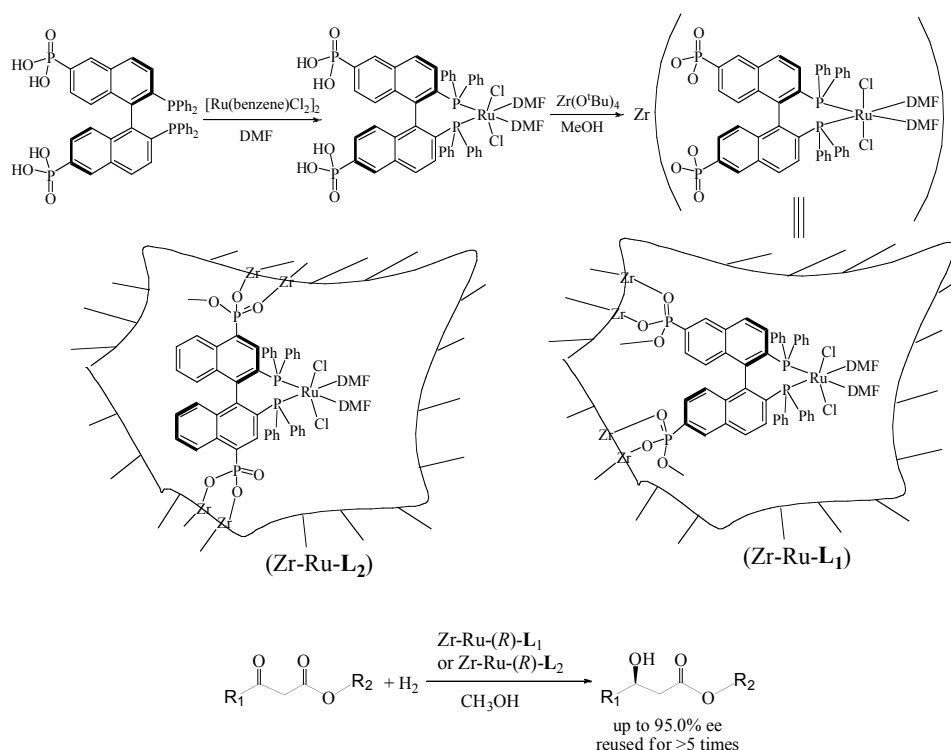
Scheme 1.2 Synthesis of Ru(BINAP)-containing zirconium phosphonates for asymmetric hydrogenation of ß-ketoesters.

The Zr-Ru-**L₁** and Zr-Ru-**L₂** solids were utilized for heterogeneous asymmetric hydrogenation of β-keto esters (Scheme 1.2). Zr-Ru-**L₁** catalyzed the hydrogenation of a wide range of β-alkyl-substituted β-keto esters with complete conversion and *ee* values ranging from 91.7% to 95.0%. Zr-Ru-**L₁** gave a turnover frequency (TOF) of 364 h^{-1} with

0.1% solid loading compared to a TOF of 810 h^{-1} for the homogeneous BINAP-Ru catalyst. In contrast, Zr-Ru-**L$_2$** catalyzed the hydrogenation of β-keto esters with only modest *ee* values.

The supernatants of Zr-Ru-**L$_1$** and Zr-Ru-**L$_2$** in MeOH did not catalyze the hydrogenation of β-keto esters, indicating the heterogeneity of the solid catalysts. In addition, analysis of the supernatants by direct current plasma spectroscopy (DCP) indicated that less than 0.01% of the ruthenium leached into the organic solution during hydrogenations. The Lin group was able to reuse the Zr-Ru-**L$_1$** system for asymmetric hydrogenation of methyl acetoacetate without significant deterioration on enantioselectivity. The Zr-Ru-**L$_1$** system was used for five cycles of hydrogenation with complete conversion and *ee* values of 93.5, 94.2, 94.0, 92.4, and 88.5 %, respectively.

This synthetic strategy was modified by the Lin group to prepare zirconium phosphonates containing the Ru-BINAP-DPEN species that were shown by Noyori et al to be highly active homogeneous catalyst for enantioselective hydrogenation of aromatic ketones.[12] Reaction of **L$_1$**-H$_4$ with [Ru(benzene)Cl$_2$]$_2$ followed by (*R,R*)-DPEN afforded the phosphonic acid-substituted Ru-BINAP-DPEN intermediate which was treated with Zr(O^{t}Bu)$_4$ under reflux conditions to give chiral porous Zr phosphonate of the approximate formula Zr[Ru(**L$_1$**)(DPEN)Cl$_2$]·4H$_2$O (Zr-Ru-**L$_1$**-DPEN) (Scheme 1.3). The solid precatalyst Zr-Ru-**L$_2$**–DPEN with a 4,4'-disubstituted BINAP was similarly prepared and also has an approximate formula of Zr[Ru(**L$_2$**)(DPEN)Cl$_2$]·4H$_2$O. The solid catalysts were characterized by a variety of techniques including TGA, adsorption isotherms, PXRD, SEM, IR, and microanalysis.
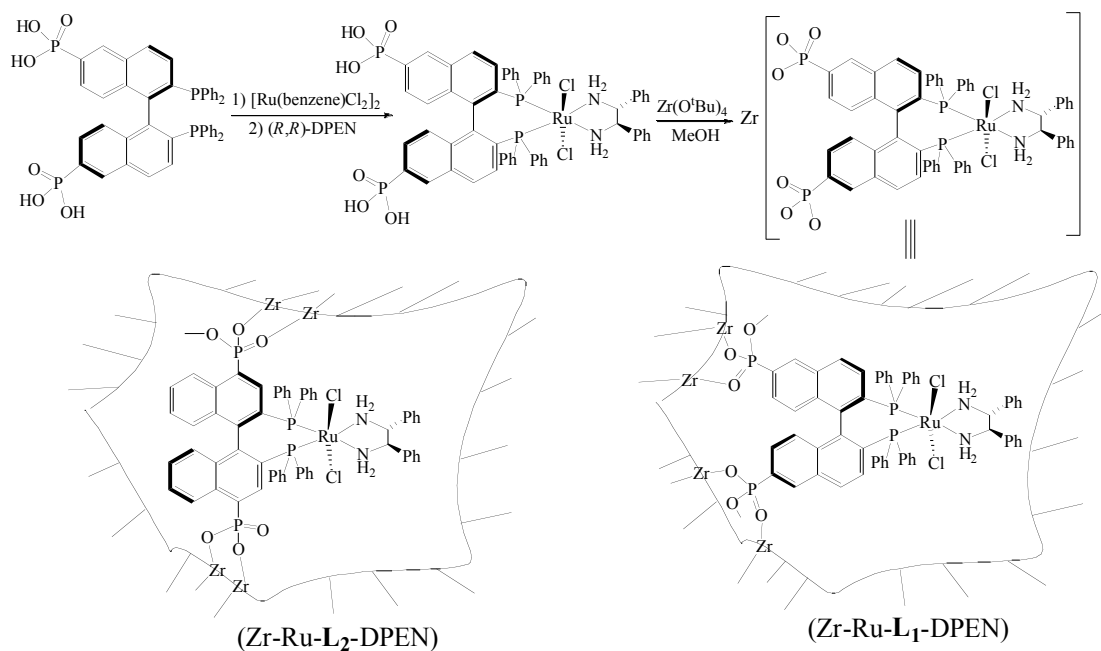
Scheme 1.3 Synthesis of Ru(BINAP)(DPEN)-containing zirconium phosphonates.

Nitrogen adsorption measurements indicate that both Zr-Ru-**L₁**-DPEN and Zr-Ru-**L₂**-DPEN are highly porous and have wide pore size distributions. Zr-Ru-**L₁**-DPEN has a surface area of 400 m^2/g and a pore volume of 0.98 cm^3/g, whereas Zr-Ru-**L₂**-DPEN exhibits a total BET surface area of 328 m^2/g and a pore volume of 0.65 cm^3/g. SEM images showed that both solids were composed of submicrometer particles, while PXRD indicated that both solids were amorphous.

Porous solids of Zr-Ru-**L₁**-DPEN and Zr-Ru-**L₂**-DPEN exhibited exceptionally high activity and enantioselectivity in the asymmetric hydrogenation of aromatic ketones. Acetophenone was hydrogenated to 1-phenylethanol with complete conversion and 96.3% *ee* in 2-propanol with 0.1 mol % loading of the Zr-Ru-**L₂**-DPEN solid. This level of *ee* is significantly higher than that observed for the parent Ru-BINAP-DPEN homogeneous

catalyst which typically gives ~80% *ee* for the hydrogenation of acetophenone under similar conditions.[12a,12b] In comparison, the Zr-Ru-**L₁**-DPEN solid gives 79.0% *ee* for the hydrogenation of acetophenone under the same conditions. The Zr-Ru-**L₂**-DPEN solid has been used to catalyze a series of aromatic ketones with remarkably high *ee*'s of 90.6-99.2% and complete conversions. In contrast, the *ee* for the hydrogenation of aromatic ketones is modest and similar to that of the parent Ru-BINAP-DPEN homogeneous catalyst. The Lin group later demonstrated that the enhanced *ee*'s exhibited by the Zr-Ru-**L₂**-DPEN solid is due to the beneficial steric influence of the bulky substituents in the 4,4'-positions of BINAP.[13]

The solid zirconium phosphonate catalysts were also extremely active for the hydrogenation of other aromatic ketones. For example, with only 0.02 mol % solid loading of Zr-Ru-**L₂**-DPEN, 1-acetonaphthone was hydrogenated with complete conversion and 98.9% *ee* in 20 h. When the solid loading was decreased to 0.005 mol %, it took longer reaction time (40 h) for the hydrogenation of 1-acetonaphthone to complete (98.6% *ee*). The TOF was calculated to be ~500 h^{-1} at complete conversion and ~700 h^{-1} at 70% conversion.

The solid catalysts were successfully reused for the asymmetric hydrogenation of 1-acetonaphthone without the deterioration of enantioselectivity. The Zr-Ru-**L₂**-DPEN system was used for eight cycles of hydrogenation without any loss of enantioselectivity. The catalyst recycling and reuse experiments were conducted without rigorous exclusion of air, and the oxygen sensitivity of the ruthenium hydride complexes may have contributed to the loss of activity after multiple runs. Therefore, the loss of activity may not reflect the intrinsic instability of the Zr-Ru-**L₂**-DPEN solid catalyst. DCP studies of the solution indicated less than 0.2% of Ru leached into the organic product during each round of hydrogenation.

Nguyen, Hupp, and co-workers recently used a similar strategy to prepare self-supported catalysts for asymmetric epoxidation reactions.[14] The [bis(catechol)-salen]Mn compound, **L₃**, was designed to have catechol groups for crosslinking with metal centers to afford a series of coordination polymers (Scheme 1.4). **Poly(Cu-L₃)** was prepared by treating **L₃** with Cu^{II} in the presence of triethylamine in DMF. After stirring, **poly(Cu-L₃)** precipitated as brown solid and was thoroughly washed with DMF. Inductively coupled plasma-mass spectrometric (ICP-MS) studies indicated that **poly(Cu-L₃)** had a Mn/Cu ratio of ~1:1.1, suggesting the formation of a quasi-one-dimensional structure where **L₃** is connected by bis(catecholate)copper linkages. The **poly(Cu-L₃)** solid has a modest surface area of 72 m^2/g and is amorphous as judged by SEM and PXRD.
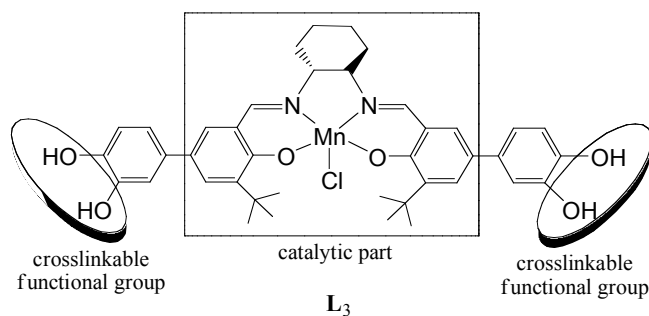
Scheme 1.4 Structure of the crosslinkable [bis(catechol)-salen]Mn compound (**L₃**).

2,2-Dimethyl-2*H*-chromene was used as a model substrate for epoxidation reactions using 2-(*tert*-butylsulfonyl)iodosylbenzene as the oxidant. A slightly lower *ee* of 76% was observed for the heterogeneous **poly(Cu-L₃)** as compared to an *ee* of 86% for the homogeneous counterpart [bis(dimethoxyphenyl)salen]Mn^{III}Cl. The **poly(Cu-L₃)** catalyst was readily recovered by centrifugation and was reused up to 10 times with little loss in activity (from 79% to 70% yield) and no loss in enantioselectivity (75-76% *ee*). After the first two cycles where 3.1% Mn and 4.7% Cu were determined to have leached from the

sample, the metal loss slowed over the next four cycles and no metals were leached from the solid by the 10th run. The initial leaching of metal ions could come from weakly bound or entrapped species in **poly(Cu-L$_3$)**.

The catalytic lifetime of the supported catalyst **poly(Cu-L$_3$)** was also studied under high oxidant concentrations (e.g., 0.17 M) which are known to rapidly degrade homogeneous epoxidation catalysts. **Poly(Cu-L$_3$)** was found to exhibit a lifetime of >3 h and a total turnover number (TON) of >2000 in that period. In comparison, the homogeneous counterpart had a lifetime of <0.5 h and a total TON of <600 in the same 3 h period. The supported catalyst **poly(Cu-L$_3$)** thus exhibited an enhanced catalytic activity over the homogeneous system.

The same strategy was also used to formulate a series of supported catalysts **poly(M-L$_3$)** with different metal nodes (M=Cr^{III}, Mn^{II}, Fe^{III}, Co^{II}, Ni^{II}, Zn^{II}, Cd^{II}, and Mg^{II}. The catalytic activities of **poly(M-L$_3$)** for the asymmetric epoxidation of 2,2-dimethyl-2*H*-chromene with 2-(*tert*-butylsulfonyl)iodosylbenzene as the oxidant were explored. The polymers assembled with the Cr^{III}, Mn^{II}, Cd^{II}, and Mg^{II} metal centers showed highest yields (>70 %). The polymers assembled with the Cr^{III}, Cd^{II}, Mg^{II}, and Zn^{II} metal centers gave the highest *ee*'s as the Cu^{II} analog (76 %). 1-3% Mn loss was observed for most of the supported catalysts during the catalysis run; this level of leaching is similar to the **poly(Cu-L$_3$)** system.

The metal-ligand coordination approach can not only afford solid catalysts with unprecedentedly high catalyst loading and uniform catalytic sites, but also allow the synthesis of single-crystalline materials which greatly facilitates their characterization by single crystal X-ray diffraction studies. For example, Hupp and coworkers have combined **L$_4$** and H$_2$bpdc with Zn(NO$_3$)$_2$ under solvothermal conditions and obtained twofold

interpenetrating 3D networks $[Zn_2(bpdc)_2L_4]\cdot 10DMF\cdot 8H_2O$ (**1**) (Scheme 1.5).[15] The **L$_4$**

ligands of the paired networks are parallel to each other with cyclohexyl and *t*-butyl groups

protruding along the [100] direction. As a result, the channel in the crystallographic *b*

direction is essentially blocked, leaving distorted-rectangular and rhombic channels in the *c*

and *a* directions with dimensions of 6.2 Å × 15.7 Å and 6.2 Å × 6.2 Å, respectively. Such a

diagonal displacement of the networks leaves all Mn^{III} sites accessible through the channels.
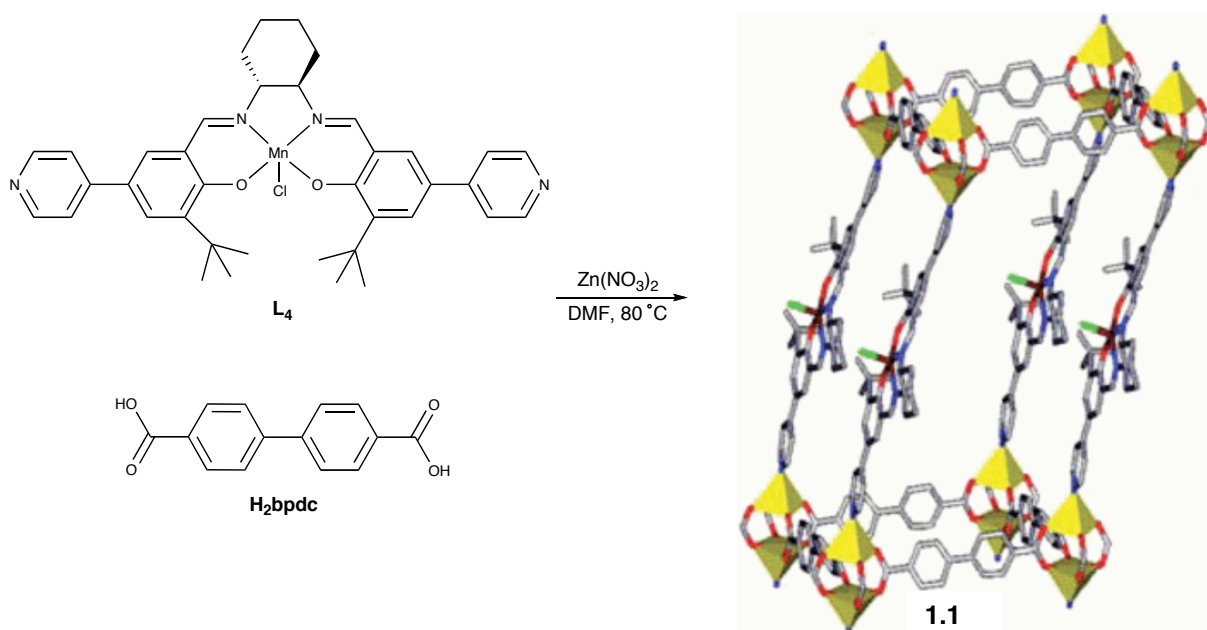
Scheme 1.5 Synthesis and framework structure of $[Zn_2(bpdc)_2L_4]\bullet 10DMF\bullet 8H_2O$ (**1.1**).

The resulting open frameworks with built-in (salen)Mn complexes showed catalytic

activity towards asymmetric olefin epoxidation reactions. In the asymmetric epoxidation of

2,2-dimethyl-2H-chromene catalyzed by **1.1**, 71% yield and 82% *ee* were obtained. This

level of *ee* is superior to those observed for the **poly(M-L$_3$)** system, demonstrating the impact

of structure and catalytic site uniformity on the enantioselectivity of self-supported catalysts.

No significant decrease of catalyst activity was observed during the reaction and the catalyst

could be recycled and reused several times. The heterogeneous catalyst **1.1** has shown higher

activity than the homogeneous counterpart (Figure 1.1), albeit with slightly lower *ee*.
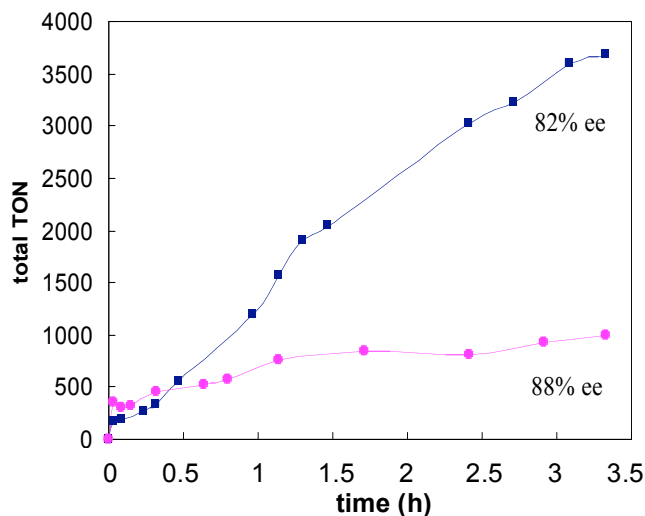
Figure 1.1 Plots of total turnover number versus time for the epoxidation of 2,2-dimethyl-2*H*-chromene catalyzed by **1.1** (blue squares) and **L₄** (magenta circles).

1.2.2 Self-supported asymmetric catalysts formed by post-synthetic modifications of coordination polymers

The coordination polymer approach described above provides a versatile method for

synthesizing a wide range of supported asymmetric catalysts, but it is not compatible with

some of the less stable Lewis acid and late transition metal catalysts. Lin et al. developed an

alternative strategy for building chiral porous solids using bridging ligands containing

functional groups that can be treated with secondary metal centers to generate active

asymmetric catalysts. A series of chiral bis(phosphonic acids) of varied length, **L₅-L₇**, were

synthesized, which contain chiral dihydroxy functionalities. Chiral porous zirconium

bis(phosphonates), **Zr-L₅** to **Zr-L₇**, were obtained by refluxing BINOL-derived

bis(phosphonic acids) with $Zr(O^nBu)_4$ in *n*-BuOH (Scheme 1.6). After refluxing overnight,

the resulting suspension was centrifuged and thoroughly washed with MeOH. Regardless of

the bis(phosphonic acid) used, amorphous solids based on zirconium phosphonates were obtained in higher than 95% yield. The solids were characterized by PXRD, solid-state CP-MAS ^{31}P NMR, IR, TGA, BET, and circular dichroism spectroscopy.
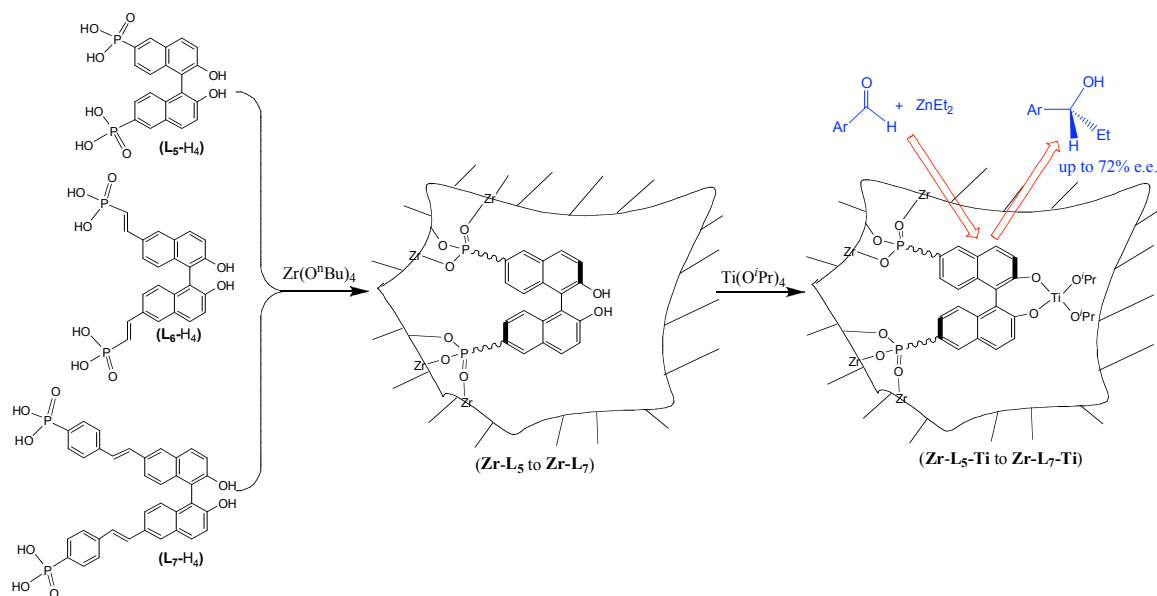
Scheme 1.6 Synthesis of BINOL-containing chiral zirconium phosphonates.

PXRD studies indicated the amorphous nature of the zirconium phosphonate solids. The broad peak observed between 0-20 ppm in the ^{31}P NMR spectra suggested the presence of many possible microenvironments of the zirconium bis(phosphate) moieties. TGA results showed the loss of 4-5 water molecules upon heating the solids to 200 °C in air while the frameworks of the solids were stable to 300 °C. IR spectra of the solids exhibited strong peaks at 915-1050 and ~3000 cm^{-1} due to the P—O stretches and OH stretches, respectively. These solids are highly porous with total surface areas ranging from 431 to 586 m^2/g and pore volumes ranging from 0.63 to 1.23 cm^3/g.

The solids **Zr-L₅** to **Zr-L₇** were treated with excess Ti(O^{i}Pr)$_4$ to generate the Ti-BINOLate species which are known to homogeneously catalyze the additions of diethylzinc to aromatic aldehydes to afford chiral secondary alcohols (upon acidic work-up). A comparison of the solid catalysts showed that the **Zr-L₇-Ti** catalyst gave the highest *ee* for the addition of diethylzinc to 1-naphthadehyde. The **Zr-L₇-Ti** system was thus further examined for diethylzinc additions to other aromatic aldehydes. The **Zr-L₇-Ti** system efficiently catalyzed the addition of ZnEt$_2$ to a wide range of aromatic aldehydes with high conversions and in e.e. values up to 72%. This level of enantioselectivity exceeds that of other heterogeneous asymmetric catalysts made by immobilization of homogeneous catalysts on mesoporous inorganic supports,[16] but is still inferior to those of homogeneous Ti-BINOL catalytic systems.[17] A control experiment using the solid derived from 2,2'-ethoxy-1,1'-binaphthyl-6,6'-bis(styrylphosphonic acid) suggested that residual phosphonic acid protons in the solids can activate Ti(O^{i}Pr)$_4$ for non-enantioselective ZnEt$_2$ addition. This type of background reaction is probably responsible for modest e.e. values observed for the solid catalysts.

In an effort to improve the enantioselectivity and also to obtain single-crystalline solids, Lin et al. designed BINOL-derived ligand (*R*)-6,6'-dichloro-2,2'-dihydroxyl-1,1'-binaphtyl-bipyridine (**L₈**). The 3D homochiral MOF [Cd$_3$(**L₈**)$_3$Cl$_6$]·4DMF·6MeOH·3H$_2$O (**1.2**) was prepared by slow vapor diffusion of diethyl ether into the mixture of (*R*)-**L₈** and CdCl$_2$ in DMF/MeOH. **1.2** is built from linking 1D zigzag [Cd(μ-Cl)$_2$]$_n$ SBUs by the **L₈** ligands via pyridine coordination, and has a highly porous structure with the largest channel opening of 1.6×1.8 nm running along the *a* axis (Figure 1.2). One third of the chiral

dihydroxy groups in **1.2** are facing the open channels and are accessible to secondary metal centers to generate active catalytic sites.
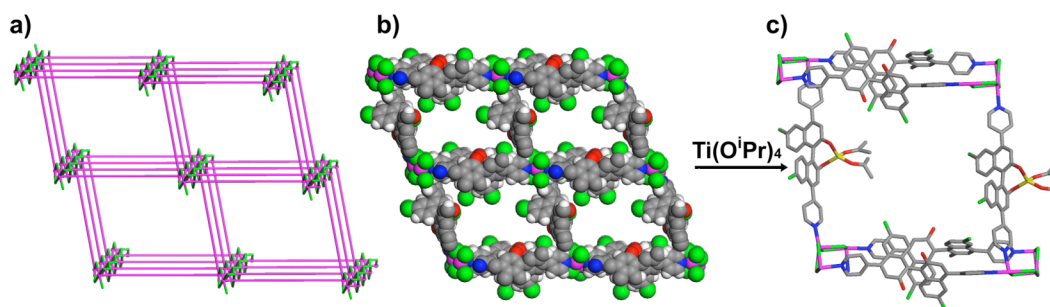
Figure 1.2 (a) Schematic representation of the 3D framework of **1.2** showing the zigzag chains of $[Cd(\mu-Cl)_2]_n$ along a axis. (b) space-filling model of **1.2** as viewed down the *a* axis, showing large 1D chiral channel (1.6×1.8 nm). (c) Schematic representation of the active (BINOLate)Ti(OiPr)$_2$ catalytic sites in the open channels of **1.2**.

1.2 was pretreated by $Ti(O^iPr)_4$ to generate the grafted Ti-BINOLate species that efficiently catalyzed the diethylzinc addiction reactions in up to 93% *ee*. This level of *ee* is comparable to the homogeneous analogue (94% *ee*) (Table 1.1). Heterogeneous nature of this solid catalyst was indicated by the nonreactive supernatant from a mixture of **1.2** and $Ti(O^iPr)_4$. Moreover, Lin et al. carried out a set of control experiments using aldehydes with different size from 0.8 nm to 2.0 nm to show that the aldehydes are accessing the Ti active sites in the interior of crystals of **1.2**. They observed decreased conversion when larger aldehyde was used. No conversion was observed for aldehyde G_2'with size of 2.0 nm which is larger than the open channels of framework **1.2**.

While using the same ligand $\mathbf{L_8}$, Lin et al. obtained two different homochiral MOFs $[Cd_3(\mathbf{L_3})_4(NO_3)_6]\cdot7MeOH\cdot5H_2O$ (**1.3**) and $[Cd(\mathbf{L_3})_5(ClO_4)_2]\cdot DMF\cdot4MeOH\cdot3H_2O$ (**1.4**) when $Cd(NO_3)_2$ and $Cd(ClO_4)_2$ were used as the metal sources, respectively. Compound **1.3** adopts 2-fold interpenetrating framework structure with each of the 3D frameworks constructed

from linking 2D grids with 1D zigzag polymeric chains. Large channels with dimension of 13.5 × 13.5 Å are present along the *c* axis (Figure 1.3c). Compound **1.4** adopts a 3D network resulted from two interpenetrating 2D grids, leading to 1D channels with size of 1.2 × 1.5 nm (Figure 1.3e).

Table 1.1 Ti(IV)-catalyzed ZnEt$_2$ additions to aromatic aldehydes.[a]
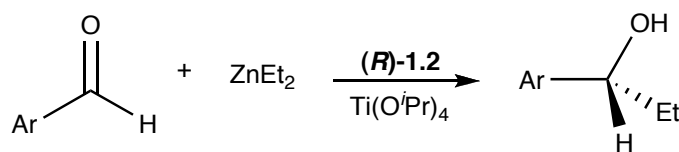
Ar	BINOL/Ti(O^{i}Pr)$_4$		**1.2** • Ti	
	Conversion %	e.e. %	Conversion %	e.e %
1-Naph	>99	94	>99	93
Ph	>99	88	>99	83
4-Cl-Ph	>99	86	>99	80
3-Br-Ph	>99	84	>99	80
4'-G$_0$OPh	>99	80	>99	88
4'-G$_1$'OPh	>99	75	73	77
4'-G$_1$OPh	>99	78	63	81
4'-G$_2$'OPh	95[b]	67[b]	0	—
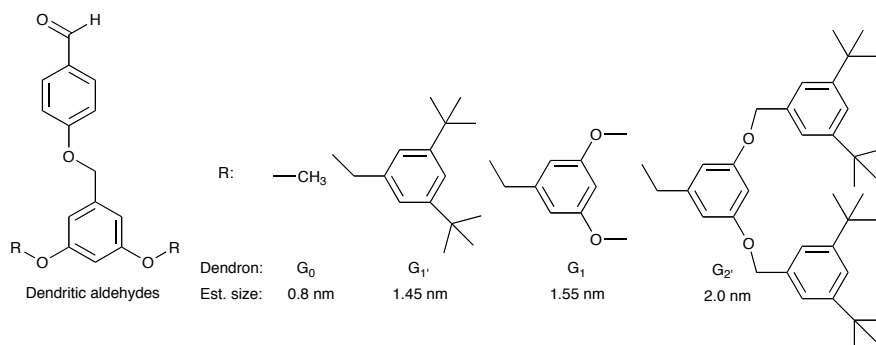
[a]All the reactions were conducted with 13 mol % of **1.2** or 20 mol % BINOL and excess amounts of Ti(O^{i}Pr)$_4$ at RT for 12 h. Conv % were determined by GC or NMR, while ee % values were determined on chiral GC or HPLC for all the secondary alcohols except for 4'-G$_2$'OPh whose ee % was determined by NMR spectrum of its Mosher's ester. [b]With 40 mol % BINOL.

Compound **1.3** was treated with $Ti(O^iPr)_4$ to lead to an active heterogeneous asymmetric catalyst for the diethylzinc addition to aromatic aldehydes with up to 90% *ee*. However, under the same conditions, a mixture of **1.4** and $Ti(O^iPr)_4$ was inactive in catalyzing the diethylzinc addition to aromatic aldehydes. Careful investigation of the structure of **1.3** revealed the close proximity of the $Cd(py)_2(H_2O)_2$ moiety in one 2D grid with the dihydroxyl groups of the other 2D grid. The dihydroxyl groups in **1.4** are thus inaccessible to $Ti(O^iPr)_4$. When treated with $Ti(O^iPr)_4$, compounds **1.3** and **1.4** had entirely different catalytic activities due to the subtle structure differences. The finding of such a drastic difference in catalytic activity is remarkable since **1.3** and **1.4** were built from exactly the same building blocks. This result points to the importance of the framework structure in determining the performance of self-supported asymmetric catalysts.
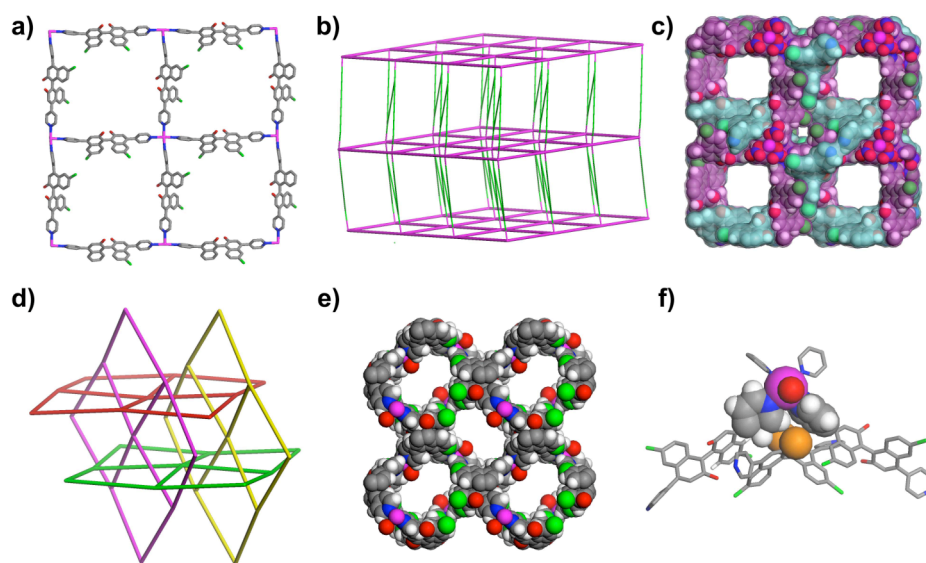
Figure 1.3 (a) The 2D square grid in **1.3**. (b) Schematic representation of the 3D framework of **1.3**. (c) Space-filling model of **1.3** as viewed down the *c* axis, the 2-fold interpenetrating networks are shown with blue and violet colors. (d) Schematic representation of the interpenetration of mutually perpendicular 2D grids in **1.4**. (e) Space-filling model of **1.4** as viewed down the *c* axis. (f) Schematic representation of steric congestion around the chiral dihydroxyl group of **L₈** (orange sphere) arising from the interpenetration of mutually perpendicular 2D grids in **1.4**.

1.2.3 Self-supported asymmetric catalysts formed by linking multitopic chiral ligands with catalytic metal centers

The third approach to self-supported asymmetric catalysts relies on directly linking multitopic chiral ligands with metal centers. Ding et al.[18] and Sasai et al.[19] independently demonstrated this concept by linking multitopic BINOL ligands with Al(III) and Ti(IV) centers to generate chiral Lewis acid catalysts. The bis(BINOL) derivatives L_{9a-d} were synthesized by linking the BINOL units at the 6-position.[20] Treatment of L_{9a-d} with equal molar LiAlH₄ in THF at 0 °C resulted in spontaneous formation of a white precipitate which was reacted with 0.5 equivalents of BuLi to afford heterogeneous versions of the Al-Li-bis(binaphthoxide) (ALB) catalyst that was reported earlier (Scheme 1.7).[21]

L_{9a}: 1,2-disubstituted; L_{9b}: 1,3-disubstituted
L_{9c}: 1,4-disubstituted; L_{9d}: no benzene ring
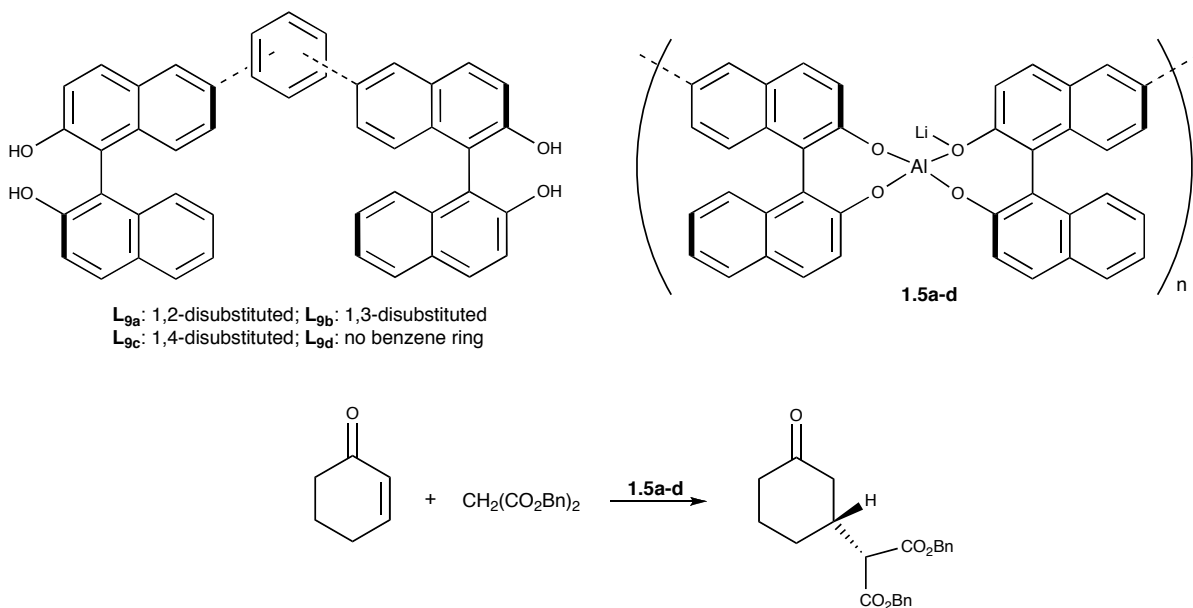
Scheme 1.7 Synthesis of self-supported Al-Li-bis(binaphthoxide) (ALB) catalysts for asymmetric Michael reactions.

With an equivalent of 20 mol% ALB catalyst loading, the self-supported catalysts **1.5a-d** effectively catalyzed Michael reaction of 2-cyclohexanenone and dibenzyl malonate. While **1.5a** and **1.5b** gave very low *ee*'s (6% and 17%, respectively), **1.5c** and **1.5d** gave the

Michael product in 88% *ee* and 96% *ee*, respectively. Sasai et al. attributed this drastic increase in *ee* over the bent derivatives (**1.5a** and **1.5b**) to the positioning of the dihydroxy groups at the opposite sides of the multitopic ligands. The enantioselectivity afforded by this immobilization technique is significant because previous attempts of immobilizing the ALB type catalyst onto polystyrene resin were unsuccessful and gave no enantioselectivity.[22] The heterogeneity of catalyst **1.5d** was confirmed by testing the clear supernatant solution which exhibited no catalytic activity. Sasai et al. also demonstrated the reusability of the self-supported catalysts. After removal of the supernatant and recharging of substrate under Argon, it was determined that **1.5d** could be reused three times with gradual deterioration of enantioselectivity (96% → 85% *ee*).

By linking L_{9d} with Ti(IV) centers, Sasai et al. also demonstrated the synthesis of self-supported catalysts for carbonyl-ene reactions.[23] Two equivalents of $Ti(O^{i}Pr)_4$ in toluene and four equivalents of H_2O were added to a solution of L_{9d} in CH_2Cl_2 to generate a precipitate which was inferred to have an idealized structure of **1.6** (Scheme 1.8) by elemental analysis and IR spectra. **1.6** catalyzed the carbonyl-ene reaction of ethyl glyoxylate and α-methylstyrene to give the product **1.7** in 81% yield and 90% *ee*. Catalyst **1.6** was readily recovered in air and used for up to 4 times without loss of activity or enantioselectivity (88% yield, 88% *ee*).
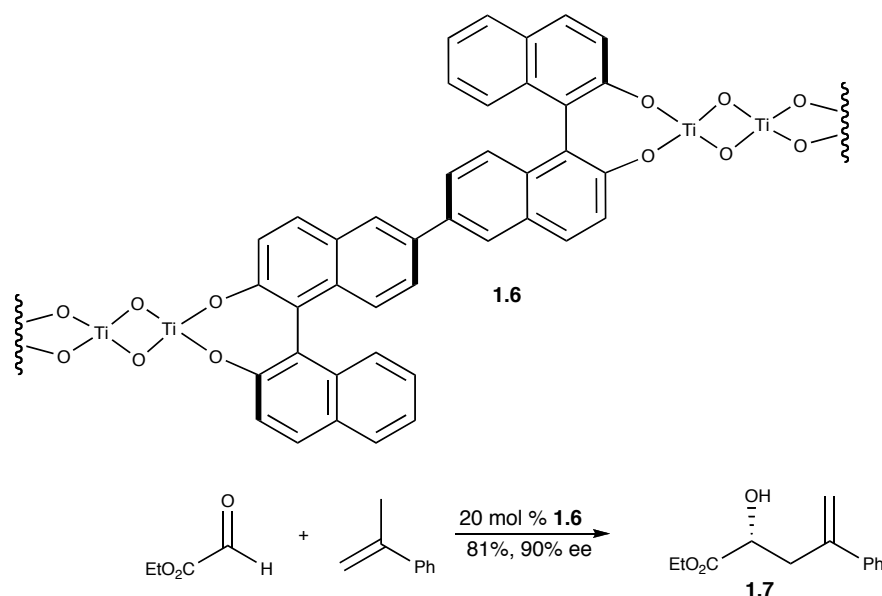
Scheme 1.8 Synthesis of the Ti/**L$_{9d}$** self-supported catalyst for carbonyl-ene reactions.

Ding et al. independently carried out the carbonyl-ene reaction with self-supported catalyst **1.6**, and observed a similar level of enantioselectivity as Sasai et al. Ding et al. further showed that a variation of the self-supported catalyst **1.6** (i.e., Kagan-Uemura type catalysts[24]) was able to catalyze the asymmetric sulfoxidation of sulfides.[25] In the presence of these self-supported catalysts, aryl methyl sulfides were oxidized by cumene hydroperoxide to chiral sulfoxides with excellent *ee*'s (99.9-96.4%). This catalyst system was also very stable and reused for up to eight times without loss of enantioselectivity or activity.

Ding et al. used a similar strategy to prepare self-supported Shibasaki's BINOL/La^{III} catalyst for enantioselective epoxidation of α,β-unsaturated ketones (Scheme 1.9).[26] Catalytically active precipitates were obtained by treating multitopic BINOL ligands **L$_{10a-i}$** with La(O^{i}Pr)$_3$ and triphenylphosphine oxide in THF.[27] The La/**L$_{10a}$** system, for example, catalyzed the epoxidation of α,β-unsaturated ketone **1.8a** by cumene oxide at >91% yield and

up to 97.9% *ee*. The enantioselectivity of the La/**L₁₀** system seems to be sensitive to the spacer geometry and length. When a linear spacer was used, the *ee* increased as the length of the spacer increases. The *ee* dropped as that the extension angle of the spacers was reduced (e.g., **L₁₀ₑ** and **L₁₀g**). Ding et al. further showed that the La/**L₁₀ₐ** system was able to catalyze the epoxidation of a variety of α,β-unsaturated ketones with high *ee*'s. The La/**L₁₀** system is also readily recoverable and reusable. For example, the La/**L₁₀ₐ** system was reusable for the epoxidation of **1.8a** for six times to afford **1.9a** in 99-83% yield and 96.5-93.2% *ee*. Furthermore, leaching of lanthanum was minimal and determined by ICP to be <0.4 ppm and the supernatant from the La/**L₁₀ₐ** system did not possess any catalytic activity under the same conditions.

$$\text{La/L}_{10a\text{-}i}\ (5.0\ \text{mol}\%)$$
$$\text{Ph}_3\text{PO}\ (15\ \text{mol}\%)$$
$$\text{MS 4A, THF, RT}$$
$$\text{CMHP}\ (1.5\ \text{equiv})$$

1.8a-h → **1.9a-h**

R = Ph, R' = Ph (**a**)
R = 4-F-Ph, R' = Ph (**b**)
R = 4-Cl-Ph, R' = Ph (**c**)
R = 4-Br-Ph, R' = Ph (**d**)

R = 4-NO₂-Ph, R' = Ph (**e**)
R = 4-NC-Ph, R' = (**f**)
R = Ph, R' = 4-MeO-Ph (**g**)
R = *i*-Pr, R' = Ph (**h**)
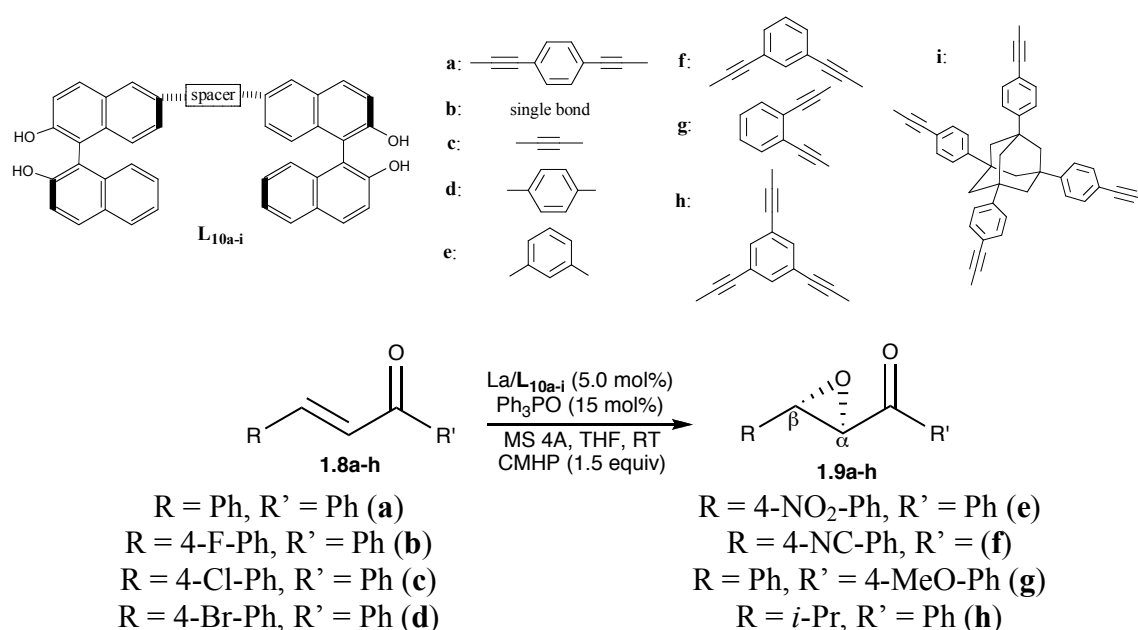
Scheme 1.9 List of bis(BINOL) ligands for the synthesis of self-supported Shibasaki's catalysts.

Ding et al. also elegantly demonstrated the synthesis of self-supported catalysts by linking multitopic chiral ligands with group 8 metal centers which are highly active for

hydrogenation reactions. Although originally proposed in 1968,[28] monodentate phosphorus ligands have received attention only recently, after pioneering work by Ferringa, de Vries, Reetz, and Pringle.[29] MonoPhos, a class of ligands consisting of a monodentate phosphorus donor atom bound to a BINOL backbone through two oxygens, is the most widely studied monodentate phosphorus ligand because of its ease of preparation, stability, and usefulness in the asymmetric catalysis of a variety of substrates.[29] Ding et al prepared multitopic MonoPhos ligands $\mathbf{L_{11a-c}}$ by bridging through the 6-position of the binapthyl ring system.[30] Treatment of linked MonoPhos ligands $\mathbf{L_{11a-c}}$ with [Rh(cod)]BF$_4$ (cod = cyclooctadiene) in a solvent mixture of dichloromethane/toluene resulted in the immediate precipitation of the Rh/$\mathbf{L_{11a-c}}$ polymers (Scheme 1.10).
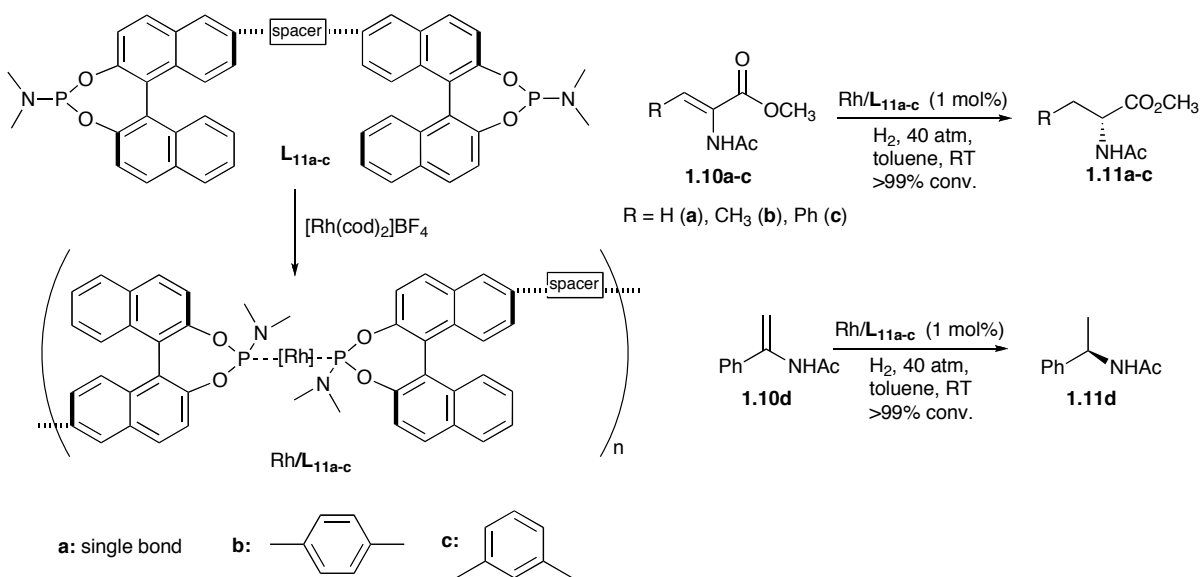
Scheme 1.10 Self-supported Rh/MonoPhos catalysts for asymmetric hydrogenation of *ß*-substituted dehydro-a-amino acid **1.10a-c** and enamide **1.10d**.

The Rh/$\mathbf{L_{11a-c}}$ polymers were explored for asymmetric hydrogenation of both *ß*-substituted dehydro-α-amino acid **1.10a-c** and enamide **1.10d** to give a variety of amino acid **1.11a-c** and secondary amines **1.11d** with good yields and high enantioselectivities. At a 1

mol% catalyst loading, similar activity and enantioselectivity were observed for the Rh/L_{11a-c} polymers and their homogeneous counterparts. Notably, the Rh/L_{11a-c} polymers gave improved enantioselectivity (95-97% *ee*) in the hydrogenation of **1.10d** over the MonoPhos/Rh homogeneous catalyst (~88% *ee*). The heterogeneous nature of the Rh/L_{11a-c} system was supported by the lack of catalytic activity by the supernatant, low Rh leaching (<3 ppm), and the reusability of the self-supported catalysts.

Ding et al. recently further extended this strategy to synthesize self-supported Noyori's [RuCl$_2$(BINAP)(DPEN)] catalysts for heterogeneous asymmetric hydrogenation of aromatic ketones.[31] The need of both chiral diphosphines and chiral diamines on the Ru center requires the design of two different multitopic chiral ligands. The bis(BINAP) and bis(DPEN) ligands used for this work are shown in Scheme 1.11.
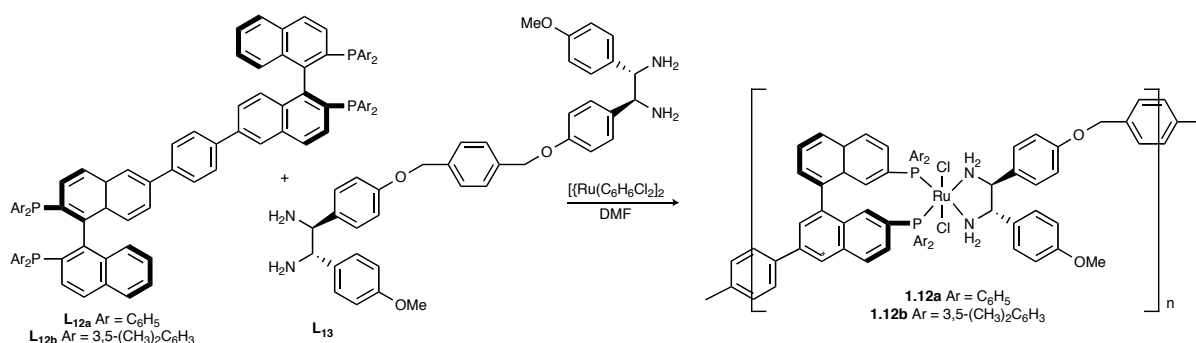
Scheme 1.11 Self-supported Noyori-type Ru(BINAP)(DPEN) catalysts.

The self-supported catalysts **1.12a-b** were prepared by reacting the bridged BINAP ligands L_{12a-b} with [Ru(benzene)Cl$_2$]$_2$ in DMF at 100°C, followed by the addition of bridged DPEN L_{13} at room temperature. The self-supported catalysts **1.12a-b** were tested for asymmetric hydrogenation of aromatic ketones in the presence of base (KO^{t}Bu) in isopropanol. At 0.1% loading, a variety of aromatic ketones were completely hydrogenated

with 78.2-98.1% *ee*. For the asymmetric hydrogenation of acetophenone, self-supported catalyst **1.12b** gave an *ee* of 97.4% which was in fact higher than its homogeneous counterpart (95.5-96.4% *ee*). Furthermore, the self-supported catalysts were capable of catalyzing the hydrogenation reactions at 0.01 mol% catalyst loading, and gave a TOF of ~500/h. The heterogeneous catalyst can be recovered and reused for up to 7 times without significant loss of activity or enantioselectivity.

1.3 Mesoporous silica supported asymmetric catalysts

Since their discovery in the early 1990's, well-ordered mesoporous materials have been examined for a number of applications.[32] Immobilization of homogeneous asymmetric catalysts on the inner walls of such mesoporous solids offers several advantages (including higher surface areas and larger open channels) over other less defined supports such as organic polymers. Mesoporous siliceous materials such as MCM-41 and SBA-15 have indeed been used as supports for the immobilization of several asymmetric catalysts.[33]

Lin et al. prepared a series of immobilized Ru complexes of 4,4'-substituted BINAPs on well-ordered mesoporous silica SBA-15 for highly enantioselective hydrogenation of ß-ketoesters.[34] SBA-15 was used as the supports due to their ease of synthesis and very large pore size to allow facile diffusion of substrates and products.[35]

Lithiation of 4,4'-bis(cylcopentanol)-2,2'-bis(diphenylphosphino)-1,1'-binapthyl and 4-(cylcopentanol)-2,2'-bis(diphenylphosphino)-1,1'-binaphthyl[36] followed by treatment with 3-iodopropyltrimethoxysilane afforded the modified BINAPs **L$_{14}$** and **L$_{15}$** (Scheme 1.12). Ligands **L$_{14}$** and **L$_{15}$** were characterized by ^{1}H{^{31}P} and ^{31}P{^{1}H} NMR spectroscopy. RuL$_{14}$(DMF)$_2$Cl$_2$ and RuL$_{15}$(DMF)$_2$Cl$_2$ were synthesized by heating [RuCl$_2$(*p*-cymene)]$_2$ and **L$_{14}$** or **L$_{15}$** in DMF at 100 °C, respectively. A suspension of SBA-15 and RuL$_{14}$(DMF)$_2$Cl$_2$ or

RuL$_{15}$(DMF)$_2$Cl$_2$ in toluene was refluxed overnight to give the heterogenized precatalysts **1.14** and **1.15**.[37]

The Ru precatalyst loadings were determined by direct current plasma (DCP) analysis of the Ru content in the modified SBA-15.[38] The pristine SBA-15 has a BJH surface area of 724 m^2/g and a BJH average pore size of 113 Å. Upon the immobilization of the Ru complexes, the solid catalysts **1.14** and **1.15** exhibited expected diminished surface areas and pore sizes (Table 1.2). **1.15** has slightly larger surface area, pore volume, and pore size than **1.14**, consistent with the presence of the bulky 1-cyclopentanol group in **1.14**.
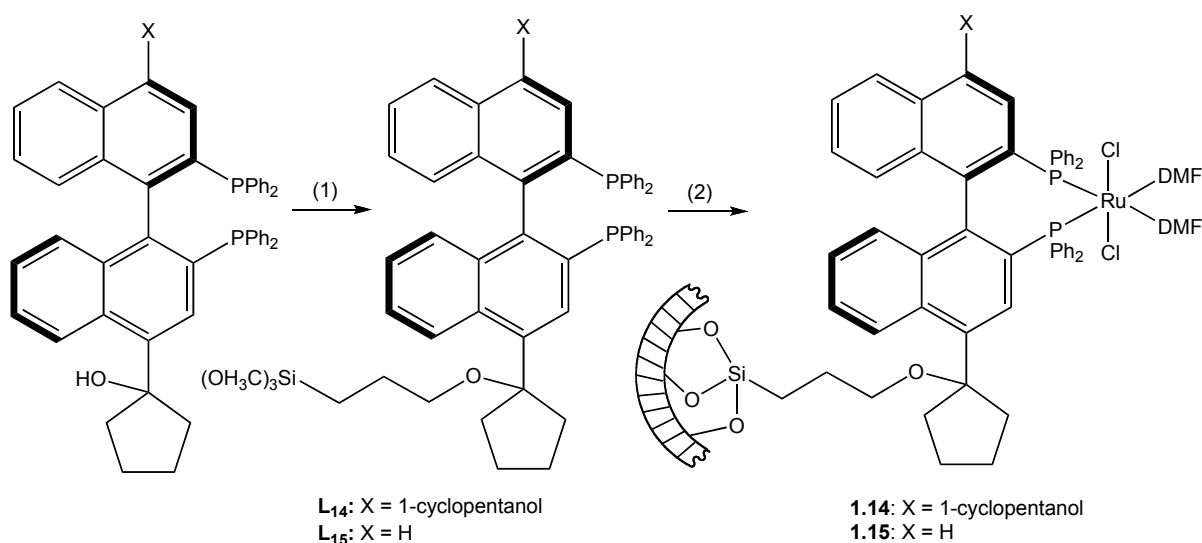
Scheme 1.12: Reagents and conditions: (1) a) ^{n}BuLi; b) 3-iodopropyltrimethoxysilane; (2) a) [Ru(p-cymene)Cl$_2$]$_2$, DMF, 100 °C; b) SBA-15, toluene, reflux.

Table 1.2 Surface area, pore volume, and pore size of SBA-15, **1.14**, and **1.15**.

	SBA-15	**1.14**	**1.15**
BJH surface area (m^2/g)	724	487	529
BJH pore volume (mL/g)	1.98	1.38	1.52
BJH pore size (Å)	113	96	101

Catalytic asymmetric hydrogenation of both ß-alkyl and ß-aryl ß-ketoesters was carried out under a hydrogen pressure of 1400 psi in the presence of **1.14** or **1.15** in methanol at r.t. for 20 h. As shown in Table 1.9 (entries 1-4), ß-alkyl ß-ketoesters were hydrogenated with complete conversion and e.e. values in the 96.3 to 98.6% range in the presence of 1 mol% of **1.14**. These ß-alkyl ß-ketoesters were hydrogenated over solid catalyst **1.15** (2 mol%) with similar e.e. values to **1.14** and complete conversions.[39] The e.e values exhibited by **1.14** and **1.15** are comparable to those of the parent Ru(BINAP) homogeneous catalyst[40] and 4-5% higher than those of zirconium phosphonate-derived heterogeneous catalysts.[41] In addition, the level of e.e.'s exhibited by **1.14** and **1.15** is also comparable to the best polymer-anchored Ru catalysts for the hydrogenation of ß-alkyl ß-ketoesters.[42]

The hydrogenation of a variety of ß-aryl ß-ketoesters was carried out in the presence of 2 mol% of solid catalyst **1.14** or 4 mol% of solid catalyst **1.15**. E.e. values in the range of 81.7-95.2% were obtained for **1.14**, while e.e. values in the range of 71.9-93.5% were obtained for **1.15**. The e.e. values are much higher than those afforded by the homogeneous Ru(BINAP)(DMF)$_2$Cl$_2$ catalyst. The 4,4'-substituent effects of BINAP are operative in the hydrogenation of ß-aryl ß-ketoesters. **1.15** gave lower e.e's than **1.14** for all the substrates tested due to the lack of a bulky substituent in the 4'-position of the modified BINAP **L$_{15}$**.

The Lin group was able to recycle and reuse **1.14** in the asymmetric hydrogenation of methyl acetoacetate for 5 consecutive runs. Complete conversions were obtained for the first three runs, and the conversion started to drop in the fourth and fifth run. The e.e. value also deteriorated as the conversion dropped. The loss of activity and deterioration of enantioselectivity is believed to be due to the air-sensitivity of the catalytically active Ru-hydride species. Control experiments showed that the supernatant did not catalyze the

hydrogenation of methyl acetoacetate. Furthermore, DCP spectroscopy showed that less than 0.12% of Ru-containing complexes leached into the organic phase during each run of asymmetric hydrogenation.

The reactions of diethylzinc with benzaldehyde using ephedrine immobilized onto amorphous silica gel[43] and mesoporous silica[44] have been investigated, but the degree of enantioselectivity is very low. Kim and co-workers developed a new heterogeneous catalyst system by employing a proline-derived ligand developed by Soai *et al*,[45] immobilized on MCM-41 and SBA-15 mesoporous silicas.[33a] Furthermore, since the free SiOH moietites on the silica surface could catalyze the background reaction,[45] thus lowering the reaction enantioselectivity, mesoporous silicas containing the chiral ligand having its surface capped with trimethylsiliyl groups have been prepared.[46] The group performed asymmetric diethylzinc addition to benzaldehyde using the catalyst systems. The enantioselectivity was found to be largely dependent upon the pore size of the mesoporous silicas, capping of free silanol moieties with trimethylsilyl group, and the employment of Bu^nLi.

To study the effect of pore size on the enantioselectivity, Kim et al. used both MCM-41 and SBA-15 as catalyst supports. While MCM-41 and SBA-15 share similar hexagonal pore arrays, their pore dimensions are very different. The synthetic procedure including preparation of the ligand, immobilization onto silicas, and capping with trimethylsilyl moieties, is shown in Scheme 1.13. The amine group of **1.16** was protected using ethyl chloroformate and the acid was converted to a methyl ester to give **1.17**. Treatment of **1.17** using phenylmagnesium chloride yielded a tertiary alcohol, and the carbamate group was converted to the corresponding methylamine through treatment with LAH to give **1.18**. Chloropropyl linkers were grafted on the walls of mesoporous silicas by treating with

$(CH_3CH_2O)_3SiCH_2CH_2CH_2Cl$ in refluxing toluene to give **1.20a-c**, followed by treatment with **1.18** to give **1.21a-c**. Free SiOH groups were capped with HMDS to give **1.22a-c** and subsequent workup gives **1.23a-c**. PXRD results indicate the mesoporous structure of SBA-15 remained unaltered during preparation of the catalyst. Surface area decreased substantially during the chloropropyl-grafting step, although the pore dimensions remain relatively unchanged.[33a]
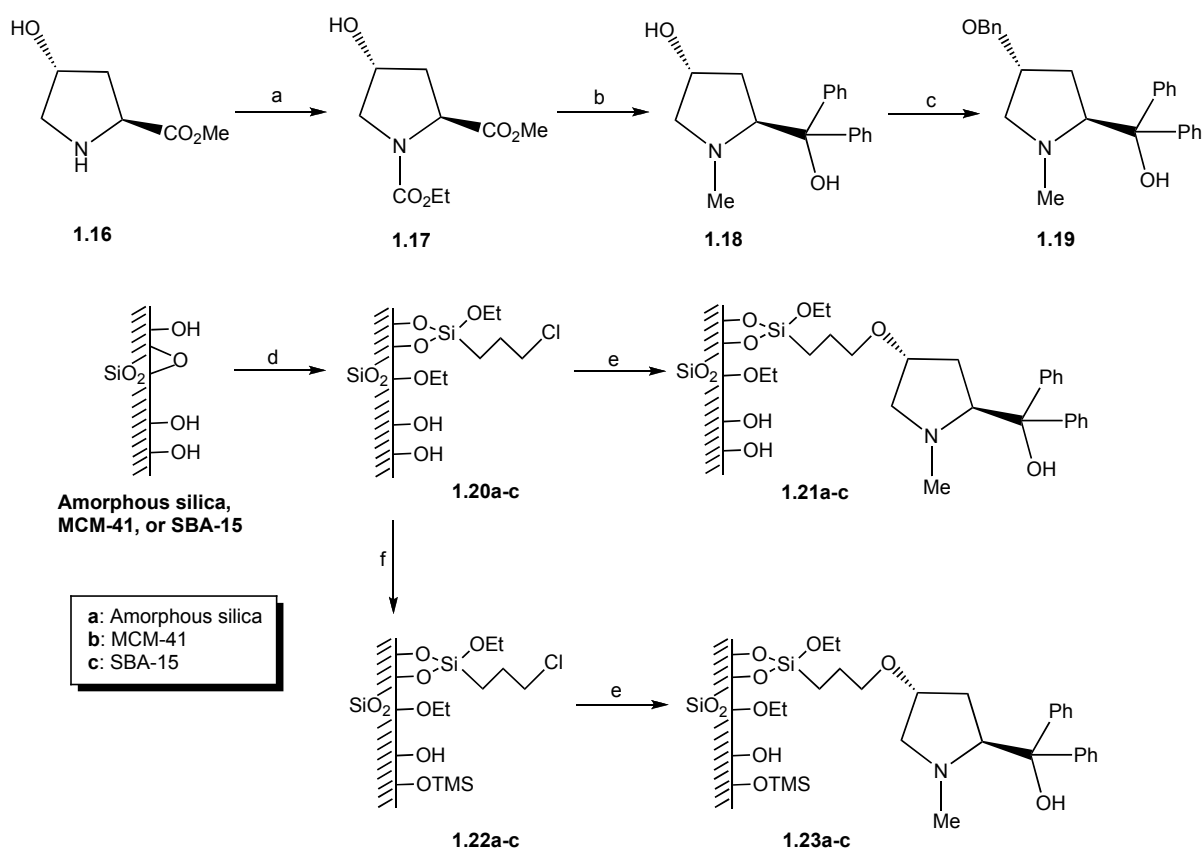
Scheme 1.13 The synthetic routes used in the preparation of various catalysts. *Reagents and conditions*: a: (i) ethyl chloroformate, $NaHCO_3$, H_2O, r.t., 16h; (ii) $SOCl_2$, MeOH, r.t., 12h; b: (i) PhMgCl, THF, 0 °C, 5h; (ii) $LiAlH_4$, THF, reflux, 3h; c: NaH, BnBr, THF, r.t., 16h; d: Chloropropyltriethoxysilane, toluene, reflux, 12h; e: **1.18**, xylene, reflux, 12h; f: HMDS, reflux 12h.

The silica-based catalysts were investigated for the asymmetric addition of diethylzinc to benzaldehydes. For each silica catalyst, two different sets of reactions were

run with 6 mol% of catalyst and either 3 eq. of diethylzinc to benzaldehyde (method A) or 7.2 mol% of Bu^{n}Li followed by 3 eq. of diethylzinc (method B). The parent homogeneous catalyst, **1.19**, provided products with 90 and 93% ee, respectively, *via* methods A and B. However, when the chiral catalysts anchored on amorphous silica were tested using method A, **1.21a** and **1.23a** gave only 16 and 37% ee, respectively. When the reactions were carried out using method B, slight improvements in the enantioselectivities were observed. A noticeably higher enantioselectivity was observed in the reactions employing MCM-41 based catalyst and consistently higher results were obtained with the catalysts based upon SBA-15. In both systems, TMS-capping as well as the employment of Bu^{n}Li improved the enantioselectivity significantly. The catalytic activity of TMS-capped SBA-15, **1.22c**, without a chiral ligand, was tested and shown to exhibit a 15% yield of the product. This indicates that even with TMS-capping, there remains some residual activity of the silica, resulting in a reduction of the enantioselectivity.

Chiral Mn^{III}(salen) complexes are excellent catalysts for enantioselective epoxidation of unfunctionalized olefins[47] and the immobilization of the complexes has received much attention.[48] A chiral Cr(salen) complex was immobilized on modified MCM-41 through the axial complexation of Cr by NH$_2$ groups grafted onto the surface of MCM-41.[19e] The salen complexes were immobilized by one coordinative bond. Li *et al* anchored a chiral Mn^{III}(salen) complex onto siliceous MCM-41 by a new strategy (Scheme 1.14).[49] The Mn(salen)/MCM-41 catalyst demonstrates excellent enantioselectivity for the asymmetric epoxidation of unfunctionalized olefins.

The Mn(salen) complex was prepared according to literature procedure. The MCM-41-anchored Mn(salen) complex was prepared as shown in Scheme 1.15. 4-

trimethoxysilylphenoxy-trimethylsilane **1.25** was obtained from 4-bromophenoxy-trimethylsilane **1.24**[50] as confirmed the by FT-IR spectrum. **1.25** was then anchored onto MCM-41[51] to form **1.26** and IR was used again to confirm the successful grafting. Modified MCM-41 **1.27**, was obtained from acidic hydrolysis of **1.26** and was confirmed by IR, EA, and NMR studies. The chiral Mn(salen) complex was then anchored onto **1.27** though the complexation of manganese by oxygen atoms of the phenoxyl groups. After stirring **1.27** in NaOH(aq), the solid was recovered by filtration and refluxed in EtOH in the presence of the Mn(salen) complex. The resulting solid catalyst **1.28** was characterized by IR, EPR, and UV-Vis.
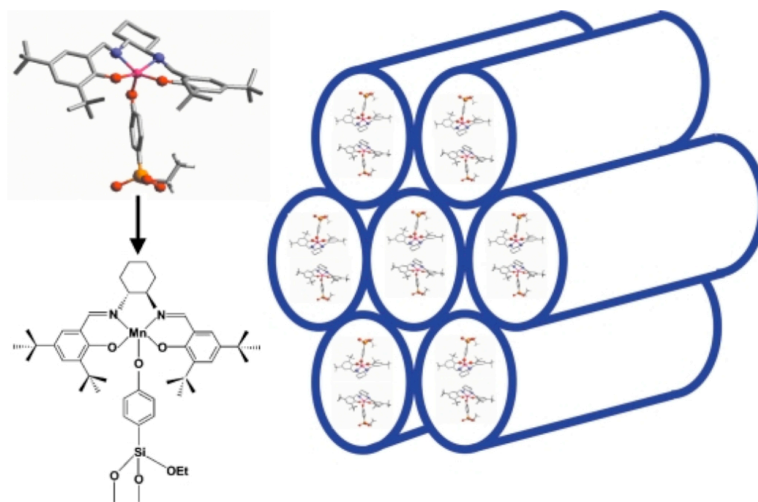
Scheme 1.14 Heterogeneous chiral catalyst, prepared by anchoring of the Mn(salen) complex onto the MCM-41 support.
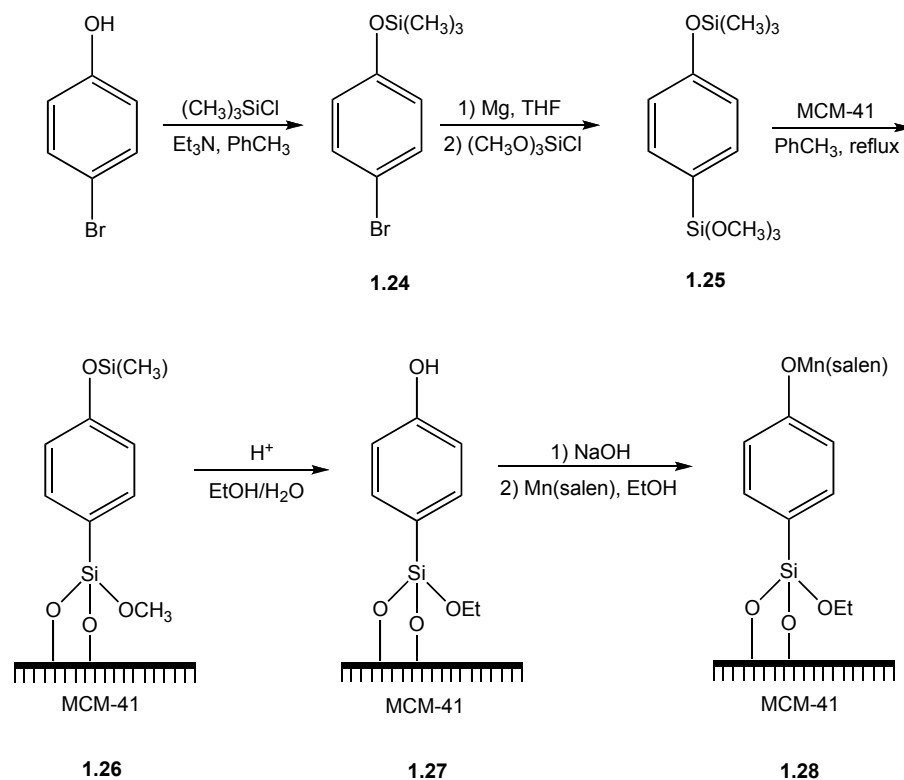
Scheme 1.15 The anchoring of the Mn(salen) complex on the MCM-41 support.

The solid catalyst was tested for the asymmetric epoxidation of simple olefins. The homogeneous Mn(salen) complex is active but has low enantioselectivity (56% ee) for the epoxidation of *a*-methylstyrene in CH_2Cl_2 with NaOCl as oxidant. After immobilization, the activity of the heterogeneous catalyst decreases but enantioselectivity increases significantly to 76%. The increase in enantiomeric excess is mainly attributed to the unique spatial environment constituted by the axial bulky group and the mesopores of the MCM-41 support. The decrease in conversion is obviously due to the slow diffusion of the reactant and the oxidant into the mesopores of the MCM-41 in the multiphase reaction system. Acetone may be used in place of CH_2Cl_2 to increase conversion (99%) with slight loss of enantioselectivity.

The catalyst could be re-used for the epoxidation of *a*-methylstyrene in EtOH. The activity and enantioselectivity did not decrease during the re-use experiments for up to 3 runs. This indicates the Mn(salen) catalyst is strongly bound to the MCM-41 through axial complexation of the manganese by oxygen atoms of the phenoxyl group. Furthermore, it was demonstrated that although the homogeneous complex is active and enantioselective for the epoxidation of 1-phenylcyclohexene, the anchored Mn(salen) catalyst is inactive. 1-phenylcyclohexene is too large to enter the pores of MCM-41, indicating the Mn(salen) species are mainly anchored in the mesopores of MCM-41.

1.4 Conclusions

This chapter provides an overview of recent developments in the design of self-supported asymmetric catalysts and mesoporous silica-supported asymmetric catalysts. Three distinct approaches have been used prepare self-supported asymmetric catalysts based on early and late transition metals as well as lanthanides. The first two approaches have the propensity to lead to highly porous and crystalline solid catalysts so that more catalytic sites are accessible to the prochiral substrates, but they require the use of two different metal centers in most cases. The third approach only uses the catalytically metal centers to link the multitopic chiral ligands and is in principle more straightforward. However, there is no information on the porosity of the solid catalysts, and there is concern that the catalytic centers in the third approach might not be as accessible to the prochiral substrates as those in the first two approaches. The three approaches are entirely complementary and together they show remarkable versatility in designing a wide range of heterogeneous asymmetric catalysts. The efficiency of these catalysts has been demonstrated for a range of asymmetric catalytic reactions.

Mesoporous silicas have been successfully employed as supports for various chiral catalysts. Immobilization of homogeneous asymmetric catalysts on the inner walls of mesoporous silicas offers inherent advantages over less-ordered supports. The recyclability, reusability, and ability to prevent leaching of toxic metals make silica-based catalysts very intriguing. The next couple of chapters will cover several novel self-supported catalyst systems based on MOFs as well as mesoporous silica nanosphere (MSN)-supported catalyst systems, including synthesis, characterization, and catalytic reactions.

1.5 References

[1] Jacobsen E.N.; Pfaltz, A.; Yamamoto, H. Eds. In *Comprehensive Asymmetric Catalysis*; Springer: Berlin, **1999**; Vols. 1-3.

[2] (a) Noyori, R. Asymmetric catalysis: science and opportunities (Nobel Lecture). *Angew. Chem., Int. Ed*. **2002**, *41* (12), 2008-2022; (b) Knowles, W. S., Asymmetric hydrogenations (Nobel lecture 2001) *Adv. Synth. Catal*., **2003**, *345* (1-2), 3-13.

[3] (a) Blaser, H.-U. The chiral switch of (S)-metalchlor: A personal account of an industrial odyssey in asymmetric catalysis. *Adv. Synth. Catal*. **2002**, *344* (1), 17-31; (b) Sheldon, R. A. Atom efficiency and catalysis in organic synthesis. *Pure Appl. Chem.* **2000**, *72* (7), 1233-1246.

[4] (a) Fan, Q. H.; Li, Y.-M.; Chan, A. S. C. Recoverable catalysts for asymmetric organic synthesis. *Chem. Rev.* **2002**, *102* (10), 3385-3466; (b) McMorn, P.; Hutchings, G. J. Heterogeneous enantioselective catalysts: Strategies for the immobilization of homogeneous catalysts. *Chem. Soc. Rev.* **2004**, *33*, 108-122; (c) Thomas, J. M.; Raja, R.; Lewis, D. W. Single-site heterogeneous catalysts. *Angew. Chem., Int. Ed.* **2005**, *44* (40), 6456-6482; (d) Hu, A.; Yee, G. T.; Lin, W. Magnetically recoverable chiral catalysts immobilized on magnetite nanoparticles for asymmetric hydrogenation of aromatic ketones. *J. Am. Chem. Soc.* **2005,** *127* (36), 12486-12487.

[5] (a) Song, C. E.; Lee, S. G. Supported chiral catalysts on inorganic materials. *Chem. Rev.,* **2002**, *102* (10), 3495-3524; (b) Fan, Q. H.; Li, Y. M.; Chan, A. S. C. Recoverable catalysts for asymmetric organic synthesis *Chem. Rev.* **2002**, *102* (10), 3385-3466; (c) Sinou, D. Asymmetric organometallic-catalyzed reactions in aqueous media. *Adv. Syn. Catal.* **2002**, *344* (3-4), 221-237; (d) Saluzzo, C.; Lemaire, M. Homogeneous-supported catalysts for enantioselective hydrogenation and hydrogen transfer reduction. *Adv. Syn. Catal.* **2002**, *344* (9), 915-928; (e) Pu, L. 1,1'-Binaphthyl dimers, oligomers, and polymers: Molecular recognition, asymmetric catalysis, and new materials. *Chem. Rev.* **1998**, *98* (7), 2405-2494.

[6] Dai, L.-X. Chiral metal-organic assemblies – a new approach to immobilizing homogeneous asymmetric catalysts. *Angew. Chem. Int. Ed.* **2004**, *43* (43), 5726-5729.

[7] (a) De Vos, D. E.; Vankelecom, I. F. J.; Jacobs, P. A. *Chiral Catalyst Immobilization and Recycling.* **2002**, Wiley-VCH, Weinheim; (b) Gladysz, J. A. Recoverable catalysts and reagents. *Chem. Rev.* **2002**, *102* (10), 3215-3892.

[8] Pu, L. Rigid and sterically regular chiral 1,1'-binaphthyl polymers in asymmetric catalysis. *Chem. Eur. J.* **1999**, *5* (8), 2227-2232.

[9] (a) Clearfield, A. Metal phosphonate chemistry. *Prog. Inorg. Chem.* **1998**, *47*, 371-510; (b) Alberti, G.; Costantino, U.; Marmottini, F.; Vivani, R.; Zappeli, P.; Zirconium phosphite (3,3',5,5'-tetramethylbiphenyl)diphosphonate, a microporous, layered, inorganic-organic polymer. *Angew. Chem. Int. Ed. Engl.* **1993**, *32* (9), 1357-1359; (c) Mallouk, T. E.; Gavin, J.

A. Molecular recognition in lamellar solids and thin films. *Acc. Chem. Res.* **1998**, *31* (5), 209-217.

[10] (a) Noyori, R.; Takaya, H. BINAP: an efficient chiral element for asymmetric catalysis. *Acc. Chem. Res.* **1990**, *23* (10), 345-350; (b) Kitamura, M; Ohkuma, T.; Inoue, S.; Sayo, N.; Kumobayashi, H.; Akutagawa, S.; Ohta, T.; Takaya, T.; Noyori, R. Homogeneous asymmetric hydrogenation of functionalized ketones. *J. Am. Chem. Soc.* **1998**, *110* (2), 629-631.

[11] Hu, A.; Ngo, H. L.; Lin, W. Chiral, porous, hybrid solids for highly enantioselective heterogeneous asymmetric hydrogenation of β-keto esters. *Angew. Chem. Int. Ed.* **2003**, *42* (48), 6000-6003.

[12] Ohkuma, T.; Ooka, H.; Ikariya, T.; Noyori, R. Preferential hydrogenation of aldehydes and ketones. *J. Am. Chem. Soc.* **1995**, *117* (41), 10417-10418; (b) Doucet, H.; Ohkuma, T.; Murata, K.; Yokozawa, T.; Kozawa, M.; Katatama, E.; England, A. F.; Ikariya, T.; Noyori, R. trans-[RuCl$_2$(phosphane)$_2$(1,2-diamine)] and chiral trans-[RuCl$_2$(diphosphane)(1,2-diamine)]: Shelf-stable precatalysts for the rapid, productive, and stereoselective hydrogenation of ketones. *Angew. Chem., Int. Ed.* **1998**, *37* (12), 1703-1707; (c) Ohkuma, T.; Ishii, D.; Takeno, H.; Noyori, R. Asymmetric hydrogenation of amino ketones using chiral RuCl$_2$(diphosphine)(1,2-diamine) complexes. *J. Am. Chem. Soc.* **2000**, *122* (27), 6510-6511; (d) Ohkuma, T.; Koizumi, M.; Doucet, H.; Pham, T.; Kazawa, M.; Murata, K.; Katayama, E.; Yokozawa, T.; Ikariya, T.; Noyori, R. Asymmetric hydrogenation of alkenyl, cyclopropyl, and aryl ketones. RuCl$_2$(xylyl-binap)(1,2-diamine) as a precatalyst exhibiting a wide scope. *J. Am. Chem. Soc.* **1998**, 120 (51), 13529-13530; (e) Ohkuma, T.; Koizumi, M.; Muniz, K.; Hilt, G.; Kabuto, C.; Noyori, R. *trans*-RuH(η^1-BH$_4$)(binap)(1,2-diamine): A catalyst for asymmetric hydrogenation of simple ketones under base-free conditions. *J. Am. Chem. Soc.* **2002**, *124* (23), 6508-6509.

[13] (a) Hu, A.; Lin, W. Ru-catalyzed asymmetric hydrogenation of α-phthalimide ketones and 1,3-daryl diketones using 4,4'-substituted BINAPs *Org. Lett*. **2005,** *7* (3)**,** 455-458; (b) Hu. A.; Ngo, H. L.; Lin, W. 4,4'-Disubstituted BINAPs for highly enantioselective Ru-catalyzed asymmetric hydrogenatin of ketones. *Org. Lett*. **2004**, *6* (17), 2937-2940; (c) Hu, A.; Ngo, H. L.; Lin, W. Remarkable 4,4'-substituent effects on binap: Highly enantioselective Ru catalysts for asymmetric hydrogenation of β-aryl ketoesters and their immobilization in room-temperature ionic liquids. *Angew. Chem., Int. Ed*. **2004**, *43* (19), 2501-2504; (d) Ngo, H. L.; Lin, W. Development of 4,4'-substituted-xylBINAP ligands for highly enantioselective hydrogenation of ketones. *J. Org. Chem*. **2005**, *70* (4), 1177-1187.

[14] Cho, S.-H.; Gadzikwa, T.; Afshari, M.; Nguyen, S. T.; Hupp, J. T. [Bis(catechol)salen]Mn^{III} coordination polymers as support-free heterogeneous asymmetric catalysts for epoxidation. *Eur. J. Inorg. Chem.* **2007**, *31*, 4863-4867.

[15] Cho, S.-H.; Ma, B.; Nguyen, S. T.; Hupp, J. T.; Albrecht-Schmitt, T. E. A metal-organic framework material that functions as an enantioselective catalyst for olefin epoxidation. *Chem. Comm.* **2006**, *24*, 2563-2565.

[16] Bae, S. J., Kim, S.-W., Hyeon, T., Kim, B. M. New chiral heterogeneous catalysts based on mesoporous silica: diethylzinc addition to benzaldehydes. *Chem. Comm.* **2000**, *1*, 31-32.

[17] (a) Pu, L.; Yu, H.-B. Catalytic asymmetric organozinc additions to carbonyl compounds. *Chem. Rev.* **2001**, *101* (3)*, 757-824; (b) Mori, M.; Nakai, T. Asymmetric catalytic alkylation of aldehydes with diethylzinc using chiral binaphthol-titanium complex. *Tetrahedron Lett.* **1997**, *38* (35), 6233-6236; (c) Zhang, F.-Y.; Yip, C.-W.; Cao, R.; Chan, A. S. C. Enantioselective addition of diethylzinc to aromatic aldehydes catalyzed by Ti(BINOL) complex. *Tetrahedron: Asymmetry* **1997**, *8* (4), 585-589.

[18] Yuan, Y.; Zhang, X.; Ding, K. Quasi solvent-free enantioselective carbonyl-ene reaction with extremely low catalyst loading. *Angew. Chem., Int. Ed.* **2003**, *42* (44), 5478-5480.

[19] Takizawa, S.; Somei, H.; Jayaprakash, D.; Sasai, H. Metal-bridged polymers as insoluble multicomponent asymmetric catalysts with high enantiocontrol: An approach for the immobilization of catalysts without any support. *Angew. Chem. Int. Ed.* **2003**, *42* (46), 5711-5714.

[20] Ma, L.; White, P. S.; Lin, W. Well-defined enantiopure 1,1'-binaphthyl-based oligomers: Synthesis, structure, photophysical properties, and chiral sensing. *J. Org. Chem.* **2002**, *67* (22), 7577-7586.

[21] (a) Arai, T.; Yamada, Y. M. A.; Yamamoto, N.; Sasai, H.; Shibasaki, M. Self-assembly of heterobimetallic complexes and reactive nucleophiles: A general strategy for the activation of asymmetric reactions promoted by heterobimetallic catalysts. *Chem. Eur. J.* **1996**, *2* (11), 1368-1372.

[22] Arai, T.; Sekiguti, T.; Iizuka, Y.; Takizawa, S.; Sakamoto, S.; Yamaguchi, K.; Sasai, H. A dendrimer-supported heterobimetallic asymmetric catalyst. *Tetrahedron: Asymmetry* **2002**, *13* (19), 2083-2087.

[23] Kitamoto, D.; Imma, H.; Nakai, T. Asymmetric catalysis by a new type of chiral binaphthol-titanium complex. *Tetrahedron Lett.* **1995**, *36* (11), 1861-1864.

[24] Jia, X.; Li, X.; Xu, L.; Li, Y.; Shi, Q.; Au-Yeung, T.-L.; Yip, C.; Yao, X.; Chan, A. S. C. Titanium-catalyzed tandem sulfoxidation-kinetic resolution process: A convenient method for higher enantioselectivities and yields of chiral sulfoxide. *Adv. Synth. Catal.* **2004**, *346* (7), 723-726.

[25] Wang, X.; Wang, X.; Guo, H.; Wang, Z.; Ding, K. Self-supported heterogeneous titanium catalysts for enantioselective carbonyl-ene and sulfoxydaton reactions. *Chem. Eur. J.* **2005**, *11* (14), 4078-4088.

[26] (a) Kinoshita, T.; Okada, S.; Park, S. R.; Matsunaga, S.; Shibasaki, M. Sequential Wittig olefination-catalytic asymmetric epoxidation with reuse of waste PH$_3$P(O): Application of α,β-unsaturated N-acyl pyrroles as ester surrogates. *Angew. Chem. Int. Ed.* **2003**, *42* (38), 4680-4684; (b) Matsunaga, S.; Kinoshita, T.; Okada, S.; Harada, S.; Shibasaki, M. Catalytic asymmetric 1,4-addition reactions using α,β-unsaturated *N*-acylpyrroles as highly reactive monodentate α,β-unsaturated ester surrogates. *J. Am. Chem. Soc.* **2004**, *126* (24), 7559-7570.

[27] Wang, X.; Shi, L.; Li, M.; Ding, K. Heterogenization of Shibasaki's binol/La catalyst for enantioselective epoxidation of α,β-unsaturated ketones with multitopic binol ligands: The impact of bridging spacers. *Angew. Chem. Int. Ed.* **2005**, *44* (39), 6362-6366.

[28] (a) Horner, L.; Siegel, H.; Buthe, H. Asymmetric catalytic hydrogenation with an optically active phosphinerhodium complex in homogeneous solution. *Angew. Chem., Int. Ed. Engl.* **1968**, *7* (12), 942; (b) Knowles, W. S.; Sabacky, M. J. Catalytic asymmetric hydrogenation employing a soluble, optically active, rhodium complex. *J. Chem. Soc., Chem. Comm.* **1968**, 1445-1446.

[29] (a) Reetz, M. T.; Mehler, G. Highly enantioselective Rh-catalyzed hydrogenation reactions based on chiral monophosphite ligands. *Angew. Chem., Int. Ed.* **2000**, *39* (21), 3889-3890; (b) van den Berg, M., Minnaard, A. J., Schudde, E. P., van Esch, J., de Vries, A. H. M., de Vries, J. G., Feringa, B. L. Highly enantioselective rhodium-catalyzed hydrogenation with monodentate ligands. *J. Am. Chem. Soc.* **2000**, *122* (46), 11539-11540; (c) Claver, C.; Fernandez, E.; Gillon, A.; Heslop, K.; Hyett, D. J.; Martorell, A.; Orpen, A. G.; Pringle, P. G. Biarylphosphonites: a class of monodentate phosphorous(III)ligands that outperform their chelating analogues in asymmetric hydrogenation studies. *Chem. Comm.* **2000,** *11*, 961-962.

[30] Wang, X.; Ding, K. Self-supported heterogeneous catalysts for enantioselective hydrogenation. *J. Am. Chem. Soc.* **2004**, *126* (34), 10524-10525.

[31] Liang, Y.; Jing, Q.; Li, X.; Shi, L.; Ding, K. Programmed assembly of two different ligands with metallic ions: Generation of self-supported Noyori-type catalysts for heterogeneous asymmetric hydrogenation of ketones. *J. Am. Chem. Soc.* **2005**, *127* (21), 7694-7695.

[32] Kresge, C. T.; Leonowicz, M. E.; Roth, W. J.; Vartuli, J. C.; Beck, J. S. Ordered mesoporous molecular sieves synthesized by a liquid-crystal template mechanism. *Nature* **1992**, *359*, 710-712.

[33] (a) Bae, S. J.; Kim, S.-W.; Hyeon, T.; Kim, B. M. New chiral heterogeneous catalysts based on mesoporous silica: asymmetric diethylzinc addition to benzaldehydes. *Chem. Commun.* **2000**, *1*, 31-32; (b) Corma, A.; Garcia, H.; Moussaif, A.; Sabater, M .J.; Zniber, R.;

Redouane, A. Chiral copper(II) bisoxazoline covalently anchored to silica and mesoporous MCM-41 as a heterogeneous catalyst for the enantioselective Friedel-Crafts hydroxyalkylation. *Chem. Commun.* **2002**, *10*, 1058-1059; (c) Xiang, S.; Zhang, Y.; Xin, Q.; Li, C. Asymmetric epoxidation of allyl alcohol on organic-inorganic hybrid chiral catalysts grafted onto the surface of silica and in the mesopores of MCM-41. *Angew. Chem. Int. Ed.* **2002**, *41* (5), 821-824; (d) Jones, M. D.; Raja, R.; Thomas, J. M.; Johnson, B. F. G.; Lewis, D. W.; Rouzaud, J.; Harris, K. D. M. Enhancing the enantioselectivity of novel homogeneous organometallic hydrogenation catalysts. *Angew. Chem. Int. Ed.* **2003**, *42* (36), 4326-4331.

[34] Kesanli, B.; Lin, W. Mesoporous silica anchored Ru catalysts for highly enantioselective hydrogenation of ß-ketoesters. *Chem. Commun.* **2004**, *20*, 2284-2285.

[35] (a) Zhao, D.; Feng, J.; Huo, Q.; Melosh, N.; Frederickson, G. H.; Chmelka, B. F.; Stucky, G. D. Triblock copolymer syntheses of mesoporous silica with periodic 50 to 500 angstrom pores. *Science* **1998**, *279* (23), 548-552; (b) Yang, P.; Zhao. D.; Margolese, D. I.; Chmelka, B. F.; Stucky, G. D.; Galen, D. Generalized synthesis of large-pore mesoporous metal oxides with semicrystalline frameworks. *Nature* **1998**, *396*, 152-155.

[36] Hu, A.; Ngo, H. L.; Lin, W. Remarkable 4,4'-substituent effects on Binap: highly enantioselective Ru catalysts for asymmetric hydrogenation of ß-aryl ketoesters and their immobilization in room-temperature ionic liquids. *Angew. Chem. Int. Ed.* **2004**, *43* (19), 2501-2504.

[37] Gao, H.; Angelici, R. J. Hydroformylation of 1-Octene under atmospheric pressure catalyzed by rhodium carbonyl thiolate complexes tethered to silica. *Organometallics*, **1998**, *17* (14), 3063-3069.

[38] Typical loadings are 0.0125 mmol of **14** and 0.0112 mmol of **15** per gram of SBA-15, respectively.

[39] Although ß-alkyl ß-ketoesters can be hydrogenated with complete conversions in the presence of 1% of **15**, much inferior e.e. values (10-15% lower) were obtained.

[40] Noyori, R.; Ohkuma, T.; Kitamura, M.; Takaya, H. Asymmetric hydrogenation of ß-keto carboxylic esters. A practical, purely chemical access to ß-hydroxy esters in high enantiomeric purity. *J. Am. Chem. Soc.* **1987**, *109* (19), 5856-5858.

[41] Hu, A.; Ngo, H. L.; Lin, W. Chiral, porous, hybrid solids for highly enantioselective heterogeneous asymmetric hydrogenation of ß-keto esters. *Angew. Chem. Int. Ed.* **2003**, *42* (48), 6000-6003.

[42] Halle, R.; Colasson, B.; Schulz, E.; Spagnol, M.; Lemaire, M. Diam-BINAP; a highly efficient monomer for the synthesis of heterogeneous enantioselective catalysts. *Tetrahedron Lett.* **2000**, *41* (5), 643-646.

[43] Soai, K. Watanabe, M.; Yamamoto, A. Enantioselective addition of dialkylzincs to aldehydes using heterogeneous chiral catalysts immobilized on alumina and silica gel. *J. Org. Chem.,* **1990**, *55* (16), 4832-4835.

[44] Lasperas, M.; Bellocq, N.; Brunel, D.; Moreau, P. Chiral mesoporous templated silicas as heterogeneous inorganic-organic catalysts in the enantioselective alkylation of benzaldehydes. *Tetrahedron: Asymmetry,* **1998**, *9* (17), 3053-3064.

[45] Soai, K.; Ookawa, A.; Kaba, T.; Ogawa, K. Catalytic asymmetric induction. Highly enantioselective addition of dialkyzincs to aldehydes using pyrrolidinylmethanols and their metal salts. *J. Am. Chem. Soc.* **1987**, *109* (23), 7111-7115.

[46] Tatsumi, T.; Koyano, K. A.; Tanaka, Y.; Nakata, S. Stabilization of mesoporous molecular sieves by trimethylsilylation. *J. Phys. Chem. B.* **1997**, *101* (46), 9436-9440.

[47] (a) Jacobsen, E. N.; Zhang, W.; Muci, A. R.; Ecker, J. R.; Deng, L. Highly enantioselective epoxidation catalysts derived from 1,2-diaminocyclohexane. *J. Am. Chem. Soc.* **1991**, *113* (18), 7063-7064; (b) Jacobsen, E. N.; Lee, N. H.; Muci, A. R. Enantiomerically pure epoxychromans via asymmetric catalysis. *Tetrahedron Lett.* **1991**, *32* (38), 5055-5058; (c) Katsuki, T. Mn-salen catalyst, competitor of enzymes, for asymmetric epoxidation. *J. Mol. Catal. A: Chem.* **1996**, *113* (1-2), 87-107; (d) Canali, L.; Sherrington, D. C. Utilization of homogeneous and supported chiral metal(salen) complexes in asymmetric catalysis. *Chem. Soc. Rev.* **1999**, *28* (2), 85-93; (e) Zhang, W.; Jacobsen, E. N. Asymmetric olefin epoixdation with sodium hypochlorite catalyzed by easily prepared chiral manganese(III) salen complexes. *J. Org. Chem.* **1991**, *56* (7), 2296-2298.

[48] Vankelecom, I. F. J.; Tas, D.; Parton, R. F.; Van de Vyver, V.; Jacobs, P. A. Chiral catalytic membranes. *Angew. Chem. Int. Ed. Engl.* **1996**, *35* (12), 1346-1348; (b) Ogunwumi, S. B.; Bein, T. Intrazeolite assembly of a chiral manganese salen epoxidation catalyst. *Chem. Commun.* **1997**, *9*, 901-902; (c) Sabater, M. J.; Corma, A.; Domenech, A.; Fornes, V.; Garcia, H. Chiral salen manganese complex encapsulated within seolite Y: a heterogeneous enantioselective catalyst. *Chem. Commun.* **1997**, *9*, 1285-1286; (d) Kim, G.-J.; Shin, J.-H. The catalytic activity of new chiral salen complexes immobilized on MCM-41 by multi-step grafting in the asymmetric epoxidation. *Tetrahedron: Lett.* **1999**, *40* (37), 6827-6830; (e) Zhou, X.; Yu, X.; Huang, J.; Li, S.; Li, L.; Che, C. Asymmetric epoxidation of alkenes catalyzed by chromium binaphthyl Schiff base complex supported on MCM-41. *Chem. Commun.* **1999**, *18*, 1789-1790.

[49] Xiang, S.; Zhang, Y.; Xin, Q.; Li, C. Enantioselective epoxidation of olefins catalyzed by Mn(salen)/MCM-41 synthesized with a new anchoring method. *Chem. Commun.* **2002**, *22*, 2696-2697.

[50] Neville, R. G. Synthesis of 4-(2,3-epoxypropoxy)-phenyltrimethylsilane. *J. Org. Chem.,* **1960**, *25* (6), 1063-1064.

[51] Rao, Y. V. S.; De Vos, D. E.; Bein, T.; Jacobs, P. A. Practical heterogenization of an active manganese triazacyclononane epoxidation catalyst via surface glycidylation. *Chem. Commun.* **1997**, *4*, 355-356.

CHAPTER 2

HOMOCHIRAL METAL-ORGANIC FRAMEWORKS FOR POTENTIAL
HETEROGENEOUS CATALYSIS

2.1 Introduction

Asymmetric reduction of prochiral olefins, ketones, and imines is one of the most powerful methods for the production of optically active compounds.[1] Among these methodologies, Ru and Rh complexes of chiral chelating bisphosphines, particularly 2,2'-bis-diphenylphosphino)-1,1'-binaphthyl (BINAP) and its derivatives, were widely used for the hydrogenation of a wide range of substrates with high chemo-and enantioselectivity.[2]

Asymmetric organocatalysis methods[3] utilizing neutral Lewis bases have recently attracted considerable attention, leading to the emergence of new types of chiral ligands based on phosphoramides[4], *N*-oxides[5], and sulfoxides[6]. Since phosphine oxide is highly polar and has a relatively low Brönsted basicity[7], its reactivity would be expected to be similar to those of Lewis bases. In addition to their favorable reactivity, chiral phosphine oxides can be readily prepared by simple oxidation of commercially available chiral phosphines.

There still remain relatively few examples of the application of chiral phosphine oxides to asymmetric organocatalysis. Once such example was demonstrated by Kobayashi, who used 2,2'-bis(diphenylphosphoryl)-1,1'-binaphthyl, BINAPO, as a promoter the allylation of α-hydrazono esters, although more than stoichiometric amounts of BINAPO were required for the reaction to proceed.[8] Nakajima *et al* recently reported the first

examples of a chiral phosphine oxide as a catalyst in the enantioselective allylation of aldehydes, the ring opening of *meso*-epoxides, and enantioselective aldol reactions of trichlorosilyl enol ethers to afford aldol adducts in high diastereo- and enantioselectivites.[9]

The practical application of homogeneous asymmetric catalysts in industrial processes were often hindered due to high costs of both noble metals and chiral ligands as well as difficulties in removing trace amounts of toxic metals from the organic products. Heterogenization of these highly enantioselective catalysts, in some cases, has proven effective in overcoming these problems. The heterogenized catalysts can potentially combine the advantages of both homogeneous and heterogeneous systems and therefore provide easily recyclable and reusable solid catalysts that have uniform and precisely engineered active sites similar to those of their homogeneous counterparts. Many heterogenization approaches have been explored, including attaching the chiral catalysts to organic polymers, dendrimers, membrane supports, and porous inorganic oxides and immobilization via biphasic systems.[10] The heterogenized catalysts afforded by these methods are, however, typically less effective that their homogenous counterparts. This chapter describes our efforts in generating homochiral metal-organic frameworks containing BINAP oxide for potential heterogeneous asymmetric catalysis.

2.2 Results and Discussion

2.2.1 Synthesis and characterization of BINAP derived ligands

The new (*R*)-1,1'-binaphthyl-derived ligand L_{16}-H_2 was synthesized in 6 steps starting from commercially available 2,2'dihydroxy 1,1'binaphthyl (BINOL) (Scheme 2.1). BINOL was treated with triflic anhydride and pyridine to give the 2,2'-triflate-protected binaphthyl.[11] The protected 2,2'-triflic-BINOL was then treated with diphenylphosphine in

the presence of NiCl$_2$(dppe) and 1,4-diazabicyclo[2.2.2]octane (DABCO) to form 2,2'-bis(diphenylphosphino)-1,1'binaphthyl (BINAP)[12]. The diphenylphosphine moieties were then oxidized following treatment with H$_2$O$_2$ in acetone to form BINAPO. The prepared BINAPO was then subjected to bromination conditions to selectively brominate at the 4,4' positions of the binaphthyl ring. The **L$_{16}$**-Me$_2$ ligand was synthesized by a Pd-catalyzed Suzuki coupling between 4,4'-Br-BINAPO and commercially available 4'-(methoxycarbonyl)phenyl boronic acid. The **L$_{16}$**-Me$_2$ ligand could then be directly hydrolyzed by refluxing in NaOH in THF/MeOH to form the dicarboxylic acid **L$_{16}$**-H$_2$. The **L$_{16}$**-Me$_2$ may also be subjected to reduction conditions in Si(OEt)$_3$H and Ti(O^{i}Pr)$_4$ to obtain the 2,2'-bis-(diphenylphosphino)-1,1'-binaphthyl derivative, **L$_{17}$**-Me$_2$. All the intermediates and ligands were characterized by ^{1}H NMR and ^{31}P{^{1}H} NMR spectroscopy (Figure 2.1).

Attempts to hydrolyze **L$_{17}$**-Me$_2$ using basic reaction conditions followed by acidic workup resulted in what is thought to be the HCl salt of the 2,2'-bis-(diphenylphosphino)-1,1'-binaphthyl derivative (Scheme 2.2). ^{31}P{^{1}H} NMR showed a single peak at ~28.7 ppm indicating the signal was not from the P=O moiety of BINAPO (~26.7 ppm). **L$_{17}$**-Me$_2$ was also used in the attempted synthesis of a RuCl$_2$(diphosphine)(diamine) complex. However, the ruthenium complex decomposed during the hydrolysis process and acidic workup (Scheme 2.3). As a result, efforts were focused on the synthesis of metal-organic frameworks based on the BINAPO derivative **L$_{16}$**-H$_2$.
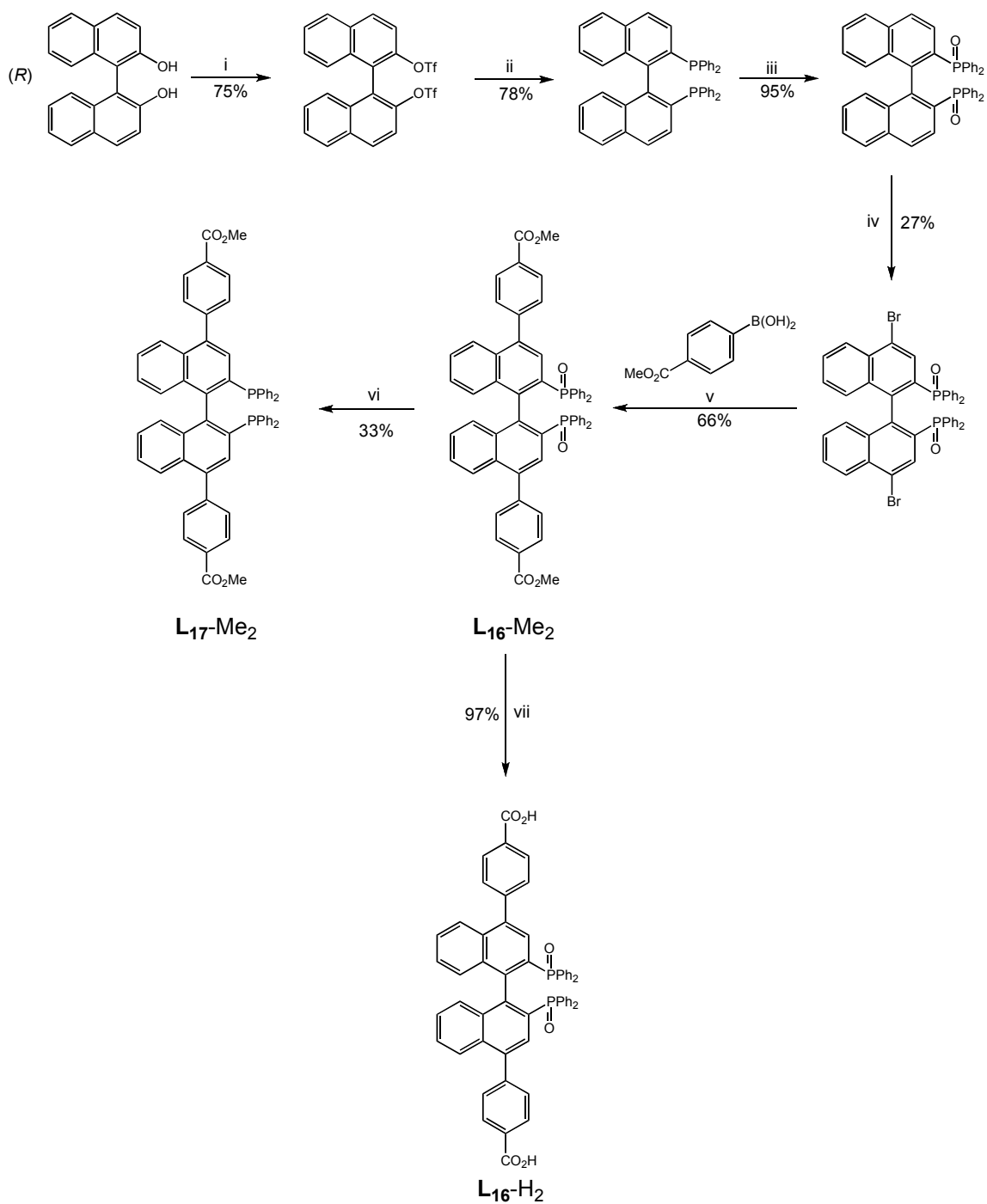
Scheme 2.1 Reagents and conditions: (i) Tf$_2$O, pyridine, O°C to RT; (ii) Ph$_2$PH, NiCl$_2$(dppe), DABCO, DMF, 100°C; (iii) 30% H$_2$O$_2$, acetone, RT, 20h; (iv) Br$_2$, pyridine, CH$_2$Cl$_2$, RT, 3d (v) Pd(PPh$_3$)$_4$, CsF, DME, 95°C, 3d; (vi) 2M NaOH, THF, MeOH, 70 °C, 24h; (vii) Si(OEt)$_3$H, Ti(O^{i}Pr)$_4$, toluene, reflux, 1h.
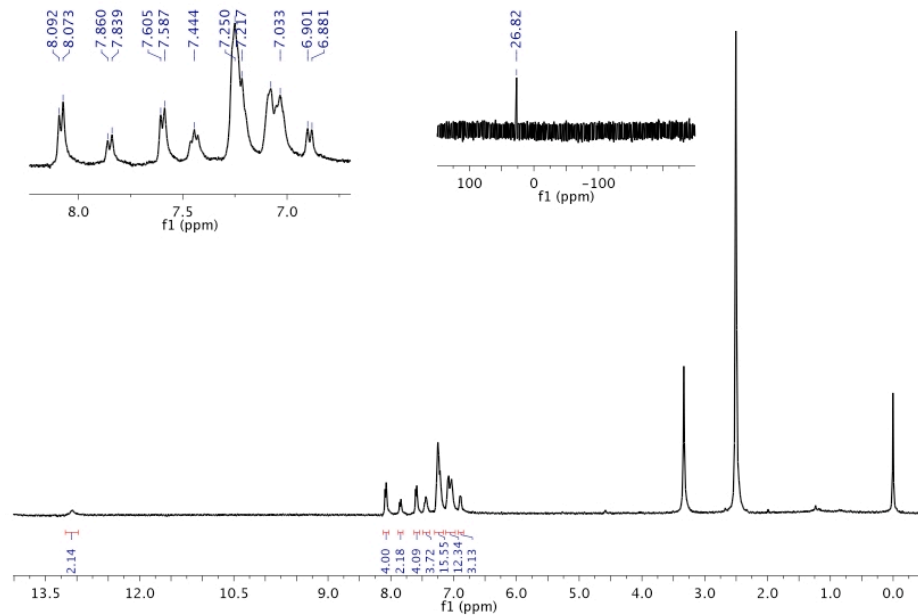
Figure 2.1 ^{1}H NMR of **L₁₆**-H₂.
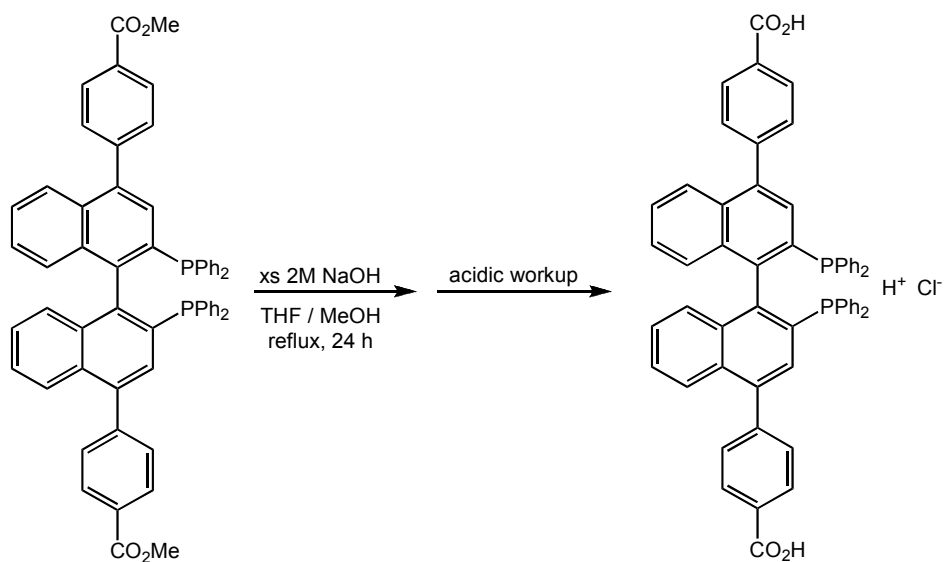
Scheme 2.2 Attempted synthesis of hydrolyzed 4,4'-benzoic acid 2,2'diphenylphosphino complex.
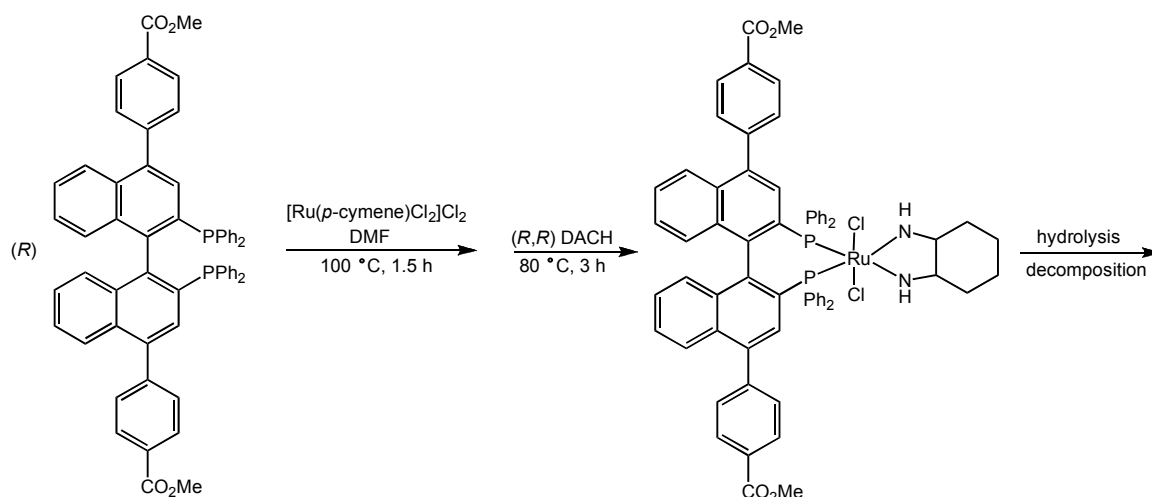
Scheme 2.3 Attempted synthesis of RuCl$_2$(diphosphine)(diamine) complex.

2.2.2 Synthesis and characterization of BINAPO crystals

When treated with Cu(II), Zn(II), Cd(II), or Mn(II) salts in DMF at 80 °C, single crystals of [Cu(**L$_{16}$**)(DMF)]·3DMF·4H$_2$O (**2.1**), [Zn(**L$_{16}$**)]·8DMF·6H$_2$O (**2.2**), [Cd(**L$_{16}$**)]·9DMF·H$_2$O (**2.3**), and [Mn(**L$_{16}$**)(H$_2$O)]·5DMF·5H$_2$O (**2.4**) were obtained (Scheme 2.4). The formulae for **2.1-2.4** were established by single crystal X-ray structure determination, ^{1}H NMR spectroscopy, and TGA analyses.
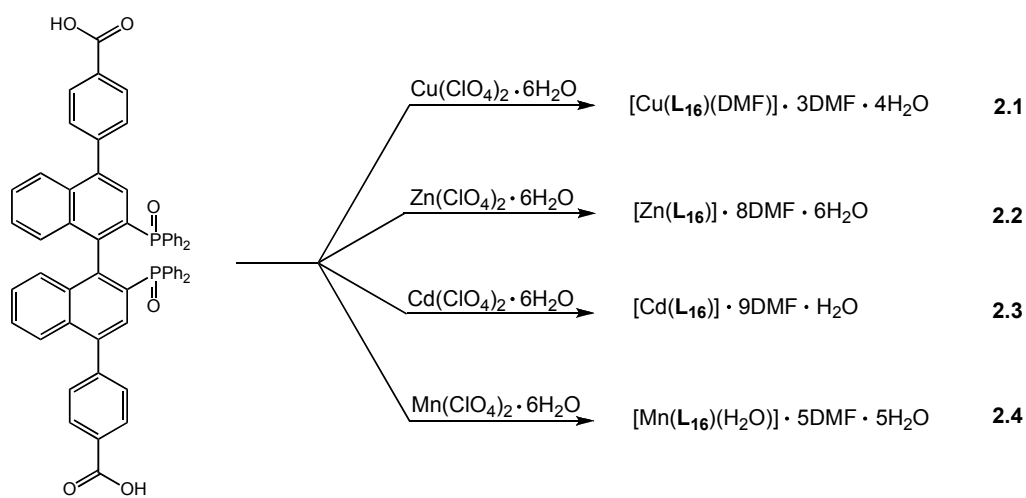
Scheme 2.4 Crystal growth and formulas of **2.1-2.4**.

To ensure consistent results, each sample was treated in exactly the same way for both TGA and ^{1}H NMR experiments (Figures 2.2 and 2.3-2.7), respectively). Fresh crystals were harvested by quick filtration, and briefly dried on filter paper under air. The sample was then divided and loaded into screw-capped vial with CD_3OD or the sample tray in TGA. The organic solvent inside the crystals is either DEF or DMF which has been exchanged by CD_3OD, and its exact amount was determined by calibrating against the internal standard, mesitylene. The total amounts of the solvents were obtained by TGA, the amount of water molecules was calculated by subtracting DEF/DMF from the total solvent amount. The framework structures of **4.1** to **4.6** were unambiguously determined by single-crystal X-ray diffraction studies.

Crystal	% Solvent Weight Loss	% Organic Weight Loss
2.1	27.7	58.3
2.2	42.4	48.6
2.3	40.0	49.0
2.4	35.2	46.8

Figure 2.2 Thermogravimetric analyses of **2.1-2.4.** The samples were heated at 5 ºC/min to 600 ºC and the temperature was held for 1 h.

$W_{crystal}$(mg)	11.17
W_{Mes}(mg)	8.6
W_{DMF} (mg) (From NMR)	2.48
W_{DMF} %	22.2%
$W_{(DMF+H_2O)}$% (From TGA)	27.7%
W_{H_2O}%	5.4%
Formula (**2.1**)	
[Cu(L$_{16}$)(DMF)]·3DMF·4H$_2$O	
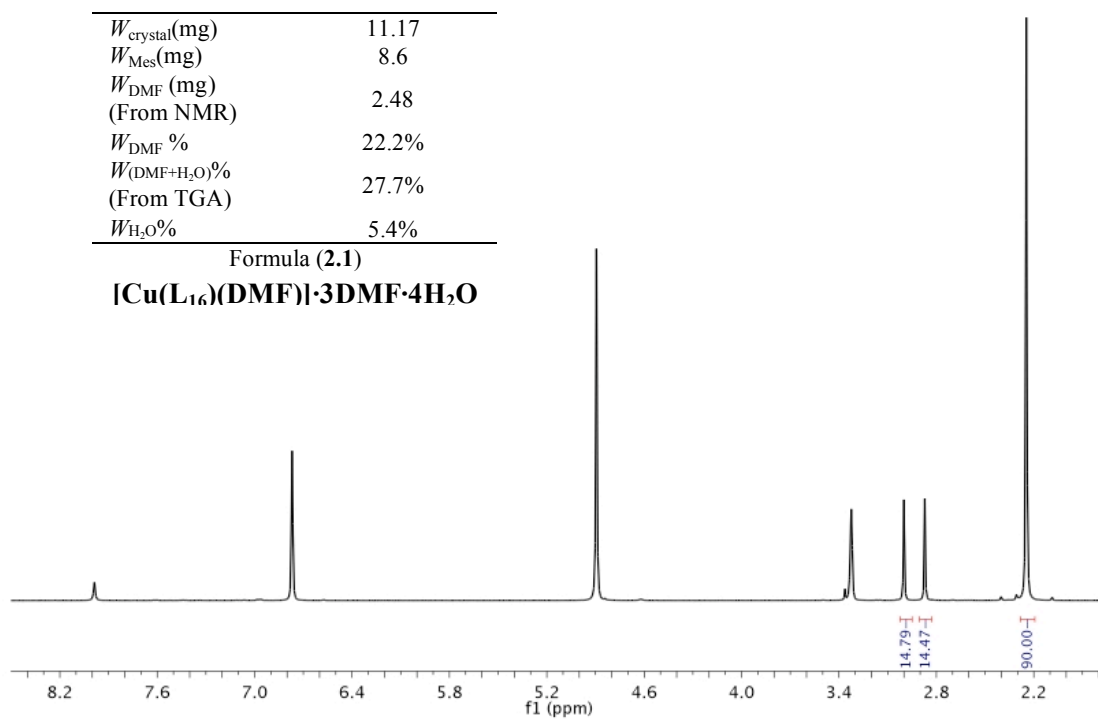
Figure 2.3 ^{1}H NMR spectroscopic determination of solvent content in **2.1**, mesitylene (Mes) was added as an internal standard

$W_{crystal}$(mg)	11.97
W_{Mes}(mg)	8.6
W_{DMF} (mg) (From NMR)	4.29
W_{DMF} %	35.8%
$W_{(DMF+H_2O)}$% (From TGA)	42.4%
W_{H_2O}%	6.5%
Formula (**2.2**)	
[Zn(L$_{16}$)]·8DMF·6H$_2$O	
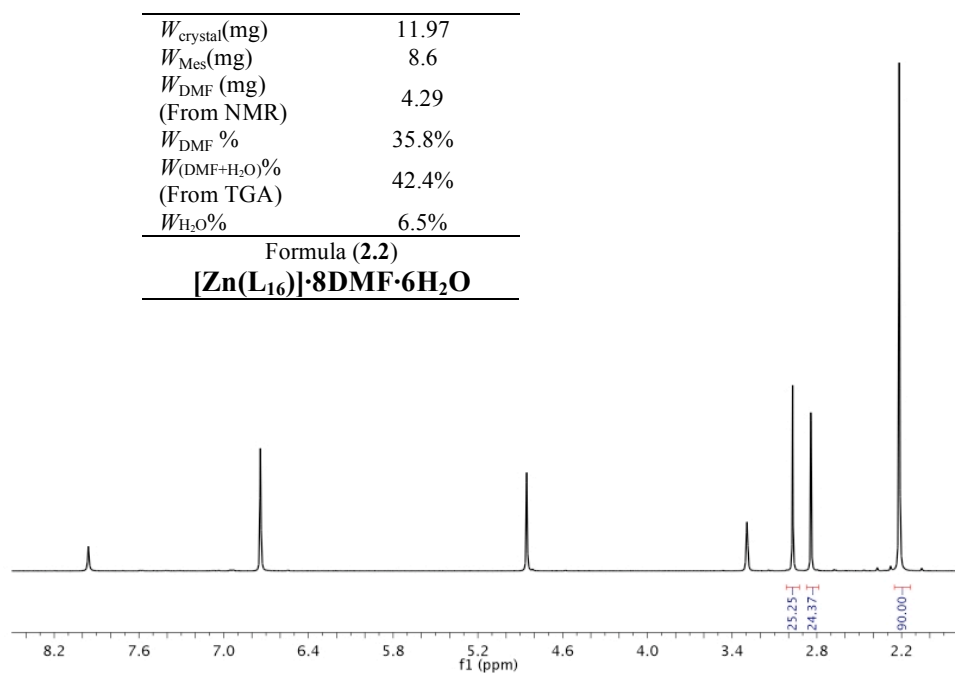
Figure 2.4 ^{1}H NMR spectroscopic determination of solvent content in **2.2**, mesitylene (Mes) was added as an internal standard

47

$W_{crystal}$(mg)	10.7
W_{Mes}(mg)	8.6
W_{DMF} (mg) (From NMR)	4.16
W_{DMF} %	38.9%
$W_{(DMF+H_2O)}$% (From TGA)	40.0%
W_{H_2O}%	1.1%
Formula (**2.3**) [Cd(L$_{16}$)]·9DMF·H$_2$O	
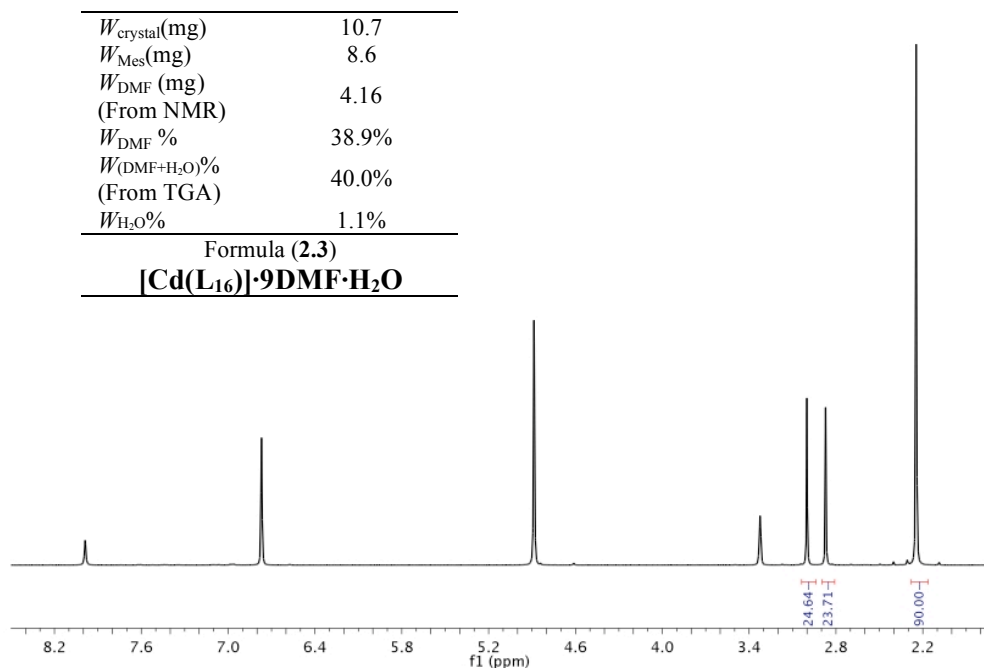
Figure 2.5 ^{1}H NMR spectroscopic determination of solvent content in **2.3**, mesitylene (Mes) was added as an internal standard

$W_{crystal}$(mg)	13.31
W_{Mes}(mg)	8.6
W_{DMF} (mg) (From NMR)	2.73
W_{DMF} %	27.3%
$W_{(DMF+H_2O)}$% (From TGA)	35.2%
W_{H_2O}%	7.8%
Formula (**2.4**) [Mn(L$_{16}$)(H$_2$O)]·5DMF·5H$_2$O	
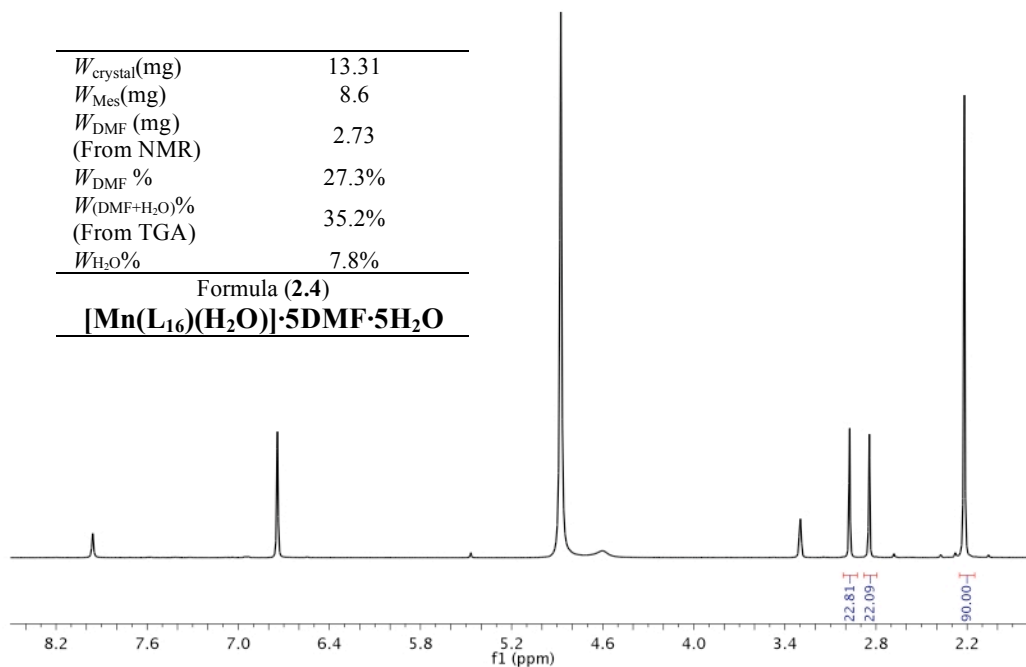
Figure 2.6 ^{1}H NMR spectroscopic determination of solvent content in **2.4**, mesitylene (Mes) was added as an internal standard

The molecular structures of Cu(II), Zn(II), Cd(II), and Mn(II) with L_{16} were established by X-ray crystallography. Compound **2.1** crystallizes in the triclinic P1 space group with a two-dimensional grid structure (Figure 2.7). The individual layers pack along the 111 direction with a very close interlayer distance of ~3.2 Å. The asymmetric unit consists of two ligands, two Cu^{II} centers, and two DMF molecules. The Cu atoms coordinate to four carboxylate oxygen atoms of four different L_{16} ligands to form $[Cu_2(O_2CR)_4]$ paddle-wheels. Each Cu atom also coordinates to a terminal DMF molecule in the axial position. The L_{16} ligand is linked to two copper paddle-wheels via the bridging carboxylate groups in a square layered fashion. This coordination environment leaves the BINAPO sites accessible to incoming substrate molecules (Figure 2.8). The size of the pores is ~1.7 x 1.7 nm leaving adequate space for substrates to enter and diffuse through the pores.
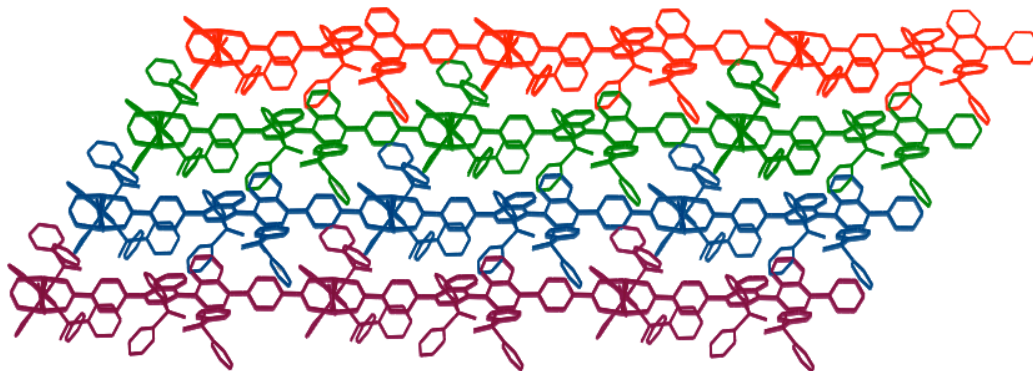
Figure 2.7 View of the layers composing the 2-D grid of **2.1**.
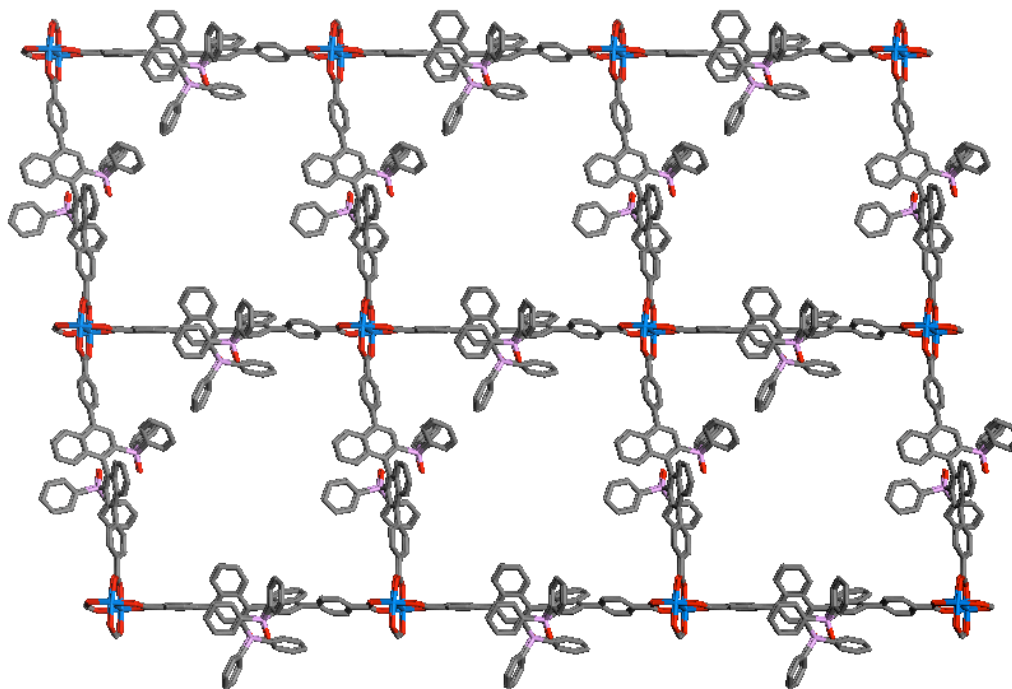
Figure 2.8 View down the *x*-axis showing the open BINAPO sites available for catalysis.

Compound **2.2** crystallizes in the orthorhombic C222$_1$ space group. The asymmetric unit consists of two ligands and two Zn^{II} centers. The 3-D structure is composed of two types of Zn coordination sites, one of which displays a Zn paddle-wheel structure that is bound to two carboxylic acids and one BINAPO site similar to that of the Cu analog (Figure 2.9). The second coordination environment consists of two carboxylic acids and two BINAPO sites (Figure 2.10a). A space filling view down the z-axis shows pores with dimensions of ~4 x 6.2 Å and 2.7 x 5.4 Å (Figure 2.10b). Because the phosphine oxide sites of the crystal are bound to Zn, the crystal will unlikely be useful for heterogeneous catalysis experiments.
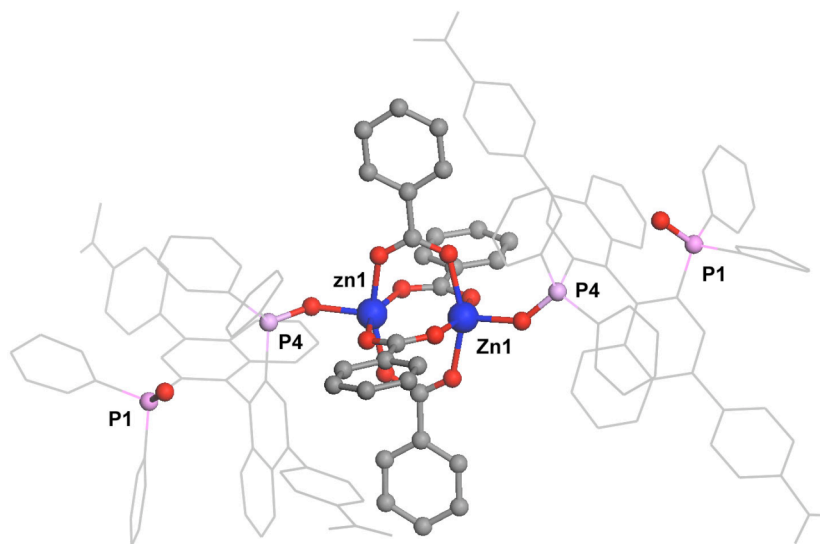
Figure 2.9 Zn paddle-wheel site where each Zn coordinates to two carboxylic acids and a single BINAPO.

a

b
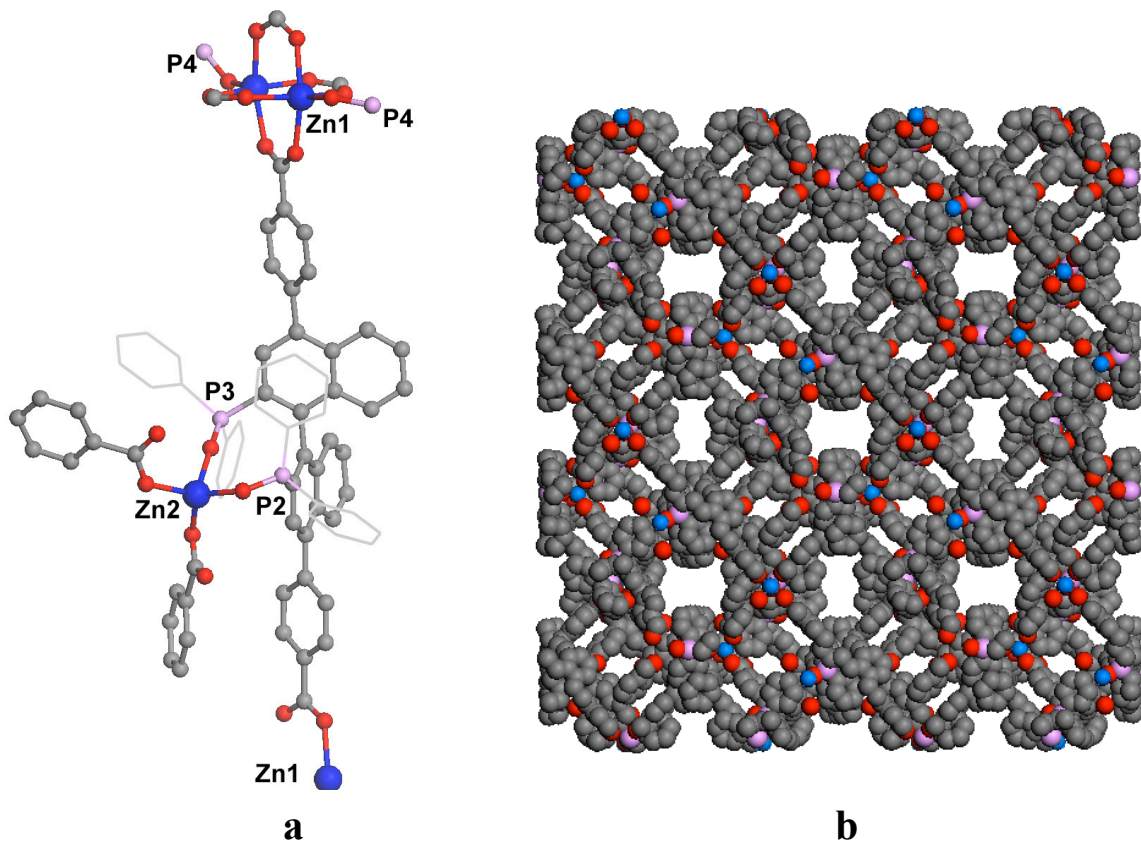
Figure 2.10 (a) The second type of Zn coordination sphere where two carboxylic acids and two BINAPOs are bound. A 3-D view along the *c*-axis; (b) Space-filling view down z-axis.

The Cd crystal **2.3** crystallizes in the monoclinic C2 space group. The asymmetric unit consists of two ligands and two Cd^{II} centers. The crystal features Cd as a six-coordinate distorted octahedral environment that forms 2-D layered network packing along the 1 0 -1 direction. The distance between the layers ranges from ~1.3 to 12.3 Å. The Cd is bound to two carboxylic acids and two BINAPO sites (Figure 2.12).
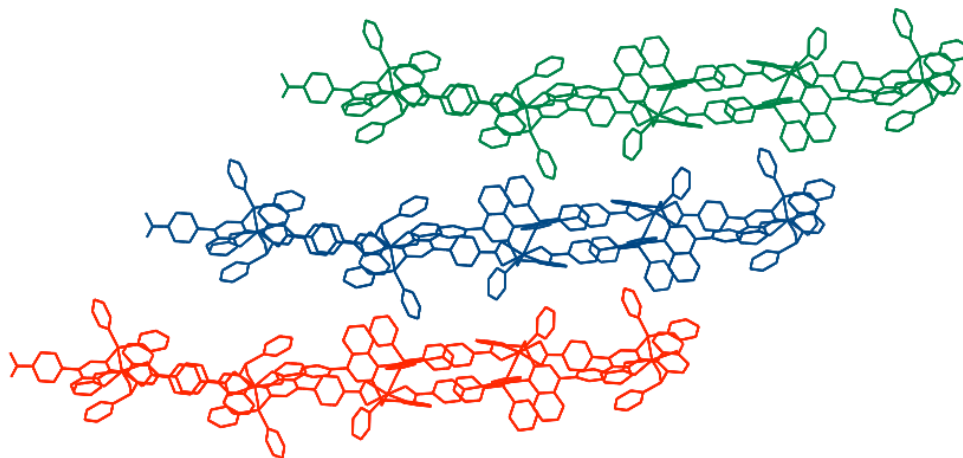
Figure 2.11 Layers of Cd crystal **2.3** packed along the 1 0 -1 direction.
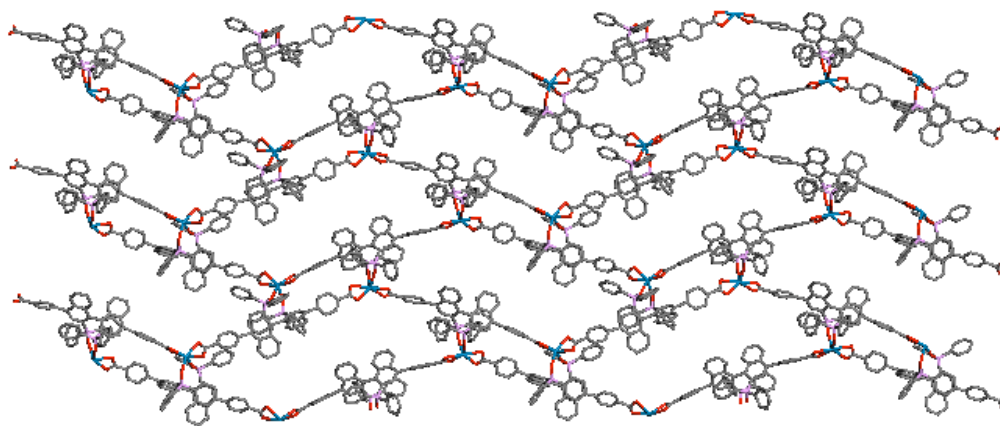
Figure 2.12 Distorted octahedral Cd coordination environment.

The Mn derivative **2.4** crystallizes in the trigonal P32 space group. The 2-D layers consist of a distorted octahedral Mn coordination environment with two carboxylic acids, two BINAPO, and one water molecule (Figure 2.13). The asymmetric unit consists of two ligands, two Mn^{II}, one DMF, and one H_2O. The layers stack along the -1 0 2 direction with an average distance of ~3.7 to 7.5 Å.
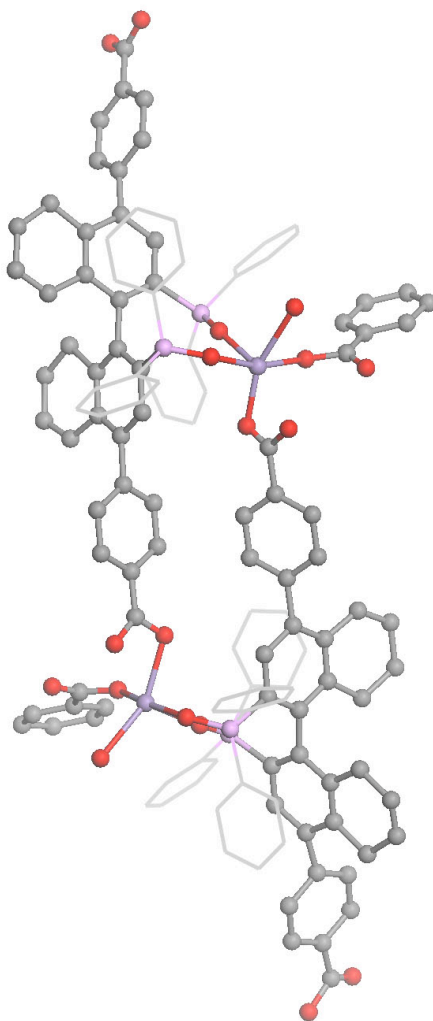
Figure 2.13 Distorted octahedral coordination environment of Mn in **2.4**.

Table 2.1 Crystal data and structure refinement for **2.1-2.4**.

Compound	**2.1**	**2.2**	**2.3**	**2.4**
Empirical formula	$C_{61}H_{45}CuNO_7P_2$	$C_{116}H_{76}O_{12}P_4Zn_2$	$C_{116}H_{77}Cd_2O_{12}P_4$	$C_{119}H_{72}Mn_2NO_{14}P_4$
Formula weight	1029.46	1916.39	2011.46	1973.54
Temperature (K)	293	293	173	293
Wavelength (Å)	0.71073	0.71073	0.71073	1.54178
Crystal system	Triclinic	Orthorhombic	Monoclinic	Trigonal
Space group	P1	$C222_1$	C2	P32
Unit cell dimensions	a = 10.3003(19)	a = 32.7288(13)	a = 33.0369(10)	a = 17.8486(4)
	b = 19.506(3)	b = 34.8494(12)	b = 16.6775(6)	b = 17.8486(4)
	c = 19.977(4)	c = 24.8904(8)	c = 31.6082(10)	c = 38.5564(11)
	α = 101.665	α = 90	α = 90	α = 90
	β = 98.514	β = 90	β = 91.781	β = 90
	γ =102.606	γ = 90	γ = 90	γ = 120
Volume ($Å^3$)	3757.8(12)	28389.5(17)	17406.8(10)	10637.4(5)
Z	2	8	4	3
Density (calcd. g/cm^3)	0.910	0.897	0.768	0.924
Absorption coeff. (mm^{-1})	0.371	0.426	0.316	2.253
F(000)	1066	7904	4100	3045
Crystal size (mm)	0.30×0.20 ×0.20	0.60×0.40×0.40	0.4×0.4×0.10	0.5×0.4×0.40
Crystal color & shape	Blue thin plate	Colorless thin plate	Colorless thin plate	Colorless thin plate
θ range data collection	1.06 – 22.00	0.85 – 24.00	1.23 – 25.00	2.86 – 50.49
Limiting indices	-10< h <10	-37< h <28	-39< h <39	-17< h <11
	-20< k <20	-38< k < 39	-19< k <19	-17< k <17
	-19< l <21	-28< l < 28	-32< l <37	-23< l <38
Reflections collected	25821	76676	64886	24818
Independent reflections	15545	20548	29372	9791
Refinement method	Full-matrix least-square on F^2			
Data/restraints/parameters	15545/521/1066	20548/377/1016	3150/242/391	9791/420/1005
Goodness-of-fit on F^2	0.817 (0.817, restrained)	0.850 (0.850, restrained)	0.813 (0.813,restrained)	1.519 (1.5, restrained)
Final R indices [I>2σ(I)][a,b]	R1 = 0.0563 wR2 = 0.1046	R1 = 0.0440 wR2 = 0.0864	R1 = 0.0593 wR2 = 0.1211	R1 = 0.1519 wR2 = 0.3489
R indices (all data)	R1 = 0.1083 wR2 = 0.1174	R1 = 0.0826 wR2 = 0.0947	R1 = 0.1274 wR2 = 0.1358	R1 = 0.1913 wR2 = 0.3719
Flack	0.040(13)	0.025(6)	0.027(18)	0.249(15)

2.2.3 Catalysis attempts using 2.1

Initial attempts towards catalysis were aimed at the *in situ* reduction of the phosphine oxide moieties within crystal **2.1**. The crystal (**2.1**) was subjected to reductive conditions using $Si(OEt)_3H$ and $Ti(^iOPr)_4$ in anhydrous toluene (Scheme 2.5). The reaction did not proceed probably due to the water contained within the framework of **2.1**. After attempts at removing excess solvent from the crystal by evacuation, the reaction again failed, presumably due to the collapse of the framework upon removal of solvate molecules, which is common for such non-robust MOFs.

$$[Cu(\textbf{L}_{16})(DMF)] \cdot 3DMF \cdot 4H_2O \xrightarrow[\text{toluene, reflux}]{\substack{\text{6 eq. } Si(OEt)_3H \\ \text{3 eq. } Ti(^iOPr)_4}}$$

2.1
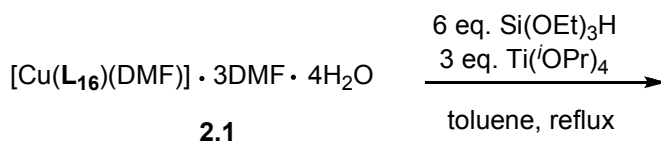
Scheme 2.5 Attempted *in situ* reduction of P=O moieties within **2.1.**

Attempts were also made towards catalysis using the BINAPO moiety within crystal **2.1**. A phosphine oxide-catalyzed allylation was attempted using a 10 mol% loading of **2.1** in the presence of allyltrichlorosilane, benzaldehyde, *N,N*- diisopropylamine, and tetrabutylammonium iodide in dicloromethane at RT (Scheme 2.6). After quenching in $NaOH_{(aq)}$ and extraction with $EA/NaHCO_3$/brine the reaction mixture was dried over $MgSO_4$. The HPLC analysis however showed no desirable products from this reaction.
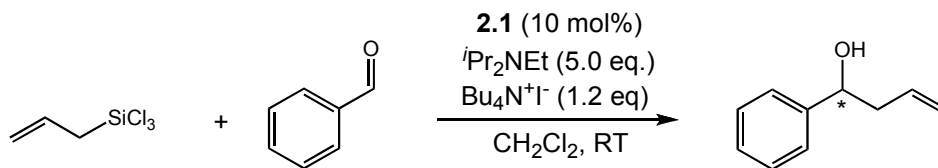
Scheme 2.6 Attempted phosphine oxide-catalyzed allylation using **2.1**.

2.3 Summary

In conclusion, a series of BINAPO based MOFs was prepared and characterized. Crystallographic studies show the formation of highly porous 2D Cu paddle-wheel structure with readily accessible catalytic phosphine oxide sites. Initial attempts at heterogeneous asymmetric catalysis using these MOFs have not yielded desirable products. More efforts are needed to either use the BINAPO sites directly for asymmetric catalysis or prepare other catalytically active species via post-synthetic modifications.

2.4 Experimental Section

2.4.1 Preparation and characterization of ligands

2.4.1.1 Synthesis of (R)-2,2'-bis(diphenylphosphoryl)-1,1'-binaphthyl

A mixture of 2,2'-bis(diphenylphosphino)-1,1'-binaphthyl (4.0 g, 6.4 mmol) in acetone (150 mL) was treated with 30% H_2O_2 (14 mL) and stirred at RT. After 1 h the mixture was in solution and let to stir at RT overnight. MnO_2 (100 mg, 1.13 mmol) was added to the solution and stirred for 10 m. The mixture was filtered and the solution was concentrated to dryness. The solid was then dissolved in CH_2Cl_2 and extracted with a saturated solution of $NaHCO_3$. The organic layer was collected and dried over $MgSO_4$ and then filtered and concentrated to dryness. Yield: (3.9 g, 95%). ^{1}H NMR ($CDCl_3$): δ 6.79 (d, 4H, (d, $^3J_{H-H}$ = 3.9 Hz, 2H), 7.22-7.44 (m, 20H), 7.66-7.71 (m, 4H), 7.79-7.85 (m, 4H). ^{31}P{^{1}H} NMR ($CDCl_3$): 28.2.

2.4.1.2 Synthesis of (R)-(4,4'-dibromo-1,1'-binaphthyl-2,2' diyl)bis(diphenylphosphine)

A solution of (R)-2,2'-bis(diphenylphosphoryl)-1,1'-binaphthyl (6.0 g, 9.16 mmol), in dichloromethane (130 mL) was degassed for 10 min. Br_2 (1.4 mL, 27.4 mmol), and pyridine

(0.75 mL, 9.16 mmol) were added to the colorless solution forming a dark brown solution. The solution was stirred at RT for 24 h. The resulting reaction mixture was extracted with sodium bisulfite, brine, and sodium bicarbonate (x 3). The resulting solution was dried over MgSO$_4$ (anhydrous) and returned to reaction flask. The above procedure was repeated twice more to obtain product mixture. The desired product (R)-(4,4'-dibromo-1,1'-binaphthyl-2,2' diyl)bis(diphenylphosphine) was obtained by Sohxlet extraction by refluxing in ethanol for 1.5 d @ 100 ºC. Yield: (2.0g, 27%). ^{1}H NMR (CDCl$_3$): δ 8.19 (d, $^3J_{H-H}$ = 8.0 Hz, 2H), 7.69 (d, $^3J_{H-H}$ = 8.0 Hz, 2H), 7.66-7.61 (m, 4H), 7.49-7.36 (m, 10H), 7.25-7.22 (m, 8H), 6.86-6.82 (m, 2H), 6.77 (d, $^3J_{H-H}$ = 8.0 Hz, 2H). ^{31}P{^{1}H} NMR (CDCl$_3$): 27.2.

2.4.1.3 Synthesis of (R)-dimethyl 4,4'-(2,2'-bis(diphenylphosphoryl)-1,1'-binaphthyl-4,4'-diyl)dibenzoate, L$_{16}$-Me$_2$

A solution of (R)-4,4'-dibromo-2,2'-bis(diphenylphosphoryl)-1,1' binaphthyl (3 g, 3.69 mmol) and 4-(methoxycarbonyl)phenylboronic acid (1.35 g, 7.5 mmol) in dimethyl ethylene glycol (100 mL) was degassed for 30 min. CsF (2.55 g, 16.7 mmol) and Pd(PPh$_3$)$_4$ (369 mg, 319 µmol) were added to the solution. The reaction vessel was sealed and the reaction mixture was stirred at 100 °C for 3 days. Upon cooling to r.t., the mixture was extracted with CH$_2$Cl$_2$/H$_2$O. The yellow solution was dried over MgSO$_4$ and the solvent removed under reduced pressure. The yellow solid was purified by silica gel column chromatography with CH$_2$Cl$_2$ /ethyl acetate (1:1 v/v) as the eluent to afford (R)-dimethyl 4,4'-(2,2'-bis(diphenylphosphoryl)-1,1'-binaphthyl-4,4'-diyl)dibenzoate Yield: (2.3g, 66%). ^{1}H NMR (CDCl$_3$): δ 8.13 (d, $^3J_{H-H}$ = 8.0 Hz, 4H), 7.84 (d, $^3J_{H-H}$ = 8.4 Hz, 2H), 7.66 (m, 6H), 7.57 (d, $^3J_{H-H}$ = 8.0 Hz, 4H), 7.42 (m, 6H), 7.26-7.41 (m, 10H), 7.18-7.24 (m, 10H), 7.03 (d, $^3J_{H-H}$ = 8.4 Hz, 2H), 6.90 (m, 2H), 3.92 (s, 6H), 3.91 (s, 12H). ^{31}P{^{1}H} NMR (CDCl$_3$): 28.59.

2.4.1.4   Synthesis   of   (*R*)-4,4'-(2,2'-bis(diphenylphosphoryl)-1,1'-binaphthyl-4,4'-diyl)dibenzoic acid, L$_{16}$-H$_2$

A solution of (*R*)-dimethyl 4,4'-(2,2'-bis(diphenylphosphoryl)-1,1'-binaphthyl-4,4'-diyl)dibenzoate (1 g, 1.08 mmol) in THF (125 mL), MeOH (50 mL), and 2M aqueous NaOH (50 mL) was heated at 70 °C for 18 h. The solution was cooled to r.t. and acidified to a pH of ~1 and extracted with ethyl acetate/H$_2$O. The organic layer was dried over MgSO$_4$ and the solvent was evaporated under reduced pressure to give a white solid of **L$_1$-H$_2$**. Yield: (940 mg, 97%). ^{1}H NMR (DMSO-d$_6$): δ 13.07 (bs, 2H), 8.62 (d, $^3J_{\text{H-H}}$ = 8.8 Hz, 4H), 7.85 (d, $^3J_{\text{H-H}}$ = 8.4 Hz, 2H), 7.59 (d, $^3J_{\text{H-H}}$ = 8.4 Hz, 4H), 7.44 (m, 4H), 7.24 (m, 16H), 7.05 (m, 12H), 6.89 (d, $^3J_{\text{H-H}}$ = 8.8 Hz, 2H). ^{31}P{^{1}H} NMR (DMSO): 26.82.

2.4.1.5 Synthesis of (*R*)- dimethyl 4,4'-(2,2'-bis(diphenylphosphino)-1,1'-binaphthyl-4,4'-diyl)dibenzoate, L$_{17}$-Me$_2$

A solution of (*R*)-dimethyl 4,4'-(2,2'-bis(diphenylphosphoryl)-1,1'-binaphthyl-4,4'-diyl)dibenzoate (0.1 g, 108 µmol) in anhydrous toluene (3 mL) was stirred at RT. Si(OEt)$_3$H (122 µL, 648 µmol) and Ti(O^{i}Pr)$_4$ (32 µL, 324 µmol) were added to the pale yellow solution quickly turning it grey and then black. The mixture was stirred at 100 °C for 1 h. The solution was cooled to r.t. and excess solvent was removed under reduced pressure. The product was obtained by silica gel chromatography using CH$_2$Cl$_2$ as the eluent to give a white solid of **L$_2$-Me$_2$**. Yield: (32 mg, 33%). ^{1}H NMR (DMSO-d$_6$): δ 13.07 (bs, 2H), 8.62 (d, $^3J_{\text{H-H}}$ = 8.8 Hz, 4H), 7.85 (d, $^3J_{\text{H-H}}$ = 8.4 Hz, 2H), 7.59 (d, $^3J_{\text{H-H}}$ = 8.4 Hz, 4H), 7.44 (m, 4H), 7.24 (m, 16H), 7.05 (m, 12H), 6.89 (d, $^3J_{\text{H-H}}$ = 8.8 Hz, 2H). ^{31}P{^{1}H} NMR (DMSO): 26.82.

2.4.2 Preparation and characterization of crystals

2.4.2.1 [Cu(L$_{16}$)(DMF)]·3DMF·4H$_2$O, 2.1

A mixture of **L$_{16}$**-H$_2$ (1.0 mg, 1.11 μmol) and Cu(ClO$_4$)$_2$·6H$_2$O (0.83 mg, 2.23 μmol) was dissolved in a solvent mixture of MeOH/DMF/H$_2$O (0.1 mL / 0.4 mL / 0.1 mL) with 1 M HCl (10μL) in a screw-capped vial. The resulting solution was placed in an oven at 80 $^{\circ}$C for 4 days. Small, clustered blue crystals (0.91 mg, 62%) were obtained after filtration. Solvent content calc. from the proposed formula: DMF, 22.1%; H$_2$O, 5.5%; determined by ^{1}HNMR/TGA: DEF, 22.2%; H$_2$O, 5.5%.

2.4.2.2 [Zn(L$_{16}$)]·8DMF·6H$_2$O, 2.2

A mixture of **L$_{16}$**-H$_2$ (1.0 mg, 1.11 μmol) and Zn(ClO$_4$)$_2$·6H$_2$O (0.83 mg, 2.22 μmol) was dissolved in a solvent mixture of MeOH/DMF/H$_2$O (0.05 mL / 0.4 mL / 0.05 mL) with 2,6-lutidine (2μL) in a screw-capped vial. The resulting solution was placed in an oven at 80 $^{\circ}$C for 2 days. Colorless crystals (1.2 mg, 65%) with very small, thin plate-shape were obtained after filtration. Solvent content calc. from the proposed formula: DMF, 35.4%; H$_2$O, 6.5%; determined by ^{1}HNMR/TGA: DEF, 35.8%; H$_2$O, 6.5%.

2.4.2.3 [Cd(L$_{16}$)]·9DMF·H$_2$O, 2.3

A mixture of **L$_{16}$**-H$_2$ (1.0 mg, 1.11 μmol) and Cd(ClO$_4$)$_2$·6H$_2$O (0.69 mg, 2.22 μmol) was dissolved in a solvent mixture of DMF/H$_2$O (0.4 mL / 0.05 mL) with 2,6-lutidine (2μL) in a screw-capped vial. The resulting solution was placed in an oven at 80 $^{\circ}$C for 1 day. Colorless crystals (1.3 mg, 72%) with relatively large, thin plate-shape, were obtained after filtration. Solvent content calc. from the proposed formula: DMF, 39.1%; H$_2$O, 1.1%; determined by ^{1}HNMR/TGA: DEF, 38.9%; H$_2$O, 1.1%.

2.4.2.4 [Mn(L$_{16}$)(H$_2$O)]·5DMF·5H$_2$O, 2.4

A mixture of **L$_{16}$**-H$_2$ (1.0 mg, 1.11 µmol) and Mn(ClO$_4$)$_2$·6H$_2$O (0.81 mg, 2.22 µmol) was dissolved in a solvent mixture of DMF/H$_2$O (0.4 mL / 0.05 mLin a screw-capped vial. The resulting solution was placed in an oven at 80 $^{\circ}$C for 2 weeks. Colorless crystals (0.82 mg, 52%) with clustered, thin plate-shape, were obtained after filtration. Solvent content calc. from the proposed formula: DMF, 25.6%; H$_2$O, 7.6%; determined by ^{1}HNMR/TGA: DEF, 27.3%; H$_2$O, 7.6%.

2.5 References

[1] (a) Knowles, W. S. Asymmetric hydrogenations. *Adv. Synth. Catal.* **2003**, *345* (1-2), 3-13; (b) Noyori, R. Asymmetric catalysis: science and opportunities. *Angew Chem. Int. Ed.* **2002**, *41* (12), 2008-2022.; (c) Zhou, Y. G.; Tang, W.; Wang, W. B.; Li, W.; Zhang, X. Highly effective chiral ortho-substituted BINAPO ligands (*o*-BINAPO): applications in Ru-catalyzed asymmetric hydrogenations of ß-aryl keto esters. J. *Am. Chem. Soc.* **2002**, *124* (18), 4952-4953; (d) Ireland, T.; Tappe, K.; Grossheimann, G.; Knochel, P. Synthesis of a new class of chiral 1,5-diphosphanylferrocene ligands and their use in enantioslective hydrogenation. *Chem. Eur. J.* **2002**, *8* (4), 843-852.

[2] Matsumoto, T.; Murayama, T.; Mitsuhashi, S.; Miura, T. Diastereoselective synthesis of a key intermediate for the preparation of tricyclic ß-lactam antibiotics. *Tetrahedron Lett.* **1999**, *40* (19), 5043-5046.

[3] (a) Dalko, P. I.; Moisan, L. Enantioselective organocatalysis. *Angew. Chem. Int. Ed.* **2001**, *40* (20), 3726-3748; (b) Benaglia, M.; Puglisi, A.; Cozzi, F. Polymer-supported organic catalysts. *Chem. Rev.* **2003**, *103* (9), 3401-3430; (c) Special issue on asymmetric organocatalysis: *Acc. Chem. Res.* **2004**, *37*, 487.

[4] (a) Denmark, S. E.; Coe, D. M.; Pratt, N. E.; Griedel, B. D. Asymmetric allylation of aldehydes with chiral lewis bases. *J. Org. Chem.* **1994**, *59* (21), 6161-6163; (b) Denmark, S. E.; Barsanti, P. A.; Wong, K.-T.; Stavenger, R. A. Enantioselective ring opening of epoxides with silicon tetrachloride in the presence of a chiral lewis base. *J. Org. Chem.* **1998**, *63*, 2428; (c) Denmark, S. E.; Winter, S. B. D.; Su, X.; Wong, K.-T. Chemistry of trichlorosilyl enolates.1. New reagents for catalytic, asymmetric aldol additions. *J. Am. Chem. Soc.* **1996**, *118* (31), 7404-7405; (d) Denmark, S. E.; Stavenger, R. A.; Su, X.; Wong, K.-T.; Nishigaichi, Y. Asymmetric catalysis with chiral Lewis bases. *Pure. Appl. Chem.* **1998**, *70*, 1469-1476; (e) Denmark, S. E.; Stavenger, R. A.; Wong, K.-T. Asymmetric aldol additions catalyzed by chiral phosphoramidites: Electronic effects of the aldehyde component. *Tetrahedron* **1998**, *54* (35), 10389-10402; (f) Denmark, S. E.; Stavenger, R. A.; Su, X.; Nishigaichi, Y. The chemistry of trichlorosilyl enolates. 6. Mechanistic duality in the lewis base-catalyzed aldol addition reaction. *J. Am. Chem. Soc.* **1998**, *120* (49), 1299012991; (g) Denmark, S. E.; Stavenger, R. A.; Wong, K.-T.; Su, X. Chiral phosphoramide-catalyed aldol additions of ketone enolates. Preparative aspects. *J. Am. Chem. Soc.* **1999**, *121* (21), 4982-4991; (h) Denmark, S. E.; Stavenger, R. A. The chemistry of trichlorosilyl enolates. Aldol reactions of methyl ketones. *J. Am. Chem. Soc.* **2000**, *122* (37), 8837-8847; (i) Denmark, S. E.; Stavenger, R. A. *Acc. Chem. Res.* **2000**, *33*, 432; (j) Denmark, S. E.; Ghosh, S. K. *Angew. Chem. Int. Ed.* **2001**, *40*, 4759; (k) Denmark, S. E.; Pham, S. M. Stereoselective aldol additions of achiral ethyl ketone-derived trichlorosilyl enolates. *J. Org Chem.* **2003**, *68* (13), 5045-5055.

[5] (a) Liu, B.; Feng, X.; Chem, F.; Zhang, G.; Cui, X.; Jiang, Y. Enantioselective Strecker reaction promoted by chiral N-oxides. *Synlett* **2001**, 1551-1554; (b) Denmark, S. E.; Fan, Y. Catalytic, enantioselective aldol additions to ketones. *J. Am. Chem. Soc.* **2002**, *124* (16), 4233-4235; (c) Malkov, A. V.; Orsini, M.; Pernazza, D.; Muir, K. W.; Langer, V.; Maghani,

P.; Kocovsky, P. Chiral 2,2'-bipyridine-type *N*-monoxides aas organocatalysts in the enantioselective allylation of aldehydes with allytrichlorosilane. *Org. Lett.* **2002**, *4* (6), 1047-1049; (d) Shimada, T.; Kina, A.; Ikeda, S.; Hayashi, T. A novel axially chiral 2,2'-bipyridine *N,N*-dioxide. Its preparation and use for asymmetric allylation of aldehydes with allyl(trichloro)silane as a highly efficient catalyst. *Org. Lett.* **2002**, *4* (16), 2799-2801; (e) Malkov, A. V.; Dufkova, L.; Farrugia, L.; Kocovsky, P. Quinox, a quinoline-type N-oxide, as organocatalyst in the asymmetric allylation of aromatic aldehydes with allyltrichlorosilanes: The role of arene-arene interactions. *Angew. Chem. Int. Ed.* **2003**, *42* (31), 3674-3677; (f) Traverse, J. F.; Zhao, Y.; Hoveyda, A. H.; Snapper, M. L. Proline-based *N*-oxides as radily available and modular chiral catalysts. Enantioselective reactions of allyltrichlorosilane with aldehydes. *Org. Lett.* **2005**, *7* (15), 3151-3154; (g) Nakajima, M.; Saito, M.; Shiro, M.; Hashimoto, S. (*S*)- 3,3'-dimethyl-2,2'-biquinoline *N,*N-dioxide as an efficient catalyst for enantioselective addition of allyltrichlorosilanes to aldehydes. *J. Am. Chem. Soc.* **1998**, *120* (25), 6419-6420; (h) Nakajima,; Saito, M.; Hashimoto, S. Selective synthesis of optically active allenic and homopropargylic alcohols from propargyl chloride. *Tetrahedron: Asymmetry* **2002**, *13* (22), 2449-2452; (i) Nakijima, M.; Yokota, T.; Saito, M.; Hashimoto, S. Enantioselective aldol reactions of trichlorosilyl enol ethers catalyzed by chiral *N,*N'-dioxides and monodentate *N*-oxides. *Tetrahedron Lett.* **2004**, *45* (1), 61-64.

[6] Massa, A.; Malkov, A. V.; Kocovsky, P.; Scettri, A. Asymmetric allylation of aldehydes with allyltrichlorosilane promoted by chiral sulfoxides. *Tetrahedron Lett.* **2003**, *44* (38), 7179-7181; (b) Kobayashi, S.; Ogawa, C.; Konishi, H.; Sugiura, M. Chiral sulfoxides as neutral coordinate-organocatalysts in asymmetric allylation of *N*-acylhydrazones using allyltrichlorosilanes. *J. Am. Chem. Soc.* **2003**, *125* (22), 6610-6611.

[7] (a) Smyth, C. P. The polarities of covalent bonds. *J. Am Chem. Soc.* **1938**, *60* (1), 183-189; (b) Hadzi, D.; Klofutar, C.; Oblak, S. *J. Chem. Soc. A* **1968**, 905.

[8] Ogawa, C.; Sugiura, M.; Kobayashi, S. Stereospecific, enantioselective allylation of a-hydrazono esters by using allyltrichlorosilanes with BINAP oxides as neutral-coordinate organocatalysts. *Angew. Chem. Int. Ed.* **2004**, *43*, 6491-6493.

[9] (a) Nakajima, M.; Kotani, S.; Ishizuka, T.; Hashimoto, S. Chiral phosphine oxide BINAPO as a catalyst for enantioselective allylation of aldehydes with allyltrichlorosilanes. *Tetrahedron Lett.* **2005**, *46* (1), 157-159; (b) Tokuoka, E.; Kotani, S.; Matsunaga, H.; Ishizuka, T.; Hashimoto, S.; Nakakima, M. Asymmetric ring opening of *meso*-epoxides catalyzed by the chiral phosphine oxide BINAPO. *Tetrahedron: Asymmetry* **2005**, *16* (14), 2391-2392; (c) Shunsuke, K.; Hashimoto, S.; Nakajima, M. Enantioselective aldol reactions of trichlorosilyl enol ethers catalyzed by the chiral phosphine oxide BINAPO. *Synlett* **2006**, *7*, 1116-1118.

[10] (a) Song, C. E.; Lee, S. G. Supported chiral catalysts on inorganic materials. *Chem. Rev.* **2002**, *102* (10), 3495-3524; (b) Fan, Q. H.; Li, Y. M.; Chan, A. S. C. *Chem. Rev.* **2002**, *344*, 221; (c) Sinou, D. Asymmetric organometallic-catalyzed reactions in aqueous media. *Adv. Synth. Catal.* **2002**, *344*, 221-237; (d) Saluzzo, C; Lemaire, M. Homogeneous-supported

catalysts for enantioselective hydrogenation and hydrogen transfer reduction. *Adv.. Synth. Catal.* **2002**, *344* (9), 915-928; (e) Pu, L. 1,1'-Binaphthyl dimers, oligomers, and polymers: Molecular recognition, asymmetric catalysis, and new materials *Chem. Rev.* **1998**, *98*, 2405-2494.

[11] Guan, X.-Y.; Jiang, Y.-C.; Shi, M. Chiral sterically congested phosphane-amide bifunctional organocatalysts in asymmetric aza-Morita-Baylis-Hillman reactions of N-sulfonated imines with methyland ethyl vinyl ketones. *Eur. J. Org. Chem.* **2008**, *12*, 2150-2155.

[12] Cai, D.; Payack, J. F.; Bender, D. R.; Hughes, D. L.; Verhoeven, T. R.; Reider, P. J. (*R*)-(+) and (*S*)-(-)-2,2'-bis(diphenylphosphino)-1,1'-binaphthyl (BINAP). *Org. Syn.* **1999**, *76*, 65.

CHAPTER 3

MESOPOROUS SILICA NANOSPHERE-SUPPORTED RUTHENIUM CATALYSTS FOR ASYMMETRIC HYDROGENATION

3.1 Introduction

Recent studies have shown that mesoporous silica materials could be obtained as uniform nanospheres under appropriate synthetic conditions.[1] Mesoporous silica nanospheres (MSNs) were further shown to be excellent supports for bifunctional catalysts that exhibit interesting cooperative catalytic activities.[2] An increase in enantioselectivity has been observed when the supported catalyst is located within the pore of the mesoporous silica. This enhancement is due to the substrate's interaction with both the pore wall and the chiral directing group. The confinement of the substrate within the mesoporous channel can lead to a larger influence of the chiral directing group on the orientation of the substrate relative to the reactive catalytic center when compared to the situation in solution.[3]

Several types of mesoporous silica have been used for immobilization. Mesoporous silicas are characterized as having very high surface areas (> 1000 m^2/g), an ordered pore structure with a narrow pore size distribution. Pore sizes tend to be in the 2-15 nm range and have pore volumes of about 1 mL/g. As shown in Figure 3.1, the mesoporous silicas may be characterized by their pore structure. MCM-48 is characterized as having a three-dimensional interconnected cubic pore system. MCM-41 has a two-dimensional hexagonal array of unidirectional pores.
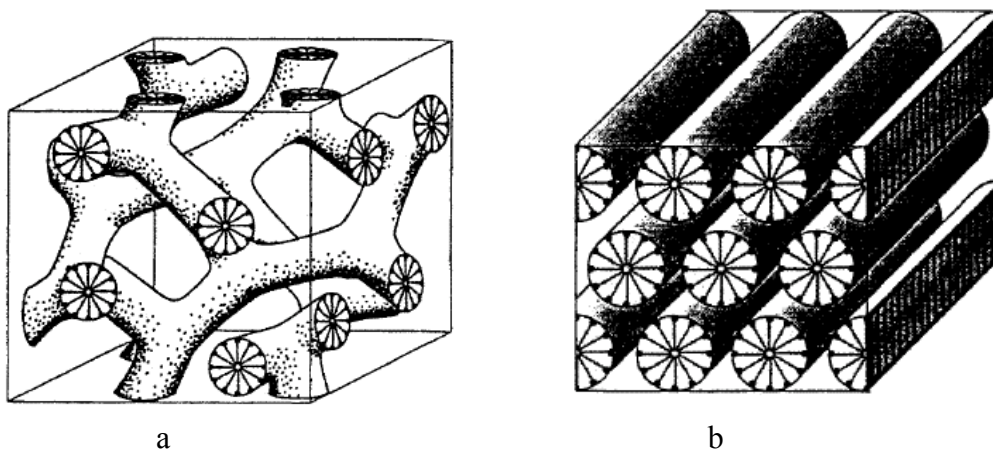
Figure 3.1 (a) MCM-48 interconnected cubic pore structure; (b) MCM-41 two-dimensional pore structure.

In this work, we have demonstrated the utility of MSNs as supports for Ru catalysts for asymmetric hydrogenation of aromatic ketones to afford chiral secondary alcohols and racemic arylaldehydes to give chiral primary alcohols. We envisage the generation of highly active heterogeneous catalysts by taking advantage of both the large channel diameters (>2 nm) of MSNs and short diffusion lengths for the organic substrates as a result of small nanoparticle sizes of <1 mm. The short diffusion length is of practical importance owing to the typically large size (and hence hindered diffusion rate) of organic substrates used in asymmetric catalytic processes.

These chiral Ru(diphosphine)(diamine)Cl$_2$ complexes were chosen to be supported on the MSNs due to their robust nature and the ability to purify the complexes by silica-gel chromatography.[4] Noyori and others have demonstrated that upon activation the Ru(diphosphine)(diamine)Cl$_2$ complexes gave highly active and enantioselective catalysts for asymmetric hydrogenation of prochiral ketones.[5] In addition, the

Ru(diphosphine)(diamine)Cl$_2$ complexes have been shown to be useful for the asymmetric hydrogenation of racemic arylaldehydes for the synthesis of chiral primary alcohols via a dynamic kinetic resolution process.

3.2 Results and discussion

3.2.1 Synthesis and characterization of Ru(diphosphine)(diamine)Cl$_2$ Complexes

As shown in Scheme 3.1, chiral Ru(diphosphine)(diamine)Cl$_2$ with pendant siloxy groups **3.1-3.10** were prepared by heating a mixture of [RuCl$_2$(*p*-cymene)]$_2$ and chiral diphosphine in 1,2-dicloroethane/DMF at 80°C followed by treatment with siloxy-derived ethylenediamine (siloxy-ED) or 1,2-cyclohexanediamine (siloxy-DACH). In all, five chiral diphosphines were used: 2,2'-bis(diphenylphosphino)-1,1'-binaphthyl (BINAP), 2,2'-bis(diphenylphosphino)-4,4'-bis(trimethylsilyl)-1,1'binaphthyl (TMS-BINAP), 2,2'-bis(di-3,5-xylylphosphino)-1,1'-binaphthyl (Xyl-BINAP), (4,4'-bi-1,3-benzodioxole)-5,5'-diyl-bis(diarylphosphine) (SEGPHOS), and (7,7'-tert-butyl-4,4'-bi-1,3-benzodioxole)-5,5'-diyl-bis(diarylphosphine) (^{t}Bu-SEGPHOS). Complexes **3.1-3.10** are air- and moisture-stable and were purified by silica gel chromotagraphy and characterized by ^{1}H and ^{31}P{^{1}H} NMR (Figure 3.2) spectroscopy as well as ESI-MS.

The Ru(II) pre-catalysts **3.1-3.10** are readily characterized by ^{1}H and ^{31}P{^{1}H} NMR spectroscopy due their diamagnetic nature. The complexes display a characteristic pair of doublets in the 37-49 ppm range in the ^{31}P{^{1}H} NMR spectra due to the unsymmetrical nature of the monosubstituted diamine. ESI-MS spectra show the presence of peaks corresponding to the loss of a chloride ligand from the molecular ion, thus confirming the synthesis of Ru(II) pre-catalysts **3.1-3.10**.
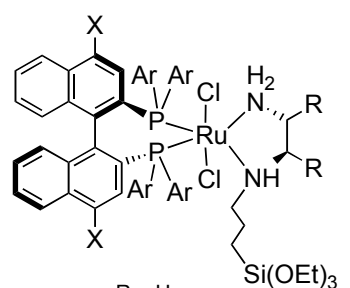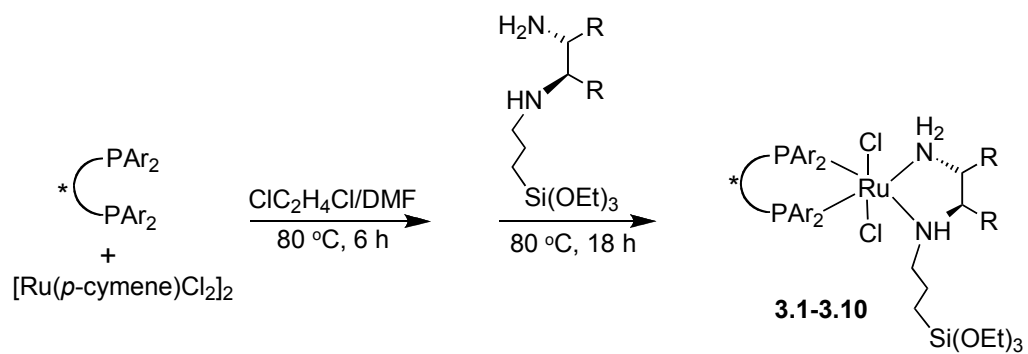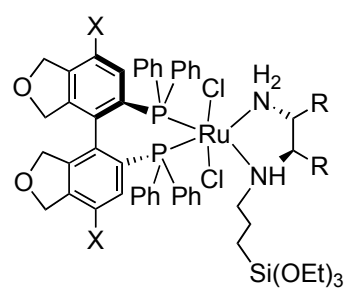
Scheme 3.1 Synthesis of Ru complexes **3**.**1-3.10**.
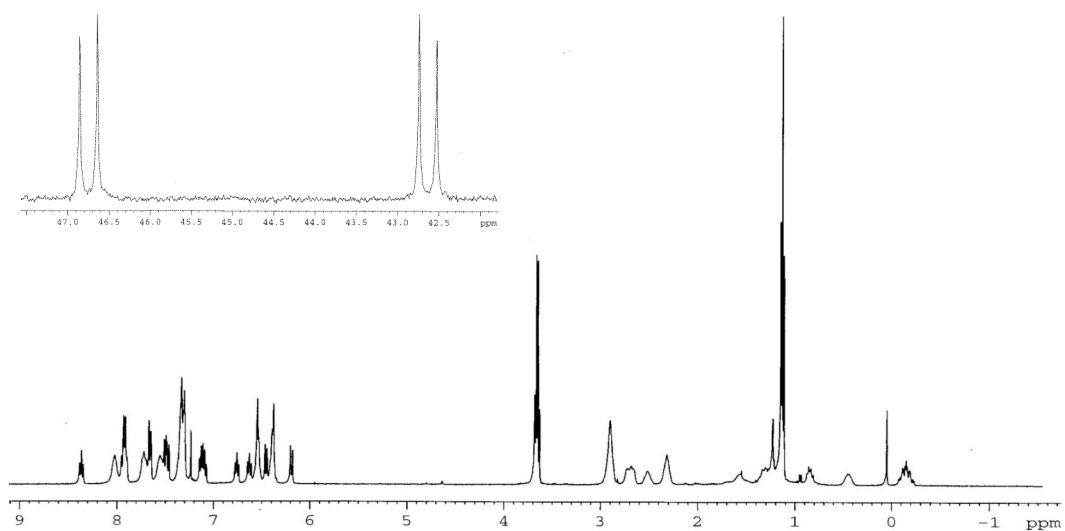
Figure 3.2 ^{1}H and ^{31}P{^{1}H} (inset) NMR spectra of **3.1**.

3.2.2 Synthesis and characterization of mesoporous silica nanospheres (MSNs)

Mesoporous silica nanospheres with both cubic three-dimensional channels MSN-48 (**a**) and hexagonal two-dimensional channels MSN-41 (**b**) were prepared according to literature procedures (Scheme 3.2).[6] **a** was prepared by hydrolysis and condensation of tetraethoxysilane (TEOS) in a water/ethanol solution of cetyltrimethylammonium bromide (CTAB) and ammonia. **b** was prepared by hydrolysis and condensation of TEOS in a basic aqueous solution of CTAB. Large pore MSN-41 (**c**) was prepared according to literature procedure which incorporates mesitylene into the solvent system to produce pore sizes >4 nm.[7] The particles were isolated by centrifugation, washed, and then calcined at 600 °C to remove the surfactant template. Spherical morphology of **a** is clearly visible in the SEM image (Figure 3.3a). The diameters of **a** particles are tunable from 75 nm to 1 μm, depending on the reagent concentrations used. TEM image of **c** shows the hexagonal array of the large and ordered unidirectional pores (Figure 3.3b).
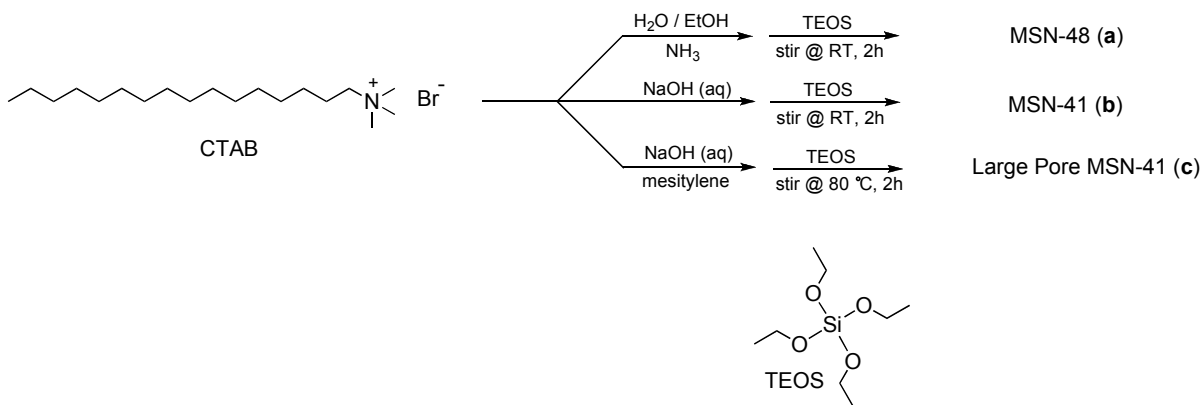
Scheme 3.2 Preparation of mesoporous nanospheres (MSNs) **a-c**.
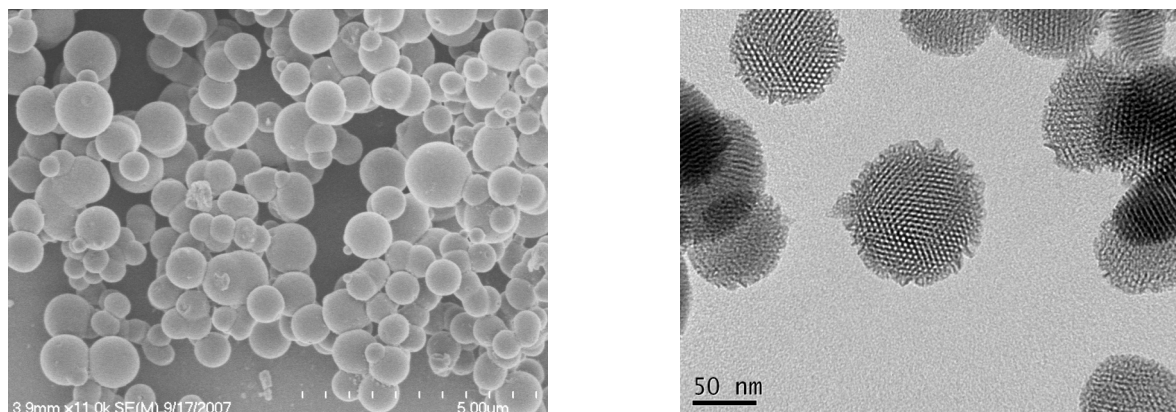
Figure 3.3 (a) Representative SEM image of **a** showing the particles range from 300 μm to 1 μm in diameter in this batch; (b) TEM image of **c** showing the unidirectional array of two-dimensional channels.

Ru(diphosphine)(siloxy-diamine)Cl$_2$ complexes **3.1-3.3** and **3.6-3.10** were grafted onto **a**, **b**, and **c** by refluxing their mixtures in toluene for 24 hours (Scheme 3.3). The morphology of the MSNs remains unchanged upon immoblization of catalysts onto the surface (Figure 3.4). BET nitrogen adsorption isotherms of bare **a** and **3.6** on **a**, or **3.6-a**, show distinct differences in surface area, pore volume, and pore diameter (Table 3.1). The calcined MSN-48 has a BJH surface area of 1737 m^2/g while upon grafting **3.6** to **a**, the surface area of **3.6-a** was reduced to 1131 m^2/g (Figure 3.5). The prepared MSN-48 has a pore diameter of 2.2 nm and the pores of **3.6-a** were reduced to 1.7 nm. The reduced surface area and pore diameter of **3.6-a** suggest the attachment of the Ru complex **3.6** via the siloxy linkage to the surface of MSN-48. Consistent with this, the pore volume decreases from 1.07 cm^3/g for **a** to 0.61 cm^3/g for **3.6-a** (Figure 3.6).
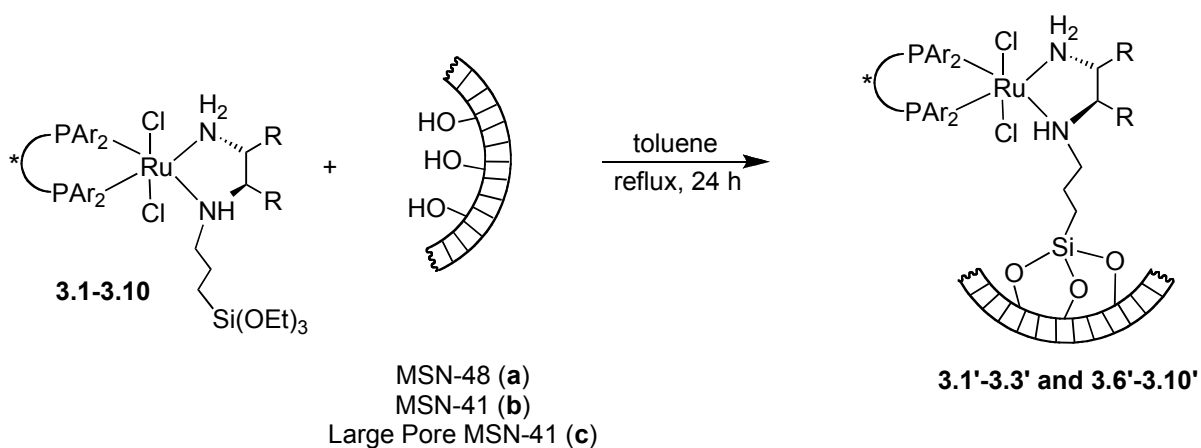
Scheme 3.3 Immobilization of **3.1-3.10** onto various mesoporous silicas.

a   b
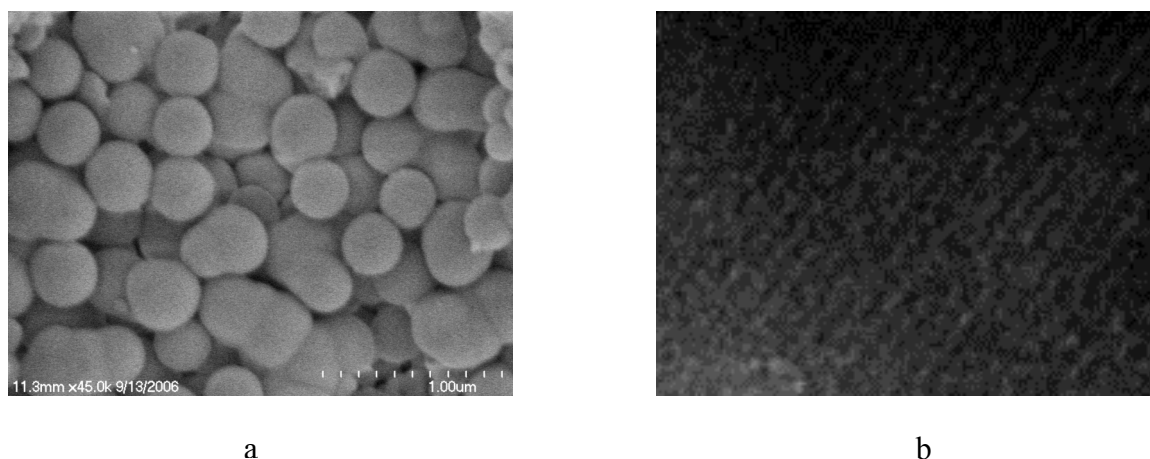
Figure 3.4 (a) SEM image of **3.6-a**, where morphology remains unchanged post-modification; (b) TEM image of a magnified view of **3.6-a**.

Table 3.1 BET data comparison for mesoporous silica nanosphere before and after loading of catalyst.

	MSN-48 (**a**)	**3.6-a**
Surface area (m^2/g)	1737	1131
Pore volume (cm^3/g)	1.1	0.61
Pore diameter (nm)	2.2	1.7
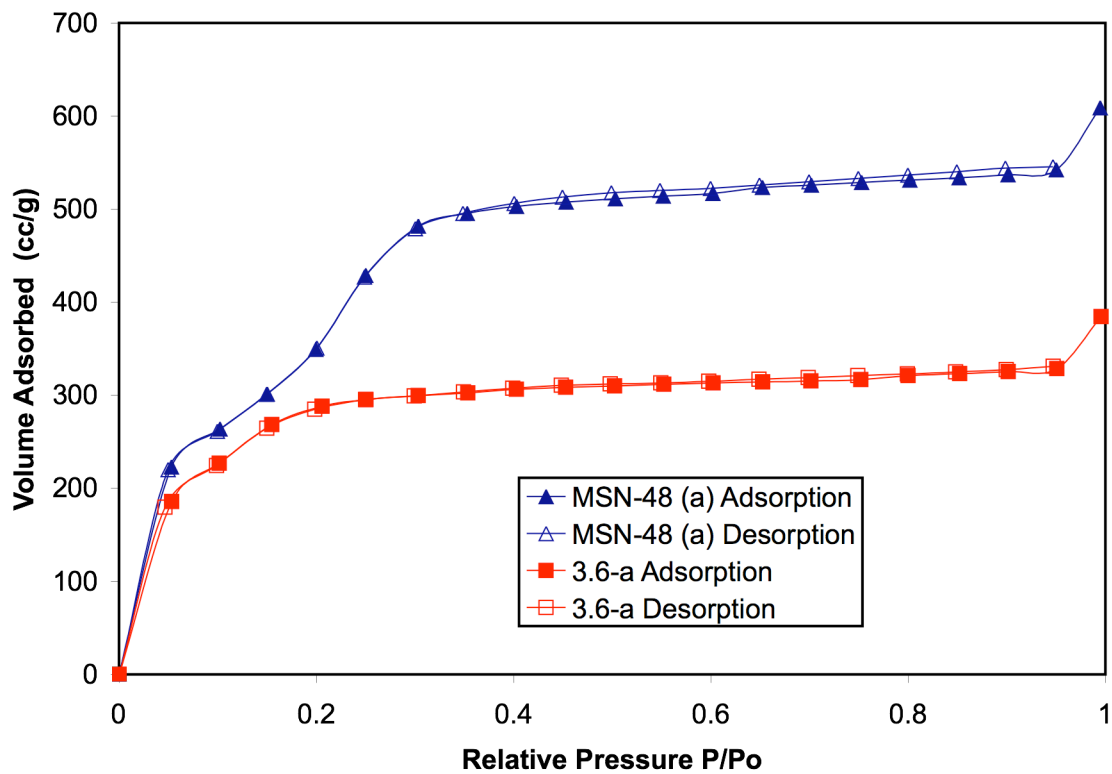
Figure 3.5 Nitrogen adsorption/desorption isotherms of bare MSN-48 (**a**) and **3.6-a**.
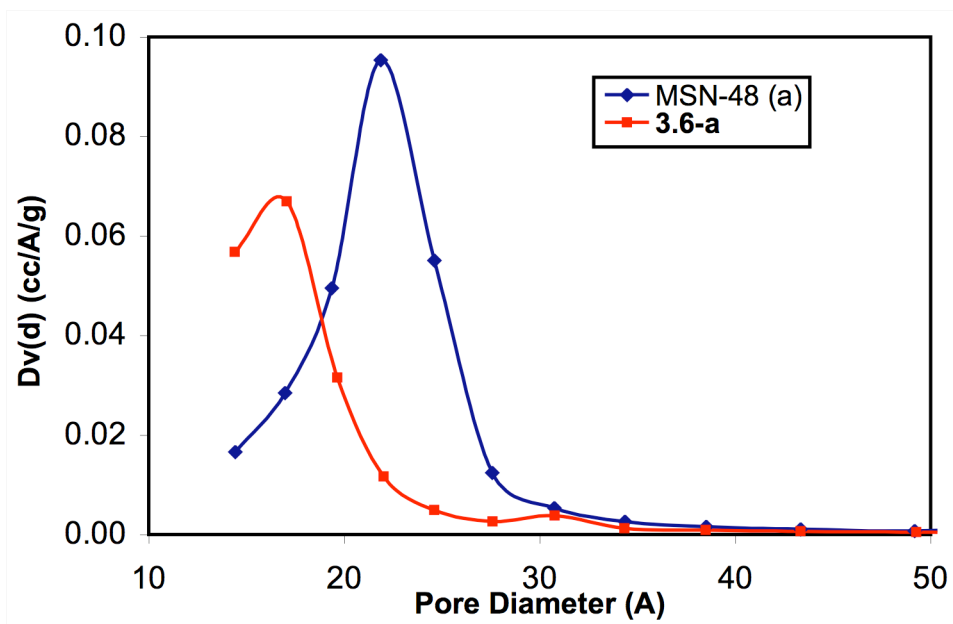
Figure 3.6 Pore size distribution of bare MSN-48 (**a**) and **3.6-a**.

Powder X-ray diffraction patterns were obtained for **a** and **3.6-a** (Figure 3.7). The 2θ values are 2.91° for **a** and 2.99° for **3.6-a**. The peaks correspond to the (211) reflection of the *Ia3d* space group. The PXRD patterns suggest both **a** and the MSN-48 solid catalysts have ordered pore structures, indicating no loss of the structural integrity upon immobilization of the catalyst.
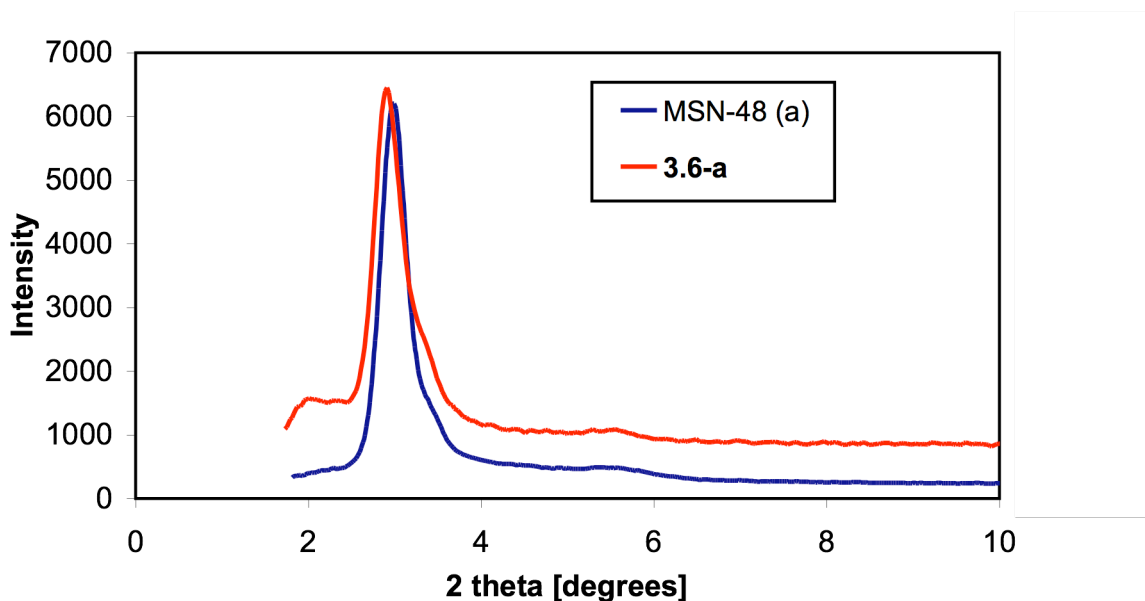
Figure 3.7 PXRD patterns of MSN-48 (**a**) and **3.6-a**.

The Ru precatalyst loadings on the mesoporous silicas were estimated by thermogravimetric analysis (TGA) which gives percent weight loss due to the organic moieties and the Ru content determined by direct current plasma (DCP) spectroscopy. The MSN-supported materials **a** and **b** of **3.6'-3.10'** prepared in this fashion have a consistent Ru(II) pre-catalyst loading of 5-7 wt% as determined by TGA and DCP (Figure 3.8).
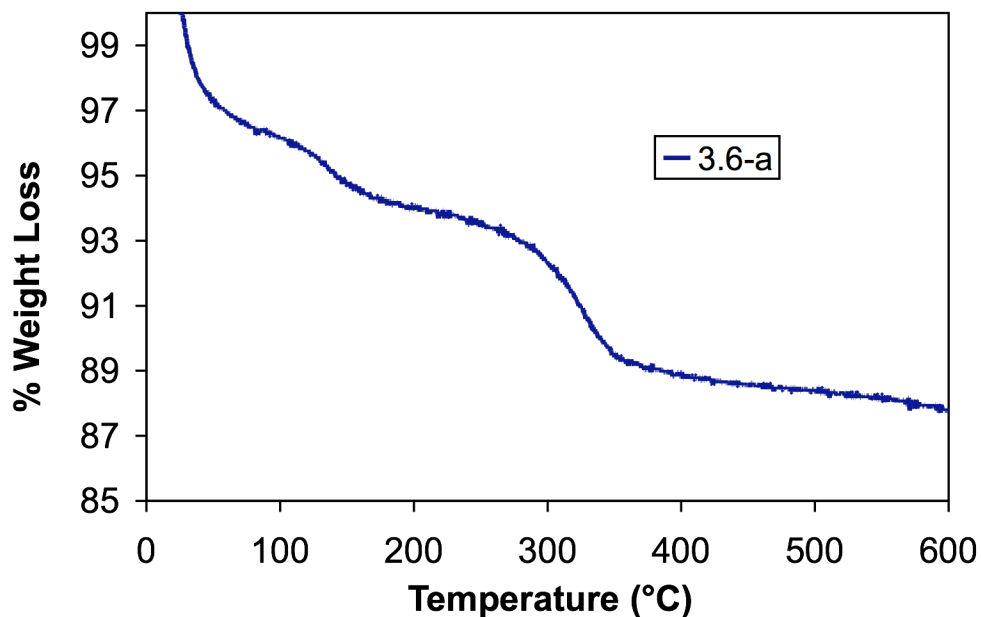
Figure 3.8 TGA curve of MSN-48 particles loading with Ru precatalyst **3.6**. The weight loss in the 200 – 400 °C range is due to the organic moieties of **3.6**, from which the Ru precatalyst loading can be estimated.

The comparison of BET data for MSN-48 (**a**), MSN-41 (**b**), and large pore MSN-41 (**c**) are shown in Table 3.2. The BET isotherms indicate that the large pore silica (**c**) has roughly one-half the surface area of **a** and **b** but has a pore size that is doubled (Table 3.2). The MSN-41 (**b**) nanoparticles have a surface area of 1548 m^2/g which is slightly lower than that of **a** and a pore diameter of 1.9 nm. The large pore MSN-41 particles have a surface area of 928 m^2/g and an average pore diameter of 4.3 nm.

Table 3.2 BET data comparison for mesoporous silica nanospheres

	MSN-48 (**a**)	MSN-41 (**b**)	Large Pore MSN-41 (**c**)
Surface Area (m^2/g)	1737	1548	928
Pore Volume (cc/g)	1.1	2.1	1.8
Pore Diameter (nm)	2.2	1.9	4.3

3.6 was grafted onto **b** and **c** to form MSN-supported catalysts. TGA indicated an 11.8 wt% loading of **3.6** onto the surface of the large pore MSN-41 nanospheres which is roughly twice the loading observed for both the MSN-48 and MSN-41 nanospheres (Table 3.3). There was a decrease in surface area from 928 m^2/g for bare large pore MSN-41 (**c**) to 477 m^2/g for the corresponding catalyst loaded MSN-41 particles **3.6-c** (Figure 3.9). Also observed was a decrease in pore volume from 1.3 to 0.65 cc/g once **3.6** was immobilized. The catalyst immobilization did not seem to affect the pore volume.

Table 3.3 Comparison of large pore MSN-41 before and after catalyst loading.

	Large Pore MSN-41 (**c**)	**3.6-c**
% Loading (TGA)	—	11.8
Surface Area (m^2/g)	928	477
Pore Volume (cc/g)	1.3	0.65
Pore Diameter (nm)	4.3	4.3
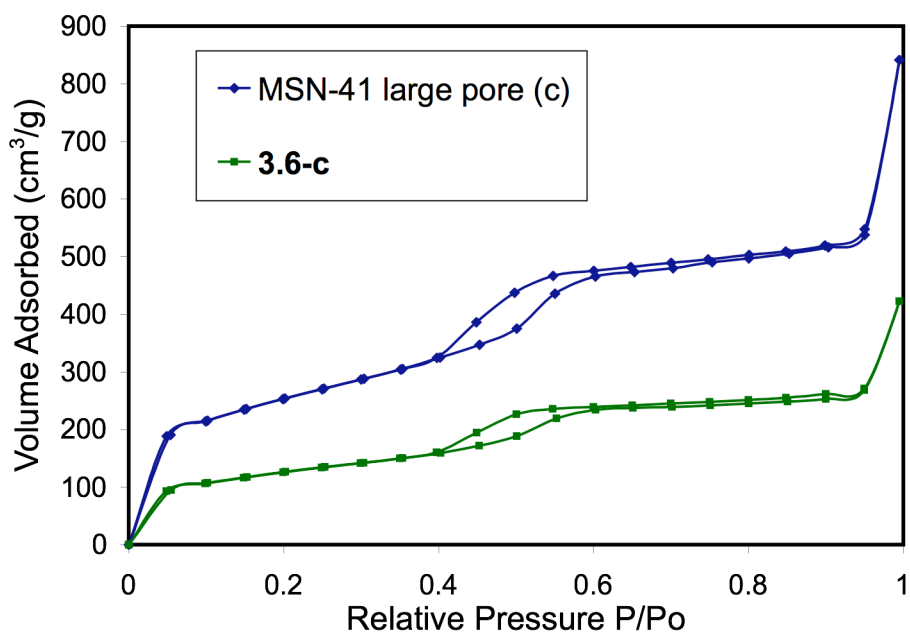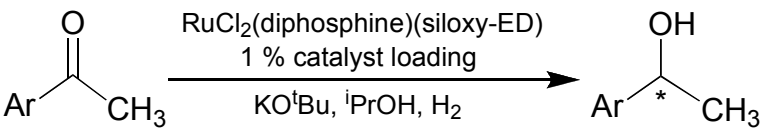
Figure 3.9 Nitrogen adsorption/ desorption isotherms depicting the larger pore size of MSN-41 large pore and decreased surface area once **3.6** is immobilized.

3.2.3 Asymmetric homogeneous and heterogeneous catalysis of aromatic ketones

Upon activation with base co-catalysts, the new Ru(diphosphine)(diamine)Cl$_2$ complexes **3.1-3.5** were shown to be highly active for the homogeneous asymmetric hydrogenation of aromatic ketones with enantiomeric excess (ee) up to 88% (Table 3.4). Due to the commercial availability of the achiral diamine 1,2-ethylenediamine, a series of chiral binaphthyl diphosphine ligands were prepared with the achiral diamine. Enantioselectivity was similar between BINAP and TMS-BINAP while yields slightly decrease when using the latter. The bulky TMS groups at the 4,4' positions of **3.2** seem to hinder the activity and also lead to a decrease in the overall enantioselectivity. The highly active **3.1** gives full conversions and increased enantioselectivity over 4,4' substituted **3.2**. **3.3,** with the 3,5-diphenylphosphine moieties, gives full conversion and e.e.'s as high as 88%. The SEGPHOS derivatives **3.4** and **3.5** were less active than the BINAP derivatives and gave modest e.e. values. There was a general trend of increase in enantioselectivity associated with $^{t\text{Bu}}$SEGPHOS (**3.5**) when compared to the less bulky SEGPHOS derivative (**3.4**). Overall, the xylyl-BINAP ethylenediamine catalyst **3.3** gave the highest overall enantioselectivity and full conversion in nearly every case.

Table 3.4 Homogeneous enantioselectivities of aromatic ketones using **3.1-3.5**.[a]

Ar–C(=O)–CH₃ → (RuCl₂(diphosphine)(siloxy-ED), 1 % catalyst loading, KO^{t}Bu, ^{i}PrOH, H₂) → Ar–*CH(OH)–CH₃

Structures:
R = H
3.1: X = H, Ar = Ph
3.2: X = TMS, Ar = Ph
3.3: X = H, Ar = C₆H₃-3,5-Me₂

R = H
3.4: X = H
3.5: X = ^{t}Bu

Ar	3.1	3.2	3.3	3.4	3.5
			Homogeneous catalysts 3.1-3.5		
Ph	39	27(97)	76	33	52(97)
1-naphthyl	31	17(97)	75	16(97)	21(97)
2-naphthyl	36	43(97)	86	23(97)	50(95)
4-MePh	32	21(97)	65	35(95)	49(96)
4-ClPh	29	29(96)	**88**	16(97)	37(94)
4-MeOPh	48	28(96)	68	42	52(91)
4-^{t}BuPh	45	43(96)	56	57(88)	80(95)
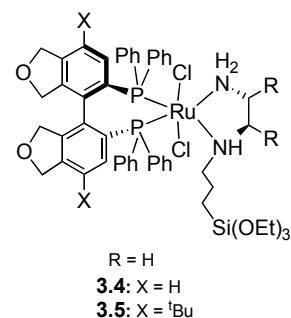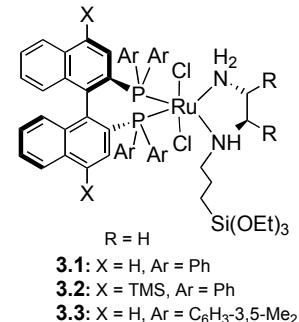
[a] Full conversions unless noted in ( ). [b] Conversion % and e.e.% were determined by GC on a Supelco ß-Dex column for all the secondary alcohols.

To gain an increase in enantioselectivity, the use of a chiral amine was explored. Control experiments with Ru(BINAP)(1,2-cyclohexanediamine)Cl₂ (**3.11**) indicated that the propyl(triethoxy)silane pendant in **3.6** significantly enhanced the enantioselectivity (Table 3.5). It is established that homogenous Ru(diphosphine)(diamine)Cl₂ complexes with two primary amine groups (such as 1,2-diphenylethylenediamine and 1,1-Bis(4-methoxyphenyl)-3-methyl-1,2-butanediamine) enjoy significant ee enhancement with either bulky substituents on the 4,4'-positions of the binaphthyl framework or the bulkier 3,5-dimethylphenyl group on the phosphino moieties. Such a beneficial substituent effect is absent in the Ru(diphosphine)(siloxy-DACH)Cl₂ complexes **3.6-3.10** with an alkylated 1,2-cyclohexanediamine. The Ru(II) complex with a BINAP ligand, **3.6**, gives higher ee values

than those with TMS-BINAP, **3.7**, or Xyl-BINAP, **3.8**. In contrast, the ^{t}Bu groups on the 7,7'-position of SEGPHOS (in **3.10**) significantly enhance the enantioselectivity, presumably as a result of the difference in dihedral angles between the binaphthyl system and the SEGPHOS system.

Table 3.5 Homogeneous enantioselectivities of aromatic ketones using **3.6-3.11**.[a]

	Homogeneous catalysts 3.6-3.11					
Ar	**3.6**	**3.7**	**3.8**	**3.9**	**3.10**	**3.11**
Ph	82	77(86)	79	67(95)	80	62(93)
1-naphthyl	**94**	80(83)	78	79(97)	92	73(94)
2-naphthyl	83	80(97)	90	61(96)	82	72(94)
4-MePh	83	64(84)	76	67(95)	81(94)	62(94)
4-ClPh	71	64(86)	86	56(95)	76	61(91)
4-MeOPh	80	47(80)	68	70(96)	85	63(95)
4-^{t}BuPh	89	76	84	74(93)	77	78(94)
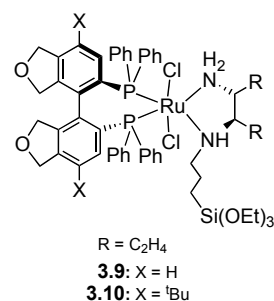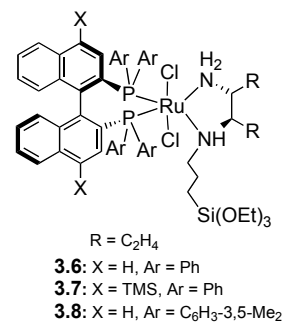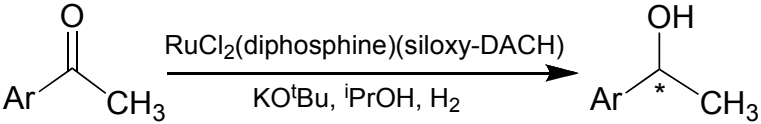
[a] Full conversions unless noted in ( ). [b] Conversion % and e.e.% were determined by GC on a Supelco ß-Dex column for all the secondary alcohols.

Upon activation with KO^{t}Bu, the MSN-48 immobilized Ru complexes **3.6-a** through **3.10-a** are also very active catalysts for asymmetric hydrogenation of aromatic ketones. As shown in Table 3.6, no decrease of catalytic activities was observed for the immobilized catalysts, but **3.6-a** through **3.10-a** exhibit lower enantioselectivities than their parent

homogeneous catalysts. The highest ee value of 82% was obtained for the hydrogenation of 2-acetonaphthone using **3.7-a**. The deterioration of enantioselectivities was observed for many asymmetric catalysts immobilized on bulk mesoporous silicas.[12]

Table 3.6 Heterogeneous enantioselectivities for aromatic ketones using catalysts **3.6-a** through **3.10-a**.[a]

$$\underset{Ar}{\overset{O}{\|}}\underset{CH_3}{} \xrightarrow[\text{KO}^t\text{Bu, }^i\text{PrOH, H}_2]{\text{RuCl}_2(\text{diphosphine})(\text{siloxy-DACH})} \underset{Ar}{\overset{OH}{|}}\underset{*}{}\underset{CH_3}{}$$

Ar	MSN-supported catalyst (mol% loading)				
	3.6'(0.8)	**3.7'(0.7)**	**3.8'(1.0)**	**3.9'(1.1)**	**3.10'(0.9)**
Ph	61(94)[a]	71	59	58(97)	73
1-naphthyl	67(96)	76(87)	52	76	72
2-naphthyl	68	**82**	66	58(97)	69
4-MePh	47	66	60	60	61
4-ClPh	57	72	62	51	57
4-MeOPh	68	64(48)	49	53	56(97)
4-^{t}BuPh	77	69	53	69(94)	49

[a] Full conversions unless noted in ( ). [b] Conversion % and e.e.% were determined by GC on a Supelco ß-Dex column for all the secondary alcohols.

These highly active MSN-48 supported catalysts were readily recovered by centrifugation and were shown to be reusable for the asymmetric hydrogenation of aromatic ketones. For example, for the hydrogenation of acetophenone, **3.6-a** was recovered and reused for at least 5 times, with a conversion of >99%, >99%, 89%, >99%, and 65% and an ee value of 61%, 58%, 70%, 68%, and 65% for the five consecutive runs.
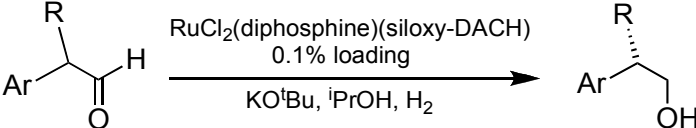
3.2.4 Asymmetric hydrogenation of arylaldehydes
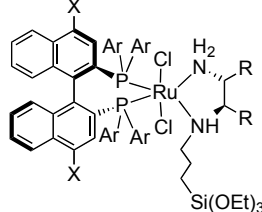
Intrigued by recent elegant work of homogeneous asymmetric hydrogenation of

racemic α-branched arylaldehydes by Ru(diphosphine)(diamine)Cl$_2$ complexes for the synthesis of chiral primary alcohols,[10] we have also examined the utility of MSN-48 (**a**) immobilized Ru complexes on such a dynamic kinetic resolution process (Table 3.7). At a 0.1 mol% catalyst loading, homogeneous catalysts **3.6-3.8** all gave complete conversion of arylaldehydes to their hydrogenated products, with ee values as high as 99% (for 3-methyl-2-phenylbutanal with a ^{i}Pr group at the a-position). This level of enantioselectivity is slightly better than that obtained with the homogenous Ru(diphosphine)(1,2-cyclohexanediamine)Cl$_2$ complexes examined by Zhou et al,[8] suggesting the positive influence of the propyl(triethoxy)silane pendant on the enantioselectivity of the dynamic kinetic resolution process. It is of interest to note that there is significant enantioselectivity enhancement with either bulky substituents on the 4,4'-positions of the binaphthyl framework (for **3.7**) or the bulkier 3,5-dimethylphenyl groups on the phosphino moieties (for **3.8**).

The MSN-48 supported Ru complexes **3.6a** thru **3.8-a** are also highly active catalysts for asymmetric hydrogenation of racemic α-branched arylaldehydes. Interestingly, unlike asymmetric hydrogenation of aromatic ketones, the immobilized catalysts **3.6-a** through **3.8-a** gave higher enantioselectivity for most of arylaldehydes we have examined (with as much as 24% ee increase for hydrogenation of a-2-naphthylpropionaldehyde using **3.6** vs. **3.6-a**). The highest ee value for the heterogeneously catalyzed reaction is 97% for 3-methyl-2-phenylbutanal with **3.7-a**. The different effects of immobilization on the enantioselectivity of two asymmetric hydrogenation reactions highlight the subtlety of catalyst immobilization and the need to examine other reaction types and immobilization strategies.
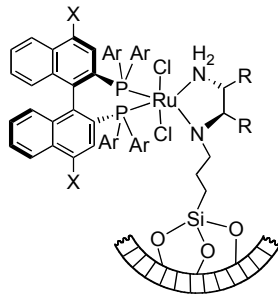
Table 3.7 Homogeneous vs. Heterogeneous enantioselectivities for arylaldehydes using catalysts **3.6-3.8** and **3.6-a** thru **3.8-a**.[a]

RuCl₂(diphosphine)(siloxy-DACH)
0.1% loading
KOtBu, iPrOH, H₂

R = C₂H₄
3.6: X = H, Ar = Ph
3.7: X = TMS, Ar = Ph
3.8: X = H, Ar = C₆H₃-3,5-Me₂

R = C₂H₄
3.6'a: X = H, Ar = Ph
3.7'b: X = TMS, Ar = Ph
3.8'c: X = H, Ar = C₆H₃-3,5-Me₂

Ar	R	Homogeneous			MSN-48 (a)		
		3.6	**3.7**	**3.8**	**3.6-a**	**3.7-a**	**3.8-a**
Ph	Me	42	70	72	52	76	84
Ph	iPr	35	97	**99**	52	**97**	86
Ph	nBu	40	80	84	55	84	49
4-ClPh	Me	47	69	74	52	78	85
4-MeOPh	Me	53	76	83	63	78	88
2-Naphthyl	Me	44	72	72	68	83	86

[a] Full conversion. [b] Conversion % and e.e.% were determined by ^{1}H NMR and HPLC on a Chiralcel AD column for all the arylaldehydes.

MSN-41 supported catalysts **3.6-b, 3.7-b, and 3.8-b** and MSN-41 LP supported catalysts **3.6-c, 3.7-c, and 3.8-c** were prepared to study the potential effects of channel walls on the enantioselectivities of these heterogeneous catalysts. Complete conversion was achieved for all runs (Table 3.8). The BINAP catalysts, **3.6-a**, **3.6-b**, and **3.6-c** gave modest e.e.'s with a trend towards substrate dependence determining the enantioselectivity. The BINAP **3.6-a** seemed to give higher e.e's for substrates having an electron donating or withdrawing group on the phenyl ring while the Xyl-BINAP **3.6-c** seemed to give higher e.e's for substrates having a bulky **R**-group. The TMS- BINAP catalyst **3.7-a** outperformed the TMS-BINAP MSN-41 catalysts in every case giving e.e.'s as high as 97%. This increase may be due to the confinement effect of the interpenetrated channels of the MSN-48

nanoparticles forcing an even tighter chiral pocket formed from the 4,4'-substituted bulky TMS groups. These bulky groups were however, not sufficiently bulky so as to clog the pores and hinder the substrates from accessing the catalytic sites via diffusion through the channels. The Xyl-BINAP catalyst **3.8-a** again seemed to induce higher enantioselectivity on the substrates with substituted phenyl rings while **3.8-c** attained the highest enantioselectivity when the substrates with bulky **R**-groups were used.

Table 3.8 Heterogeneous enantioselectivity comparison for arylaldehydes using catalysts **3.6-3.8** on **a, b,** and **c**.[a]

$$\text{Ar—CH(R)—CHO} \xrightarrow[\text{KO}^{t}\text{Bu, }^{i}\text{PrOH, H}_2]{\substack{\text{RuCl}_2\text{(diphosphine)(siloxy-DACH)}\\ \text{0.1\% loading}}} \text{Ar—CH(R)—CH}_2\text{OH}$$

MSN-48 (**a**)   MSN-41 (**b**)   MSN-41 Large Pore (**c**)
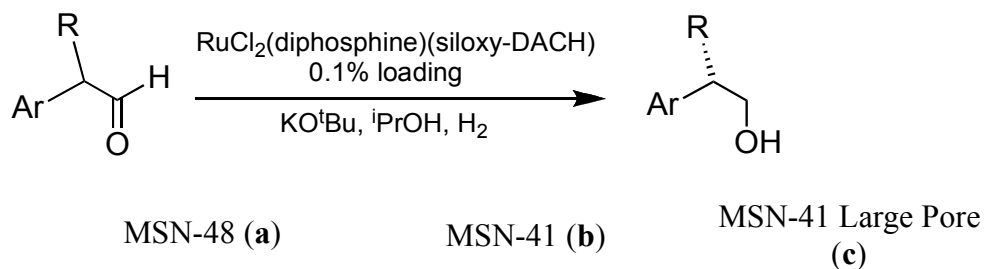
Ar	R	3.6-a	3.7-a	3.8-a	3.6-b	3.7-b	3.8-b	3.6-c	3.7-c	3.8-c
Ph	Me	52	76	84	55	54	75	45	53	75
Ph	^{i}Pr	52	**97**	86	59	84	86	73	86	92
Ph	^{n}Bu	55	84	49	56	68	85	76	71	67
4-ClPh	Me	52	78	85	42	71	87	44	75	85
4-MeOPh	Me	63	78	88	61	60	81	55	65	86
2-Naphthyl	Me	68	83	86	65	68	80	53	57	82

[a] Full conversion. [b] Conversion % and e.e.% were determined by ^{1}H NMR and HPLC on a Chiralcel AD column for all the arylaldehydes.

Because of the large excess of base required for the heterogeneous catalytic reactions, protection of the silynol groups was achieved using hexamethyldisilazane.[9] This protection allowed for the use of equimolar concentrations of base for the heterogeneous catalysis as

was used for the homogeneous (10 mol%) (Table 3.9). BET data indicated that the protection of the silynol groups did not significantly affect the pore size or pore volume of the mesoporous silica once the catalyst was immobilized on the surface (Table 3.10).

Table 3.9 Comparison of amounts of base required for enantioselective catalysis of 4-^{t}BuPh ketone.
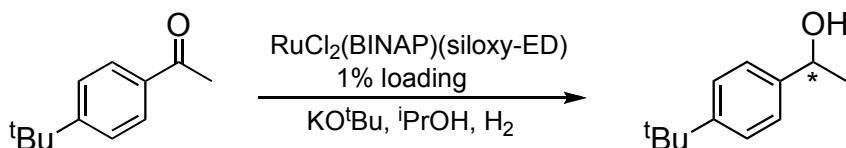
Catalyst	mol catalyst	mol base	x base	e.e.
Homogeneous **3.1**	0.38 µmol	3.8 µmol	x 10	78
MSN-48 **3.1-a**	0.58 µmol	294 µmol	x 500	42
Protected MSN-48 **3.1-d**	0.67µmol	6.7 µmol	x 10	38

Table 3.10 BET comparison of Large Pore MSN-41 materials.

	Large pore protected MSN-41 (**c**)	**3.7** on large pore, **3.7-c**	**3.7** on large pore protected, **3.7-e**
% loading	—	10.4	10.4
Surface Area (m^2/g)	928	464	465
Pore Volume (cc/g)	1.3	0.64	0.71

As is shown in Table 3.11, when solid catalyst **3.7'** large pore MSN-41 is protected (**e**), **3.7-e**, there is a significant decrease in enantioselectivity. The loss in enantioselectivity may be due to the bulky trimethylsilyl groups associated with the protection that inhibit proper interaction of substrate with the active catalytic site of the diphosphine catalysts.

Table 3.11 Comparison of enantioselectivity of arylaldehydes using **3.7'** on several different MSNs.[a]

$$Ar\overset{R}{\underset{O}{\overset{|}{C}}}H \xrightarrow[\text{KO}^{t}\text{Bu, }^{i}\text{PrOH, H}_2]{\substack{\text{RuCl}_2\text{(TMS-BINAP)(siloxy-DACH)}\\ \text{0.1\% loading}}} Ar\overset{R}{\underset{OH}{\overset{|}{C}}}$$
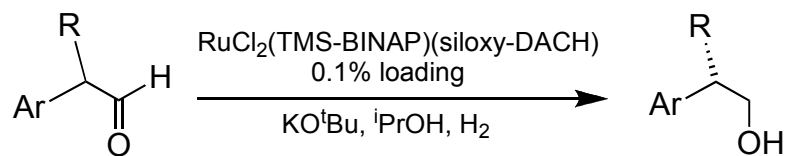
Ar	R	3.7	MSN-48 3.7-a	MSN-41 3.7-b	MSN-41 Large Pore 3.7-c	MSN-41 Large Pore Protected 3.7'e
Ph	Me	70	76	54	53	46
Ph	^{i}Pr	97	97	84	86	52
Ph	^{n}Bu	80	84	68	71	50
4-ClPh	Me	69	78	71	75	44
4-MeOPh	Me	76	78	60	65	49
2-Naphthyl	Me	72	83	68	57	40

[a] Full conversion. [b] Conversion % and e.e.% were determined by ^{1}H NMR and HPLC on a Chiralcel AD column for all the arylaldehydes.

To verify the immobilization of the Ru(II) catalysts on the inner surface of the pores of the mesoporous silica, a control experiment comparing solid silica to mesoporous silica was performed. Shown in Table 3.12, **3.1** was used in the asymmetric hydrogenation of aryladehydes. A decrease of enantioselectivity was observed for all the substrates when solid silica was used. This decrease in enantioselectivity is presumably due to the fact that the convex outer surface of the solid silica did not have a beneficial effect on the e.e.'s. In contrast, the mesoporous silica offers the concave environment that reinforces the chiral induction by the immobilized catalysts.

Table 3.12 Comparison of the enantioselectivity for asymmetric hydrogenation of arylaldehydes catalyzed by **3.6** supported on MSN-48 (**a**) and solid silica (**f**).
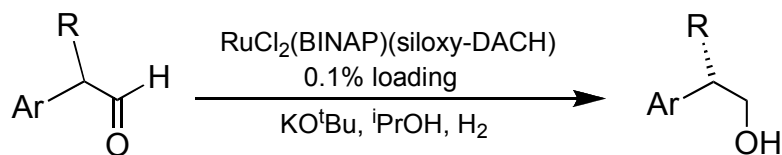
Ar	R	MSN-48, **3.6-a**	Silica Gel
Ph	Me	52	33
Ph	^{i}Pr	52	36
Ph	^{n}Bu	55	45
4-ClPh	Me	52	47
4-MeOPh	Me	63	33
2-Naphthyl	Me	68	52

[a] Full conversion. [b] Conversion % and e.e.% were determined by ^{1}H NMR HPLC on a Chiralcel AD column for all the arylaldehydes.

3.3 Summary

In conclusion, we have prepared chiral Ru(diphosphine)(diamine)Cl$_2$ complexes with siloxy functionalities that can be readily attached to the silica surface. We have successfully immobilized these Ru complexes onto mesoporous silica nanospheres with both two and three-dimensional channels, and demonstrated for the first time the utility of MSNs as supports for Ru catalysts in asymmetric hydrogenation of aromatic ketones to afford chiral secondary alcohols and racemic arylaldehydes to give chiral primary alcohols. The generality of this catalyst immobilization strategy should allow the design of many highly active and enantioselective heterogeneous asymmetric catalysts.

3.4 Experimental Section

3.4.1 General Information

All of the chemicals were obtained from commercial sources and used without further purification, unless otherwise noted. All of the reactions and manipulations were carried out under Argon with the use of standard inert atmosphere and Schlenk techniques. Solvents used in all the reactions were dried by standard procedures. NMR spectra were recorded on a Bruker NMR 400 DRX spectrometer. ^{1}H NMR spectra were recorded at 400 MHz and referenced to the proton resonance resulting from incomplete deuteration of the deuterated chloroform (δ 7.24). ^{31}P{^{1}H} NMR spectra were recorded at 161 MHz and all the chemical shifts are reported in ppm relative to the phosphorous resonance of 85% phosphonic acid (external standard). Scanning Electron Microscopy (SEM) images taken with Hitachi 4700 field emission microscope. Transmission Electron Microscopy (TEM) images were taken with a Philips CM 12 electron microscope at 100 KV. Thermogravimetric analysis (TGA) was performed using a Shimadzu TGA-50 analyzer. Ru contents were measured on an Applied Research Laboratories (ARL) SpectraSpan7 Direct Current Plasma (DCP) Spectrometer. BET measurements were taken on a Quantachrome Autosorb-1. Siloxy-(*R,R)*1,2-diaminocyclohexane (siloxy-DACH) was prepared according to a literature procedure.[10] Arylaldehyde substrates were prepared according to literature procedures.[8]

3.4.1.1 A typical procedure for Immobilization onto MSN-48 using grafting method

A 10% w/w loading mixture of (*R,RR*)-(xylyl-BINAP)RuCl$_2$(siloxy-DACH) (11mg, 8.9μmol) and MCM-48 (110mg) in toluene (3ml) was heated @113°C under Argon for 24h. Upon cooling to RT, the mixture was washed with toluene (10ml X 3) and dichloromethane (10ml X 2). The loaded silica was dried under reduced pressure for 18 h. TGA indicated 6.3% loading by weight.

3.4.1.2 A typical procedure for the homogeneous asymmetric hydrogenation of aromatic ketones

Stock solutions of Ru(diphosphine)(diamine)Cl$_2$ precatalyst (2.0mg, 1.5μmol) and KO^{t}Bu (1.8mg, 15μmol) were each prepared in anhydrous isopropanol (0.7ml X 2) under Argon. Aliquots of (0.1ml) were then individually transferred from each of the stock solutions to seven septum-sealed ½ dram vials containing substrate (18μmol). Each reaction vessel was to contain: stir bar, 0.18μmol precatalyst, 1.8μmol base, 18μmol substrate, and 0.2ml isopropanol. A needle was added to each vial through the septum before quickly transferring the vials into a stainless steel autoclave and sealed. After purging with H$_2$ six times, the final H$_2$ pressure was adjusted to 700psi. After 24 hours the autoclave was depressurized and the reaction mixture was washed with diethyl ether and water twice. The diethyl ether layer was then passed through a mini silica gel column. The resulting solution was concentrated and an aliquot was analyzed on GC to give conversion and ee values.

3.4.1.3 A typical procedure for the heterogeneous asymmetric hydrogenation of aromatic ketones

KO^{t}Bu (33mg, 20mmol) and precatalyst supported on MCM-48 (10mg silica /0.50μmol precatalyst) were added to a 1 dram vial containing substrate (50μmol) and stir bar. Under Argon, isopropanol (1ml) was added and a septum with needle was added and the reaction vessel was quickly transferred to a stainless steel autoclave and sealed. After purging with H$_2$ six times, the final H$_2$ pressure was adjusted to 700psi. After 24 hours the autoclave was depressurized and the reaction mixture was removed and centrifuged (3200rpm X 5min). The supernatant was collected and the remaining silica was washed with ether and once again centrifuged. This process was performed a total of 3 times. The collected ether fractions

were washed with water (5mL X 3). The ether layer was then collected and passed through a mini silica gel column. The resulting solution was concentrated and an aliquot was analyzed on GC to give conversion and ee values.

3.4.2 Preparation and characterization of Ru(diphosphine)(siloxy-ED)Cl$_2$ precatalysts
3.4.2.1 [(R,RR)-Ru(BINAP)(siloxy-ED)Cl$_2$], 3.1

(R)-BINAP (25mg, 40.1 μmol) and [Ru(p-cymene)Cl]$_2$Cl$_2$ (12.5mg, 20.5 μmol) were added to a Schlenk flask. Dichloromethane (2mL) and DMF (0.5mL) were added to form an orange solution while stirring at RT for 15 min. The solution was heated at 50°C with stirring, for 24 hours, and then cooled to RT. Following addition of ethylenediamine (10.6μL, 40.1μmol), the reaction was stirred at 50°C for 36h. The excess solvent was pulled off under reduced pressure yielding a dark red solid. The resulting solid was purified on silica gel (H:EA/2:1) to give a pure product. Following concentration, the yellow product was collected (36mg, 85% yield). ^{1}H NMR in CDCl$_3$: δ 8.36 (t, $^3J_{H-H}$ = 8.0 Hz, 1H), 8.02 (bs, 2H), 7.92 (m, 3H), 7.72 (m, 2H), 7.65 (d, $^3J_{H-H}$ = 8.4 Hz, 2H), 7.55 (m, 2H), 7.48 (m, 2H), 7.32 (m, 6H), 7.11 (m, 2H), 6.76 (t, $^3J_{H-H}$ = 8.0 Hz, 1H), 6.63 (t, $^3J_{H-H}$ = 8.0 Hz, 1H), 6.54 (m, 3H), 6.45 (d, $^3J_{H-H}$ = 8.4 Hz, 1H), 6.38 (m, 3H), 6.19 (d, $^3J_{H-H}$ = 8.4 Hz, 1H), 3.66 (q, $^3J_{H-H}$ = 7.1 Hz, 6H), 2.9 (bs, 4H), 2.72 (m, 2H), 2.52 (bs, 1H), 2.32 (bs, 2H), 1.56 (m, 1H), 1.31 (m, 1H), 1.13 (t, $^3J_{H-H}$ = 6.0 Hz, 6H) 0.45 (bs, 1H). ^{31}P{^{1}H} NMR in CDCl$_3$: δ 46.7 (d, $^5J_{P-P}$ = 37 Hz), 42.6 ppm (d, $^5J_{P-P}$ = 35 Hz). MS m/z 1058.23 (observed m/z 1023.3 for [M-Cl]$^+$).

3.4.2.2 [(R,RR)-Ru(4,4'-TMS-BINAP)(siloxy-ED)Cl$_2$], 3.2

(R)-4,4'-TMS-BINAP (120mg, 0.16mmol) and [Ru(p-cymene)Cl]$_2$Cl$_2$ (49mg,

0.08mmol) were added to a Schlenk flask under Argon. Following addition of dichloromethane (4mL) and DMF (1mL), a dark orange solution formed and was stirred at RT for 15min. The reaction was heated at 50°C for 24 hours and then was cooled to RT. Triethoxysilane-ethylenediamine (43μL, 0.16mmol) was added to the solution and stirred at RT for 15 min. The solution was then heated at 50°C for an additional 48 hours. The resulting solution was concentrated under reduced pressure and the resulting red solid was purified on silica gel (H:EA/3:1). The dark yellow product was collected (41mg, 21% yield). ^{1}H NMR in CDCl$_3$: δ 8.54 (d, $^3J_{H-H}$ = 7.6 Hz, 1H), 8.17 (d, $^3J_{H-H}$ = 8.0 Hz, 1H), 7.99 (m, 2H), 7.94 (m, 2H), 7.71 (d, $^3J_{H-H}$ = 8.4 Hz, 2H), 7.64 (m, 2H), 7.57 (m, 2H), 7.31 (m, 6H), 7.11 (m, 2H), 6.67 (m, 2H), 6.46 (m, 4H), 6.36 (bs, 4H), 3.71 (q, $^3J_{H-H}$ = 7.1 Hz, 6H), 2.87 (bs, 4H), 2.76 (m, 2H), 2.47 (bs, 1H), 2.38 (bs, 2H), 1.56 (m, 1H), 1.31 (m, 1H), 1.15 (t, $^3J_{H-H}$ = 6.0 Hz, 6H), 0.50 (s, 9H), 0.45 (s, 9H), 0.40 (bs, 1H). ^{31}P{^{1}H} NMR in CDCl$_3$: δ 47.1 (d, $^5J_{P-P}$ = 34 Hz), 42.6 ppm (d, $^5J_{P-P}$ = 35 Hz). MS m/z 1202.31 (observed m/z 1167.4 for [M-Cl]$^+$).

3.4.2.3 [(*R*,*RR*)-Ru(xylyl-BINAP)(siloxy-ED)Cl$_2$], 3.3

(*R*)-xylyl-BINAP (50mg, 0.068mmol) and [Ru(*p*-cymene)Cl]$_2$Cl$_2$ (20.8mg, 0.034mmol) were added to a Schlenk flask under Argon and dichloromethane (2mL) and DMF (0.5mL) were added to form a dark orange solution. After stirring at RT for 15 min, the solution was heated at 50°C for 18h. After cooling to RT, triethoxysilane-ethylenediamine (siloxy-ED) (18.1μL, 0.068mmol) was added under Argon and the solution was stirred at RT for 15min. The reaction was then heated to 50°C for 24h. After cooling to RT the solvent was removed under reduced pressure to give a dark red solid. The solid was purified on silica gel (H:EA/3:1) to give an orange product (18mg, 23% yield). ^{1}H NMR in CDCl$_3$: δ 8.40 (t, $^3J_{H-H}$ = 8.0, 1H), 8.09 (t, $^3J_{H-H}$ = 8.4, 1H), 7.78 (bs, 2H), 7.68 (m, 2H), 7.60

(d, $^3J_{H-H}$ = 8.8, 2H), 7.54 (m, 2H), 7.36 (d, $^3J_{H-H}$ = 8.0Hz, 1H), 7.27 (bs, 2H), 7.05-7.13 (m, 3H), 6.98 (s, 1H), 6.94 (s, 1H), 6.74 (t, $^3J_{H-H}$ = 7.8Hz, 1H), 6.65 (t, $^3J_{H-H}$ = 7.6Hz, 1H), 6.23 (d, $^3J_{H-H}$ = 8.8Hz, 1H), 6.08 (d, $^3J_{H-H}$ = 8.8Hz, 1H), 5.92 (s, 1H), 5.79 (s, 1H), 3.67 (q, $^3J_{H-H}$ = 6.9 Hz, 6H), 2.83 (m, 4H), 2.70 (m, 2H), 2.47 (bs, 1H), 2.32 (m, 12H), 2.18 (bs, 2H), 1.75 (m, 12H), 1.56 (m, 1H), 1.31 (m, 1H), 1.14 (t, $^3J_{H-H}$ = 3.6 Hz, 6H) 0.85 (bs, 1H), 0.45 (bs, 1H). $^{31}P\{^1H\}$ NMR in CDCl$_3$: δ 45.5 (d, $^5J_{P-P}$ = 34 Hz), 40.4 ppm (d, $^5J_{P-P}$ = 32 Hz). MS m/z 1170.25 (observed m/z 1135.5 for [M-Cl]$^+$).

3.4.2.4 [(*S,SS*)-Ru(SEGPHOS)(siloxy-ED)Cl$_2$], 3.4

(*S*)-SEPGHOS (25mg, 41μmol) and [Ru(*p*-cymene)Cl]$_2$Cl$_2$ (12.5mg, 20.5μmol) were added under Argon to a schlenk flask. Dichloromethane (2ml) and anhydrous DMF (0.5ml) were added to the flask under Argon. The dark orange solution was stirred at RT for 10 m. The solution was heated at 50°C for 36h and then cooled to RT to allow for the addition of siloxy-ED (10.9μL, 41μmol) and stirred at that temperature for 5 m. The solution was then heated to 50°C for 24h. Upon completion, the solvent was removed under reduced pressure with gentle heating. The solid product was purified on a silica gel column using hexane/EA (2:1) as the eluent. The yellow product was isolated and characterized (7mg, 16% yield). ^1H NMR in CDCl$_3$: δ 7.85 (bs, 2H), 7.78 (m, 2H), 7.18-7.40 (m, 8H), 7.10 (t, $^3J_{H-H}$ = 6.2 Hz, 4H), 7.01 (t, $^3J_{H-H}$ = 7.0 Hz, 4H), 6.85 (m, 2H), 6.47 (d, $^3J_{H-H}$ = 8.0 Hz, 1H), 6.40 (d, $^3J_{H-H}$ = 8.4 Hz, 1H), 5.77 (s, 1H), 5.69 (d, $^3J_{H-H}$ = 1.6 Hz, 1H), 5.34 (s, 1H), 5.18 (d, $^3J_{H-H}$ = 1.6 Hz, 1H), 3.65 (q, $^3J_{H-H}$ = 6.9 Hz, 6H), 3.01 (m, 4H), 2.72 (m, 1H), 2.64 (m, 1H), 2.56 (m, 1H), 2.46 (m, 2H), 1.13 (t, $^3J_{H-H}$ = 7.0 Hz, 9H), 0.51 (m, 2H). $^{31}P\{^1H\}$ NMR in CDCl$_3$: δ 45.3 (d, $^5J_{P-P}$ = 34 Hz), 41.5 (d, $^5J_{P-P}$ = 34 Hz). MS m/z 1046.18 (observed m/z 1011.2 for [M-Cl]$^+$).

3.4.2.5 [(*S,SS*)-Ru(4,4'-$^{\text{tBu}}$SEGPHOS)(siloxy-ED)Cl$_2$], 3.5

(*S*)-(4,4'-$^{\text{tBu}}$SEPGHOS) (25mg, 35μmol) and [Ru(*p*-cymene)Cl]$_2$Cl$_2$ (10.5mg, 18μmol) were added under Argon to a schlenk flask. 1,2-Dichloroethane (2ml) and anhydrous DMF (0.5ml) were added to the flask under Argon. The dark orange solution was stirred at RT for 5 m. The solution was heated at 50°C for 24h and then cooled to RT to allow for the addition of siloxy-ED (10.9μL, 41μmol) and stirred at that temperature for 5 m. The solution was then heated to 50°C for 24h. Upon completion, the solvent was removed under reduced pressure with gentle heating. The solid product was purified on a silica gel column using hexane/EA (2:1) as the eluent. The yellow product was isolated and characterized (7mg, 17% yield). ^{1}H NMR in CDCl$_3$: δ 7.86 (bs, 2H), 7.78 (bs, 2H), 7.10-7.45 (m, 8H), 7.10 (t, $^3J_{\text{H-H}}$ = 7.4 Hz, 4H), 7.01 (t, $^3J_{\text{H-H}}$ = 7.6 Hz, 4H), 5.72 (d, $^3J_{\text{H-H}}$ = 1.6 Hz, 1H), 5.69 (d, $^3J_{\text{H-H}}$ = 1.6 Hz, 1H), 5.30 (d, $^3J_{\text{H-H}}$ = 1.6 Hz, 1H), 5.16 (d, $^3J_{\text{H-H}}$ = 1.6 Hz, 1H), 3.67 (q, $^3J_{\text{H-H}}$ = 7.1 Hz, 6H), 2.89 (m, 2H), 2.75 (m, 1H), 2.41 (m, 2H), 1.35 (m, 2H), 1.22 (s, 9H), 1.18 (s, 9H), 1.13 (t, $^3J_{\text{H-H}}$ = 7.0 Hz, 9H), 0.85 (m, 1H), 0.49 (m, 1H). ^{31}P{^{1}H} NMR in CDCl$_3$: δ 46.1 (d, $^5J_{\text{P-P}}$ = 41 Hz), 41.5 (d, $^5J_{\text{P-P}}$ = 35 Hz). MS *m/z* 1158.3 (observed *m/z* 1123.4 for [M-Cl]$^+$).

3.4.3 Preparation and characterization of Ru(diphosphine)(siloxy-DACH)Cl$_2$ precatalysts

3.4.3.1 [(*R,RR*)-Ru(BINAP)(siloxy-DACH)Cl$_2$], 3.6

A mixture of *R*-BINAP (25 mg, 0.04 mmol) and [Ru(*p*-cymene)Cl]$_2$Cl$_2$ (12.5 mg, 0.0205 mmol) was added under Argon to a 2-neck Schlenk flask and stirred in dry dichloromethane(2 mL) and anhydrous DMF (0.5 mL). The dark orange solution was heated at 50 °C for 18 h and then cooled to room temperature with continued stirring. Siloxy-1,2-

diaminocyclohexane (siloxy-DACH) (10.6 μL, 0.033 mmol) was added to the solution and the mixture was stirred at room temperature for an additional 15 min. The solution was then heated to 50 °C and stirred for 36 h. After completion of the reaction, the solvents were under removed under reduced pressure. The resulting red/orange solid was collected and purified on silica gel using eluent of hexanes/ethyl acetate (2:1 v/v). The yellow bands were collected and the solvent was removed to afford pure **1** (Yield: 8 mg, 18%). ^{1}H NMR CDCl$_3$: 8.36 (t, $^3J_{H-H}$ = 7.6 Hz, 1H), 7.91 (m, 2H), 7.74 (m, 2H), 7.64 (m, 3H), 7.53 (m, 2H), 7.50 (m, 2H), 7.44 (d, $^3J_{H-H}$ = 8.4 Hz, 2H), 7.34 (bs, 3H), 7.29 (bs, 3H), 7.12 (m, 2H), 6.74 (t, $^3J_{H-H}$ = 7.6 Hz, 1H), 6.62 (t, $^3J_{H-H}$ = 7.6 Hz, 1H) 6.54 (m, 3H), 6.47 (d, $^3J_{H-H}$ = 8.8 Hz, 1H), 6.37 (m, 3H), 6.17 (d, $^3J_{H-H}$ = 8.8 Hz, 1H), 3.62 (m, 6H) 2.94 (m, 1H), 2.65 (m, 2H), 2.25 (s, 12H), 2.21 (s, 2H), 2.12 (m, 1H), 1.74 (s, 12H), 1.13 (t, $^3J_{H-H}$ = 6.0 Hz, 6H), 1.10 (m, 1H), 0.95 (m, 1H), 0.80 (m, 2H). ^{31}P{^{1}H} NMR in CDCl$_3$: δ 47.2 (d, $^5J_{P-P}$ = 42 Hz), 37.3 (d, $^5J_{P-P}$ = 39 Hz). MS m/z 1112.27 for M$^+$ (observed m/z 1077.3 for [M-Cl]$^+$)

3.4.3.2 [(*R,RR*)-Ru(4,4'-TMS-BINAP)(siloxy-DACH)Cl$_2$], 3.7

(*R*)-4,4'-TMS-BINAP (25 mg, 0.033 mmol) was added to a Schlenk flask containing [Ru(*p*-cymene)Cl]$_2$Cl$_2$ (10.1 mg, 0.016 mmol). Dry 1,2-dichloroethane (2 mL) and anhydrous DMF (0.5 mL) were added to the mixture to give a dark orange solution. After stirring at r.t. for 15 min, the mixture was heated at 80 °C for 6 hours. The dark orange solution was cooled to r.t. and siloxy-DACH (10.6 μL, 0.033 mmol) was added. After stirring at r.t. for 15 min, the solution was heated at 80 °C for 18 hours. The solvents were removed under reduced pressure and the dark red solid was purified on silica gel column (hexanes/ethyl acetate: 4:1 v/v). Yield: 20 mg (48% yield). ^{1}H NMR CDCl$_3$: δ 8.54 (d, $^3J_{H-H}$ = 7.6 Hz, 1H), 8.14 (d, $^3J_{H-H}$ = 8.0 Hz, 2H), 8.05 (m, 2H), 7.94 (m, 4H), 7.64 (m, 2H), 7.57

(m, 2H), 7.31 (m, 6H), 7.11 (m, 2H), 6.67 (m, 2H), 6.46 (m, 4H), 6.36 (bs, 4H), 3.62 (q, $^3J_{H-H}$ = 6.9 Hz, 6H) 2.94 (m, 1H), 2.65 (m, 2H), , 2.21 (s, 2H), 2.12 (m, 1H), 1.13 (t, $^3J_{H-H}$ = 6.0 Hz, 6H), 1.10 (m, 1H), 0.95 (m, 1H), 0.80 (m, 2H) 0.55 (s, 9H), 0.45 (s, 9H). ^{31}P{^{1}H} NMR in CDCl$_3$: δ 49.1 (d, $^5J_{P-P}$ = 37 Hz), 39.6 ppm (d, $^5J_{P-P}$ = 35 Hz). MS m/z 1256.35 for M$^+$ (observed m/z 1221.5 for [M-Cl]$^+$).

3.4.3.3 [(*R,RR*)-Ru(xylyl-BINAP)(siloxy-DACH)Cl$_2$], 3.8

A mixture of (*R*)-xylyl-BINAP (25 mg, 0.034 mmol) and [Ru(*p*-cymene)Cl]$_2$Cl$_2$ (10.5 mg, 0.017 mmol) was added to a Schlenk flask. Dry 1,2-dichloroethane (2 mL) and anhydrous DMF (0.5 mL) were added to the mixture to form a dark orange solution. After stirring at r.t. for 15 min, the solution was heated to 80 °C for 6 hours. Upon cooling the mixture to r.t., siloxy-DACH (10.6 μL, 0.033 mmol) was added and the solution was stirred at r.t. for 15 min. The mixture was then heated at 80 °C for 18 hours. The solvents were removed under reduced pressure and the resulting solid was purified on silica gel (hexanes/ethyl acetate: 3:1 v/v). Yield: 18mg (43%). ^{1}H NMR in CDCl$_3$: δ 8.39 (t, $^3J_{H-H}$ = 8.0 Hz, 1H), 8.12 (t, $^3J_{H-H}$ = 8.0 Hz, 1H), 7.71 (d, $^3J_{H-H}$ = 8.4 Hz, 2H), 7.60 (m, 4H), 7.32 (bs, 2H), 7.09 (m, 2H), 6.95 (d, $^3J_{H-H}$ = 8.4 Hz, 2H), 6.70 (m, 2H), 6.25 (d, $^3J_{H-H}$ = 8.4 Hz, 1H), 6.11 (d, $^3J_{H-H}$ = 8.4 Hz, 1H), 5.95 (s, 3H), 3.62 (m, 6H) 2.94 (m, 1H), 2.65 (m, 2H), 2.25 (s, 12H), 2.21 (s, 2H), 2.12 (m, 1H), 1.74 (s, 12H), 1.13 (t, $^3J_{H-H}$ = 6.0 Hz, 6H), 1.10 (m, 1H), 0.95 (m, 1H), 0.80 (m, 2H). ^{31}P{^{1}H} NMR in CDCl$_3$: δ 47.2 (d, $^5J_{P-P}$ = 42 Hz), 37.3 (d, $^5J_{P-P}$ = 39 Hz). MS m/z 1224.40 for M$^+$ (observed m/z 1189.4 for [M-Cl]$^+$).

3.4.3.4 [(*S,SS*)-Ru(SEGPHOS)(siloxy-DACH)Cl$_2$], 3.9

(*S*)-SegPhos (25 mg, 41 μmol) and [Ru(p-cymene)Cl]$_2$Cl$_2$ (12.5 mg, 20.5 μmol) were

added under Argon to a schlenk flask. 1,2-Dicloroethane (2 mL) and anhydrous DMF (0.5 mL) were added to the flask under Argon. The dark orange solution was stirred at r.t. for 10 min, and then heated at 80°C for 6 h. Upon cooling to r.t., siloxy-DACH (13 μL, 41 μmol) was added and the mixture was stirred at r.t. for 5 min and then at 80°C for 18 h. The solvents were removed under reduced pressure, and the the solid product was purified on a silica gel column using hexane/ethyl acetate (2:1 v/v). Yield: 11mg (24% yield). ^{1}H NMR in CDCl$_3$: δ 7.95 (m, 2H), 7.77 (m, 2H), 7.41 (m, 2H), 7.20 -7.29 (m, 6H), 7.10 (t, $^3J_{H-H}$ = 8.0 Hz, 4H), 7.01 (t, $^3J_{H-H}$ = 7.2 Hz, 4H), 6.85 (m, 2H), 6.48 (d, $^3J_{H-H}$ = 7.6 Hz, 1H), 6.40 (d, $^3J_{H-H}$ = 7.6 Hz, 1H), 5.75 (d, $^3J_{H-H}$ = 1.2 Hz, 1H), 5.69 (d, $^3J_{H-H}$ = 1.2 Hz, 1H), 5.34 (d, $^3J_{H-H}$ = 1.6 Hz, 1H), 5.18 (d, $^3J_{H-H}$ = 1.6 Hz, 1H), 3.65 (q, $^3J_{H-H}$ = 6.9 Hz, 6H), 3.20 (m, 1H), 2.78 (m, 2H), 2.59 (m, 1H), 2.48 (m, 1H), 2.24 (m, 2H), 1.55 (m, 2H), 1.23 (m, 4H), 1.13 (t, $^3J_{H-H}$ = 7.0 Hz, 9H), 1.05 (m, 2H), 0.80 (m, 2H). ^{31}P{^{1}H} NMR in CDCl$_3$: δ 46.5 (d, $^5J_{P-P}$ = 35 Hz), 38.5 (d, $^5J_{P-P}$ = 32 Hz). MS *m/z* 1100.22 for M$^+$ (observed *m/z* 1065.3 for [M-Cl]$^+$).

3.4.3.5 [(*S,SS*)-Ru(^{tBu}SEGPHOS)(siloxy-DACH)Cl$_2$], 3.10

(*S*)-(4,4'-^{t}BuSegPhos) (25 mg, 35 μmol) and [Ru(p-cymene)Cl]$_2$Cl$_2$ (10.5 mg, 18 μmol) were added under Argon to a schlenk flask. 1,2-Dicloroethane (2 mL) and anhydrous DMF (0.5 mL) were added to the flask under Argon. The dark orange solution was stirred at r.t. for 15 m and then at 80°C for 7 h. Upon cooling to r.t., siloxy-DACH (11.1 μL, 35 μmol) was added and the mixture was stirred at r.t. for 5 min and then at 80 °C for 12 h. The solvents were under reduced pressure, and the resulting solid was purified on a silica gel column using hexane/ethyl acetate (4:1 v/v) as the eluent. Yield: 10 mg (24%). ^{1}H NMR in CDCl$_3$: δ 7.89 (bs, 2H), 7.76 (m, 2H), 7.44 (s, 1H), 7.41 (s, 1H), 7.15 -7.31 (m, 6H), 7.10 (t, $^3J_{H-H}$ = 8.0 Hz, 4H), 7.05 (t, $^3J_{H-H}$ = 7.2 Hz, 4H), 6.99 (m, 2H), 6.48 (d, $^3J_{H-H}$ = 7.6 Hz, 1H),

6.40 (d, $^3J_{H-H}$ = 7.6 Hz, 1H), 5.72 (d, $^3J_{H-H}$ = 1.6 Hz, 1H), 5.69 (d, $^3J_{H-H}$ = 1.6 Hz, 1H), 5.29 (d, $^3J_{H-H}$ = 1.6 Hz, 1H), 5.16 (d, $^3J_{H-H}$ = 1.6 Hz, 1H), 3.65 (q, $^3J_{H-H}$ = 7.1 Hz, 6H), 3.15 (m, 1H), 2.73 (m, 2H), 2.41 (m, 1H), 2.23 (m, 1H), 1.59 (m, 2H), 1.54 (m, 2H), 1.23 (s, 9H), 1.15 (s, 9H), 1.13 (t, $^3J_{H-H}$ = 7.0 Hz, 9H), 0.80-1.05 (m, 4H). $^{31}P\{^1H\}$ NMR in CDCl$_3$: δ 47.6 (d, $^5J_{P-P}$ = 34 Hz), 38.5 (d, $^5J_{P-P}$ = 35 Hz). MS m/z 1212.35 for M$^+$ (observed m/z 1177.4 for [M-Cl]$^+$).

3.5 References

[1] (a) Huh, S.; Wiench, J. W.; Trewyn, B. G.; Song, S.; Pruski, M.; Lin, V. S.-Y. Tuning of particle morphology and pore properties in mesoporous silicas with multiple organic functional groups. *Chem. Commun.* **2003**, *18*, 2364-2365. (b) Nooney, R. I.; Thirunavukkarasu, D.; Chen, Y. M.; Josephs, R.; Ostafin, A. E. Synthesis of nanoscale mesoporous silica spheres with controlled particle size. *Chem. Mater.* **2002,** *14* (11), 4721-4728; (c) Cai, Q.; Luo, Z. S.; Pang, W. Q.; Fan, Y. W.; Chen, X. H.; Cui, F. Z. Dilute solution routes to various controllable morphologies of MCM-41 silica with a basic medium. *Chem. Mater.* **2001,** *13* (2), 258-263.

[2] (a) Huh, S.; Chen, H.-T.; Wiench, J.W.; Pruski, M.; Lin, V. S.-Y. Controlling the selectivity of competitive nitroaldol condensation by using a bifunctionalized mesoporous silica nanosphere-based catalytic system. *J. Am. Chem. Soc.* **2004**, *126* (4), 1010-1011. (b) S. Huh, H.-T. Chen, J. W. Wiench, M. Pruski, Lin, V. S.-Y. Cooperative catalysis by general acid and base bifunctionalized mesoporous silica nanosphere. *Angew. Chem. Int. Ed.* **2005**, *44* (12), 1826-1830. (c) Chen, H.-T.; Huh, S.; Wiench, J. W.; Pruski, M.; Lin, V. S.-Y. Dialkylaminopyridine-functionalized mesoporous silica nanosphere as an efficient and highly stable heterogeneous nucleophilic catalyst. *J. Am. Chem. Soc.* **2005**, *127* (38), 13305-13311.

[3] Thomas, J. M.; Maschmeyer, T.; Johnson, B. F. G.; Shephard, D. S. Constrained chiral catalysts. *J. Mol. Cat. A. Chem.* **1999**, *141* (1-3), 139-144.

[4] Ngo, H. L.; Lin. W. Development of 4,4'-substituted-XylBINAP ligands for highly enantioselective hydrogenation of ketones. *J. Org. Chem.* **2005**, *70* (4), 1177-1187.

[5] (a) Ohkuma, T.; ooka, H.; Ikariya, T.; Noyori, R. Preferential hydrogenation of aldehydes and ketones. *J. Am. Chem. Soc.* **1995**, *117* (41), 10417-10418; (b) Doucet, H.; Ohkuma, T.; Murata, K.; Yokozawam T.; Kozawa, M.; Katayama, E.; England, A. F.; Ikariya, T.; Ishii, D.; Takeno, H.; Noyori, R. trans-[RuCl$_2$(phosphane)$_2$(1,2-diamine) and chiral trans-[RuCl$_2$(diphosphane)(1,2-diamine)]: Shelf-stable precatalysts for the rapid, productive, and stereoselective hydrogenation of ketones. *Angew. Chem. Int. Ed.* **1998**, *37* (12), 1703-1707; (c) Ohkuma, T.; Ishii, D.; Takeno, H.; Noyori, R. Asymmetric hydrogenation of amino ketones using chiral RuCl$_2$(diphosphine)(1,2-diamine) complexes. *J. Am. Chem. Soc.,* **2000**, *122* (27), 6510-6511; (d) Sandoval, C. A.; Ohkuma, T.; Muniz, K.; Noyori, R. Mechanism of asymmetric hydrogenation of ketones catalyzed by BINAP/1,2-diamine-Ruthenium(II) complexes. *J. Am. Chem. Soc.* **2003**, *125* (44), 13490-13503.

[6] (a) Schumacher, K.; Ravikovich, P. I.; Du Chesne, A.; Neimark, A. V.; Unger, K. K. Characterization of MCM-48 materials. *Langmuir* **2000**, *16* (10), 4648-4654; (b) Lai, C.-Y.; Trewyn, B. G.; Jeftinija, D. M.; Jeftinija, K.; Xu, S.; Jeftinija, S.; Lin, V. S.-Y. A mesoporous silica nanosphere-based carrier system with chemically removeable CdS nanoparticle caps for stimuli-responsive controlled release of neurotransmitters and drug molecules. *J. Am. Chem. Soc.* **2003,** *125* (15), 4451-4459.

[7] Slowing, I. I.; Trewyn, B. G.; .; Lin, V. S.-Y. Mesoporous silica nanoparticles for

intracellular delivery of membrane-impermeable proteins. *J. Am. Chem. Soc.* **2007**, *129* (40), 12976-12077.

[8] Xie, J-H.; Zhou, Z-T.; Kong, W-L.; Zhou, Q-L. Ru-catalyzed asymmetric hydrogenation of racemic aldehydes via dynamic kinetic resolution: Efficient synthesis of optically active primary alcohols. *J. Am. Chem. Soc.* **2007**, *129* (7), 1868-1869.

[9] Anwander, R.; Nagi, I.; Engelhardt, M. W.; Groeger, O.; Palm, C.; Roser, T. Surface characterization and functionalization of MCM-41 silicas via silazane silylation. *J. Phys. Chem. B* **2000**, *104* (15), 3532-3544.

[10] Adiam, A.; Moreau, J. J. E.; Wong C. M. M. Immobilization of rhodium complexes in chiral organic-inorganic hybrid materials. *Chirality* **2000**, *12* (5-6), 411-420.

CHAPTER 4

HYDROGEN STORAGE IN METAL-ORGANIC FRAMEWORKS

4.1 Introduction

With the dwindling fossil fuel reserve and escalating environmental impact from the current energy technologies, the world economy is in desperate need of alternative forms of energy. Generating energy from hydrogen- and oxygen-based fuel cells would relieve the world's, and more specifically, the US's demand on fossil fuels for transportation. Such a "hydrogen economy" would make the US less dependent on foreign oil and curb its world-leading output of CO_2 emissions.

The United States Department of Energy has set several goals for the hydrogen research community. On-board hydrogen storage systems for vehicles must be capable of powering an average sized car for a distance of 300 miles, a distance requiring 5 kg of onboard hydrogen storage.[1] The DOE set its numbers at 6.0 wt% and 45 g/L by the year 2010 and 9.0 wt% and 81 g/L by 2015.[2] More recently, the 2010 goal has been revised to 4.5 wt%. These numbers are calculated at near-ambient temperatures and applicable pressures (less than 100 bar).

Several methods are being studied to facilitate hydrogen storage for transportation requirements. One method relies on liquefaction of hydrogen gas which requires cryogenic temperatures and/or extremely high pressures. Compressed H_2 technologies have addressed storage of hydrogen at pressures of up to 700 bar. Another storage method receiving notable

consideration is storage of hydrogen by way of chemisorption. Such storage techniques often suffer from binding hydrogen too tightly. For example, metal hydrides such as $LaNi_5H_{6.5}$ must be at temperatures above 400 K to release hydrogen.[1] Physisorption techniques on carbon nanotubes and other porous materials often require very low temperatures to adequately store hydrogen.

Various metal-organic frameworks (MOFs) have been shown to successfully store hydrogen via physisorption. Metal-organic frameworks benefit from being highly porous, and having uniform and tunable pore sizes in addition to their well defined hydrogen occupation sites. The pores are often filled with various solvents used in preparations of the MOFs. Upon evacuation of the solvent from the pores of the MOFs, framework integrity can remain intact to allow guest molecules (H_2) to be readily adsorbed onto the porous structure.[3] H_2 is known to interact with both the secondary building unit (SBU) and the organic linkers of the MOF.

4.1.1 Effects of pore volume and surface area

Several factors affect the hydrogen storage abilities of a MOF. Much attention has been focused on preparing highly porous frameworks. The series of "MIL" MOFs have been reported by Ferey et al., including MOFs with pore sizes greater than 25 Å,[4] and the isostructural "IRMOF" series with progressively larger pores were reported by Yaghi et al.[5] Both systems are based on non-interpenetrated networks of carboxylate ligands with pore volumes greater than 1.5 cm^3/g, and in turn, absorb a large amount of hydrogen at high pressures: 6.01 wt% for MIL-101[4] and 6.7 wt% for IRMOF-20[6] at 77K. As highlighted by Zhou et al., large pore volumes and surface areas are necessary for high hydrogen saturation uptakes at 77 K.[7]

Yaghi et al prepared seven MOF materials and studied their sorption behavior at 77 K which leads to saturation at pressures between 25 and 80 bar with uptakes from 2.0 to 7.5 wt %[8]. The chosen MOFs represent a subset of well-characterized materials that exhibit some of the highest surface areas experimentally determined to date. Figure 4.1 shows the metal oxide secondary building units (SBUs) and the carboxylate links of the MOFs that were investigated. The isoreticular (IRMOF) series, IRMOF-1,-6,-11, and -20 are derived from linking the basic zinc acetate unit, $Zn_4O(CO_2)_6$, with linear ditopic carboxylates.[5a,9] MOF-177 uses the same SBU and instead uses a tritopic link BTB.[10] MOF-74 is constructed from infinite 3_1 (or 3_2) helical rods of composition $Zn[(O)_3(CO_2)_3]$, and HKUST-1[11] is composed of the $Cu_2(CO_2)_4$ paddlewheel SBU linked by benzene-1,3,5-tricarboxylate.[12]
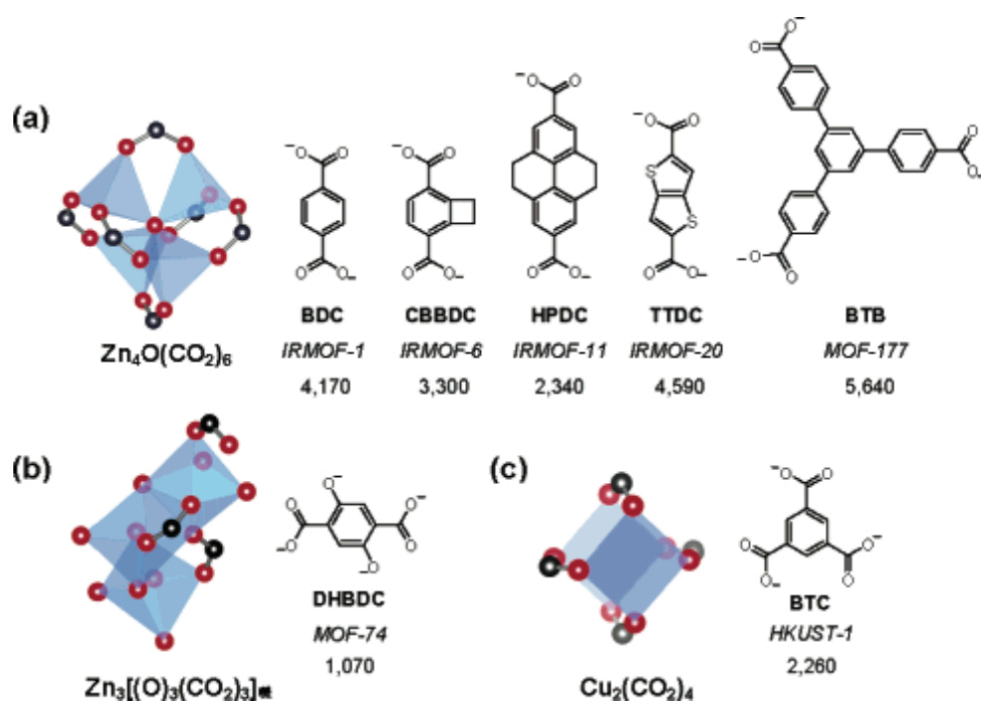
Figure 4.1 (a) $Zn_4O(CO_2)_6$-based MOFs in italics derived from the link in parentheses: *IRMOF-1* (BDC), *IRMOF-6* (CBBDC), *IRMOF-11* (HPDC), *IRMOF-20* (TTDC), and *MOF-177* (BTB). (b) *MOF-74*, based on $[Zn_3[(O)_3(CO_2)_3]]\infty$ 3_1 helices and DHBDC. (c) *HKUST-1*, based on $Cu_2(CO_2)_4$ paddlewheels and BTC. Langmuir surface areas (m^2/g) are given below each link for the corresponding MOF.

Figure 4.2 shows gravimetric H_2 adsorption studies performed on the above MOFs at 77 K and pressures of up to 90 bar. Saturation uptake in these MOFs correlates well with surface area. MOF-74 which has a Langmuir surface area of 1,070 m^2/g is capable of H_2 saturation (26 bar) of 2.3 wt %. For IRMOF-20 (SA: 4,590 m^2/g) and MOF-177 (SA: 5,640 m^2/g), saturation is reached between 70-80 bar, giving H_2 uptakes of 6.7 and 7.5 wt %, respectively (Figure 4.3). It is believed that this trend demonstrates the critical role of the organic linker and cannot be applied to MOFs mostly composed of metal oxide sorption sites.
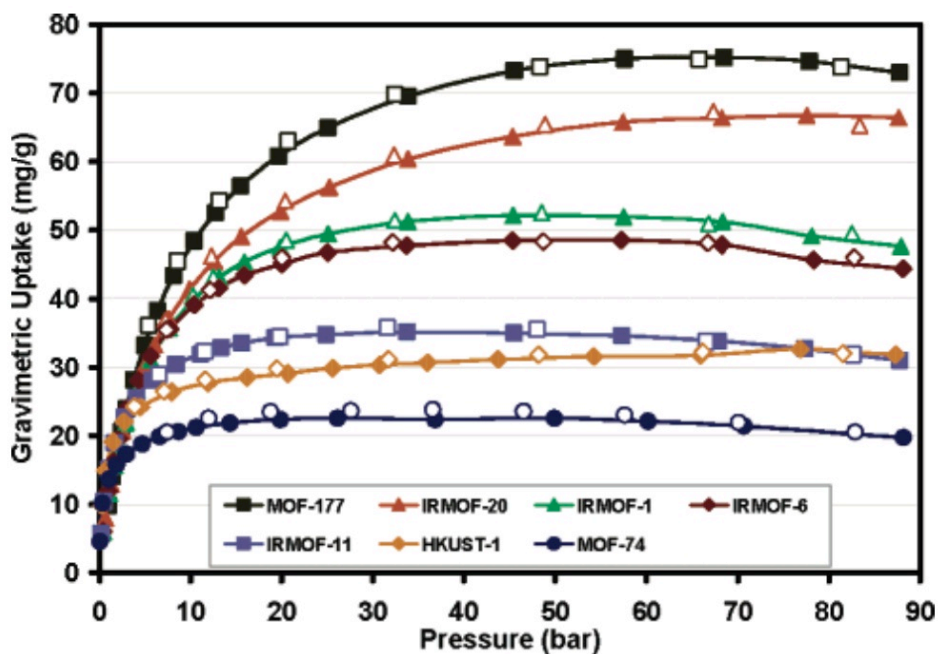
Figure 4.2 High-pressure H_2 isotherms for activated materials at 77 K in gravimetric units (mg/g) representing surface excess adsorption, that is, the amount of H_2 in excess of what would occupy the same free volume if the adsorbent was absent. Filled markers represent adsorption, open markers denote desorption.
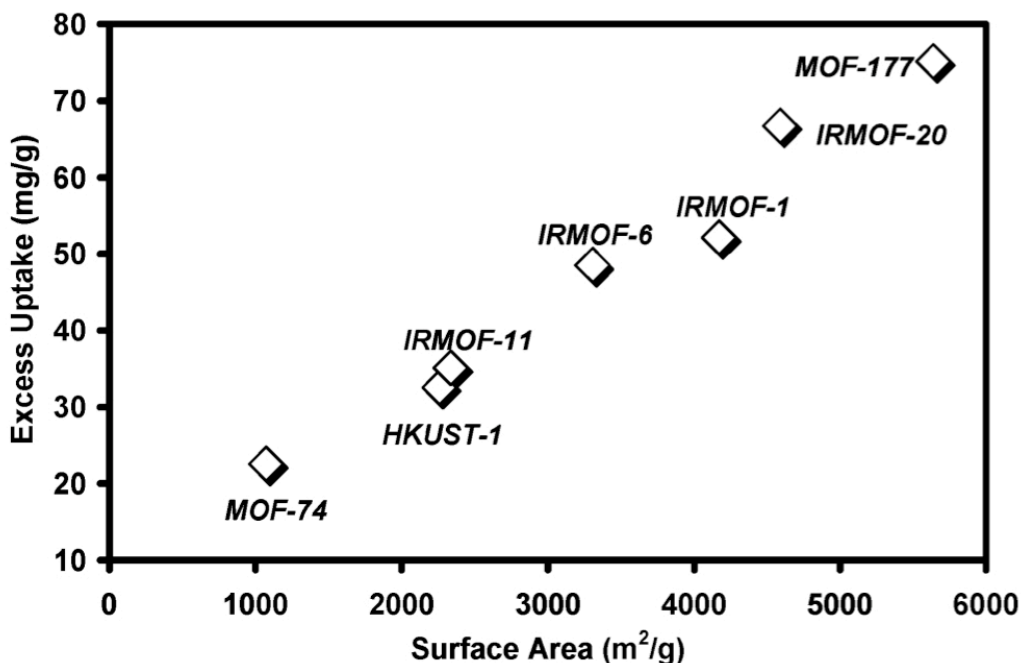
Figure 4.3 Saturation H_2 uptake plotted against Langmuir surface area.

When looking at the volumetric uptake of H_2 for these MOFs, an interesting trend was observed. At low pressures (Figure 4.4), Yaghi et al observed the three lowest surface area materials, MOF-74, HKUST-1, and IRMOF-11, displayed maximal uptake.[8b] When accounting for the density of the materials, the MOF materials are much more similar in their sorption capacities due to canceling effect of the different densities of the MOFs. IRMOF-20 and MOF-177 show the best uptake on volumetric basis (at high pressures) due to a combination of substantial H_2 uptake and moderate densities. Yaghi concluded that even with materials with extremely high porosity, volumetric storage density could be excellent because even highly porous materials can have small pores.
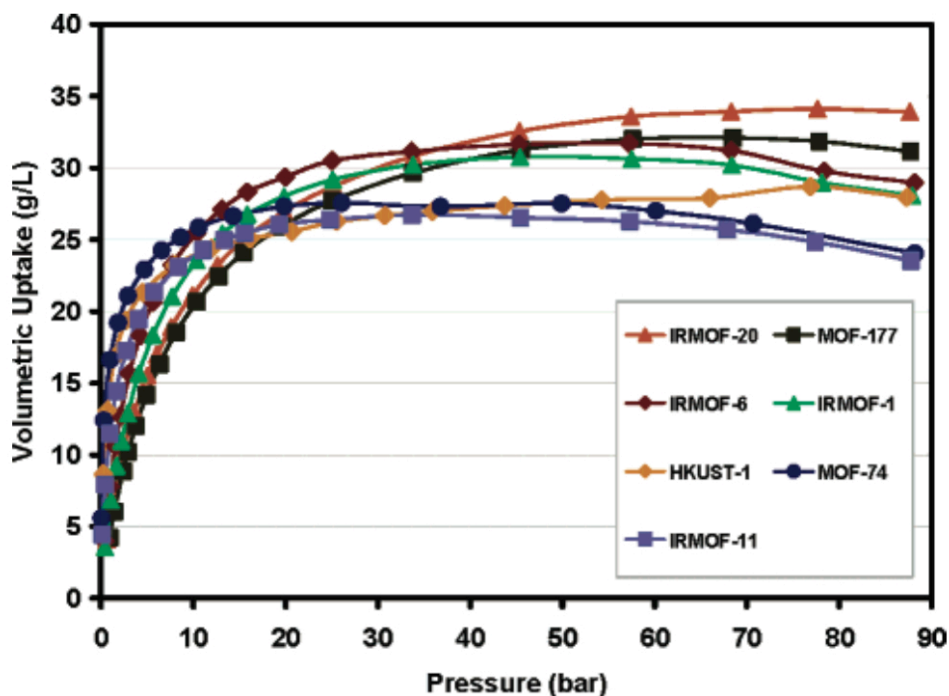
Figure 4.4 High-pressure H_2 isotherms for activated materials measured at 77 K in volumetric untis (g/L).

4.1.2 Effects of pore size and interpenetration

Pore size and interpenetration also play an integral part in the hydrogen uptake ability of a MOF. Studies indicate that smaller pores tend to take up hydrogen more effectively than MOFs with larger pores.[13] The ideal pore size seems to be on average, 4.5-5 Å or 2.8-3.3 Å when van der Waals radii of the atoms composing the pore walls are excluded; this size is comparable to the kinetic diameter of H_2 (~2.8Å).[7] Pores of this size maximize the interaction energy between H_2 and the multiple interaction sites within the MOF.

Interpenetrated MOFs are described as those with two or more networks physically entangling in the structure to subdivide larger pores of the MOFs into several smaller ones.[14] Since many MOFs are composed of aromatic organic linkers, interpenetration acts as an entrapment mechanism in which a hydrogen molecule is in close proximity with several

aromatic rings from the interpenetrating networks.[15]   Interpenetrated MOFs are much less

common than non-penetrated frameworks.[8,16]

Lin et al prepared two novel fourfold interpenetrated MOFs of cubic topology using

new aromatic-rich dicarboxylic acids 6,6'-dichloro-2,2'-diethoxy-1,1'-binaphthyl-4,4'-

dibenzoic acid (**L₁-H₂**) and 6,6'-dichloro-2,2'-dibenzyloxy-1,1'-binaphthyl-4,4'-dibenzoic

acid (**L₂-H₂**).   Single crystals of [Zn₄(μ₄-O)(**L₁₈**)₃(dmf)₂]•4DMF•3CH₃OH•2H₂O (**1a**) and

[Zn₄(μ₄-O)(**L₂**)₃]•5DMF•5C₂H₅OH•H₂O (**2a**) were obtained by treating Zn(ClO₄)₂ with **L₁**-

H₂ in DMF and MeOH or ZnI₂ with **L₁₉**-H₂ in DMF and EtOH in the presence of

dimethylaniline at 50 ºC for two days (Scheme 4.1).
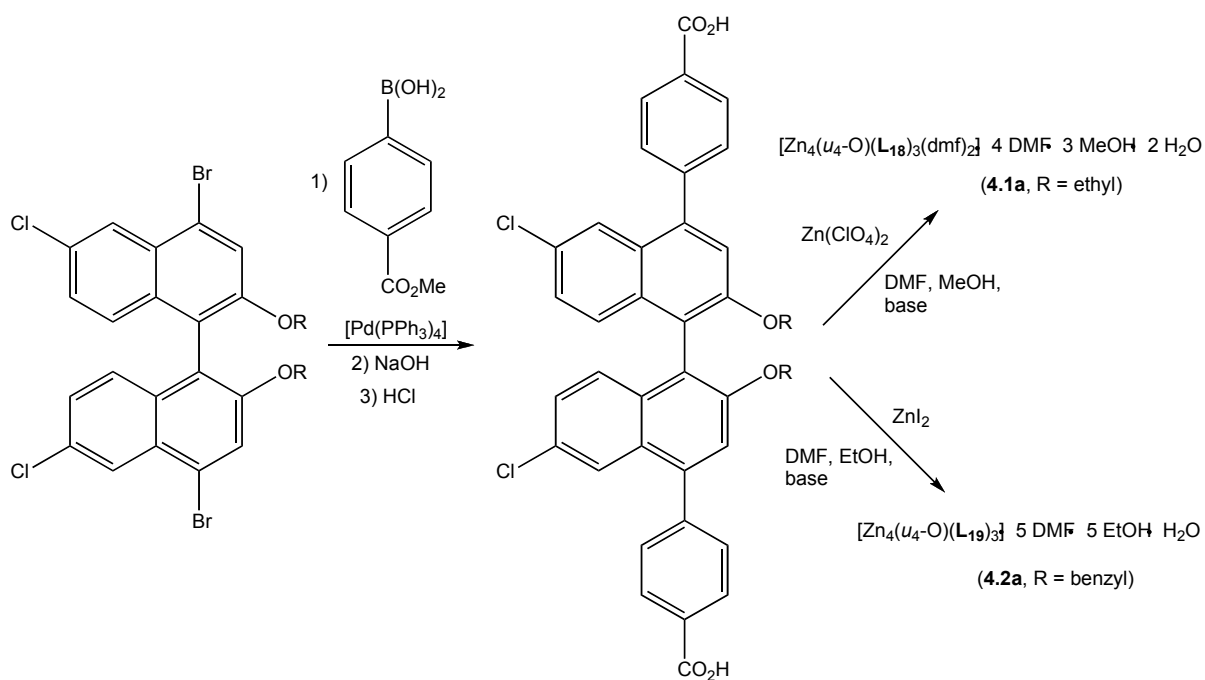
Scheme 4.1 Synthesis of **4.1a** and **4.2a**.

Compound **4.1a** adopts a 3D interpenetrating network structure that is built from two

distinct [Zn₄(μ-O)(**L₁₈**)₃(dmf)₂] clusters (Figure 4.5a).[13a]   Each type of [Zn₄(μ-

O)(**L₁₈**)₃(dmf)₂] cluster in **4.1a** is interlinked by the carboxylate groups of **L₁₈** ligands to

generate an extended neutral 3D network of a cubic topology that is built upon six-connected nodes. The 3D network of **4.1a** thus possesses very large cubic cavities of approximately 19 x 19 x 19 Å (Figure 4.5b). However, **4.1a** avoids extremely large void space by forming a fourfold interpenetrated structure (Figure 1c). Even after fourfold interpenetration, **4.1a** still possesses significant void space that is occupied by disordered DMF, MeOH, and H_2O guest molecules.

Compound **4.2a** adopts a similar fourfold 3D interpenetrating network structure that is built from C_3-symmetric $[Zn_4(\mu_4\text{-}O)(\mathbf{L_{19}})_3]$ clusters. Just like **4.1a**, the $[Zn_4(\mu_4\text{-}O)(\mathbf{L_{19}})_3]$ clusters in **4.2a** are linked by $\mathbf{L_{19}}$ ligands to form extended 3D network structure of cubic topology also similar to that of **4.1a**.

Powder X-ray diffraction studies indicate the long-range order of the framework for structures **4.1a** and **4.2a** was retained upon complete removal of the guest molecules. CO_2 uptake studies of **4.1a** and **4.2a** indicate a Type 1 behavior, which is indicative of microporous solids. Compounds **4.1a** and **4.2a** possess BET surface area of 502 and 396 m^2/g, respectively. The micropore volume for **4.1a** is 0.20 mL/g and for **4.2a** is 0.13mL/g. All above characteristics make compounds **4.1a** and **4.2a** feasible hosts for gas uptake. Hydrogen adsorption isotherms were taken in the 0.9-48 bar pressure range on **4.1a** and **4.2a** after excess solvent was removed from the frameworks by heating at 150 ºC for 1 h. The room temperature H_2 uptakes were calculated to be 1.12 wt % for **4.1a** and 0.98 wt % for **4.2a** at 48 bar which is comparable to MOFs with surface areas 5-10 times greater.[17] This finding indicates H_2 storage materials with lower surface areas such as these MOFs can efficiently store H_2 because the interpenetration strengthens the interaction between H_2

molecules and the framework by multiple contacts with several aromatic rings from the interpenetrating networks.
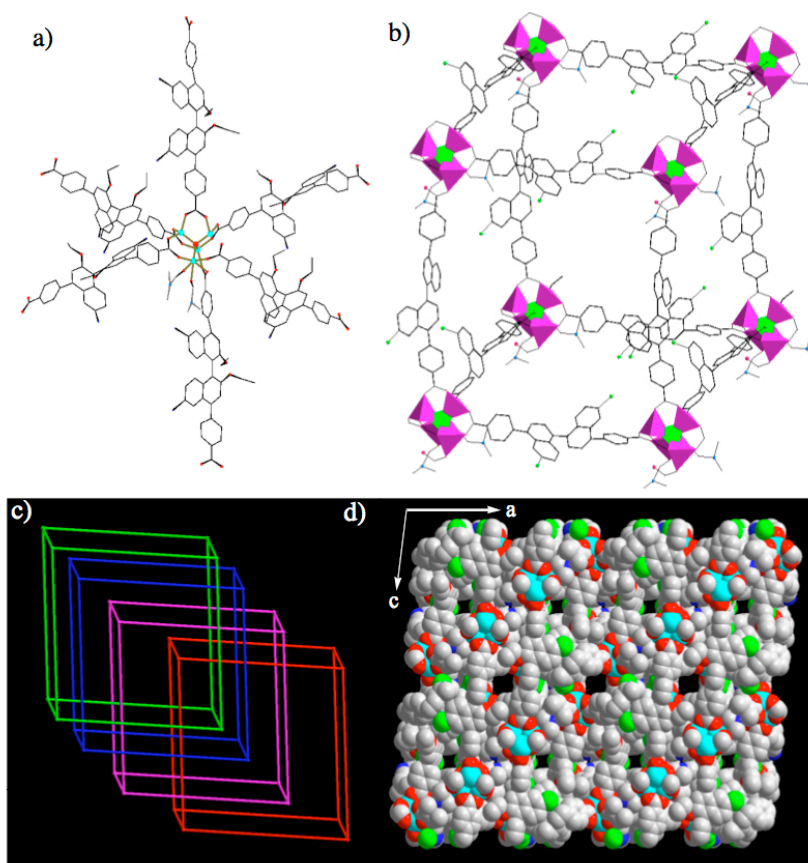
Figure 4.5 (a) A view of one of the $[Zn_4(\mu\text{-}O)(\mathbf{L_1})_3(dmf)_2]$ clusters of **1**; (b) A view of the cubic cavity formed by the 3D network (ethoxy groups omitted for clarity; the purple and green polyhedra represent the cluster building unit; (c) A schematic presentation of the fourfold interpenetration in **1**; (d) A space-filling model of **1** as viewed down the *b* axis (solvent molecules have been omitted); gray C, red O, blue N, green Cl, turquoise Zn.

Thermal activation of MOFs prior to gas uptake experiments has proven to increase the amount of hydrogen able to be adsorbed.[18] Activation of the MOF removes both free solvent from the within the channels as well the solvent molecules coordinatively bound to the metal centers or the metals contained within the SBUs. Removal of solvent ligands from the metals with a MOF leaves the unsaturated metal center (UMC) exposed on the interior

surfaces and open to hydrogen interaction. Incorporation of UMCs into a MOF offers a viable method to increase hydrogen uptake.

Chen et al. prepared MOF-505 by way of solvothermal reaction of 3,3',5,5'-buphenyltetracarboxylic acid (H_4bptc) and $Cu(NO_3)_2 \cdot 2.5H_2O$ and DMF/EtOH/H_2O. The compound was formulated to be $[Cu_2(bptc)(H_2O)_2(dmf)_3(H_2O)]$.[18a] To determine whether the framework structure is maintained upon evacuation of the pores, gas sorption isotherms were obtained using an instrument capable of measuring the change in mass of samples. MOF-505 was activated by washing in acetone to exchange DMF guest molecules. The resulting blue-green solid was loaded onto the instrument and was evacuated in three stages (I-III), with both weight loss, color change, and gas uptake being recorded. Stage I consists of evacuation ($<10^{-3}$ Torr) and 42% weight loss, change in color to light blue. Stage 2 consisted of heating the sample to 70 °C for 15 h under vacuum to give 5.3% weight loss and produced a dark blue colored material. Stage III heated sample to 120 °C for 12h decreasing the weight 4.7%, turning the material a purple color.

Nitrogen and hydrogen isotherms were obtained at each of the activation stages (I-III) (Table 4.1). The nitrogen isotherms demonstrate reversible type-1 behavior indicative of permanent porosity. Each stage represents removal of non-coordinated guests which has two positive effects on adsorption capacity: a decrease in sample mass and an increase in available micropore volume and specific surface area.

Removal of the water ligands axially bound to the copper centers also increases micropore volume and specific surface area and in addition, introduces open metal sites that enhance hydrogen-framework interaction. Stage I yields an initial hydrogen uptake of 14.1 mg/g (1.41 wt % H_2). The second activation step removes an additional 5.3 wt % (partial

dehydration) and increases the H_2 uptake by 5.6 mg/g (19.7 mg/g, 1.97 wt % H_2). Further removal of 4.7 wt % at Stage III (complete dehydration) increases the hydrogen uptake capacity by an additional 5.0 mg/g tp 24.7 mg/g or 2.47 wt %. Stage I yields an initial increase in H_2 uptake of 0.34 mg/g per percent mass loss whereas the last two activation steps (Stages II and III, dehydration with loss of six water molecules per Cu_2bptc formula unit) show a corresponding increase of 1.06 mg/g per percent mass loss. At stage I, the H_2 uptake is 14.1 mg/g while the fully activated material at Stage III containing open metal sites displays an uptake nearly twice as high (24.7 mg/g) despite only a 10 % mass loss.

4.1.3 Effects of bridging ligands

Consideration must also be given to the structure and functionalization of the ligands contained within a MOF. Roswell et al. shows that an increase in the aromaticity of the organic linkers may lead to a dramatic increase in hydrogen uptake.[5] This study includes measurements performed on a set of MOF materials in which the $Zn_4O(CO_2)_6$ cluster is linked by chemically diverse organic units. The internal surface area and the number of rings in the organic linker are thought to increase the ability of the MOFs to store hydrogen.

Five materials were prepared from the caboxylate links shown in Figure 4.6. The IRMOFs studied include IRMOFs-1, -8, -11[9], and more recent compounds MOF-177[10] and IRMOF-18.[5] These materials in particular were chosen for their large surface areas and subtle chemical diversity. Each framework is constructed by octahedrally linking $Zn_4O(CO_2)_6$ clusters with organic units. As a result, the surface sites on the inorganic component should be identical in each case, and any difference in hydrogen capacity can be attributed to differences in the organic units.
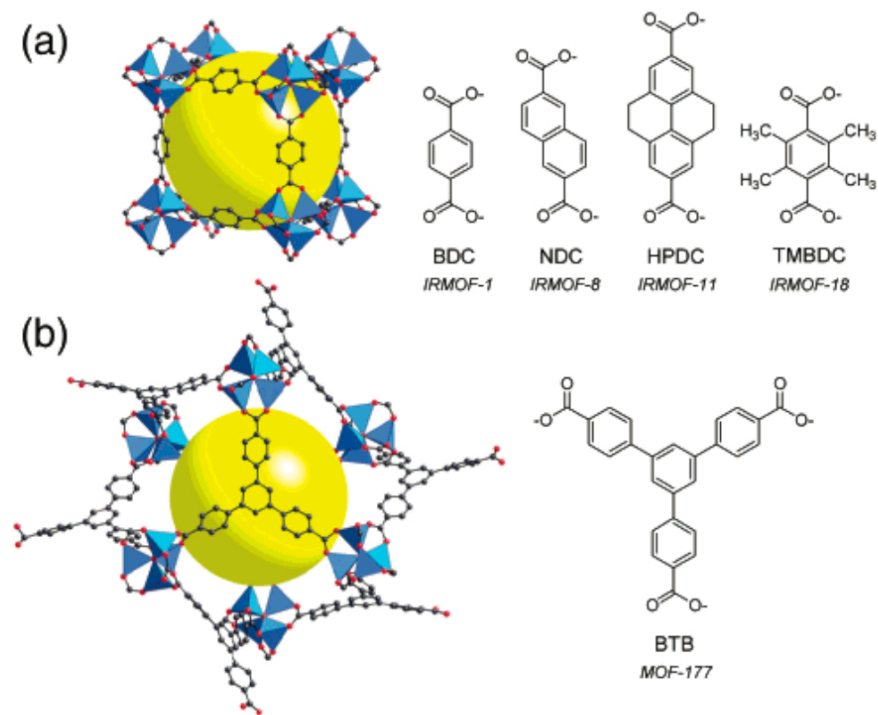
Figure 4.6 (a) Isoreticular metal organic frameworks, $Zn_4O(L)_3$, are constructed by linking zinc oxide clusters with linear carboxylates **L** such as those shown. (b) The structure of MOF-177, $Zn_4O(BTB)_2$, is formed by linking the same clusters with a trigonal carboxylate. The large void regions are illustrated by yellow spheres with diameters equal to the distance of separation between the frameworks' van der Waals surfaces.

The materials were activated by exchanging the guest solvent molecules with chloroform followed by evacuation and then subjected to N_2 and H_2 adsorption experiments. At the highest pressure achieved in these experiments (~750 Torr), the maximum uptake varies significantly ranging from 4.2 H_2 molecules for IRMOF-18 to 9.3 molecules for IRMOF-11 (Table 4.1). Quantitatively, the maximum uptake scales with the number of organic rings per unit formula. In addition, when comparing IRMOFs-1 and -18 whose organic linkers differ only by the pendant methyl groups on the phenylene spacer, similar adorption results are obtained. The slight difference in gravimetric capacity of H_2 is mainly due to their difference in density.

Table 4.1 Sorption Data for MOFs measured Gravimetrically at 77 K.

Material	N_2 (mg/g)	SA^a (m^2/g)	H_2^b (mg/g)	H_2 per f.u.^{b}
IRMOF-1	965	3362	13.2	5.0
IRMOF-8	421	1466	15.0	6.9
IRMOF-11	548	1911	16.2	9.3
IRMOF-18	431	1501	8.9	4.2
MOF-177	1300	4526	12.5	7.1

^{a}Calculated assuming a monolayer coverage of close-packed N_2 with a cross-sectional area of 16.2 Å^2/molecule. ^{b}At 1 atm, f.u. = Zn_4OL_x formula unit.

Hydrogen isotherms for the activated materials were measured gravimetrically at 77 K. (Figure 4.7). The isotherms do not exhibit hysteresis which confirms the hydrogen interaction with the MOFs is a physisorption. The large initial slopes for IRMOFs-11, and -8 indicate a higher affinity for hydrogen when compared to the other MOFs tested. As shown in Figure 4.7 inset, complete uptake and desorption can be achieved in a matter of minutes at 77 K and can be repeated for a number of runs. This behavior is expected for such weak hydrogen-framework interaction.
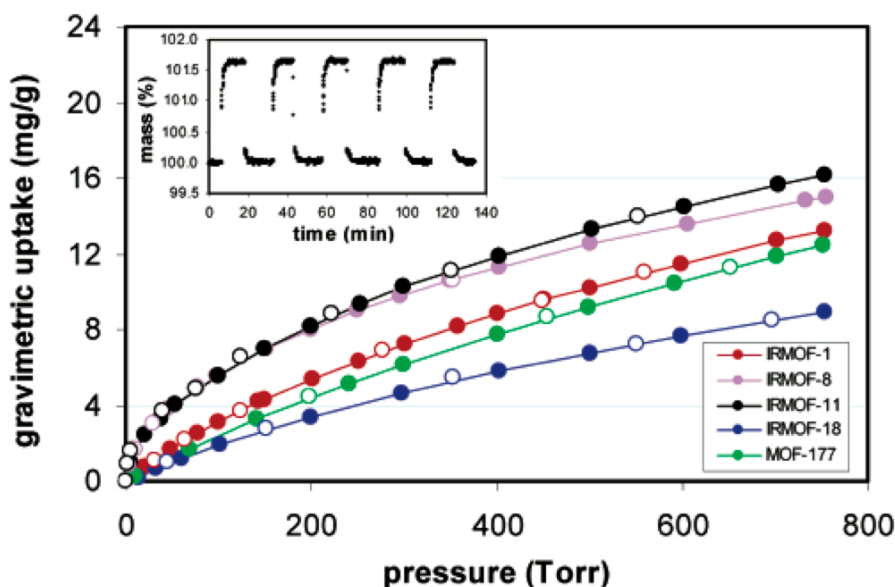
Figure 4.7 Hydrogen isotherms for the activated materials measured gravimetrically at 77 K(adsorption, filled circles; desorption, empty circles). The inset shows the time-dependent cycling of IRMOF-11 between 0 and 1 atm of H_2.

4.2 4,8-connected metal-organic frameworks

Metal-organic frameworks (MOFs) have emerged as a class of very promising hybrid functional materials due to the ability to tune their properties in a modular fashion.[19] As described earlier, a family of MOFs of the primitive cubic network (**pcu**) topology was systematically constructed from 6-connected $[Zn_4(\mu_4\text{-}O)(O_2CR)_6]$ secondary building units (SBUs) and 2-connected linear dicarboxylate bridging ligands of varied lengths to afford isoreticular porous materials with tunable pore/channel sizes, shapes, and functionalities.[20]

Carboxylate-bridged copper paddle-wheels represent another interesting SBU for the isoreticular synthesis of MOFs because of their enhanced stability over the $[Zn_4(\mu4\text{-}O)(O_2CR)_6]$ SBUs. Indeed, the HKUST-1 with the framework formula of $[Cu_3(BTC)_2(H_2O)_3]$ that is built from copper paddle-wheel SBUs still serves as a benchmark material in both stability and gas uptake capacity.[12] However, the lower connectivity (4) of the paddle-wheel SBU makes it difficult to implement the isoreticular synthesis. For example, when copper paddle-wheels are combined with readily available linear dicarboxylate bridging ligands, 2-D networks are expected based on topological considerations.

We and others have recently demonstrated the ability to construct 4,4-connected MOFs of the PtS and related topology based on copper paddle-wheels and tetracarboxylate bridging ligands.[21,22] We are particularly interested in designing robust MOFs based on aromatics-rich bridging ligands for gas storage applications.[13a] The use of elongated aromatic tetracarboxylate bridging ligands has however led to severe framework distortion (breathing) of these MOFs upon solvent removal which significantly reduces the porosity and negatively impacts the gas uptake capacity.[4] This chapter describes a new strategy to rigidify the

frameworks by constructing 4,8-connected MOFs of the **scu** topology based on copper paddle-wheels and aromatics-rich octa-carboxylic acid bridging ligands.
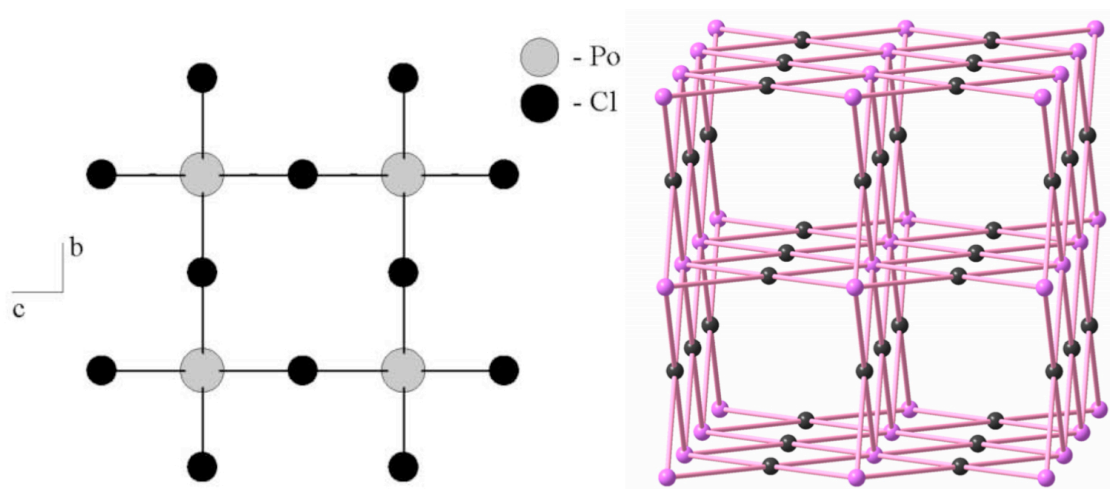
Figure 4.8 Representative structures of the rare **scu** topology.

4.3 Results and discussion

4.3.1 Synthesis and characterization of L48 and La48 ligands

The new 1,1'-binaphthyl-derived ligand L_{20}-H_8 of the L48 series was synthesized by a Pd-catalyzed Suzuki coupling between 4,4',6,6'-tetrabromo-2,2'-diethoxy-1,1'-binaphthyl and dimethyl-5-(pinacolboryl)isophthalate followed by base-catalyzed hydrolysis (Scheme 4.2). L_{21}-H_8 was obtained by deprotecting the ethoxy groups of the methyl ester of L_{20}-H_8. L_{22}-H_8 was prepared in a similar manner, starting with the 2,2'-benzyl protected tetra-bromo compound in place of the 2,2'-ethoxy protected compound (Scheme 4.3).

The new 1,1'-binaphthyl-derived ligand L_{24}-H_8 of the La48 series was synthesized by starting from a Pd-catalyzed Sonogashira coupling between 4,4',6,6'-tetrabromo-2,2'-diethoxy-1,1'-binaphthyl and trimethylsilylacetylene followed by base-catalyzed deprotection (Scheme 4.4). The deprotected 4,4'6,6'-tetraacetylene intermediate was then

reacted with dimethyl 5-bromoisophtalate under Sonogashira coupling conditions. The resulting methyl ester was then either directly hydrolyzed to give the 2,2'-ethoxy-protected octa-acid compound (**L₂₃**-H₈) or subjected to a series of deprotection and hydrolysis steps to give 2,2'-hydroxy compound (**L₂₄**-H₈). **L₆**-H₈ was prepared in a similar manner, starting with the 2,2'-benzyl protected tetra-bromo compound in place of the 2,2'-ethoxy protected compound (Scheme 4.5). All the intermediates and ligands were characterized by NMR spectroscopy and high resolution mass spectrometry. Representative ¹H NMR spectra of the methyl ester of **L₂₂**-Me₈ and **L₂₂**-H₈ are shown in Figure 4.9 and Figure 4.10, respectively.
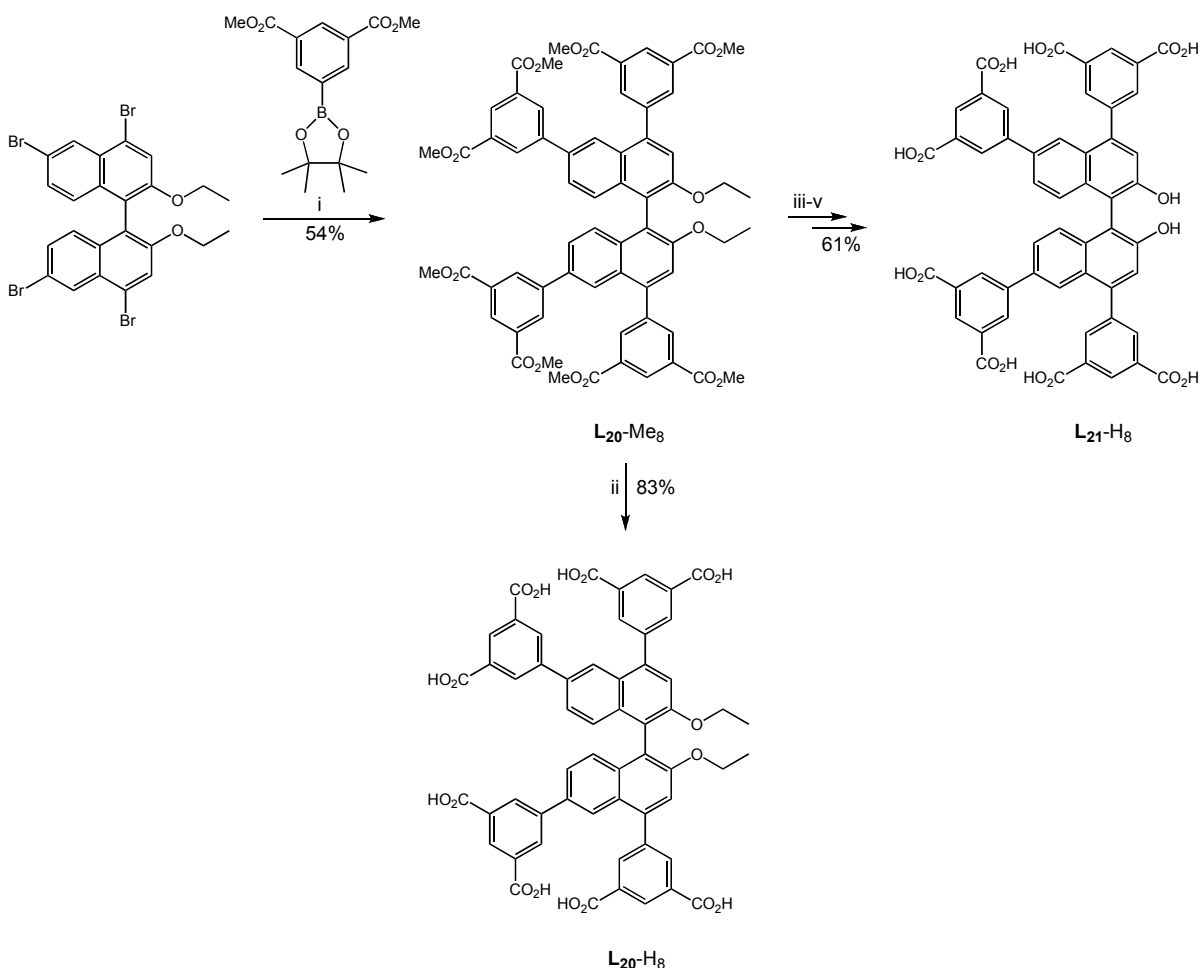
Scheme 4.2 Reagents and conditions: (i) Pd(PPh₃)₄, CsF, DME, 95ºC, 3d; (ii) 2M NaOH, THF, MeOH, 70 ºC, 24h; (iii) BBr₃, CH₂Cl₂, 0 ºC to RT, 24h; (iv) cat. H₂SO₄, MeOH, 70 ºC, 4h; (v) 2M NaOH, THF, MeOH, 70 ºC, 24h.
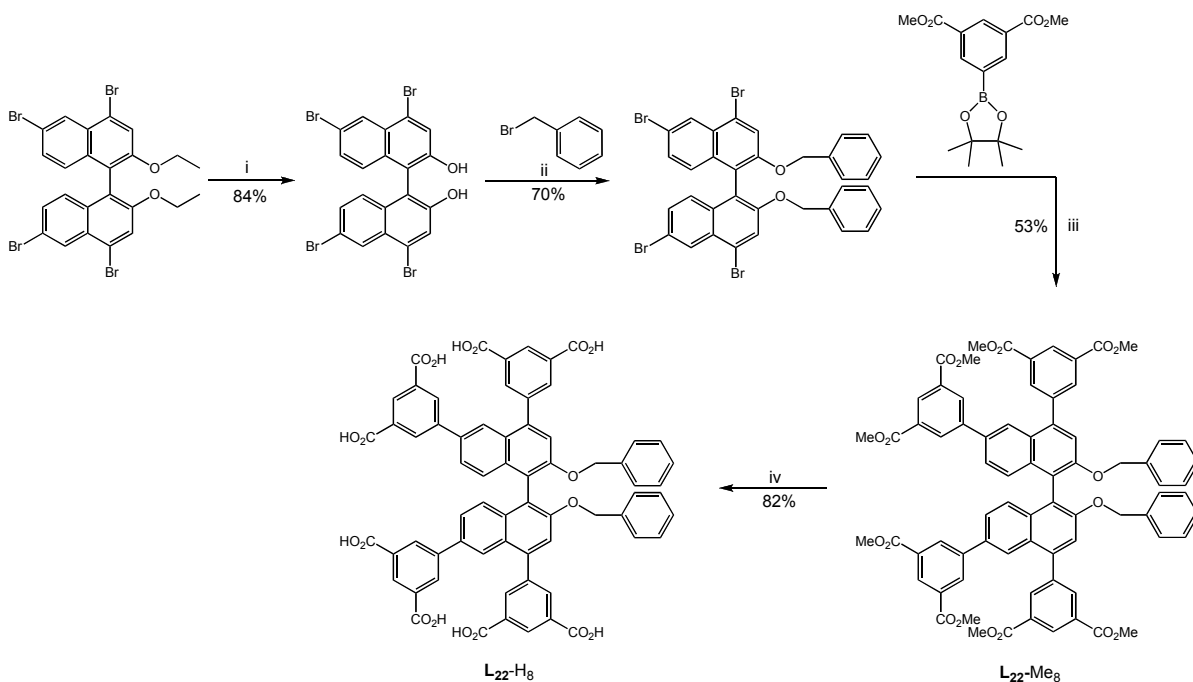
Scheme 4.3 Reagents and conditions: (i) BBr$_3$, CH$_2$Cl$_2$, 0 °C to RT (ii) KOH, acetone, reflux, 2h; (iii) Pd(PPh$_3$)$_4$, CsF, DME, 95ºC, 3d; (iv) 2M NaOH, THF, MeOH, 70 ºC, 24h.
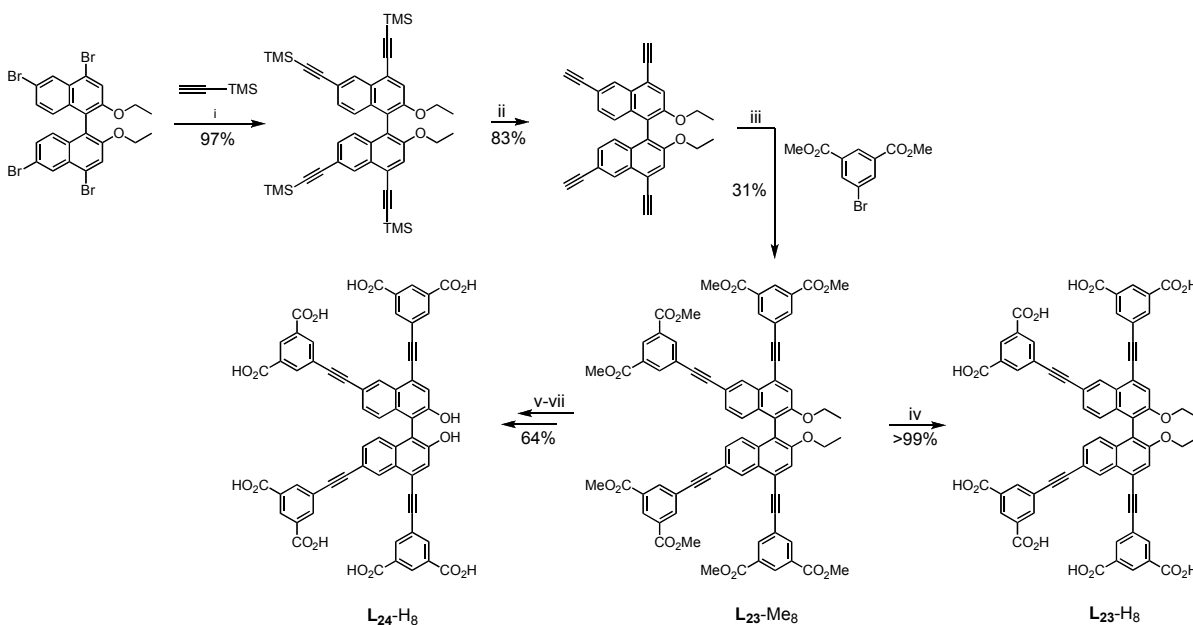
Scheme 4.4 Reagents and conditions: (i) Pd(PPh$_3$)$_2$Cl$_2$, CuI, NEt$_3$, toluene, 100 ºC, 3d; (ii) K$_2$CO$_3$, THF, MeOH, RT. 1.5 h; (iii) Pd(PPh$_3$)$_2$Cl$_2$, CuI, NEt$_3$, THF, 70 ºC, 3d (iv) 2M NaOH, THF, MeOH, 70 ºC, 24h; (v) BBr$_3$, CH$_2$Cl$_2$, 0 ºC to RT, 24h; (vi) cat. H$_2$SO$_4$, MeOH, 70 ºC, 4h; (vii) 2M NaOH, THF, MeOH, 70 ºC, 24h.
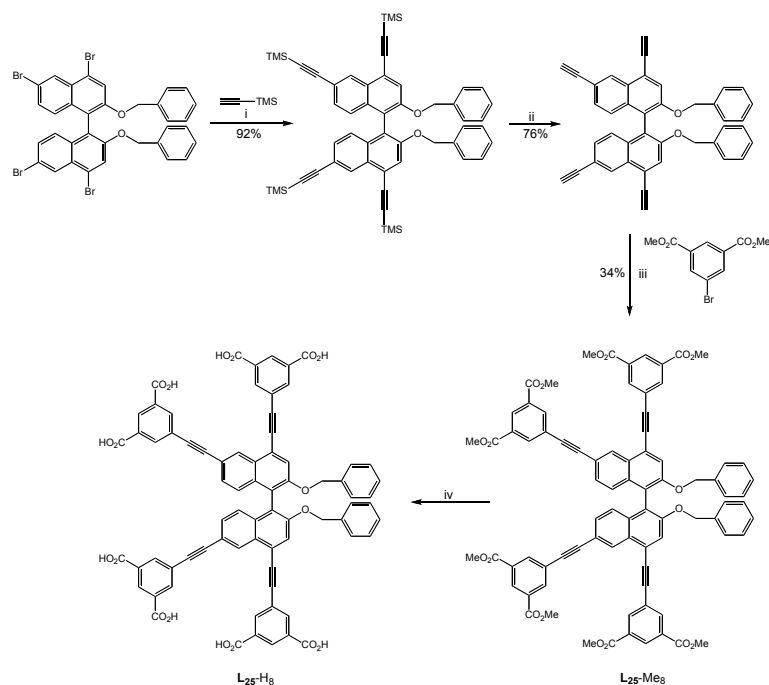
Scheme 4.5 Reagents and conditions: (i) Pd(PPh₃)₂Cl₂, CuI, NEt₃, toluene, 100 ºC, 3d; (ii) K₂CO₃, THF, MeOH, RT. 1.5 h; (iii) Pd(PPh₃)₂Cl₂, CuI, NEt₃, THF, 70 ºC, 3d (iv) 2M NaOH, THF, MeOH, 70 ºC, 24h.
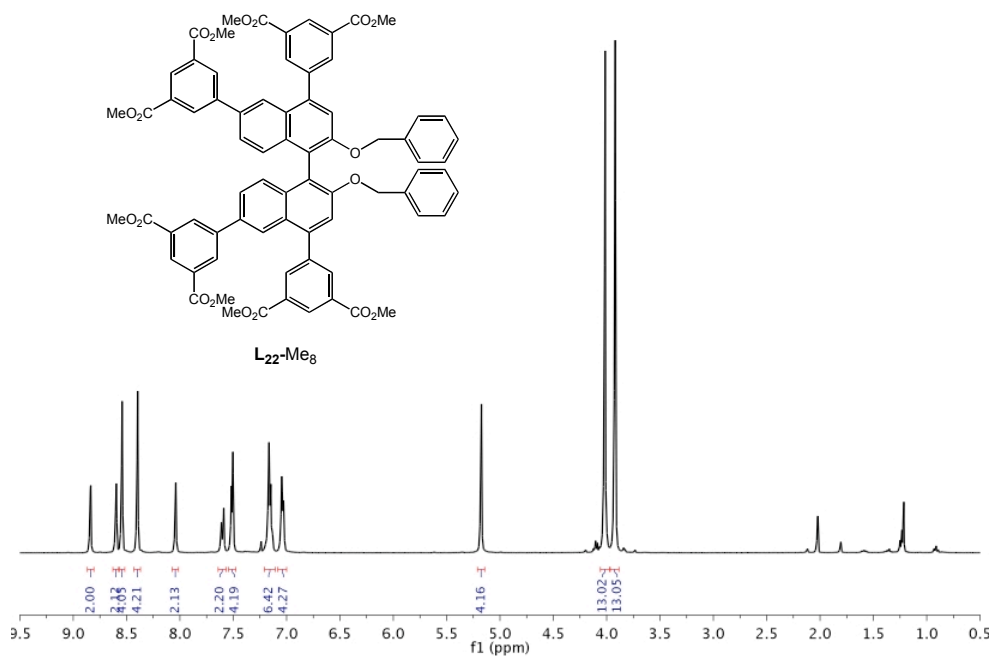
Figure 4.9 ¹H NMR of **L₂₂**-Me₈.
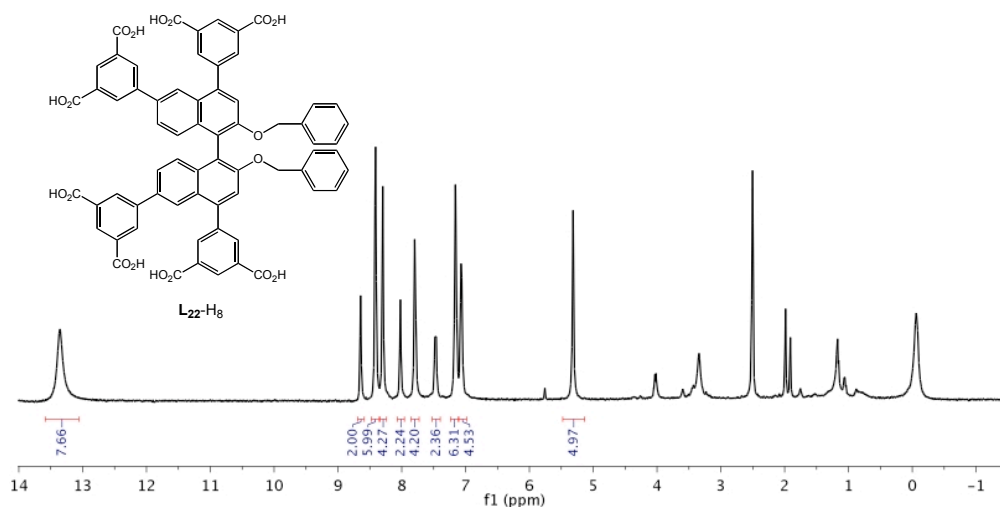
Figure 4.10 ^{1}H NMR of **L₂₂**-H₈.

4.3.2 Synthesis and characterization of 4,8-connected MOFs

When treated with Cu(II) salts in DEF or DMF at 80 ºC, single crystals of

$[Cu_4(L_{20})(H_2O)_4]\cdot12DEF\cdot2H_2O$ (**4.1**), $[Cu_4(L_{21})(H_2O)_4]\cdot14DMF\cdot2H_2O$ (**4.2**), and

$[Cu_4(L_{22})(H_2O)_4]\cdot8DMF\cdot13H_2O$ (**4.3**), $[Cu_4(L_{23})(H_2O)_4]\cdot20DEF$ (**4.4**),

$[Cu_4(L_{24})(H_2O)_4]\cdot16DMF\cdot H_2O$ (**4.5**), and $[Cu_4(L_{25})(H_2O)_4]\cdot14DMF$ (**4.6**) were obtained

(Scheme 4.6). The formulae for **4.1-4.6** were established by TGA analyses, ^{1}H NMR

spectroscopy, and single crystal X-ray structure determination. To ensure consistent results,

each sample was treated in exactly the same way for both TGA and ^{1}H NMR experiments

(Figures 4.11-4.12 and 4.13-4.19, respectively). Fresh crystals were harvested by quick

filtration, and briefly dried on filter paper under air. The sample was then divided and loaded

into screw-capped vial with CD_3OD or the sample tray in TGA. The organic solvent inside

the crystals is either DEF or DMF which has been exchanged by CD_3OD, and its exact

amount was determined by calibrating against the internal standard, mesitylene. The total

amounts of the solvents were obtained by TGA, the amount of water molecules was

calculated by subtracting DEF/DMF from the total solvent amount. The framework

structures of **4.1** to **4.6** were unambiguously determined by single-crystal X-ray diffraction

studies.

$[Cu_4(\mathbf{L_{20}})(H_2O)_4] \cdot (DEF)_{12} \cdot (H_2O)_2$

4.1

$[Cu_4(\mathbf{L_{21}})(H_2O)_4] \cdot (DMF)_{14} \cdot (H_2O)_2$

4.2

$[Cu_4(\mathbf{L_{22}})(H_2O)_4] \cdot (DMF)_8 \cdot (H_2O)_{13}$

4.3

(R=Et, **L₂₀**-H$_8$; R=H, **L₂₁**-H$_8$; R=Bz, **L₂₂**-H$_8$)

$[Cu_4(\mathbf{L_{23}})(H_2O)_4] \cdot (DEF)_{20}$

4.4

$[Cu_4(\mathbf{L_{24}})(H_2O)_4] \cdot (DMF)_{16} \cdot (H_2O)_5$

4.5

$[Cu_4(\mathbf{L_{25}})(H_2O)_4] \cdot (DMF)_{14}$

4.6
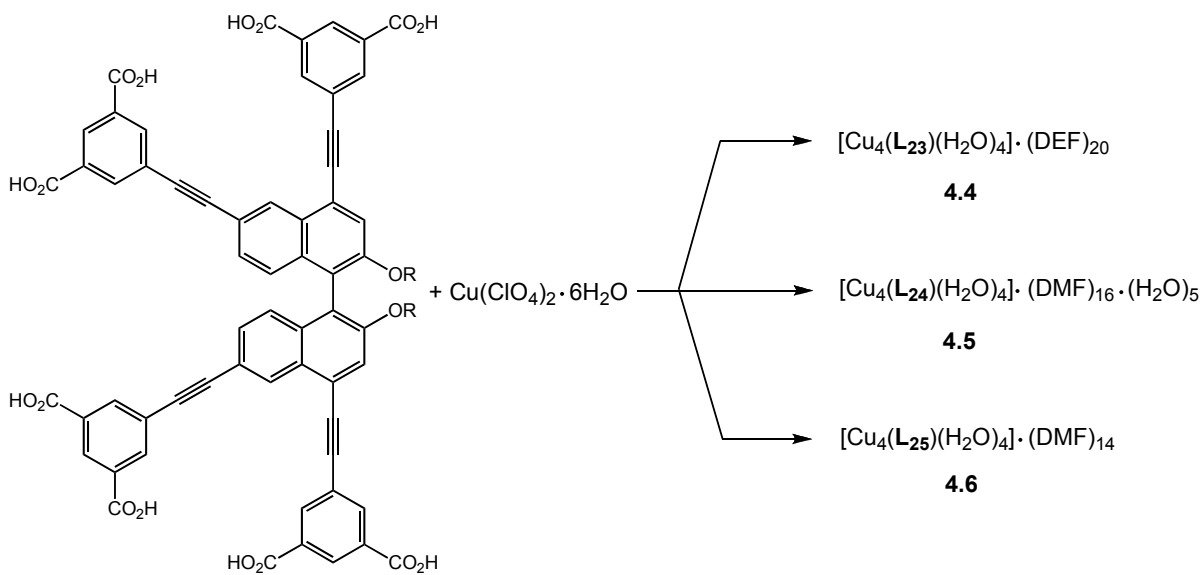
(R=Et, **L₂₃**-H$_8$; R=H, **L₂₄**-H$_8$; R=Bz, **L₂₅**-H$_8$)

Scheme 4.6 Crystal growth of **4.1-4.6**.
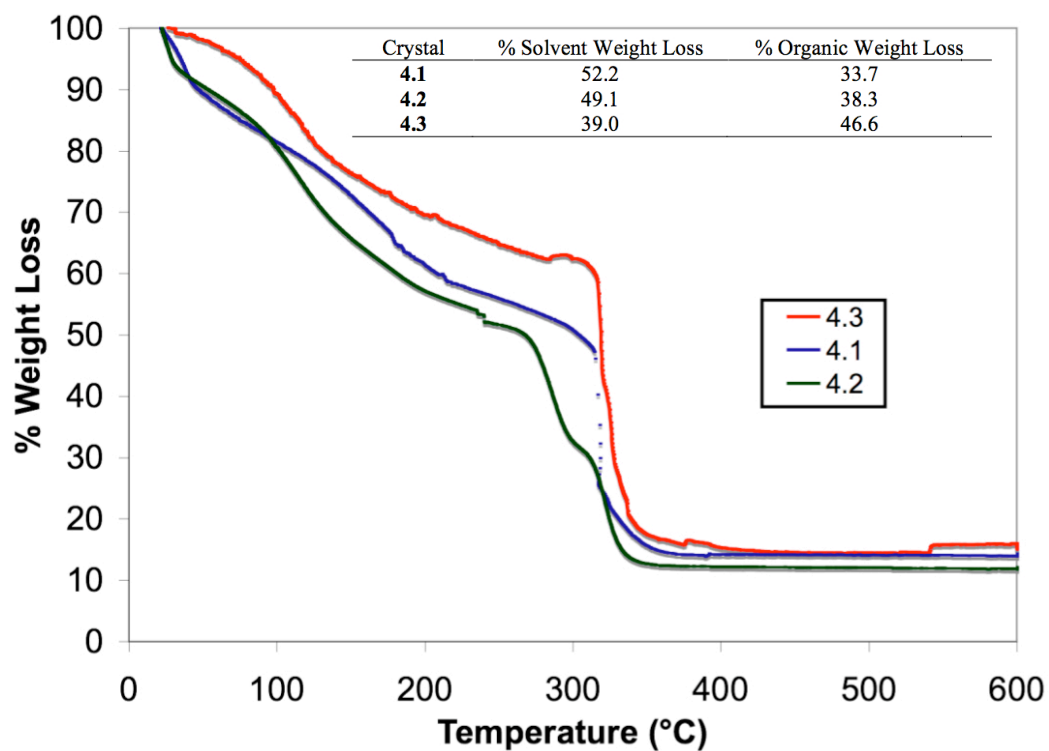
Figure 4.11 Thermogravimetric analyses for **4.1-4.3**.
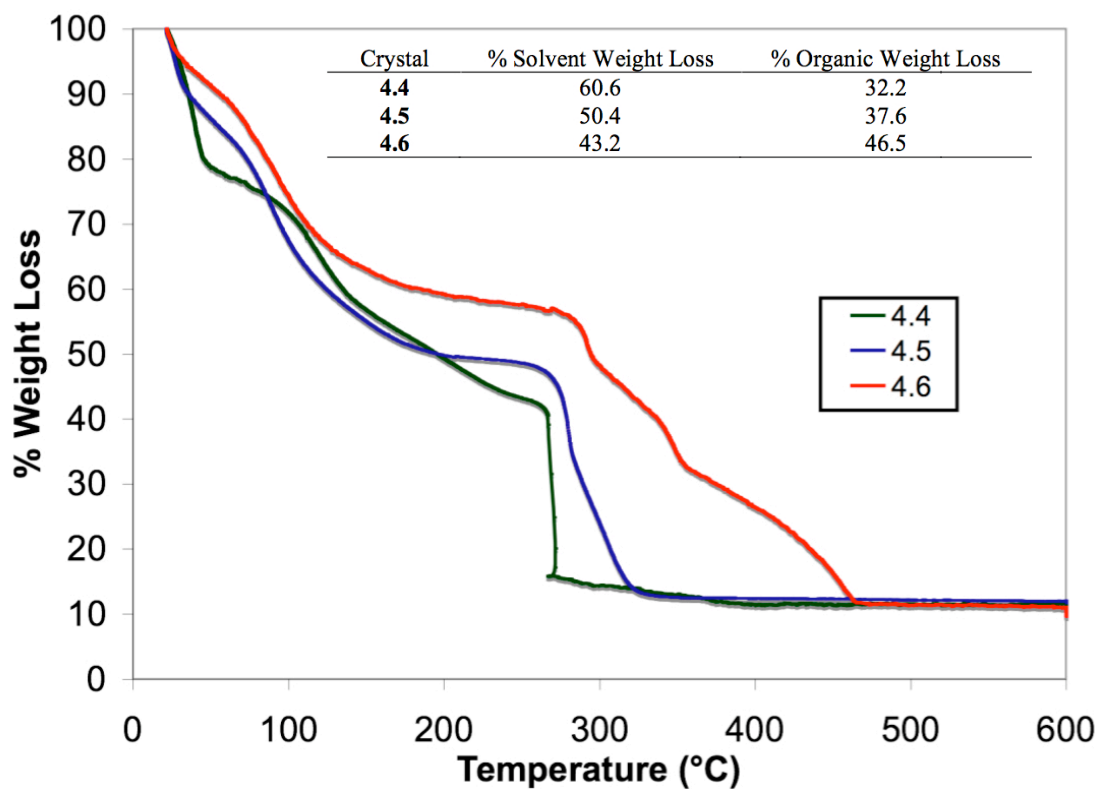
Figure 4.12 Thermogravimetric analyses (TGA) measurements for **4.4-4.6.**

117

$W_{crystal}$(mg)	17.4
W_{Mes}(mg)	8.6
W_{DEF} (mg) (From NMR)	8.3
W_{DEF} %	48.2%
$W_{(DEF+H_2O)}$% (From TGA)	52.2%
W_{H_2O}%	4.0%
Formula (**4.1**)	
$[Cu_4(R\text{-}L_{20})(H_2O)_4]\cdot12DEF\cdot2H_2O$	
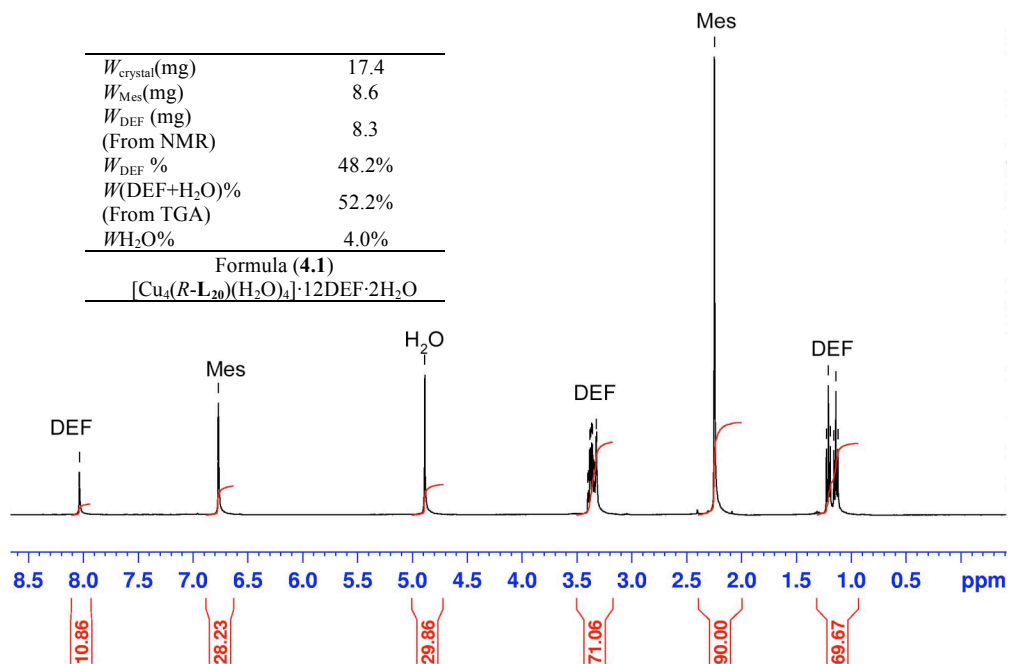
Figure 4.13 ^{1}H NMR spectroscopic determination of solvent content in **4.1**, mesitylene (Mes) was added as an internal standard.

$W_{crystal}$(mg)	15.3
W_{Mes}(mg)	8.6
W_{DEF} (mg) (From NMR)	7.1
W_{DEF} %	46%
$W_{(DEF+H_2O)}$% (From TGA)	50.9%
W_{H_2O}%	4.3%
Formula (**4.1'**)	
$[Cu_4(rac\text{-}L_{20})(H_2O)_4]\cdot12DEF\cdot2H_2O$	
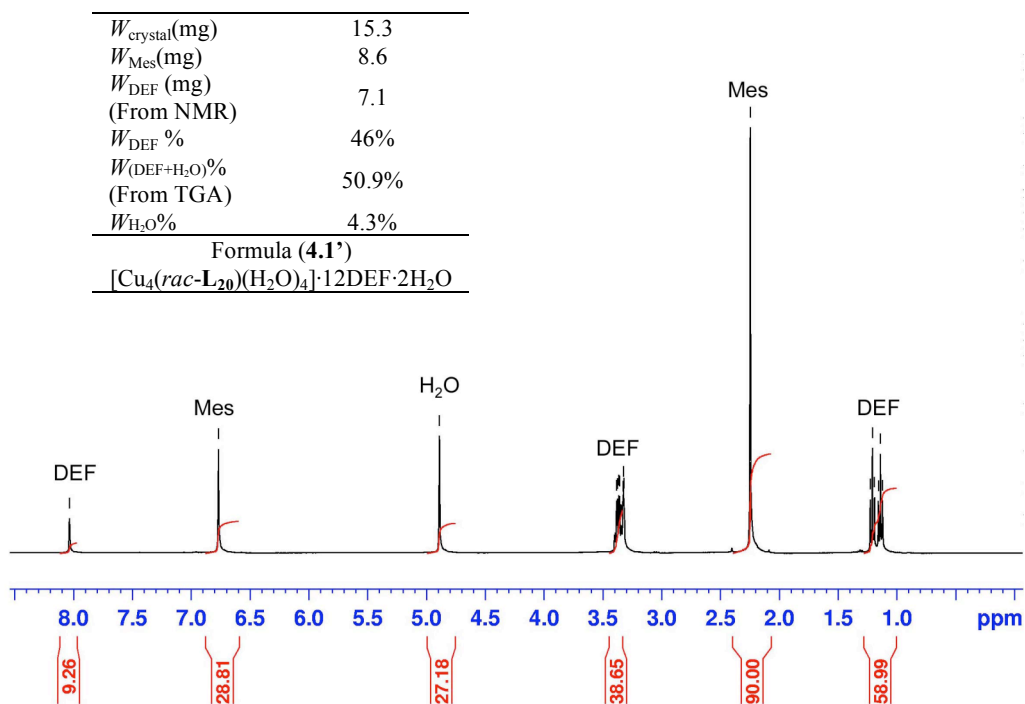
Figure 4.14 ^{1}H NMR spectroscopic determination of solvent content in **4.1'**, mesitylene (Mes) was added as an internal standard.

$W_{crystal}$(mg)	11.9
W_{Mes}(mg)	8.6
W_{DEF} (mg) (From NMR)	5.3
W_{DEF} %	44.6%
$W_{(DEF+H_2O)}$% (From TGA)	49.1%
W_{H_2O}%	4.4%
Formula (**4.2**)	
$[Cu_4(R\text{-}L_{21})(H_2O)_4]\cdot14DMF\cdot2H_2O$	
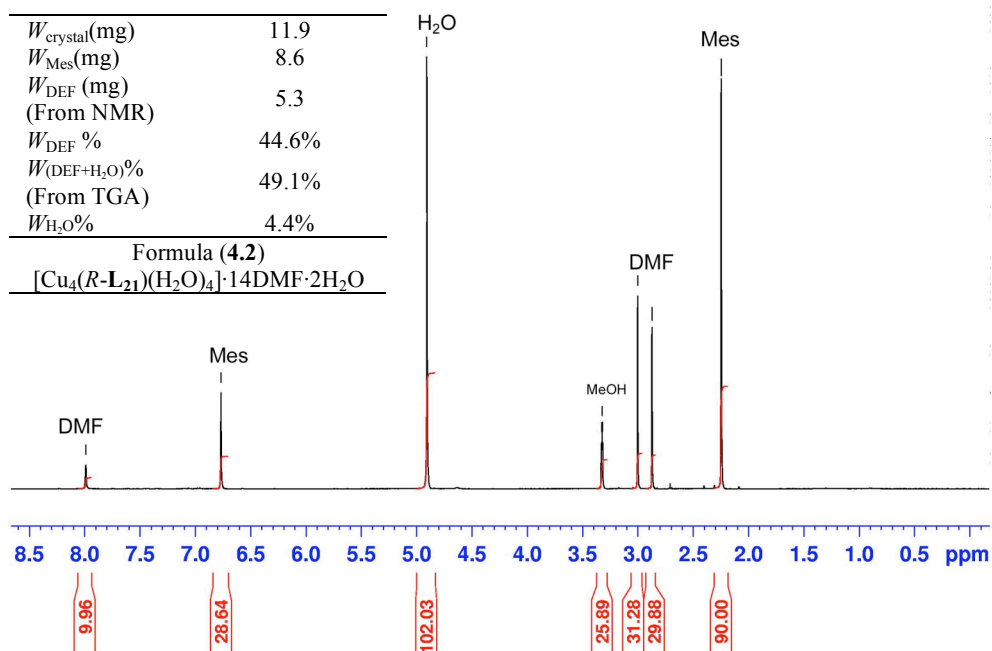
Figure 4.15 ^{1}H NMR spectroscopic determination of solvent content in **4.2**, mesitylene (Mes) was added as an internal standard.

$W_{crystal}$(mg)	20.14
W_{Mes}(mg)	8.6
W_{DEF} (mg) (From NMR)	5.22
W_{DEF} %	25.4
$W_{(DEF+H_2O)}$% (From TGA)	39.0%
W_{H_2O}%	13.6%
Formula (**4.3**)	
$[Cu_4(R\text{-}L_{22})(H_2O)_4]\cdot8DMF\cdot13H_2O$	
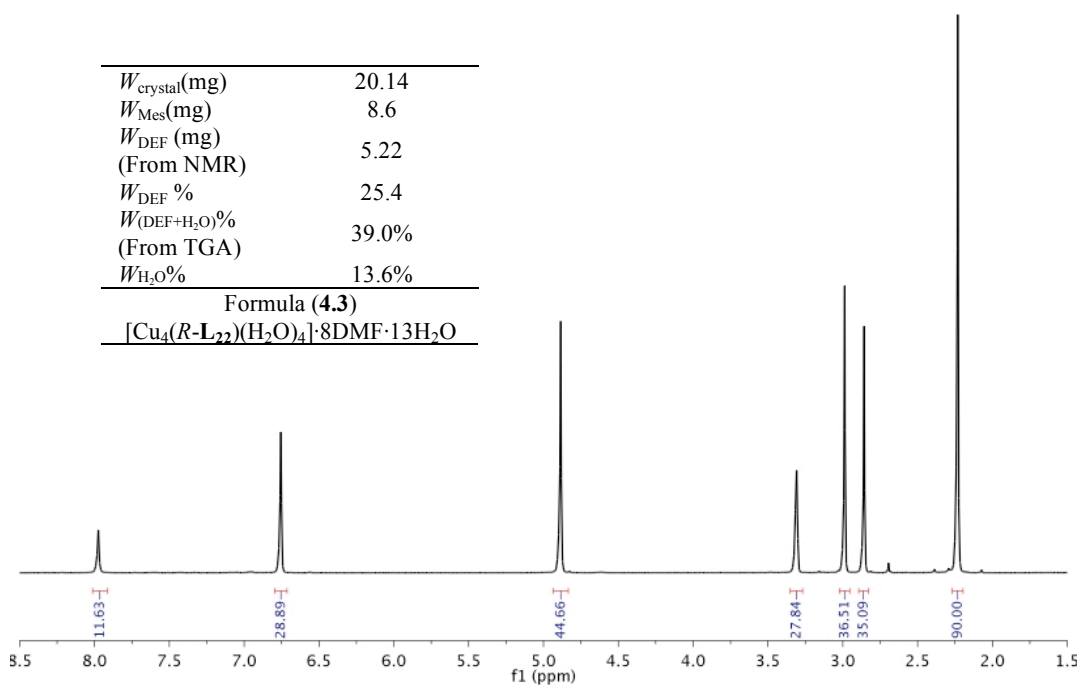
Figure 4.16 ^{1}H NMR spectroscopic determination of solvent content in **4.3**, mesitylene was added as an internal standard.

$W_{crystal}$(mg)	8.32
W_{Mes}(mg)	8.6
W_{DEF} (mg) (From NMR)	4.88
W_{DEF} %	58.7%
$W_{(DEF+H_2O)}$% (From TGA)	60.6%
W_{H_2O}%	1.9%
Formula (**4.4**)	
[Cu$_4$(R-**L$_{23}$**)(H$_2$O)$_4$]·20DEF	
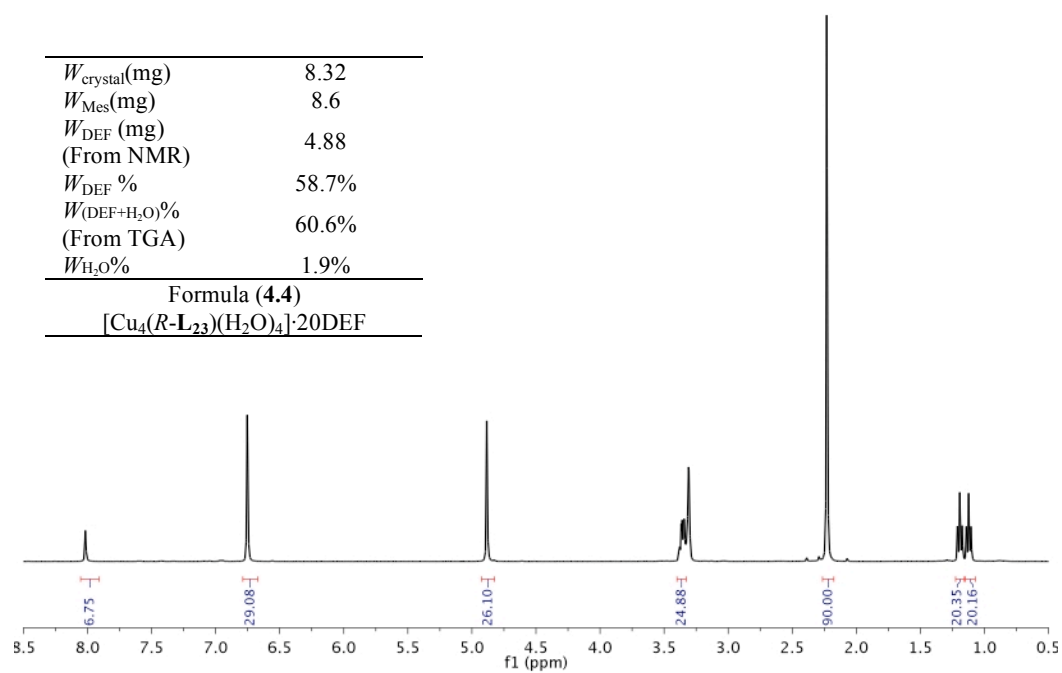
Figure 4.17 ^{1}H NMR spectroscopic determination of solvent content in **4.4**, mesitylene was added as an internal standard.

$W_{crystal}$(mg)	14.2
W_{Mes}(mg)	8.6
W_{DMF} (mg) (From NMR)	6.26
W_{DMF} %	44.1%
$W_{(DMF+H_2O)}$% (From TGA)	50.4%
W_{H_2O}%	6.3%
Formula (**4.5**)	
[Cu$_4$(R-**L$_{24}$**)(H$_2$O)$_4$]·16DMF·5H$_2$O	
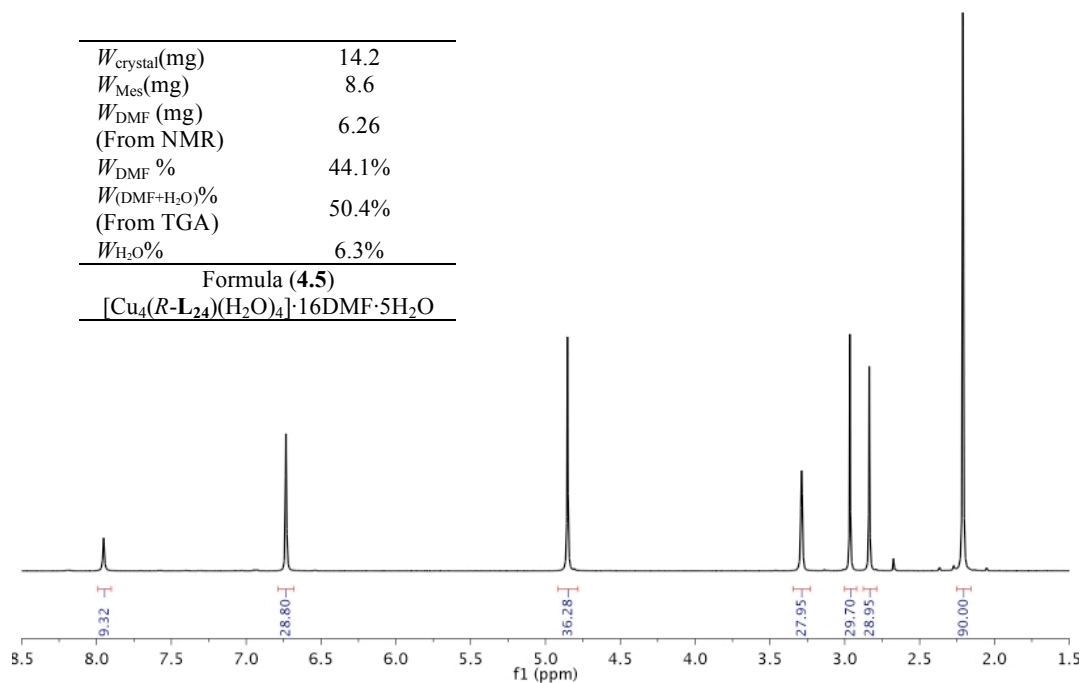
Figure 4.18 ^{1}H NMR spectroscopic determination of solvent content in **4.5**, mesitylene was added as an internal standard.

$W_{crystal}$(mg)	9.55
W_{Mes}(mg)	8.6
W_{DMF} (mg) (From NMR)	3.87
W_{DMF} %	40.5%
$W_{(DMF+H_2O)}$% (From TGA)	43.2%
W_{H_2O}%	2.6%
Formula (**4.6**)	
$[Cu_4(R\text{-}\mathbf{L_{25}})(H_2O)_4]\cdot14DMF$	
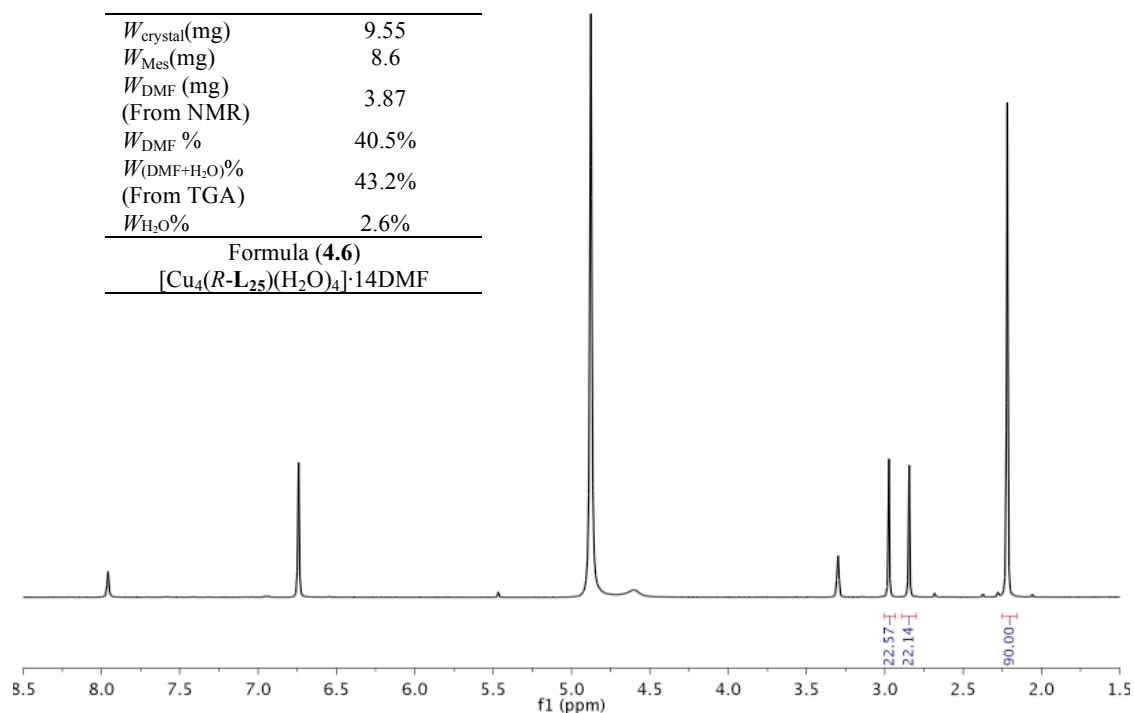
Figure 4.19 ^{1}H NMR spectroscopic determination of solvent content in **4.6**, mesitylene was added as an internal standard.

Compound **4.1** crystallizes in the tetragonal $P4$ space group with two copper atoms, one half **L$_{20}$** ligand, and two water molecules for the framework in the asymmetric unit (Table 4.2). We obtained a similar crystalline MOF **4.1'** when racemic **L$_{20}$**-H$_8$ was used in place of (R)-**L$_{20}$**-H$_8$. Interestingly, single crystal X-ray structure determination showed that the racemic **L$_{20}$**-H$_8$ self-resolved during the MOF growth to give single crystals of **4.1'** that contained racemically twinned domains. The structure of **4.1'** is thus the same as that of **4.1** with the exception of racemic twinning.

Table 4.2 Crystal data and structure refinement for **4.1**, **4.1'**, **4.2** and **4.3**.

Compound	4.1	4.1'	4.2	4.3
Empirical formula	$C_{28}H_{15}O_{11}Cu_2$	$C_{28}H_{15}O_{11}Cu_2$	$C_{26}H_{11}O_{11}Cu_2$	$C33H6O11Cu2$
Formula weight	645.41	645.41	621.39	705.48
Temperature (K)	143	200	200	200
Wavelength (Å)	1.54178	1.54178	1.54178	1.54178
Crystal system	Tetragonal	Tetragonal	Tetragonal	Tetragonal
Space group	P4	P4	P4	P4
Unit cell dimensions	$a = 18.2715(3)$	$a = 18.2959(3)$	$a = 18.0725(9)$	$a = 18.0648(12)$
	$b = 18.2715(3)$	$b = 18.2959(3)$	$b = 18.0725(9)$	$b = 18.0648(12)$
	$c = 17.0912(3)$	$c = 17.1099(3)$	$c = 17.1854(11)$	$c = 17.1132(12)$
	$\alpha = 90$	$\alpha = 90$	$\alpha = 90$	$\alpha = 90$
	$\beta = 90$	$\beta = 90$	$\beta = 90$	$\beta = 90$
	$\gamma = 90$	$\gamma = 90$	$\gamma = 90$	$\gamma = 90$
Volume ($Å^3$)	5705.86(17)	5727.37(17)	5613.0(5)	5584.7(5)
Z	4	4	4	4
Density (calcd. g/cm^3)	0.751	0.748	0.735	0.839
Absorption coeff. (mm^{-1})	1.178	1.174	1.185	1.236
F(000)	1280	1280	1232	1400
Crystal size (mm)	0.5×0.4 ×0.05	0.4×0.4×0.05	0.4×0.4×0.05	0.4×0.2×0.05
Crystal color & shape	Blue thin plate	Blue thin plate	Blue thin plate	Blue thin plate
θ range data collection	2.59 – 59.04	2.41 – 66.07	2.44-39.90	2.58-44.47
Limiting indices	$-20< h <12$	$-21< h <19$	$-15< h <10$	$-16< h <16$
	$-19< k <19$	$-21< k < 21$	$-9< k <14$	$-16< k <16$
	$-16< l <18$	$-20< l < 19$	$-12< l <13$	$-15< l <15$
Reflections collected	15723	28709	5220	10516
Independent reflections	7236	9676	3150	4016
Refinement method		Full-matrix least-square on F^2		
Data/restraints/parameters	7236/239/401	9676/239/403	3150/242/391	4016/251/314
Goodness-of-fit on F^2	0.936 (0.938, restrained)	1.02 (1.03, restrained)	0.842 (0.850,restrained)	1.046 (1.012, restrained)
Final R indices $[I>2\sigma(I)]^{a,b}$	R1 = 0.0563 wR2 = 0.1473	R1 = 0.0546 wR2 = 0.1519	R1 = 0.0644 wR2 = 0.1424	R1 = 0.0774 wR2 = 0.1899
R indices (all data)	R1 = 0.0697 wR2 = 0.1564	R1 = 0.0650 wR2 = 0.1606	R1 = 0.1262 wR2 = 0.1614	R1 = 0.1295 wR2 = 0.2113
Flack	0.10(5)	0.47(6)	0.01(1)	0.27(14)

$^a R(F) = \Sigma ||F_o| - |F_c|| / \Sigma |F_o|.$ $^b R_W(F^2) = [\Sigma\{w(F_o^2 - F_c^2)^2\}/\Sigma\{w(F_o^2)^2\}]^{0.5}; w^{-1} = \sigma^2(F_o^2) + (aP)^2 + bP,$

where $P = [F_o^2 + 2F_c^2]/3$ and a and b are constants adjusted by the program.

The Cu atoms coordinate to four carboxylate oxygen atoms of four different L_{20} ligands to form $[Cu_2(O_2CR)_4]$ paddle-wheels that are shown as red rectangles in Figure 4.20. Each Cu atom also coordinates to a terminal water molecule in the axial position. The L_{20} ligand is linked to eight copper paddle-wheels via the bridging carboxylate groups in a rectangular prismatic fashion. The copper paddle-wheels thus serve as 4-connected nodes whereas the L_{20} ligands act as 8-connected nodes, and as a result, **4.1** adopts the known but very rare (4,8)-connected **scu** topology with the Schlafli symbol $\{4^4 \cdot 6^2\}_2\{4^{16} \cdot 6^{12}\}$ (Figure 4.21). Compound **4.1** represents only the third MOF with the **scu** topology and the first one that is built from an 8-connected bridging ligand.
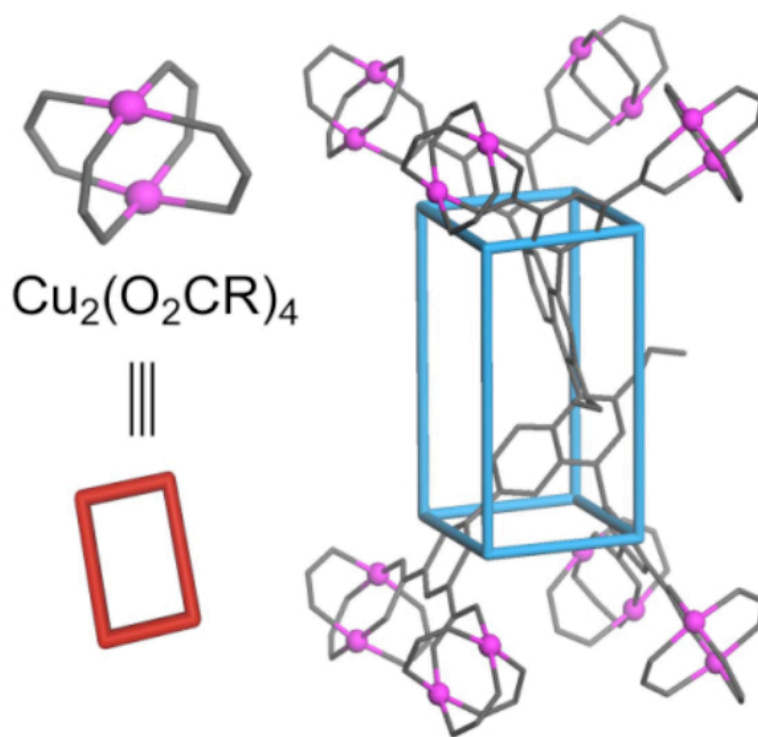
Figure 4.20 (a) A view of $[Cu_2(O_2CR)_4]$ paddle-wheels (represented as red rectangles) and their connectivity with the L_{20} ligand (represented as blue rectangular prism) in **4.1**.
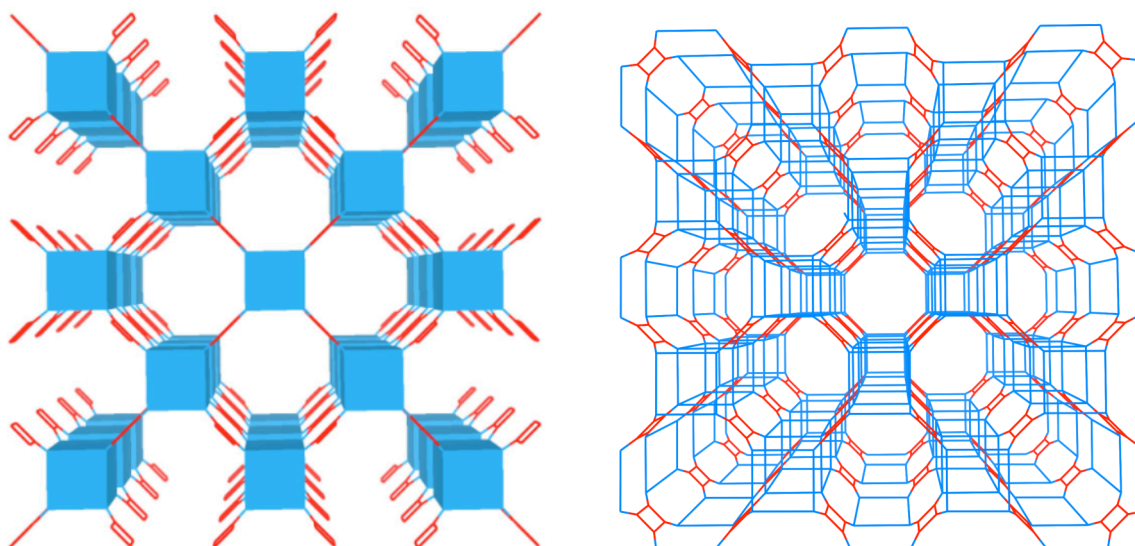
Figure 4.21 A simplified connectivity scheme of **4.1** showing the **scu** topology.

Compounds **4.2**, **4.3**, **4.4**, and **4.6** are isostructural to compound **4.1** with the same space group and connectivity (Table 4.3). Compound **4.5** crystallizes in the orthorhombic C222 space group and has very similar structural characteristics to the other compounds. Because of the elongated L_{20}- L_{22} ligands, **4.1**, **4.2**, and **4.3** possess very large solvent accessible volume of 61.0%, 64.7%, and 52.7% of the unit cell volume as calculated by PLATON,[23] respectively. Consistent with this, **4.1**, **4.2**, and **4.3** exhibited significant TGA solvent weight loss of 51%, 49%, and 39% in the 25-280 ^{o}C temperature range, respectively. As expected, the larger pore compounds **4.4-4.6**, show even greater solvent accessible volumes of 67.9%, 70.3%, and 62.6%, respectively. Experimental weight losses of 61%, 50%, and 41%, respectively, were obtained by TGA for **4.4-4.6**. These numbers show significant increase in solvent capacity when compared to the shorter L48 system. Comparisons between calculated and experimental values are in Table 4.4.

Table 4.3 Crystal data and structure refinement for **4.4**, **4.5**, and **4.6**.

Compound	4.4	4.5	4.6
Empirical formula	$C_{32}H_6O_{11}Cu_2$	$C_{30}H_6O_{11}Cu_2$	$C_{77}H_{12}O_{22}Cu_4$
Formula weight	693.45	669.45	1543.03
Temperature (K)	200	200	296
Wavelength (Å)	1.54178	1.54178	1.54178
Crystal system	Tetragonal	Orthorhombic	Tetragonal
Space group	P4	C222	P4
Unit cell dimensions	$a = 18.8423(19)$	$a = 24.495(8)$	$a = 19.02890(10)$
	$b = 18.8423(19)$	$b = 27.929(10)$	$b = 19.02890(10)$
	$c = 21.921(3)$	$c = 22.130(11)$	$c = 21.9107(3)$
	$\alpha = 90$	$\alpha = 90$	$\alpha = 90$
	$\beta = 90$	$\beta = 90$	$\beta = 90$
	$\gamma = 90$	$\gamma = 90$	$\gamma = 90$
Volume ($Å^3$)	7782.7(14)	15140(11)	7933.84(12)
Z	4	8	2
Density (calcd. g/cm^3)	0.592	0.587	0.646
Absorption coeff. (mm^{-1})	0.882	0.897	0.895
F(000)	1376	2656	1532
Crystal size (mm)	0.4×0.2 ×0.03	0.3×0.3×0.02	0.4×0.4×0.03
Crystal color & shape	Blue thin plate	Blue thin plate	Blue thin plate
θ range data collection	2.02 – 40.18º	2.00 – 33.48º	2.02-50.45º
Limiting indices	$-14< h <15$	$0< h <17$	$-19< h <19$
	$-15< k <15$	$0< k < 19$	$-16< k <16$
	$-17< l <18$	$0< l < 15$	$-20< l <21$
Reflections collected	10165	1616	16071
Independent reflections	4193	1616	7594
Refinement method	Full-matrix least-square on F^2		
Data/restraints/parameters	4193/458/427	1616/169/179	7594/227/458
Goodness-of-fit on F^2	0.883 (0.883, restrained)	0.849 (0.849, restrained)	0.808 (0.850,restrained)
Final R indices $[I>2\sigma(I)]^{a,b}$	R1 = 0.0635 wR2 = 0.1265	R1 = 0.0856 wR2 = 0.1804	R1 = 0.0495 wR2 = 0.1026
R indices (all data)	R1 = 0.1046 wR2 = 0.1402	R1 = 0.1010 wR2 = 0.1841	R1 = 0.0688 wR2 = 0.1108
Flack	0.36(11)	-0.3(2)	0.17(6)

^{a} $R(F) = \Sigma ||F_o| - |F_c||/\Sigma |F_o|$. ^{b} $R_W(F^2) = [\Sigma \{w(F_o^2 - F_c^2)^2\}/\Sigma \{w(F_o^2)^2\}]^{0.5}$; $w^{-1} = \sigma^2(F_o^2) + (aP)^2 + bP$, where $P = [F_o^2 + 2F_c^2]/3$ and a and b are constants adjusted by the program.

Table 4.4: Comparison of theoretical solvent accessible pore volume and experiemtnal solvent weight loss.

Crystal	Theoretical void space	Experimental weight loss
4.1	61.0	51
4.2	64.7	49
4.3	52.7	39
4.4	67.9	61
4.5	70.3	50
4.6	62.6	41

As shown in Figures 4.22c and 4.22d, compound **4.2** possess square channels of ~7×7 Å along the c axis and rectangular channels of ~5.3×10.6 Å along the (110) direction. The ethoxy groups of the L_{20} ligands protrude into the open channels that run along the c axis and the (110) direction in **4.1**, thus reducing the open channel sizes. As expected, the bulkier benzyloxy groups in **4.3** reduce the open channel sizes even further, with the open channel of ~7×4 Å along the c axis (Figure 4.22e) and the open channels of ~5.3×4.4 Å and 4.0×2.4 Å along the (110) direction due to the protruding benzyloxy groups (Figure 4.22f).

As shown in Figures 4.23c and 4.23d, compound **4.5** possess channels of ~7×10.3 Å along the c axis and rectangular channels of ~9.2×16 Å along the (110) direction compared to 10.6 Å diameter in the shorter octa-acid system. The ethoxy groups of the L_{23} ligands protrude into the open channels that run along the c axis and the (110) direction in **4.4**, thus reducing the open square channel sizes to ~9.5×9.5 Å along the c axis and rectangular channels of ~9.2×16 Å along the (110) direction. As expected, the bulkier benzyloxy groups in **4.6** reduce the open channel sizes even further, with the open channel of ~7.2×7.2 Å along the c axis (Figure 4.23e) and the open channels of ~6.0×6.7 Å and 6.7×7.8 Å along the (110) direction due to the protruding benzyloxy groups (Figure 4.23f).
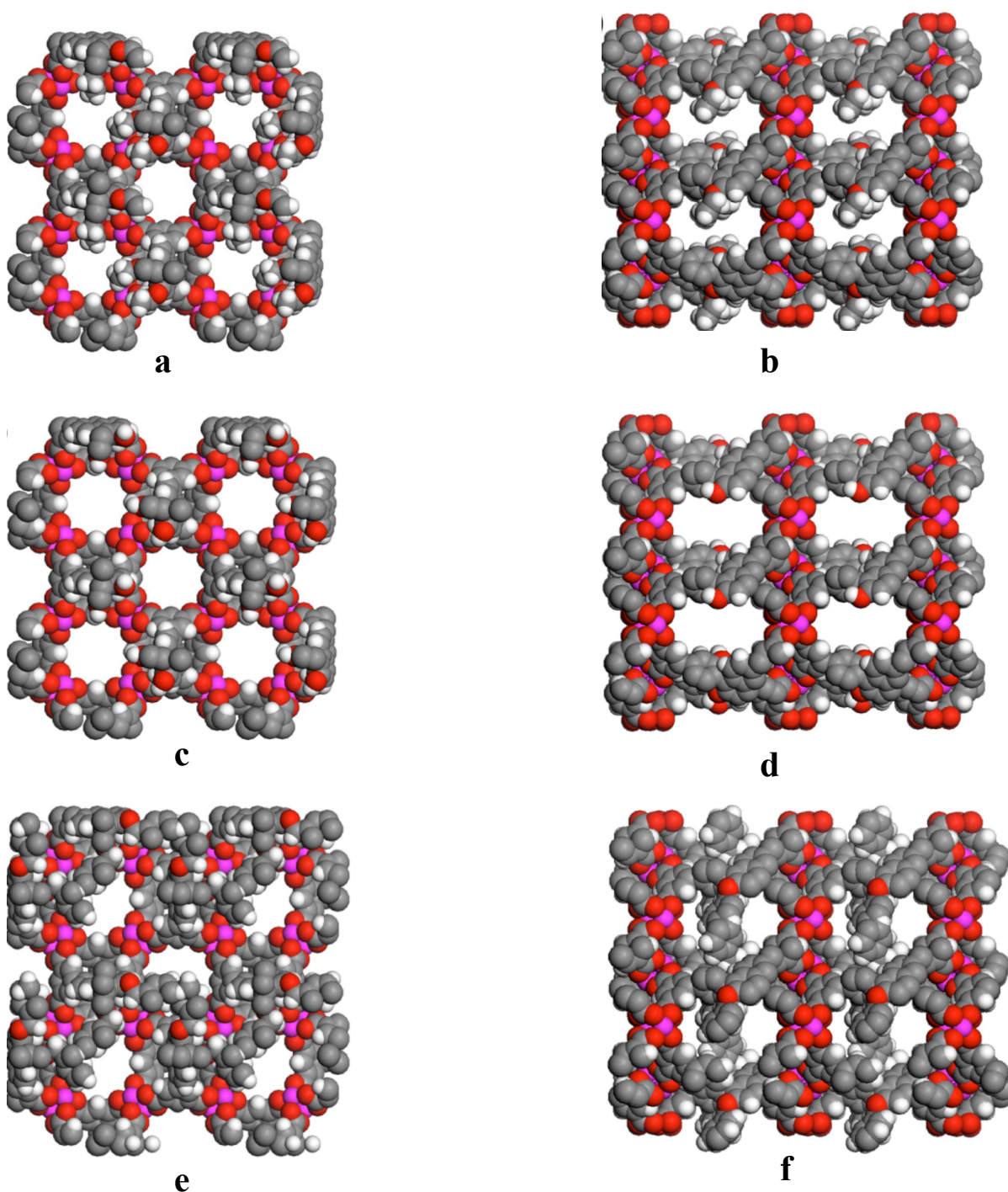
Figure 4.22 (a) Space-filling model of **4.1** as viewed down the *c* axis, showing irregular open channels with the largest dimension of ~7 Å. (b) Space-filling model of **4.1** as viewed along the (110) direction, showing irregular channels with the largest dimension of 10.6 Å. (c) Space-filling model of **4.2** as viewed down the *b* axis, showing square open channels of ~7 Å in each side. (d) Space-filling model of **4.2** as viewed along the (110) direction, showing rectangular channels of ~5.3×10.6 Å. (e) Space-filling model of **4.3** as viewed down the *c* axis, showing open channels of ~7 × 4 Å. (f) Space-filling model of **4.3** as viewed along the (110) direction, showing two different open channels of ~5.3×4.4 Å and 4.0×2.4 Å.
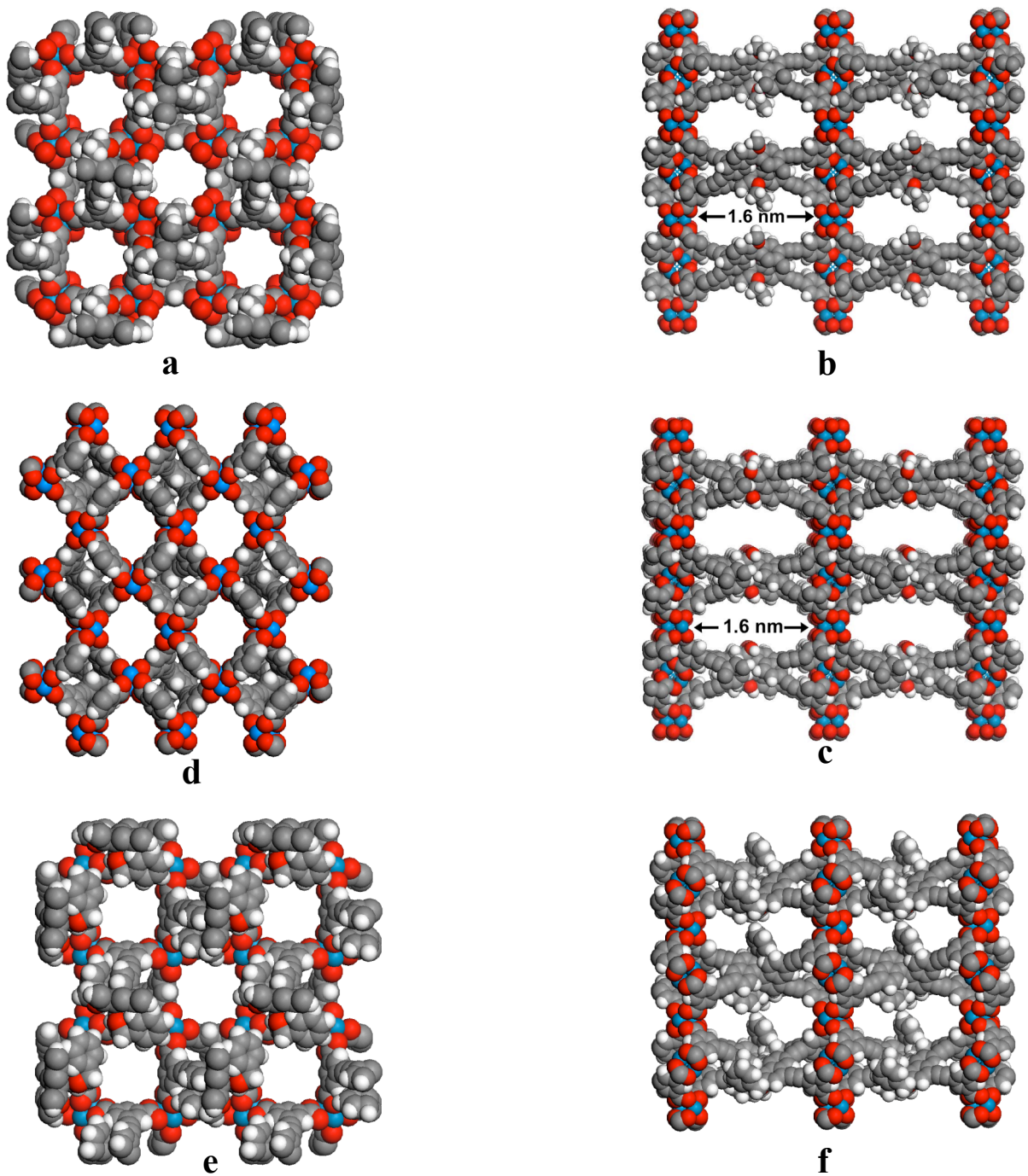
Figure 4.23 (a) Space-filling model of **4.4** as viewed down the *c* axis, showing open square channels with the largest dimension of ~9.5×9.5 Å. (b) Space-filling model of **4.4** as viewed along the (110) direction, showing channels with the largest dimension of 16 Å. (c) Space-filling model of **4.5** as viewed down the *c* axis, showing open channels with dimensions of ~7×10.3 Å. (d) Space-filling model of **4.5** as viewed along the (110) direction, showing rectangular channels of ~9.2×16 Å. (e) Space-filling model of **4.6** as viewed down the *c* axis, showing open channels of ~7.2×7.2 Å. (f) Space-filling model of **4.6** as viewed along the (110) direction, showing two different open channels of ~6.0×6.7 Å and 6.7×7.8 Å.

128

4.3.3 Nitrogen adsorption characterization studies

The permanent porosity of **4.1**, **4.2**, and **4.3** was established by nitrogen adsorption at 77 K. After activation at 60 $^{\circ}$C under vacuum, **4.1** exhibited a Langmuir surface area of 2486 m^2/g (Figure 4.24) whereas **4.2** exhibited a Langmuir surface area of 2650 m^2/g. Compound **4.3** exhibited a significantly lower Langmuir surface area of 1841 m^2/g. BET surface areas are 2149, 2285, and 1605 m^2/g for **4.1**, **4.2** and **4.3**, respectively.[24] This porosity trend is entirely consistent with the increasing steric bulk of hydroxy, ethoxy, and benzyloxy groups on the 2,2'-position of the binaphthyl moieties of the *octa*-carboxylic acid bridging ligands.
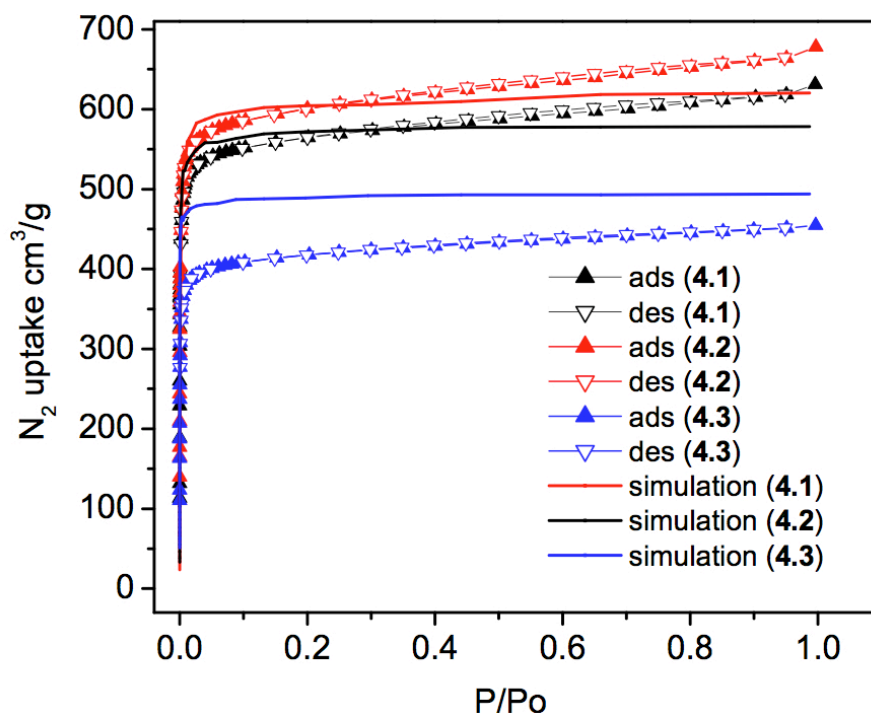
Figure 4.24 Experimental and calculated N$_2$ adsorption isotherms for **4.1** (black), **4.2** (red), and **4.3** (blue). Solid triangles (adsorption), open triangles (desorption), and solid lines (GCMC simulation results).

Notably, the experimental surface areas of **4.1** and **4.2** perfectly agree with those calculated using the simulated N$_2$ adsorption isotherms; grand canonical Monte Carlo (GCMC) simulations[25] gave calculated Langmuir surface areas of 2502 and 2592 m^2/g for

4.1 and **4.2**, respectively. The GCMC simulation of **4.3** gave slightly higher Langmuir surface area of 2134 m^2/g than the experimental result (1841 m^2/g). This discrepancy could be caused by the flexible (and disordered) nature of the bulky benzyloxy groups. Upon desolvation, the benzyloxy group can move around to generate a portion of pores that are smaller than the dynamic diameter of adsorbate molecules (N_2). The GCMC simulation, on the other hand, assumes rigid orientation of the protruding benzyloxy groups and gives the idealized surface area. The N_2-inaccessible pores can account for the discrepancy between the experimental and GCMC simulated surface areas for **4.3**.

The BET and Langmuir surface areas were calculated from the pressure range of P/P_0=0.01-0.10 and 0.001-0.30, respectively (Figure 4.25). All of the BET plots have large negative BET constants, indicating no multilayer adsorption (Table 4.5). The Langmuir model is thus more appropriate for **4.1-4.3** (Figure 4.26)**.**

Table 4.5 BET and Langmuir surface areas obtained by N_2 adsorption isotherms.

Crystal	BET Surface Area (m^2/g) P/P_o= 0.01-0.10	BET Constant Value	Langmuir Surface Area (m^2/g) P/P_o = 0.001-0.30
4.1	2149	-680	2486
4.2	2285	-770	2650
4.3	1605	-1065	1841
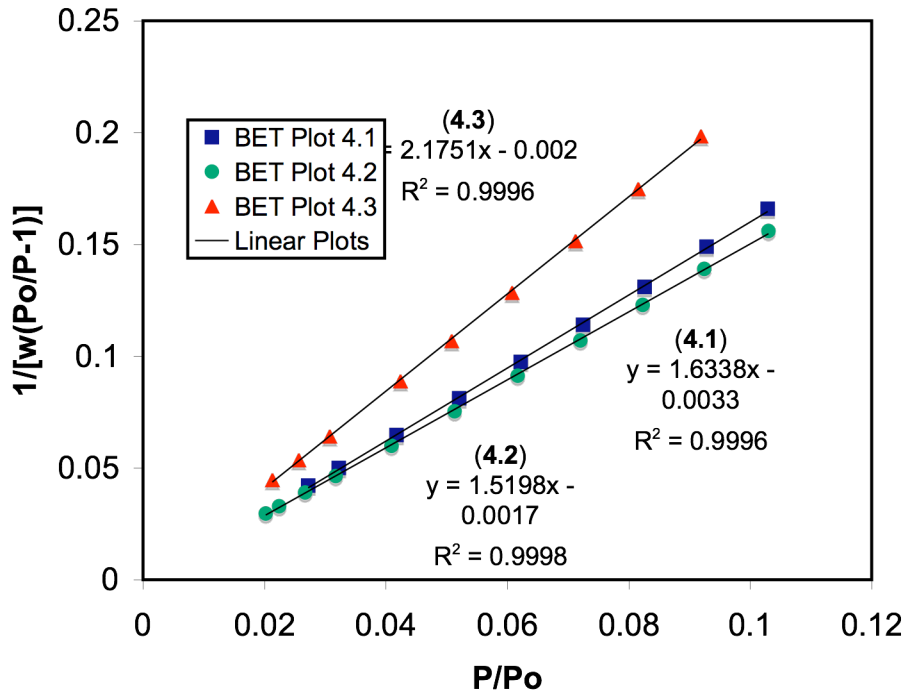
4.25 BET plots of **4.1-4.3** and their linear fit lines. Selected range of P/P$_o$ from 0.02 to 0.10.
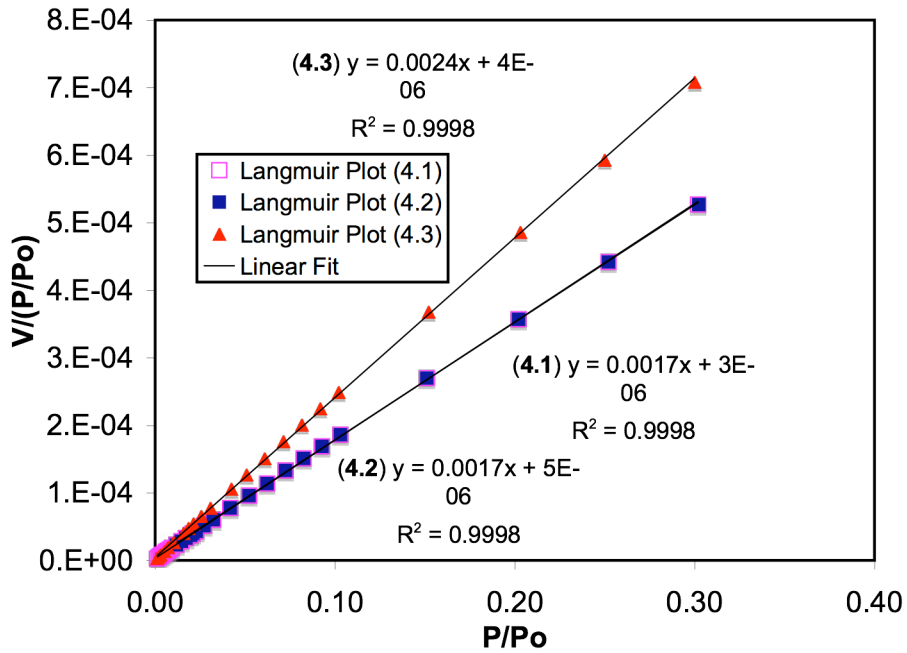
4.26 Langmuir plots of **4.1-4.3** and their linear fit lines. Selected range of P/P$_o$ from 0.001 to 0.30.

The pore sizes of **4.2** have also slightly increased compared to those of **4.1** (Figure 4.27). This trend is consistent with the slightly less porous structure of **4.1** due to the steric bulk of the ethoxy groups. The pore sizes of **4.3** are however very similar to those of **4.1**, which is inconsistent with the steric difference between the ethoxy and benzyloxy groups. In fact, the pore sizes derived from GCMC simulated adsorption isotherm for **4.3** are smaller than those for **4.1** (Figure 4.28). This discrepancy between experimental and calculated pore sizes for **4.3** is presumably a result of the disordered nature of the bulky benzyloxy groups. Consistent with the porosity trend, the HK method cumulative pore volume is 0.92, 0.86, and 0.64 cc/g for **4.2**, **4.1** and **4.3**, respectively.

Figure 4.27 Pore size distributions (HK method) for **4.1** (black), **4.2** (red), and **4.3** (blue) with the *x* axis showing pore diameter in Å and the *y* axis showing Dv(w) in cm³/Å/g.
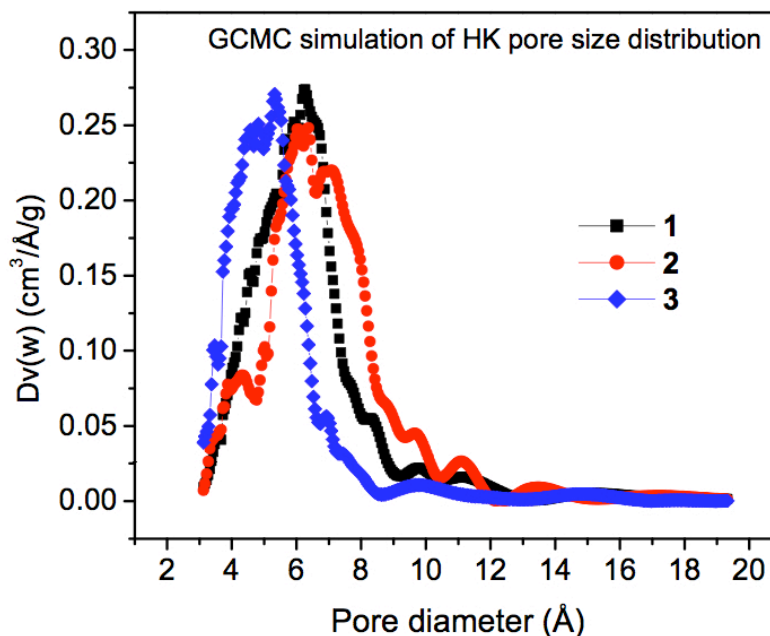
Figure 4.28 GCMC simulation of pore size distributions (HK method) for **4.1** (black), **4.2** (red), and **4.3** (blue) with the *x* axis showing pore diameter in Å and the *y* axis showing Dv(w) in cm^3/Å/g.

The surface areas of **4.4** and **4.5** were also very high. After activation at 60 ^{o}C under vacuum the permanent porosity of **4.4** and **4.5** was established by nitrogen adsorption at 77 K (Figure 4.29). Unlike **4.1-4.3**, the surface areas do not necessarily agree with the simulated N_2 adsorption isotherms calculated by GCMC method which gave calculated Langmuir surface areas of 3947, 4027, and 3450 m^2/g for **4.4-4.6**, respectively. The experimental Lanmuir surface areas obtained for **4.4** and **4.5** were 2245 and 2819 m^2/g, respectively (N_2 adsorption data for **4.6** not yet obtained). This porosity trend is consistent with the increasing steric bulk of hydroxy and ethoxy groups on the 2,2'-position of the binaphthyl moieties of the *octa*-carboxylic acid bridging ligands in **4.4** and **4.5**. However, the calculated and experimental surface area values are not similar. It is thought that due to the extended nature of the *octa*-carboxylic acid bridging ligands in **4.4** and **4.5,** slightly different activation (solvent removal) techniques must be employed.

133
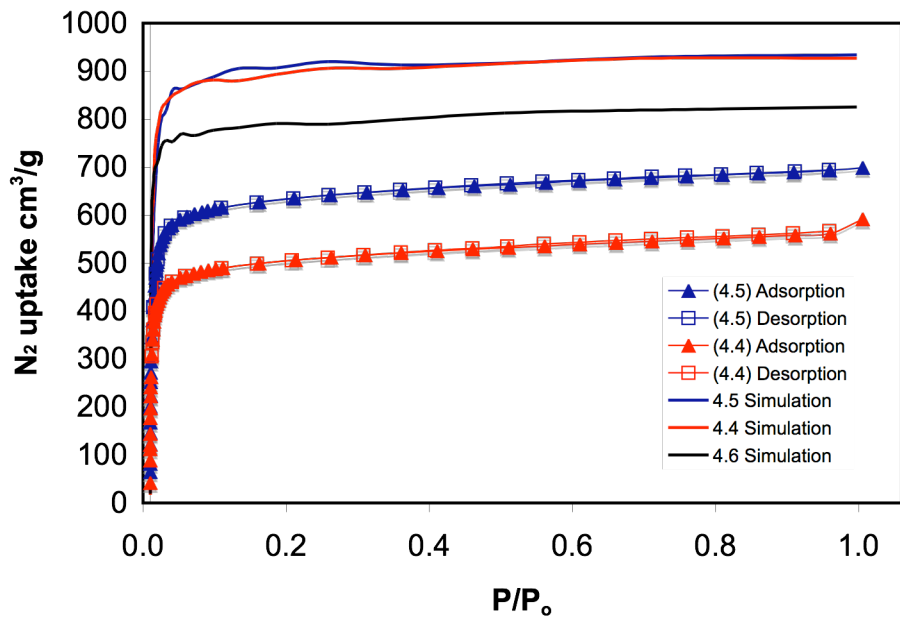
Figure 4.29 Experimental and calculated N_2 adsorption isotherms for **4.4** (red), **4.5** (blue), and calculated N_2 adsorption isotherm for **4.6** (black). Solid lines (GCMC simulation results).
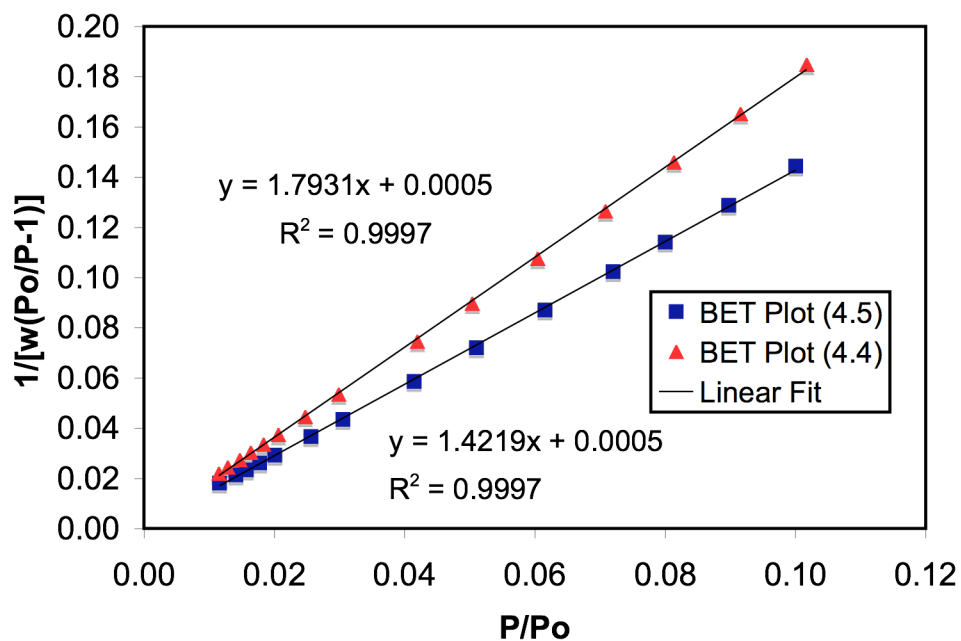
Figure 4.30 BET plots of **4.4** and **4.5** and their linear fit lines. Selected range of P/P_o from 0.01 to 0.10.
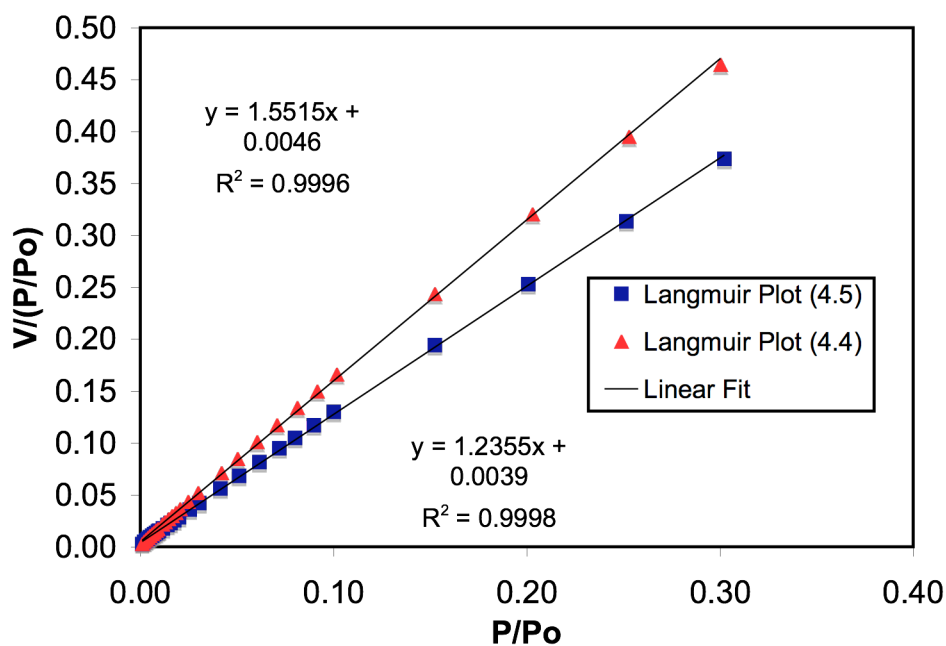
Figure 4.31 Langmuir plots of **4.4** and **4.5** and their linear fit lines. Selected range of P/P_o from 0.001 to 0.30.

An HK cumulative pore size comparison shows that on average, **4.5** has slightly smaller pores that **4.4** (Figure 4.32). This porosity trend is consistent with the increasing steric bulk of hydroxy and ethoxy groups on the 2,2'-position of the binaphthyl moieties of the *octa*-carboxylic acid bridging ligands. The HK cumulative pore volumes for **4.4** and **4.5** were 0.77 and 0.96 cc/g, respectively (Table 4.6). The theoretical pore size comparison indicates a slightly larger pore size is to be expected from the La48 series (Figure 4.33).

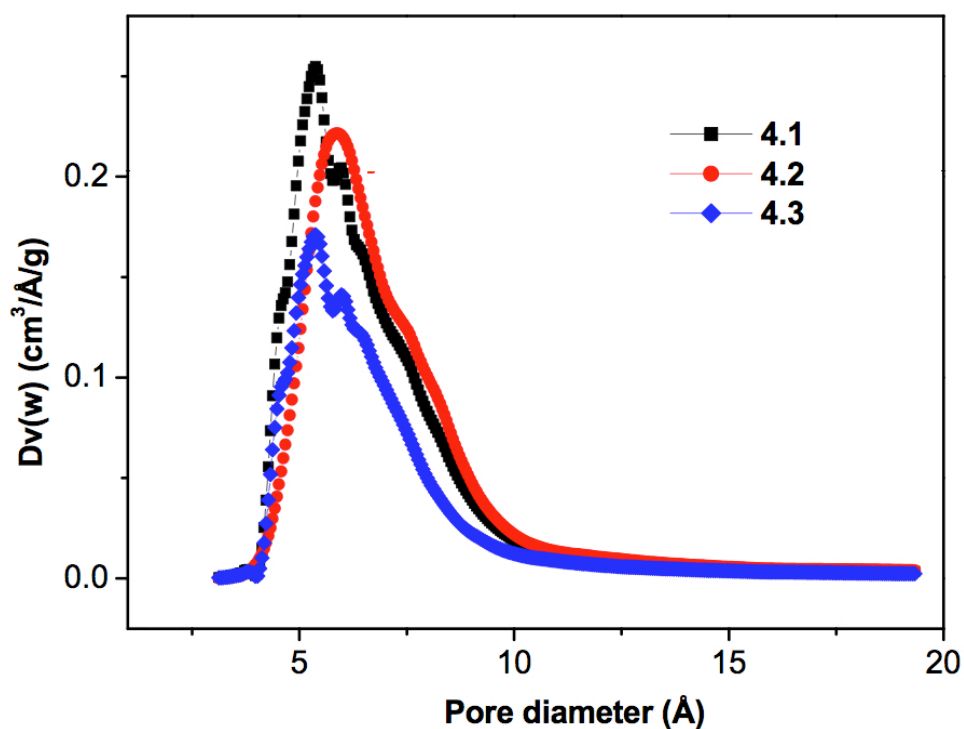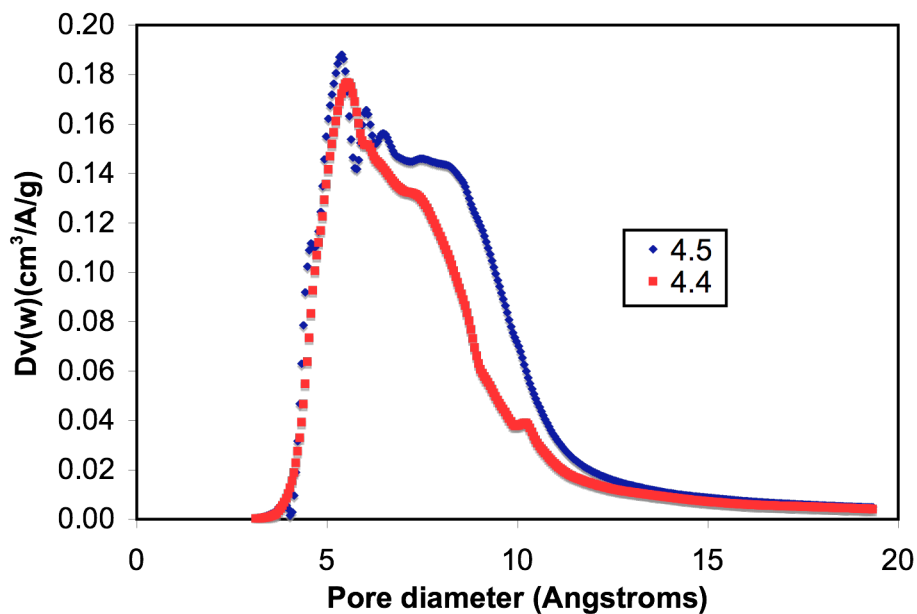**Figure 4.32** Pore size distributions (HK method) for **4.4** and **4.5** with the *x* axis showing pore diameter in Å and the *y* axis showing Dv(w) in cm^3/Å/g.
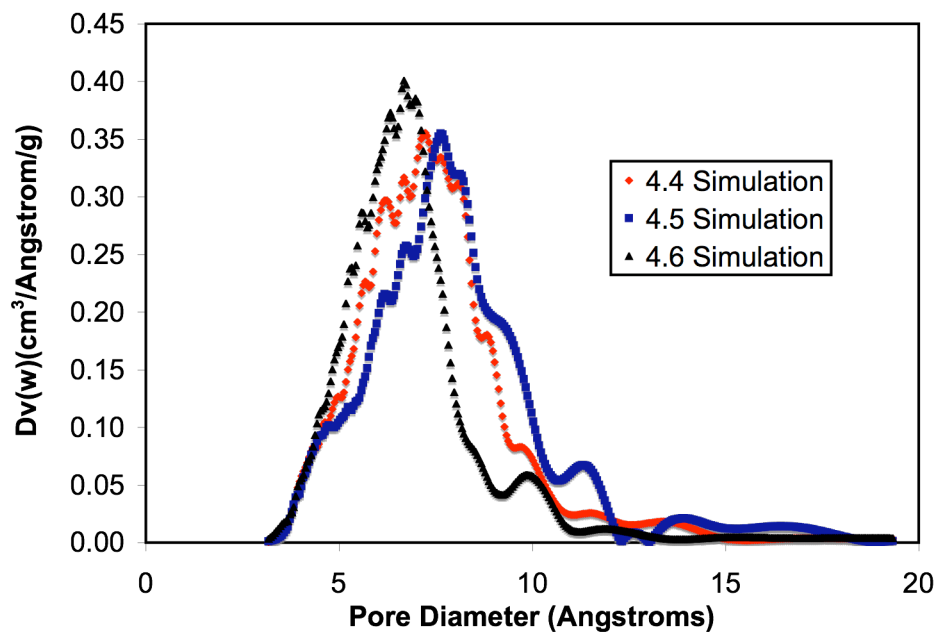
Figure 4.33 Calculated pore size distributions (HK method) for **4.4-4.6** with the *x* axis showing pore diameter in Å and the *y* axis showing Dv(w) in cm^3/Å/g.

Table 4.5: Summary of surface areas and pore volumes for **4.1-4.5**.

	GCMC Simulated Surface Area (m^2/g)	Experimental Langmuir Surface Area (m^2/g)
4.4	3947	2245
4.5	4027	2819
4.6	3450	—

4.3.4 Powder X-ray diffraction studies

As expected, the powder X-ray diffraction (PXRD) patterns of **4.1**, **4.2**, and **4.3** are very similar to each other, consistent with their isostructural nature (Figure 4.34). Furthermore, the PXRD patterns of the evacuated samples of **4.1**, **4.2**, and **4.3** are essentially the same as those of pristine **4.1**, **4.2**, and **4.3,** further demonstrating the maintenance of the framework structure upon solvent removal (Figure 4.35). This is in stark contrast with our earlier results which showed that the frameworks of 4,4-connected MOFs based on copper paddle-wheel SBUs and elongated tetracarboxylate bridging ligands severely distorted (as evidenced by the loss of PXRD peaks) to give experimental surface areas only a very small fraction of those calculated by GCMC simulations.[23] The higher connectivity of the L_{20} – L_{22} ligands has apparently stabilized the frameworks of **4.1** – **4.3** against distortion (also called breathing in recent literatures).[34] The use of bridging ligands of high connectivity thus presents an alternative strategy to the reliance on high-nuclearity metal clusters for building highly stable and porous MOFs.[26]
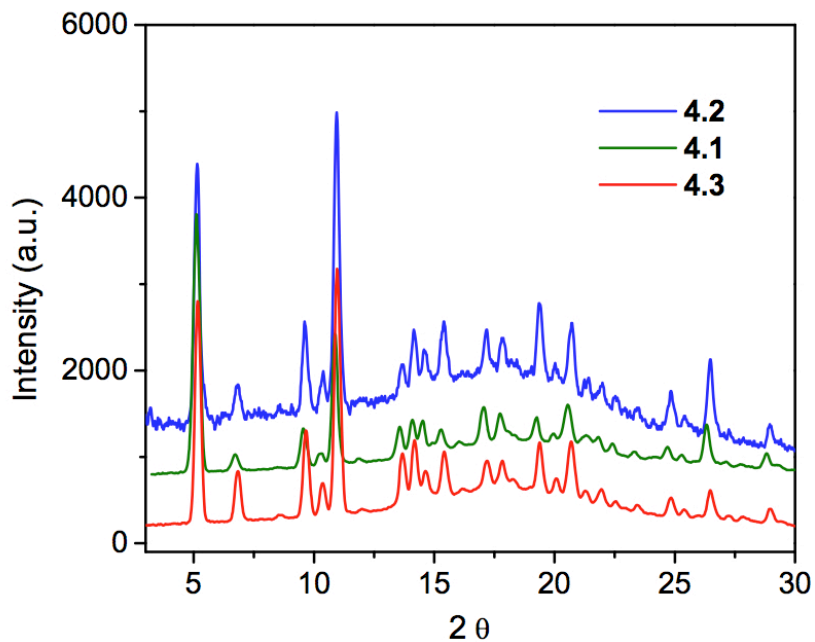
Figure 4.34 Powder X-ray diffraction patterns of fresh crystals **4.1** (green), **4.2** (blue), **4.3** (red).
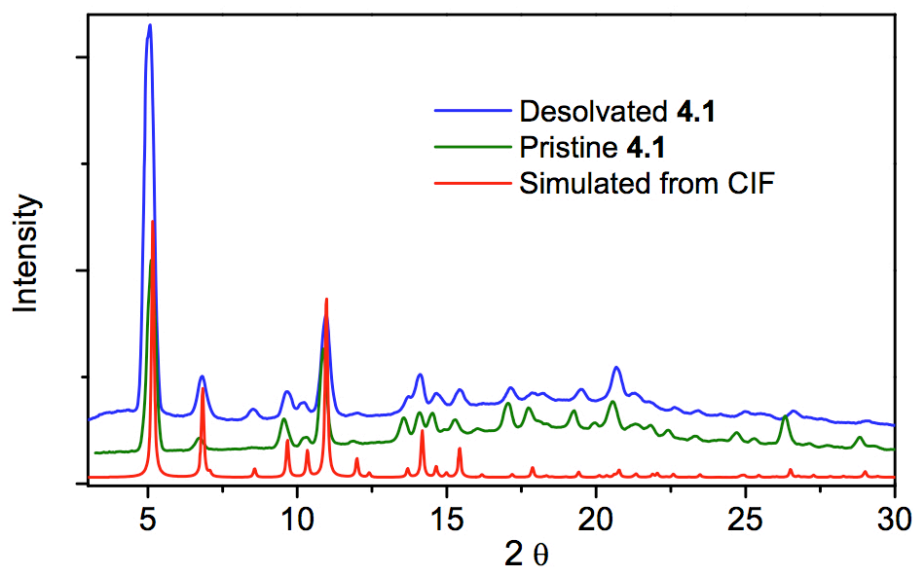
Figure 4.35 PXRD of pristine (green) and evacuated (blue) samples of **4.1** along with calculated PXRD pattern (red).

4.3.4 Hydrogen adsorption studies

Hydrogen adsorption experiments show **4.1** is capable of 2.5 wt% H_2 at 77 K and 1 atm (Figure 4.36), which is among the highest for MOFs at 1 atm.[27] In the volumetric sense, **4.1** has a H_2 uptake of 17.4 g/L, superior to other aromatics-rich MOFs (e.g., 5.34 g/L for MOF-177).[36] Despite having a higher surface area, **4.2** exhibits a lower hydrogen uptake of 2.1 wt%. This result is not entirely surprising as earlier work has shown that MOFs with smaller pore sizes tend to have higher hydrogen uptake capacities.[36] However, our intent to further reduce the pore size by using the bulkier benzyloxy groups did not yield the expected results. As mentioned earlier, the pore size distribution for **4.3** is essentially the same as that of **4.1**. Compound **4.3** exhibited an even lower hydrogen uptake of 1.8 wt%, probably as a result of its smallest surface area and pore volume. This demonstrates the ability to tune the surface area, pore size, and gas uptake by systematically changing the alkoxy groups of the *octa*-carboxylic acid bridging ligands in **4.1**-**4.3**.
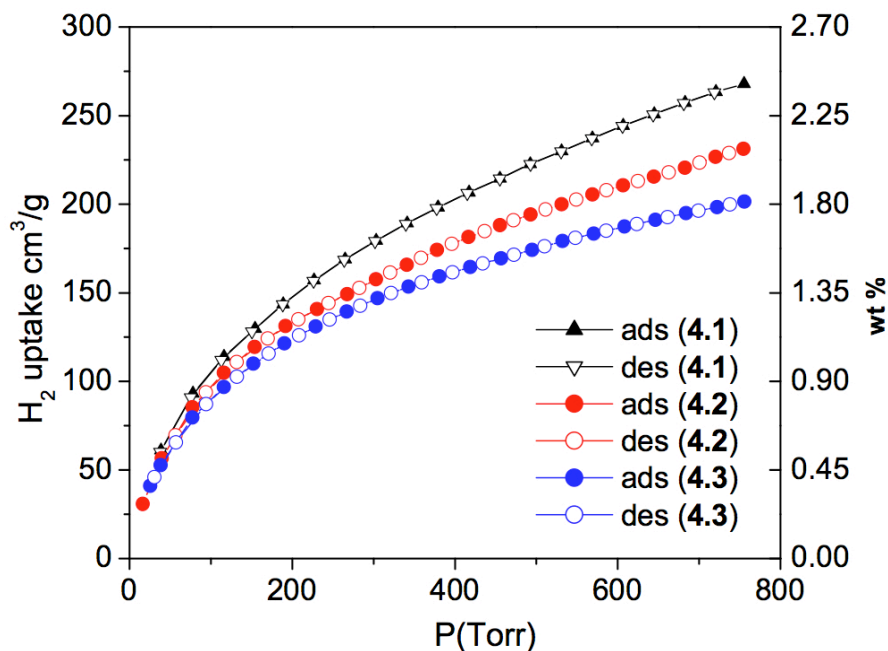
Figure 4.36 Experimental hydrogen adsorption isotherms of **4.1** (black), **4.2** (red), and **4.3** (blue). Solid triangles and circles (adsorption) and open triangles and circles (desorption).

Saturation hydrogen uptake capacity of **4.1** and **4.2** was analyzed (Figures 4.37 and 4.38). At 30 bar pressure and 77 K, **4.1** demonstrates a hydrogen uptake capacity of 4.6%. **4.2** shows an uptake capacity of 5.5 wt% at 30 bar and 77 K. The uptake is highly dependent upon temperature of the sample; when the temperature is raised to 87 K, H_2 adsoprtion at 30 bar drops nearly 1 wt %. Conversely, when the temperature is dropped to 30 K, a saturation uptake of 8.2% is achieved at just 5 bar.
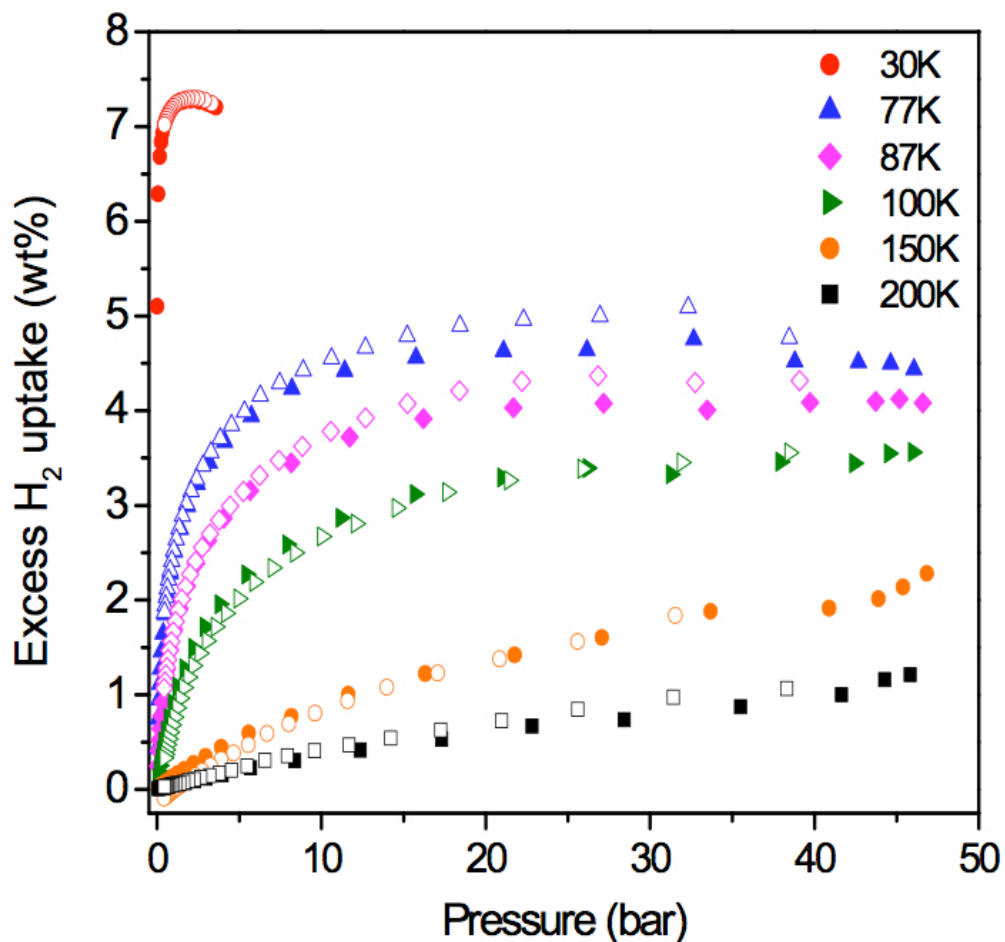
Figure 4.37 Saturation hydrogen uptake of **4.1** temperatures ranging from 30 K to 200 K.
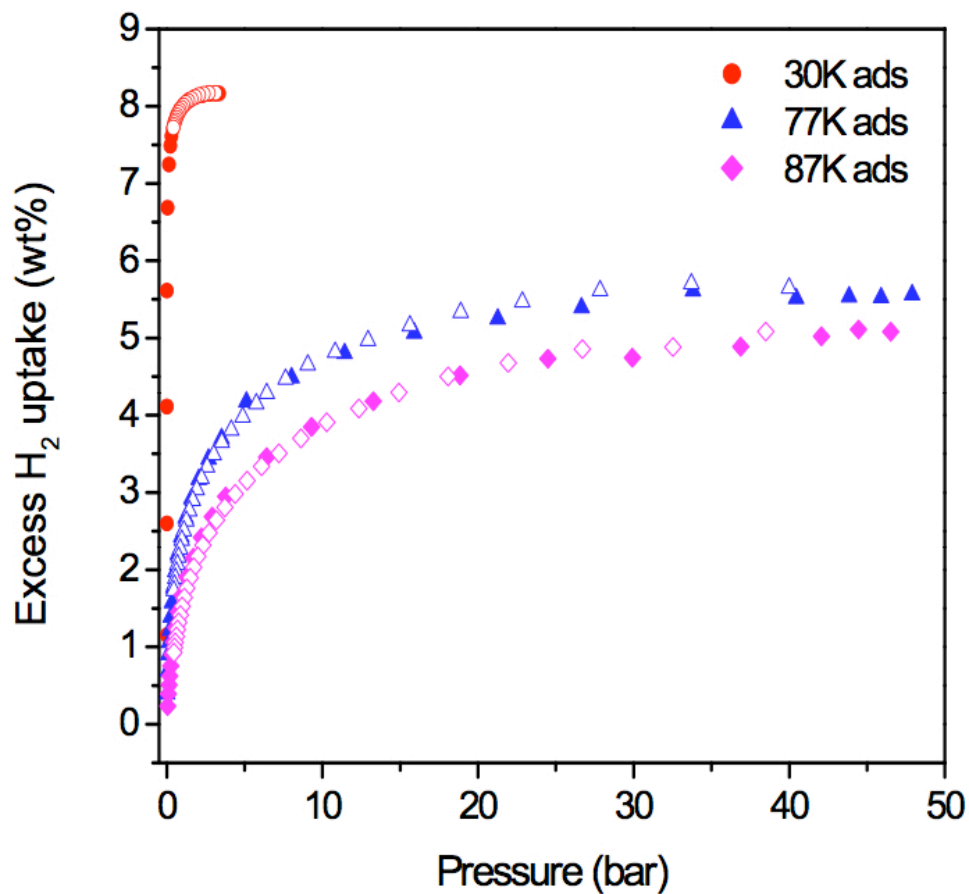
Figure 4.38 Saturation hydrogen uptake of **4.2** temperatures ranging from 30K to 87K.

Compounds **4.4** and **4.5** also exhibit significant H_2 storage capacities. **4.4** has a hydrogen uptake of 1.7 wt% while **4.5** is capable of adsorbing 1.8% at 1 atm and 77 K (Figure 4.39). Saturation studies are currently underway.
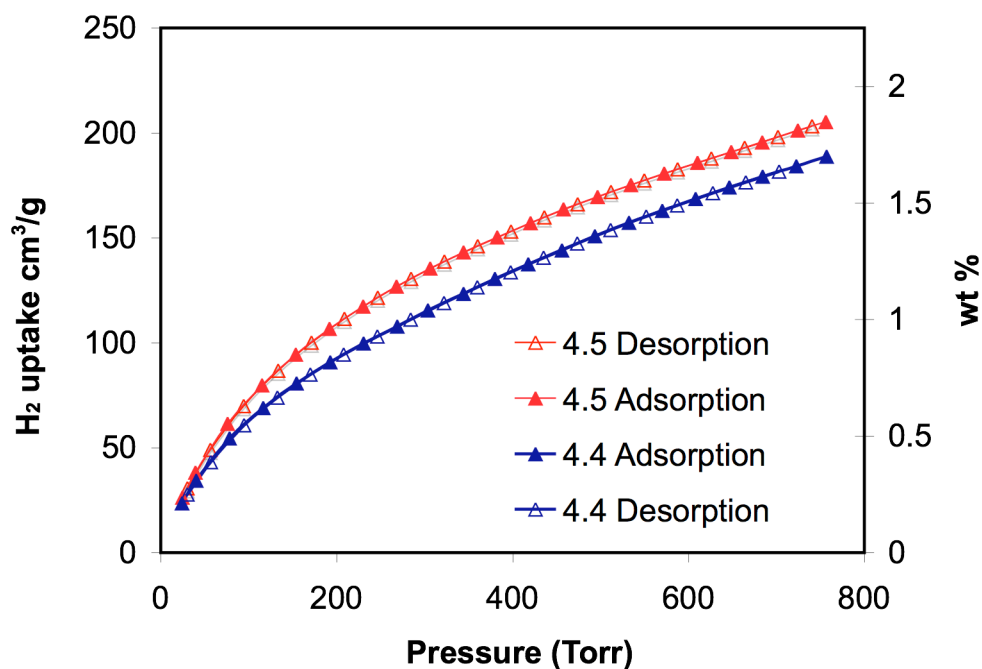
Figure 4.39 N_2 adsorption/desorption isotherms for **4.5** indicate 1.8 % H_2 uptake at 1 atm.

4.4 Conclusion

In summary, we have constructed highly porous and robust (4,8)-connected MOFs based on new *octa*-carboxylate ligands and copper paddle-wheel SBUs. The new MOFs exhibit remarkable framework stability as a result of high connectivity of the bridging ligands and show significant hydrogen uptake. This work thus represents a new approach toward designing highly porous, robust, tunable, and functional MOFs using multidentate bridging ligands of high connectivity.

4.5 Experimental

4.5.1 General information

All solvents were purchased from Fisher and used without further purification. Thermogravimetric analysis (TGA) was performed in air using a Shimadzu TGA-50

equipped with a platinum pan and heated at a rate of 5 °C per minute. Single-crystal X-ray diffraction and Powder X-ray diffraction (PXRD) patterns were collected on a Bruker SMART APEX II diffractometer using Cu radiation. The PXRD patterns were processed with the APEX 2 package using PILOT plug-in.   Nitrogen and hydrogen adsorption experiments were performed with Autosorb-1C from Quantachrome, Inc.

All crystallographic measurements were made on a Bruker SMART Apex II CCD-based X-ray diffractometer system equipped with Cu –target X-ray tube and operated at 1600 watts. The frames were integrated with the Bruker SAINT[©] build in APEX II software package using a narrow-frame integration algorithm, which also corrects for the Lorentz and polarization effects. Absorption corrections were applied using SADABS. All of the structures were solved by direct methods and refined to convergence by least squares method on F^2 using the SHELXTL software suit. All non-hydrogen atoms are refined anisotropically, except the ethoxyl groups.

Adsorption isotherm simulations were performed under the 'Sorption' module of *Materials Studio*. The Metropolis Monte Carlo method was chosen for the calculation of the nitrogen loading in the frameworks under a given fugacity. Universal forcefield was selected for the energy calculation. For the simulation of each framework, forty (40) fugacity steps in logarithmic scale ($10^{-5} \sim 100$ kPa) were calculated to give the isotherm. Simulation temperature: 77.35K; equilibrium steps: 500000; Production steps: 100000. These steps are chosen to assure the creation/destruction steps ratio about 1.00.

4.5.2. Preparation and characterization of ligands

4.5.2.1   (*R*)-octamethyl-5,5',5'',5'''-(2,2'-diethoxy-1,1'-binaphthyl-4,4',6,6' tetrayl)tetraisophthalate (L$_{20}$-Me$_8$)

A solution of (*R*)-4,4',6,6'-tetrabromo-2,2'-ethoxy-1,1'-binaphthalene (500 mg, 0.76 mmol) and dimethyl-5-(pinacolboryl)isophthalate (979 mg, 3.06 mmol) in dimethyl ethylene glycol (20 mL) was degassed for 15 min. CsF (929 mg, 6.1 mmol) and $Pd(PPh_3)_4$ (135 mg, 0.12 mmol) were added to the solution. The reaction vessel was sealed and the reaction mixture was stirred at 110 °C for 3 days. Upon cooling to r.t., the mixture was extracted with CH_2Cl_2/H_2O. The yellow solution was dried over $MgSO_4$ and the solvent removed under reduced pressure. The yellow solid was purified by silica gel column chromatography with hexanes/ethyl acetate (1:1 v/v) as the eluent to afford (*R*)-5,5',5'',5'''-(2,2'-diethoxy-1,1'-binaphthyl-4,4',6,6'-tetrayl)tetraisophthalate. Yield: (460 mg, 54%). ^{1}H NMR ($CDCl_3$): δ 8.83 (s, 2H), 8.58 (s, 2H), 8.57 (s, 4H), 8.36 (s, 4H), 7.97 (s, 2H), 7.53 (d, [3]J_{H-H} = 7.2 Hz, 2H), 7.44 (s, 2H), 7.39 (d, [3]J_{H-H} = 8.8 Hz, 2H), 4.15 (m, 4H), 4.00 (s, 12H), 3.91 (s, 12H), 1.15 (m, 6H). (*Rac*)-5,5',5'',5'''-(2,2'-diethoxy-1,1'-binaphthyl-4,4',6,6'-tetrayl)tetraisophthalate was prepared in the same fashion except (*Rac*)-4,4',6,6'-tetrabromo-2,2'-ethoxy-1,1'-binaphthalene was used.

4.5.2.2 (*R*)-5,5',5'',5'''-(2,2'-diethoxy-1,1'-binaphthyl-4,4',6,6'-tetrayl)tetraisophthalic acid (L_{20}-H_8)

A solution of octamethyl 5,5',5'',5'''-(2,2'-diethoxy-1,1'-binaphthyl-4,4',6,6'-tetrayl)tetraisophthalate (180 mg, 0.16 mmol) in THF (10 mL), MeOH (5mL), and 2M aqueous NaOH (5 mL) was heated at 70 °C for 18 h. The solution was cooled to r.t. and acidified to a pH of ~1 and extracted with ethyl acetate/H_2O. The organic layer was dried over $MgSO_4$ and the solvent was evaporated under reduced pressure to give a white solid of L_{20}-H_8. Yield: (135 mg, 83%). ^{1}H NMR $(CD_3)_2CO$: δ 13.5 (bs, 8H), 8.62 (s, 2H), 8.43 (s, 4H), 8.38 (s, 2H), 8.26 (s, 4H), 7.97 (s, 2H), 7.73 (m, 2H), 7.69 (s, 2H), 7.33 (d, [3]J_{H-H} = 8.8

Hz, 2H), 4.24 (m, 4H), 1.04 (m, 6H). IR data: 2918vb, 1681vs, 1598w, 1446w, 1259s, 1207vs, 1107w, 1037w, 800w, 790 w, 758vs, 665s, 640s. *rac*- IR data: 2978w, 1635s, 1558s, 1417s, 1367vs, 1265w, 1215w, 1112w, 1016m, 773s, 732vs, 700s.

4.5.2.3 (*R*)-5,5',5'',5'''-(1,1'-bi-2-naphthol-4,4',6,6'-tetrayl)tetraisophthalic acid (L$_{21}$-H$_8$)

A solution of (*R*)-octamethyl 5,5',5'',5'''-(2,2'-diethoxy-1,1'-binaphthyl-4,4',6,6'-tetrayl)tetraisophthalate (388 mg, 0.35 mmol) in anhydrous CH_2Cl_2 (20 mL) was degassed for 15 minutes. BBr_3 (1 mL, 10.4 mmol) was added under Argon at 0 °C. The dark brown solution was allowed to warm to r.t. and stirred at r.t. for 18 h. The solution was poured into iced water and then extracted with CH_2Cl_2/H_2O. The organic layer was dried over $MgSO_4$ and the solvent was removed under reduced pressure. The crude reaction mixture was then refluxed in MeOH (20 mL) with a catalytic amount of H_2SO_4 for 4 h. The solution was extracted with ethyl acetate/H_2O and the organic layer dried over $MgSO_4$. Upon evaporating the solvent, the crude product was dissolved in a solution of THF (20 mL), MeOH (10 mL), and 2M NaOH (10 mL) which was heated at 70 °C for 18 h. The solution was acidified to a pH of ~1 using 4M HCl. The solution was extracted with ethyl acetate/H_2O and the organic layer briefly dried over $MgSO_4$. The remaining solvent was removed under reduced pressure to give a white solid of L$_{21}$-H$_8$. Yield: (200 mg, 61%). ^{1}H NMR (DMSO-d$_6$): δ 13.50 (bs, 8H), 9.80 (s, 2H), 8.62 (s, 2H), 8.39 (s, 2H), 8.38 (s, 4H), 8.26 (s, 4H), 7.94 (s, 2H), 7.70 (d, $^3J_{H-H}$ = 8.8 Hz, 2H), 7.41 (s, 2H), 7.36 (d, $^3J_{H-H}$ = 8.8 Hz, 2H). IR data: 2922vb, 2536b, 1681 vs, 1597m, 1373m, 1238vs, 1205vs, 1190vs, 1149s, 1112m, 1041m, 877s, 821s, 802s, 706vs, 686vs, 657vs.

4.5.2.4 (*R*)-4,4',6,6'-tetrabromo-1,1'-binaphthyl-2,2'-diol

A solution of (R)-4,4',6,6'-tetrabromo-2,2'-ethoxy-1,1'-binaphthalene (5.0 g, 7.6 mmol) in CH_2Cl_2 (75 mL) was cooled to 0 °C in an ice/water bath, and 21.9 mL of BBr_3 (57 g, 228 mmol) was added via a syringe slowly. The reaction mixture was allowed to warm to r.t. and stirred at r.t. for 18 hrs. The solution was poured into iced water and then extracted with CH_2Cl_2 and washed with H_2O. The organic layer was dried over $MgSO_4$ and the solvent was removed under reduced pressure. ^{1}H NMR spectrum of the resulting solid (3.8 g, 84% yield) indicated good purity of the desired product. The product was used for subsequent synthesis without further purification. ^{1}HNMR (CDCl$_3$, 400 MHz), 8.43 (d, $^4J_{H-H}$ = 2 Hz, 2H), 7.21 (s, 2H), 7.39 (dd, $^4J_{H-H}$ = 2 Hz, $^3J_{H-H}$ = 9 Hz, 6.93(d, $^3J_{H-H}$ = 9 Hz, 2H), 5.09 (s, 2H).

4.5.2.5 (R)-2,2'-bis(benzyloxy)-4,4',6,6'-tetrabromo-1,1'-binaphthyl

A solution of (R)- 4,4',6,6'-tetrabromo-1,1'-binaphthyl-2,2'-diol (2 g, 3.32 mmol), (bromomethyl)benzene (3.94 mL, 33.2 mmol), and KOH (1.9g, 34 mmol) in acetone (100 mL) was refluxed under Argon for 2 h. Upon cooling to RT, acetone was removed under reduced pressure and the remaining mixture was extracted with ethyl acetate/H_2O. The white solid was purified by silica gel chromatography with hexanes/ethyl acetate (8:1 v/v) as the eluent to afford the desired product (R)-2,2'-bis(benzyloxy)-4,4',6,6'-tetrabromo-1,1'-binaphthyl as a white solid. Yield: (1.8g, 70%). ^{1}H NMR (CDCl$_3$): δ 8.39 (s, 2H), 7.72 (s, 2H), 7.29 (d, $^3J_{H-H}$ = 8.8 Hz, 2H), 7.10-7.17 (m, 6H), 6.91-6.96 (m, 6H), 5.01 (s, 4H).

4.5.2.6　　(R)-octamethyl-5,5',5'',5'''-(2,2'-bis(benzyloxy)-1,1'-binaphthyl-4,4',6,6'-tetrayl)tetraisophthalate (L$_{22}$-Me$_8$)

A solution of (R)-2,2'-bis(benzyloxy)-4,4',6,6'-tetrabromo-1,1'-binaphthyl (300 mg, 0.384 mmol) and dimethyl-5-(pinacolboryl)isophthalate (736 mg, 2.29 mmol) in dimethyl

ethylene glycol (25 mL) was degassed for 10 min. CsF (466 mg, 3.07 mmol) and Pd(PPh$_3$)$_4$ (53 mg, 0.046 mmol) were added to the solution. The reaction vessel was sealed and the reaction mixture was stirred at 95 °C for 4 days. Upon cooling to r.t., the mixture was extracted with CH$_2$Cl$_2$/H$_2$O. The yellow solution was dried over MgSO$_4$ and the solvent removed under reduced pressure. The yellow solid was purified by silica gel column chromatography with hexanes/ethyl acetate (1:1 v/v) as the eluent to afford (*R*)-octamethyl 5,5',5'',5'''-(2,2'-bis(benzyloxy)-1,1'-binaphthyl-4,4',6,6'-tetrayl)tetraisophthalate. Yield: (250 mg, 53%). ^{1}H NMR (CDCl$_3$): δ 8.84 (s, 2H), 8.59 (s, 2H), 8.54 (s, 4H), 8.39 (s, 4H), 8.03 (s, 2H), 7.59 (d, $^3J_{H\text{-}H}$ = 8.8 Hz, 2H), 7.50 (d, $^3J_{H\text{-}H}$ = 8.4 Hz, 4H), 7.15 (d, $^3J_{H\text{-}H}$ = 6.8 Hz, 6H), 7.03 (d, $^3J_{H\text{-}H}$ = 6.8 Hz, 4H), 5.17 (s, 4H), 4.02 (s, 12H), 3.92 (s, 12H).

4.5.2.7   **(*R*)-5,5',5'',5'''-(2,2'-bis(benzyloxy)-1,1'-binaphthyl-4,4',6,6'-tetrayl)tetraisophthalic acid (L$_{22}$-H$_8$)**

A solution of (*R*)-octamethyl 5,5',5'',5'''-(2,2'-bis(benzyloxy)-1,1'-binaphthyl-4,4',6,6'-tetrayl)tetraisophthalate (200 mg, 0.162 mmol) in THF (10 mL), MeOH (5mL), and 2M aqueous NaOH (5 mL) was heated at 70 °C for 18 h. The solution was cooled to r.t. and acidified to a pH of ~1 and extracted with ethyl acetate/H$_2$O. The organic layer was dried over MgSO$_4$ and the solvent was evaporated under reduced pressure to give a white solid of **L$_{22}$**-H$_8$. Yield: (150 mg, 82%). ^{1}H NMR (DMSO-d$_6$): δ 13.21 (bs, 8H), 8.64 (s, 2H), 8.41 (s, 6H), 8.30 (s, 4H), 8.02 (s, 2H), 7.80 (s, 4H), 7.46 (d, $^3J_{H\text{-}H}$ = 8.8 Hz, 2H), 7.16 (s, 6H), 7.07 (s, 4H), 5.32 (s, 4H). IR data: 2926w, 2534w, 2160w, 2027w, 1977w, 1681vs, 1598m, 1579m, 1450m, 1259vs, 1195vs, 1105s, 1041m, 1010m, 918w, 867m, 819m, 800m, 758vs, 734m, 696vs, 661vs.

4.5.2.8 **(*R*)-(2,2'-diethoxy-1,1'-binaphthyl-4,4',6,6'-tetrayl)tetrakis(ethyne-2,1-diyl)tetrakis(trimethylsilane)**

A solution of (*R*)-4,4',6,6'-tetrabromo-2,2'-ethoxy-1,1'-binaphthalene (6.5 g, 9.88 mmol) and ethynyltrimethylsilane (17.5 ml, 125 mmol) in toluene (50 ml) and triethylamine (60 ml) was degassed for 10 min. CuI (380 mg, 2 mmol) and $Pd(PPh_3)_2Cl_2$ (710 mg, 1mmol) were added to the solution. The reaction flask was fitted with a reflux condenser and the mixture was stirred under argon at 100 °C for 2 days. Upon cooling to r.t., the mixture was extracted with CH_2Cl_2/H_2O. The orange solution was dried over $MgSO_4$ and the solvent removed under reduced pressure. The orange solid was purified by silica gel column chromatography with CH_2Cl_2 as the eluent to afford (*R*)-(2,2'-diethoxy-1,1'-binaphthyl-4,4',6,6'-tetrayl)tetrakis(ethyne-2,1-diyl)tetrakis(trimethylsilane). Yield: (7.0 g, 97%). ^{1}H NMR ($CDCl_3$): δ 8.44 (s, 2H), 7.56 (s, 2H), 7.22 (m, 2H), 6.95 (d, $^3J_{H-H}$ = 11.6 Hz, 2H), 4.00 (m, 4H), 1.00 (t, $^3J_{H-H}$ = 6.1 Hz, 6H), 0.37 (s, 9H), 0.25 (s, 9H).

4.5.2.9 (*R*)-2,2'-diethoxy-4,4',6,6'-tetraethynyl-1,1'-binaphthyl

A mixture of (*R*)-(2,2'-diethoxy-1,1'-binaphthyl-4,4',6,6'-tetrayl)tetrakis(ethyne-2,1-diyl)tetrakis(trimethylsilane) (7.0 g, 9.62 mmol) and K_2CO_3 (7.9 g, 57.6 mmol) in THF (100 mL) and MeOH (100 mL) was stirred at r.t. under N_2 for 1.5 h. The dark brown mixture was extracted with CH_2Cl_2/H_2O and dried over $MgSO_4$ and the solvent removed under reduced pressure. The dark brown solid was purified by silica gel column chromatography with CH_2Cl_2 as the eluent to afford (*R*)-2,2'-diethoxy-4,4',6,6'-tetraethynyl-1,1'-binaphthyl as an dark orange solid. Yield: (3.5 g, 83%). ^{1}H NMR ($CDCl_3$): δ 8.53 (s, 2H), 7.63 (s, 2H), 7.25 (m, 2H), 7.02 (d, $^3J_{H-H}$ = 11.6 Hz, 2H), 4.03 (m, 4H), 3.56 (s, 2H), 3.12 (s, 2H), 1.05 (t, $^3J_{H-H}$ = 9.2 Hz, 6H).

4.5.2.10 (*R*)-octamethyl-5,5',5'',5'''-(2,2'-diethoxy-1,1'-binaphthyl-4,4',6,6'-tetrayl)tetrakis(ethyne-2,1-diyl)tetraisophthalate (L$_{23}$-Me$_8$)

A solution of (*R*)-2,2'-diethoxy-4,4',6,6'-tetraethynyl-1,1'-binaphthyl (2.0 g, 4.56 mmol) and dimethyl 5-bromoisophthalate (12.45 g, 45.6 mmol) in toluene (150 mL) and triethylamine (6.27 mL, 45.6 mmol) was degassed for 10 min. CuI (34.7 mg, 0.18 mmol) and Pd(PPh$_3$)$_2$Cl$_2$ (640 mg, 0.91 mmol) were added to the brown solution. The reaction vessel was fitted with a reflux condenser and the mixture was stirred under argon at 110 °C for 3 days. Upon cooling to r.t., the dark brown reaction mixture was extracted with CH$_2$Cl$_2$/H$_2$O. The dark orange solution was dried over MgSO$_4$ and the solvent removed under reduced pressure. The dark orange solid was purified by silica gel chromatography with hexanes/ethyl acetate as the eluent to afford (*R*)-octamethyl 5,5',5'',5'''-(2,2'-diethoxy-1,1'-binaphthyl-4,4',6,6'-tetrayl)tetrakis(ethyne-2,1-diyl)tetraisophthalate. Yield: (1.7g, 31%). ^{1}H NMR (CDCl$_3$): δ 8.69 (s, 2H), 8.59 (m, 4H), 8.55 (s, 4H), 8.39 (s, 4H), 7.73 (s, 2H), 7.39 (d, $^3J_{H-H}$ = 8.8 Hz, 2H), 7.16 (d, $^3J_{H-H}$ = 9.2 Hz, 2H), 4.12 (m, 4H), 3.99 (s, 12H), 3.94 (s, 12H), 1.13 (t, $^3J_{H-H}$ = 6.8 Hz, 6H).

4.5.2.11 (*R*)-5,5',5'',5'''-(2,2'-diethoxy-1,1'-binaphthyl-4,4',6,6'-tetrayl)tetrakis(ethyne-2,1-diyl)tetraisophthalic acid (L$_{23}$-H$_8$)

A solution of (*R*)-octamethyl 5,5',5'',5'''-(2,2'-diethoxy-1,1'-binaphthyl-4,4',6,6'-tetrayl)tetrakis(ethyne-2,1-diyl)tetraisophthalate (268 mg, 0.22 mmol) in THF (10 mL), MeOH (5 mL), and 2M NaOH (5 mL) was stirred at 70 °C for 18 h. Upon cooling to r.t., the dark brown solution was acidified to pH ~2 using 4M HCl. The pale orange solution was worked up in EA/H$_2$O and the organic layer was dried over MgSO$_4$. The solvent was removed under reduced pressure to give L$_{23}$-H$_8$ as a yellow solid. Yield: (240 mg, >99%).

^{1}H NMR (DMSO): δ 13.51 (bs, 8H), 8.65 (s, 2H), 8.51 (m, 6H), 8.42 (s, 2H), 8.30 (s, 4H), 8.09 (s, 2H), 7.54 (d, $^3J_{H-H}$ = 8.8 Hz), 7.10 (d, $^3J_{H-H}$ = 8.8 Hz), 4.19 (m, 4H), 1.04 (t, $^3J_{H-H}$ = 7.0 Hz).

4.5.2.12 (*R*)-5,5',5'',5'''-(2,2'-dihydroxy-1,1'-binaphthyl-4,4',6,6'-tetrayl)tetrakis(ethyne-2,1-diyl)tetraisophthalic acid (L$_{24}$-H$_8$)

A solution of (*R*)-octamethyl 5,5',5'',5'''-(2,2'-diethoxy-1,1'-binaphthyl-4,4',6,6'-tetrayl)tetrakis(ethyne-2,1-diyl)tetraisophthalate (330 mg, 0.273 mmol) in dry CH_2Cl_2 (25 mL). The yellow solution was cooled to 0 °C and BBr_3 (790 μL, 8.19 mmol) was added turning the solution a dark brown color. After several minutes, precipitate formed. The mixture was allowed to warm to r.t. overnight (18 h). The solution was poured into iced water and then extracted with CH_2Cl_2/H_2O. The organic layer was dried over $MgSO_4$ and the solvent was removed under reduced pressure. The crude reaction mixture was then refluxed in MeOH (20 mL) with a catalytic amount of H_2SO_4 for 4 h. The solution was extracted with ethyl acetate/H_2O and the organic layer dried over $MgSO_4$. Upon evaporating the solvent, the crude product was dissolved in a solution of THF (20 mL), MeOH (10 mL), and 2M NaOH (10 mL) which was heated at 70 °C for 18 h. The solution was acidified to a pH of ~1 using 4M HCl. The solution was extracted with ethyl acetate/H_2O and the organic layer briefly dried over $MgSO_4$. The remaining solvent was removed under reduced pressure to give a yellow solid of **L$_{24}$-H$_8$**. Yield: (180 mg, 64%). ^{1}H NMR (DMSO): δ 13.45 (bs, 8H), 10.08 (s, 2H), 8.56 (s, 2H), 8.50 (s, 2H), 8.47 (s, 4H), 8.42 (s, 2H), 8.28 (s, 4H), 7.73 (s, 2H), 7.53 (d, $^3J_{H-H}$ = 8.8 Hz), 7.11 (d, $^3J_{H-H}$ = 8.8 Hz).

4.5.2.13 (*R*)-(2,2'-bis(benzyloxy)-1,1'-binaphthyl-4,4',6,6'-tetrayl)tetrakis(ethyne-2,1-diyl)tetrakis(trimethylsilane)

A solution of (*R*)-2,2'-bis(benzyloxy)-4,4',6,6'-tetrabromo-1,1'-binaphthyl (1.0 g, 1.27 mmol) and ethynyltrimethylsilane (2.2 ml, 16 mmol) in toluene (10 ml) and triethylamine (15 ml) was degassed for 10 min. CuI (48 mg, 0.254 mmol) and Pd(PPh$_3$)$_2$Cl$_2$ (89 mg, 0.127 mmol) were added to the solution. The reaction flask was fitted with a reflux condenser and the mixture was stirred under argon at 100 °C for 2 days. Upon cooling to r.t., the mixture was extracted with CH$_2$Cl$_2$/H$_2$O. The orange solution was dried over MgSO$_4$ and the solvent removed under reduced pressure. The orange solid was purified by silica gel column chromatography with CH$_2$Cl$_2$ as the eluent to afford (*R*)-(2,2'-bis(benzyloxy)-1,1'-binaphthyl-4,4',6,6'-tetrayl)tetrakis(ethyne-2,1-diyl)tetrakis(trimethylsilane). Yield: (1.0 g, 92%). ^{1}H NMR (CDCl$_3$): δ 8.55 (s, 2H), 7.68 (s, 2H), 7.32 (d, $^3J_{H-H}$ = 8.8 Hz, 2H), 7.17 (m, 6H), 7.08 (d, $^3J_{H-H}$ = 8.4 Hz, 2H), 6.95 (d, $^3J_{H-H}$ = 6.4 Hz, 4H), 5.05 (s, 4H), 0.44 (s, 18H), 0.33 (s, 18H).

4.5.2.14 (*R*)-2,2'-bis(benzyloxy)-4,4',6,6'-tetraethynyl-1,1'-binaphthyl

A mixture of (*R*)-(2,2'-bis(benzyloxy)-1,1'-binaphthyl-4,4',6,6'-tetrayl)tetrakis(ethyne-2,1-diyl)tetrakis(trimethylsilane) (1.0 g, 1.17 mmol) and K$_2$CO$_3$ (1.0 g, 7.02 mmol) in THF (25 mL) and MeOH (25 mL) was stirred at r.t. under N$_2$ for 1.5 h. The dark brown mixture was extracted with CH$_2$Cl$_2$/H$_2$O and dried over MgSO$_4$ and the solvent removed under reduced pressure. The dark brown solid was purified by silica gel column chromatography with CH$_2$Cl$_2$ as the eluent to afford (*R*)-2,2'-diethoxy-4,4',6,6'-tetraethynyl-1,1'-binaphthyl as an dark orange solid. Yield: (0.5 g, 76%). ^{1}H NMR (CDCl$_3$): δ 8.58 (s, 2H), 7.68 (s, 2H), 7.33 (d, $^3J_{H-H}$ = 8.4 Hz, 2H), 7.13 (d, $^3J_{H-H}$ = 6.8 Hz, 10H), 5.05 (s, 4H), 3.57 (s, 2H), 3.15 (s, 2H).

4.5.2.15 (*R*)-octamethyl-5,5',5'',5'''-(2,2'-bis(benzyloxy)-1,1'-binaphthyl-4,4',6,6'-tetrayl)tetrakis(ethyne-2,1-diyl)tetraisophthalate (L₂₅-Me₈)

A solution of (*R*)-2,2'-diethoxy-4,4',6,6'-tetraethynyl-1,1'-binaphthyl (486 mg, 0.863 mmol) and dimethyl 5-bromoisophthalate (2.3 g, 8.63 mmol) in toluene (25 mL) and triethylamine (1.2 mL, 8.63 mmol) was degassed for 10 min. CuI (6.6 mg, 0.0345 mmol) and Pd(PPh₃)₂Cl₂ (121 mg, 0.173 mmol) were added to the brown solution. The reaction vessel was fitted with a reflux condenser and the mixture was stirred under argon at 110 °C for 3 days. Upon cooling to r.t., the dark brown reaction mixture was extracted with CH₂Cl₂/H₂O. The dark orange solution was dried over MgSO₄ and the solvent removed under reduced pressure. The dark orange solid was purified by silica gel chromatography with hexanes/ethyl acetate (1:1 v/v) as the eluent to afford (*R*)-octamethyl 5,5',5'',5'''-(2,2'-bis(benzyloxy)-1,1'-binaphthyl-4,4',6,6'-tetrayl)tetrakis(ethyne-2,1-diyl)tetraisophthalate **L₂₅**-Me₈ . Yield: (392 mg, 34%). ¹H NMR (CDCl₃): δ 8.70 (s, 2H), 8.61 (s, 4H), 8.55 (s, 4H), 8.40 (s, 4H), 7.76 (s, 2H), 7.41 (d, ³J_{H-H} = 8.4 Hz, 2H), 7.14-7.22 (m, 8H), 6.98 (m, 4H), 5.12 (s, 4H), 3.99 (s, 12H), 3.92 (s, 12H).

4.5.2.16 (*R*)- 5,5',5'',5'''-(2,2'-bis(benzyloxy)-1,1'-binaphthyl-4,4',6,6'-tetrayl)tetrakis(ethyne-2,1-diyl)tetraisophthalic acid (L₂₅-H₈)

A solution of (*R*)-octamethyl 5,5',5'',5'''-(2,2'-bis(benzyloxy)-1,1'-binaphthyl-4,4',6,6'-tetrayl)tetrakis(ethyne-2,1-diyl)tetraisophthalate (130 mg, 0.097 mmol) in THF (10 mL), MeOH (5 mL), and 2M NaOH (5 mL) was stirred at 70 °C for 18 h. Upon cooling to r.t., the dark brown solution was acidified to pH ~2 using 4M HCl. The pale yellow solution was worked up in EA/H₂O and the organic layer was dried over MgSO₄. The solvent was removed under reduced pressure to give **L₂₅**-H₈ as a yellow solid which was recrystallized from acetone. Yield: (52 mg, 42%). ¹H NMR (DMSO): δ 13.59 (bs, 8H), 8.68 (s, 2H), 8.51

(m, 6H), 8.44 (s, 2H), 8.30 (s, 4H), 8.17 (s, 2H), 7.58 (d, $^3J_{H-H}$ = 8.8 Hz, 2H), 7.16 (s, 8H), 7.02 (s, 4H), 5.30 (s, 4H).

4.5.3 Preparation and characterization of crystals

4.5.3.1 [Cu$_4$(*R*-L$_{20}$)(H$_2$O)$_4$]·12DEF·2H$_2$O (4.1)

A mixture of **L$_{20}$**-H$_8$ (10 mg, 0.01 mmol) and Cu(NO$_3$)$_2$·2.5H$_2$O (10 mg, 0.043 mmol) was dissolved in a solvent mixture of DEF/H$_2$O (1.5 mL/0.5 mL) with several drops of HCl (3M, aq.) in a screw-capped vial. The resulting mixture was placed in an oven at 80 ^{o}C for 2days. Green-blue crystals (17 mg, 67%) with very thin plate-shape were obtained after filtration. Solvent content calc. from the proposed formula: DEF, 47.2%; H$_2$O, 4.2%; determined by ^{1}H NMR/TGA: DEF, 48.2%; H$_2$O, 3.9%. IR data: 2980w, 1705m, 1570m, 1435s, 1369vs, 1213s, 1112m, 1043m, 775vs, 732vs, 694s.

4.5.3.2 [Cu$_4$(*rac*-L$_{20}$)(H$_2$O)$_4$]·12DEF·2H$_2$O (4.1')

The same procedure as **1**, except *rac*-**L**-H$_8$ was used. Green-blue crystals (15 mg, 59%) with very thin plate-shape were obtained after filtration. Solvent content calc. from the proposed formula: DEF, 47.2%; H$_2$O, 4.2%; determined by ^{1}H NMR/TGA: DEF, 46.6%; H$_2$O, 4.3%. IR data: 2978w, 1635m, 1558s, 1417s, 1367vs, 1265m, 1215m, 1112m, 1016m, 773s, 732vs, 700s.

4.5.3.3 [Cu$_4$(L$_{21}$)(H$_2$O)$_4$]·14DMF·2H$_2$O (4.2)

A mixture of **L$_{21}$**-H$_8$ (11 mg, 0.012 mmol) and Cu(ClO$_4$)$_2$ • 6H$_2$O (17.3 mg, 0.0465 mmol) was dissolved in a solvent mixture of DMF/H$_2$O (1.1 mL/0.55 mL) with 110 μL of HCl (1M, aq.) in a screw-capped vial. The resulting mixture was placed in an oven at 80 ^{o}C for 18 h. Green-blue crystals (16 mg, 60 %) with very thin plate-shape were obtained after

filtration. Solvent content calc. from the proposed formula: DMF, 44.0 %; H_2O, 4.6 %; determined by ^1H NMR/TGA: DMF, 44.6 %; H_2O, 4.4 %. IR data: 2943w, 1635s, 1564m, 1436s, 1369vs, 1018w, 775s, 732vs, 694s.

4.5.3.4 [Cu$_4$(L$_{22}$)(H$_2$O)$_4$]·8DMF·13H$_2$O (4.3)

A mixture of **L$_{22}$**-H$_8$ (1 mg, 0.89 μmol) and $Cu(ClO_4)_2 \cdot 6H_2O$ (1.31 mg, 3.53 μmol) was dissolved in a solvent mixture of DMF/H_2O (0.1 mL/0.05 mL) with HCl (2.0 M, 10μL) in a screw-capped vial. The resulting mixture was placed in an oven at 80 ºC for 1 day. Green-blue crystals (1.87 mg, 64%) with very thin octagonal plate-shape were obtained after filtration. Solvent content calc. from the proposed formula: DMF, 26.0%; H_2O, 12.9%; determined by ^1H NMR/TGA: DMF, 25.4%; H_2O, 13.6%. IR data: 2160w, 1699w, 1633s, 1579m, 1417s, 1367vs, 1327m, 1263m, 1234m, 1205m, 1107w, 1028w, 879w, 819w, 773s, 731vs, 696s.

4.5.3.5 [Cu$_4$(L$_{23}$)(H$_2$O)$_4$]·20DEF (4.4)

A mixture of **L$_{23}$**-H$_8$ (1 mg, 0.91 μmol) and $Cu(ClO_4)_2 \cdot 6H_2O$ (1.35 mg, 3.65 μmol) was dissolved in a solvent mixture of DEF/H_2O (0.3 mL/0.025 mL) with 1M HCl (10 μL) in a screw-capped vial. The resulting solution was placed in an oven at 80 ^{o}C for 2 days. Blue-green crystals (2.2 mg, 69%) with very thin plate-shape were obtained after filtration. Solvent content calc. from the proposed formula: DEF, 58.8%; H_2O, 2.0%; determined by ^1H NMR/TGA: DEF, 58.7%; H_2O, 1.9%.

4.5.3.6 [Cu$_4$(L$_{24}$)(H$_2$O)$_4$]·16DMF·5H$_2$O (4.5)

A mixture of **L$_{24}$**-H$_8$ (1 mg, 0.96 μmol) and $Cu(ClO_4)_2 \cdot 6H_2O$ (1.42 mg, 3.85 μmol) was dissolved in a solvent mixture of DMF/H_2O (0.1 mL/0.050 mL) with 10 μL of 1M HCl

(10 μL) in a screw-capped vial. The resulting solution was placed in an oven at 80 $^{\circ}$C for 4

h. Dark green crystals (1.8 mg, 75%) with very thin plate-shape were obtained after

filtration. Solvent content calc. from the proposed formula: DMF, 44.6%; H_2O, 6.1%;

determined by ^{1}H NMR/TGA: DMF, 44.1%; H_2O, 6.3%.

4.5.3.7 [Cu$_4$(L$_{25}$)(H$_2$O)$_4$]·14DMF (4.6)

A mixture of **L$_{25}$**-H$_8$ (1 mg, 0.82 μmol) and Cu(ClO$_4$)$_2$·6H$_2$O (1.21 mg, 3.26 μmol)

was dissolved in a solvent mixture of DMF/H$_2$O (0.1 mL/0.025 mL) with 10 μL of 2M HCl

(10 μL) in a screw-capped vial. The resulting solution was placed in an oven at 80 $^{\circ}$C for 18

h. Green crystals (1.42 mg, 68%) with very thin plate-shape were obtained after filtration.

Solvent content calc. from the proposed formula: DMF, 40.0%; H_2O, 2.8%; determined by

^{1}H NMR/TGA: DMF, 40.5%; H_2O, 2.7%.

4.6 References

[1] Schlapbach, L.; Zuttel, A. Hydrogen-storage materials for mobile applications. *Nature* **2001**, *414*, 353-358.

[2] Hydrogen Fuel Cells & Infrastructure Technologies Program: Multi-year Research, Development, and Demonstration Plan, U. S. Dept. of Energy, **2005**.

[3] Fletcher, A. J.; Thomas, K. M.; Rosseinsky, M. J. Flexibility in metal-organic framework materials: Impact on sorption properties. *J. Solid State Chem.* **2005**, *178*, 2491-2510.

[4] Latroche, M.; Surble, S.; Serre, C.; Mellot-Draznieks, C.; Llewellyn, P. L.; Lee, J.-H., Chang, J.-S.; Jhung, S. H.; Ferey, G. Hydrogen storage in the giant-pore metal-organic frameworks MIL-100 and MIL-101. *Angew. Chem. Int. Ed.* **2006**, *45* (48), 8227-8231.

[5] (a) Rowsell, J. L. C.; Yaghi, O. M. Effects of functionalization, catenation, and variation of the metal oxide and organic linking units on the low-pressure hydrogen adsorption properties of metal-organic frameworks. *J. Am. Chem. Soc.* **2006**, *128* (4), 1304-1315; (b) Rowsell, J. L. C.; Millward, A. R.; Park, K. S.; Yaghi, O. M. Hydrogen sorption in functionalized metal-organic frameworks. *J. Am. Chem. Soc.* **2004**, *126* (18), 5666-5667.

[6] Wong-Foy, A. G.; Matzger, A. J.; Yaghi, O. M. Exceptional H_2 saturation uptake in microporous metal-organic frameworks. *J. Am. Chem. Soc.* **2006**, *128* (11), 3494-3495.

[7] Collins, D. J.; Zhou, H.-C. Hydrogen storage in metal organic frameworks. *J. Mater. Chem.*, **2007**, *17* , 3154-3160.

[8] Wong-Foy, A. G.; Matzger, A. J.; Yaghi, O. M. Exceptional H_2 saturation uptake in microporous metal-organic frameworks. *J. Am. Chem. Soc.* **2006**, *128* (11), 3494-3495.

[9] Eddaoudi, M.; Kim, J.; Rosi, N.; Vodak, D.; Wachter, J.; O'Keeffe, M.; Yaghi, O. M. Systematic design of pore size and functionality in isoreticular MOFs and their application in methane storage. *Science*, **2002**, *295*, 469-472.

[10] Chae, H. K.; Siberio-Perez, D. Y.; Kim, J.; Go, Y.-B.; Eddaoudi, M.; Li, J. L. C.; Yaghi, O. M. A route to high surface area, porosity and inclusion of large molecule in crystals. *Nature*, **2004**, *427*, 523-527.

[11] Rosi, N. L.; Kim, J.; Eddaoudi, M.; Chen, B.; O'Keeffe, M.; Yaghi, O. M. Rod packings and metal-organic frameworks constructed from rod-shaped secondary building units. *J. Am. Chem. Soc.* **2005**, *127* (5), 1504-1518.

[12] Chui. S. S.-Y.; Lo, S. M.-F.; Charmant, J. P. H.; Orpen, A. G.; Williams, I. D. A chemically functionalizable nanoporous material [Cu$_3$(TMA)$_2$(H$_2$O)$_3$]$_n$. *Science*, **1999**, *283*, 1148-1150.

[13] (a) Kesanli, B.; Cui, Y.; Smith, M. R.; Bittner, E. W.; Bockrath, B. C.; Lin, W. Highly interpenetrated metal-organic frameworks for hydrogen storage. *Angew. Chem. Int. Ed.*, **2005**, *44* (1), 72-75; (b) Chun, H.; Dybtsev, D. N.; Kim, H.; Kim, K. Synthesis, X-ray crystal structures, and gas sorption properties of pillared square grid nets based on paddle-wheel motifs: Implications for hydrogen storage in porous materials. *Chem.-Eur. J.* **2005**, *11* (12), 3521-3529.

[14] Batten, S. T.; Robson, R. Interpenetrating nets: Ordered, periodic entanglement. *Angew. Chem. Int. Ed.* **1998**, *37* (11), 1460-1494.

[15] Li, J.; Furuta, T.; Goto, H.; Ohashi, T.; Fujiwara, Y.; Yip, S. Theoretical evaluation of hydrogen storage capacity in pure carbon nanostructures. *J. Chem. Phys.* **2003**, *119* (4), 2376-2385.

[16] (a) Reineke, T. M.; Eddaoudi, M.; Moler, D.; O'Keeffe, Yaghi, O. M. Large free volume in maximally interpenetrating networks: The role of secondary building units exemplified by Tb$_2$(ADB)$_3$[(CH$_3$)$_2$SO]$_4$• 16[(CH$_3$)$_2$SO] *J. Am. Chem. Soc.* **2000**, *122* (19), 4843-4844; (b) Evans, O. R.; Wang, Z.; Xiong, R.-G., Foxman, B. M.; Lin, W. Nanoporous, interpenetrated metal-organic diamondoid networks. *Inorg. Chem.*, **1999**, *38*, 2969-2973; (c) Ma, S.; Sun, D.; Ambrogio, M. W.; Fillinger, J. A.; Parkin, S.; Zhou, H.-C. Framework-catenation isomerism in metal-organic frameworks and its impact on hydrogen uptake. *J. Am. Chem. Soc.* **2007**, *129* (7), 1858-1859.

[17] (a) Rosi, N. L.; Eckert, J.; Eddaoudi, M.; Vodak, D. T.; Kim, J.; O'Keeffe, M.; Yaghi, O. M. Hydrogen storage in microporous metal-organic frameworks. *Science*, **2003**, *300*, 1127-1129; (b) Smith, M. R.; Bittner, E. W.; Shi, W.; Johnson, J. K.; Bockrath, B. C. Chemical activation of single-walled carbon nanotubes for hydrogen adsorption. *J. Phys. Chem. B,* **2003**, *107*, 3752-3760; (c) Pan, L.; Sander, J. K.; Huang, X.; Li, J.; Smith, M.; Bittner, E.; Bockrath, B.; Johnson, J. K. Microporous metal organic materials: Promising candidates as sorbents for hydrogen storage. *J. Am. Chem. Soc.* **2004**, *126* (5), 1308-1309; (d) Dybstev, D. N.; Chun, H.; Yoon, S. H.; Kim, D.; Kim, K. Microporous manganese formate: A simple metal-organic porous material with high framework stability and highly selective gas sorption properties. *J. Am. Chem. Soc.* **2004**, *126* (1), 32-33; (e) Ferey, G.; Latroche, M.; Serre, C.; Millange, F.; Loiseau, T.; Percheron-Guegan, A. Hydrogen adsorption in the nanoporous metal-benzenedicarboxylate M(OH)(O$_2$C-C$_6$H$_4$-CO$_2$)(M = Al^{3+}, Cr^{3+}), MIL-53. *Chem. Commun.*, **2003**, *24*, 2976-2977.

[18] (a) Chen, B.; Ockwig, N. W.; Millward, A. R.; Contreras, D. S.; Yaghi, O. M. High H$_2$ adsoprtion in a microporous metal-organic framework with open metal sites. *Angew. Chem. Int. Ed.*, **2005**, *44* (30), 4745-4749; (b) Dinca, M.; Yu, A. F.; Long, J. R. Microporous metal-organic frameworks incorporating 1,4-benzeneditetrazolate: Synthesis, structures, and

hydrogen storage properties. *J. Am. Chem. Soc.* **2006**, *128* (27), 8904-8913; (c) Prestipino, C.; Regli, L.; Vitillo, J. G.; Bonino, F.; Damin, A.; Lamberti, C.; Zecchina, A.; Solari, P. L.; Kongshaug, K. O.; Bordiga, S. *Chem. Mater.* **2006**, *18*(2), 278-.

[19] (a) Kitagawa, S.; Kitaura, R.; Noro, S. Functional porous coordination polymers. *Angew. Chem. Int. Ed.* **2004**, *43* (18), 2334-2375. (b) Bradshaw, D.; Warren, J. E.; Rosseinsky, M. J. Reversible concerted ligand substitution at alternating metal sites in an extended solid. *Science* **2007**, *315* (5814), 977-980. (c) Evans, O. R.; Lin, W. Crystal engineering of NLO materials based on metal-organic coordination networks. Acc. Chem. Res. **2002**, *35* (7), 511-522.

[20] Eddaoudi, M.; Kim, J.; Rosi, N.; Vodak, D.; Wachter, J.; O'Keeffe, M.; Yaghi, O. M. Systematic design or pore size and functionality in isoreticular MOFs and their application in methane storage. *Science* **2002**, *295* (5554), 469-472.

[21] (a) Ma, L.; Lee, J. Y.; Li, J.; Lin, W. 3D metal-organic frameworks based on elongated tetracarboxylate building blocks for hydrogen storage. *Inorg. Chem.* **2008**, *47* (10), 3955-3957. (b) Wu, S.; Ma, L.; Long, L.-S.; Zheng, L.-S.; Lin, W. Three-dimensional metal-organic frameworks based on functionalized tetracarboxylate linkers: Synthesis, structures, and gas sorption studies. *Inorg. Chem.* **2009**, *48* (6), 2436-2442; (c) Ma, L.; Lin, W. Chirality-controlled and solvent-templated catnation isomerism in metal-organic frameworks. *J. Am. Chem. Soc.* **2008**, *130* (42), 13834-13835.

[22] Lin, X.; Jia, J. H.; Zhao, X. B.; Thomas, K. M.; Blake, A. J.; Walker, G. S.; Champness, N. R.; Hubberstey, P.; Schröder, M. High H_2 adsorption by coordination-framework materials. *Angew. Chem. Int. Ed* **2006**, *45*(44), 7358-7364.

[23] Spek, A. L. Single-crystal structure validation with the program PLATON. *J. Appl. Crystallogr.* **2003**, 36 (1), 7-13.

[24] Walton, K.S.; Snurr, R.Q. Applicability of the BET method for determining surface areas of microporous metal-organic frameworks. *J. Am. Chem. Soc.* **2007,** *129* (27), 8552-8556.

[25] (a) Serre, C.; Millange, F.; Thouvenot, C.; Noguès, M.; Marsolier, G.; Louër, D.; Férey, G. Very large breathing effect in the first nanoporous chromium(III)-based solids: MIL-53 or $Cr^{III}(OH) \bullet \{O_2C\text{-}C_6H_4\text{-}CO_2\} \bullet \{HO_2C\text{-}C_6H_4\text{-}CO_2H\}_x \bullet H_2O_y$. *J. Am. Chem. Soc.* **2002,** *124* (45), 13519-13526. (b) Llewellyn, P.L.; Maurin, G.; Devic, T.; Loera-Serna,S.; Rosenbach, N.; Serre, C.; Bourrelly, S.; Horcajada, P.; Filinchuk, Y.; Ferey, G. Prediction of the conditions for breating of metal organic framework materials using a combination of X-ray powder diffraction, microcolorimetry, and molecular simlation. *J. Am. Chem. Soc.* **2008,** *130* (38), 12808-12814.

[26] Cavka, J.H.; Jakobsen, S.; Olsbye, U.; Guillou, N.; Lamberti, C.; Bordiga, S.; Lillerud, K.P. A new zirconium inorganic building brick forming metal organic frameworks with exceptional stability. *J. Am. Chem. Soc.* **2008**, *130* (42)*,* 13850–13851.

[27] (a) Mircea, D.; Long, J. R. Hydrogen storage in microporous metal-organic frameworks with exposed metal sites. *Angew. Chem. Int. Ed.* **2008**, *47* (36), 6766-6779. (b)Zhao, D.; Yuan, D.; Zhou, H-C. The current status of hydrogen storage in metal-organic frameworks. *Energy Environ. Sci.* **2008**, *1*, 222-235. (c) Rowsell, J. L. C.; Yaghi, O. M. Strategies for hydrogen storage in metal-organic frameworks. *Angew. Chem. Int. Ed.* **2005**, *44* (30), 4670-4679; (d) Farha, O.K.; Spokoyny, A.M.; Mulfort, K.L.; Hawthorne, M.F.; Mirkin, C.A.; Hupp, J.T. Synthesis and hydrogen sorption properties of carborane bases metal-organic framework materials. *J. Am. Chem. Soc*. **2007**, *129* (42), 12680-12681.